

# **Funktionale Nanobausteine mittels kontrollierter Exfolierung von Schichtsilicaten**

## **Dissertation**

zur Erlangung des akademischen Grades eines

**Doktor der Naturwissenschaften (Dr. rer. nat.)**

im Fach Chemie

an der Fakultät Biologie, Chemie und Geowissenschaften

der Universität Bayreuth

vorgelegt von

**Matthias Stöter**

geboren in Leer (Ostfriesland)

Bayreuth, 2016



Die vorliegende Arbeit wurde in der Zeit von Oktober 2010 bis September 2015 in Bayreuth am Lehrstuhl für Anorganische Chemie I unter Betreuung von Herrn Prof. Dr. Josef Breu angefertigt.

Vollständiger Abdruck der von der Fakultät für Biologie, Chemie und Geowissenschaften der Universität Bayreuth genehmigten Dissertation zur Erlangung des akademischen Grades eines Doktors der Naturwissenschaften (Dr. rer. nat.).

Dissertation eingereicht am 13.01.2016

Zulassung durch die Promotionskommission: 20.01.2016

Wissenschaftliches Kolloquium: 03.05.2016

Amtierender Dekan: Prof. Dr. Stefan Schuster

Prüfungsausschuss:

Prof. Dr. Josef Breu (Erstgutachter)

Prof. Dr. Georg Papastavrou (Zweitgutachter)

Prof. Dr. Peter Strohriegl (Vorsitz)

Prof. Dr. Hans-Werner Schmidt



*Stöte drüppen höln dee steen*

(Ostfriesisches Sprichwort, unbekannter Verfasser)



*Meiner Frau Ann-Kathrin  
sowie meinen beiden Kindern Eike Dirk und Antje Lina*



# Inhaltsverzeichnis

<b>Abkürzungsverzeichnis</b>	3
<b>1. Zusammenfassung</b>	4
<b>2. Summary</b>	6
<b>3. Einleitung</b>	8
3.1 Herausforderungen an die Materialchemie	8
3.2 Maßgeschneiderte Materialien durch Exfolierung von Schichtverbindungen	10
3.3 Optimierung der Materialeigenschaften durch Kontrolle der Schichtanzahl	11
3.4 Synthese alternierender Schichtstrukturen mittels Intercalationsreaktionen	14
3.5 Schmelzsynthese zur Herstellung ladungshomogener Schichtsilicate	17
3.6 Synthese von Janus-Partikeln mittels geordneter Wechsellagerung	18
3.7 Literatur	21
<b>4. Synopsis</b>	26
4.1 Ladungshomogener Natriumhectorit	27
4.2 Bildung geordneter Wechsellagerungen	29
4.3 Synthese funktionaler Doppelschichten	30
4.4 Mechanisch verstärkte Doppelschichten zur Synthese von Janus-Plättchen	32
4.5 Kontrollierte Exfolierung von Schichtsilicaten	34
<b>5. Ergebnisse</b>	36
5.1 Ladungshomogener Natriumhectorit	36
5.1.1 Nanoplatelets of sodium hectorite showing aspect ratios of $\approx 20000$ and superior purity	37
5.1.2 Supporting information	43
5.2 Bildung geordneter Wechsellagerungen	52
5.2.1 Ordered heterostructures of two strictly alternating types of nanoreactors	53
5.2.2 Supporting information	61
5.3 Synthese funktionaler Doppelschichten	71
5.3.1 Encapsulation of functional organic compounds in nanoglass for optically anisotropic coatings	72
5.3.2 Nanoglas-Verkapselung funktionaler organischer Verbindungen für optisch anisotrope Beschichtungen	77
5.3.3 Supporting information	82

5.4 Mechanisch verstärkte Doppelschichten zur Synthese von Janus-Plättchen	98
5.4.1 Controlled exfoliation of layered silicate heterostructures into bilayers and their conversion to giant Janus platelets	100
5.4.2 Supporting information	106
5.5 Kontrollierte Exfolierung von Schichtsilicaten	123
5.5.1 Tunable exfoliation of synthetic clays	124
5.6 Neue Einblicke in die Delaminierung von Schichtverbindungen	147
5.6.1 In depth insights into the key steps of delamination of charged 2D materials	148
5.6.2 Supporting information	165
<b>6. Publikationsliste</b>	178
6.1 Publikationen	178
6.2 Konferenzbeiträge	179
6.3 Presseveröffentlichungen	179
<b>7. Danksagung</b>	180
<b>8. Erklärung des Verfassers</b>	182

## Abkürzungsverzeichnis

AFM	Rasterkraftmikroskopie (atomic force microscopy)
CEC	Kationenaustauschkapazität (cation exchange capacity)
LBL	Schicht-für-Schicht (layer by layer)
LDH	Doppelschichthydroxid (layered double hydroxide)
OLED	Organische Leuchtdiode (organic light emitting diode)
PB	Polybutadien
PEI-EO	Polyethylenoxid-co-polyethylenimin
PDMS	Polydimethylsiloxan
PMMA	Polymethylmethacrylat
PS	Polystyrol
PVOH	Polyvinylalkohol
PXRD	Röntgendiffraktometrie an Pulvern (powder x-ray diffraction)
SANS	Neutronenkleinwinkelstreuung (small angle neutron scattering)
SAXS	Röntgenkleinwinkelstreuung (small angle x-ray scattering)
T <sub>c</sub>	Kritische Supraleitungstemperatur
TEM	Transmissionselektronenmikroskopie
TGA	Thermogravimetrische Analyse

## 1. Zusammenfassung

In der vorliegenden Dissertation wird ein neuartiges Konzept zur kontrollierten Exfolierung von Schichtverbindungen in funktionale Doppelschichten vorgestellt.

Das entwickelte Syntheseprinzip basiert auf der Bildung von streng alternierenden Wechsellagerungen, in denen sowohl funktionelle Zwischenschichten als auch definierte Sollbruchstellen generiert werden.

Die auf diese Weise hergestellten Doppelschichten sind aufgrund der hohen strukturellen Anisotropie zum Aufbau von komplexen funktionalen Systemen verwendbar. Als mögliche Anwendungen werden optisch-anisotrope Beschichtungen, die Herstellung mechanisch verstärkter Nanofüllstoffe und die Verwendung von Doppelschichten als Ausgangsverbindung für die asymmetrische Oberflächenmodifikation von Nanoplättchen exemplarisch vorgestellt.

Zur Realisierung dieses Konzeptes wurde zunächst ein Schichtsilicat aus einer Schmelzsynthese untersucht, das nach einem Langzeittempern ideale Eigenschaften für diese Studie aufwies. So konnte durch die Nachbehandlung eine deutliche Erhöhung der Phasenreinheit, der intrakristallinen Reaktivität, sowie eine Homogenisierung der Ladungsdichteverteilung nachgewiesen werden. Durch die niedrige und homogene Schichtladung zeigt dieses Schichtsilicat in Wasser ein homogenes osmotisches Quellverhalten und delaminiert vollständig in einzelne Silicatschichten. Die osmotische Quellung ist als besonders schonendes Verfahren ideal geeignet, um Schichtstapel kontrolliert in definierte Doppelschichten zu exfolieren.

Aufgrund der homogenen Ladungsdichteverteilung konnte im nächsten Schritt die Ausbildung von geordneten Wechsellagerungen mit verschiedenen organischen Kationen untersucht und der Ordnungsmechanismus aufgeklärt werden. Es zeigte sich, dass in der geordneten Wechsellagerung die Moleküle im Zwischenschichtraum eine dichte Packung realisieren, wobei die Kationendichte lokal von der mittleren Ladungsdichte der Wirtsverbindung abweicht. Dadurch wird eine lokale Ladung erzeugt, welche in der nächsten Zwischenschicht durch eine entsprechend angepasste Kationendichte ausgeglichen wird, was wiederum die alternierende Abfolge der Zwischenschichten erklärt.

Mit dem Wissen über die Synthese und den Bildungsmechanismus von geordneten Wechsellagerungen war es anschließend möglich, funktionale organische Zwischenschichten einzufügen, welche mit Natriumzwischenschichten alternieren. Letztere können als definierte Sollbruchstellen aufgefasst werden, da sie nach

Wasserzugabe osmotisch quellen und dabei die geordnete Wechsellagerung kontrolliert in Doppelschichten mit darin verkapselten, funktionalen Molekülen exfolieren.

Als funktionale Modellverbindung wurde ein fluoreszierendes Stilbazoliumderivat ausgewählt. Durch Intercalation und Bildung der Doppelschichten wurde die Dispergierbarkeit dieser funktionellen Spezies in Wasser ermöglicht, die thermische Stabilität verbessert, sowie die Quantenausbeute erhöht. Ein interessantes Anwendungsfeld eröffnet sich durch die Ausrichtung der Emittermoleküle innerhalb der strukturell anisotropen Doppelschicht. Dadurch können optisch-anisotope Systeme realisiert werden, die eine Effizienzsteigerung in optoelektronischen Anwendungen bei gleichzeitiger chemischer und thermischer Stabilisierung des Emitters versprechen.

Im letzten Schritt dieser Arbeit wurden Doppelschichten hergestellt, die als Zwischenschichtkation Ammonium-Ionen besitzen. Durch die strukturelle Passung des Ammoniumkations mit den hexagonalen Kavitäten kollabieren die Zwischenschichten nach dem Trocknen irreversibel und werden durch die eingeschlossenen Ammoniumionen miteinander verzahnt. Die dadurch zu erwartende mechanische Verstärkung wurde durch die Messung des in-plane Moduls mittels der von Kunz et al. entwickelten Wrinkling-Methode bestätigt.

Ein weiterer Vorteil dieser Ammonium-Doppelschichten besteht in der möglichen Spaltung durch Anbasen und gleichzeitigem Austausch mit Kationen, welche eine hohe Hydratationsenthalpie besitzen (z.B. Lithiumionen). Auf diese Weise wird die Doppelschicht mittels osmotischer Quellung gespalten. Nach der externen Modifikation mit einem kationischen Copolymer konnte durch Zugabe von Lithiumhydroxid die Symmetrie des Silicatplättchens gezielt gebrochen werden. Die so erzeugte Janusmodifikation wurde mittels selektiver Adsorption von Dendrimeren an die polymerfreie Silicatoberfläche belegt. Die Dendrimeroberfläche ließ sich dabei sowohl topographisch als auch hinsichtlich der Adhäsion von der geschützten Copolymeroberfläche, an die kaum Dendrimere adsorbieren, unterscheiden.

Das innovative Konzept zur Synthese von Januspartikeln lässt sich auf verschiedene deprotonierbare Doppelschichten und beliebige kationische Modifikatoren übertragen. Aus diesem Grund bietet die Doppelschichtsynthese vielfältige Anwendungsmöglichkeiten für Systeme, in denen sowohl die Grenzflächenchemie als auch die mechanischen Eigenschaften zu optimieren sind, z.B. im Bereich von stabilisierten Emulsionen, Coatings und Polymerblends.

## 2. Summary

A novel concept for the controlled exfoliation of layered compounds into functional bilayers is presented within this thesis. The synthesis is based on simple intercalation reactions. Ordered interstratified structures are formed where a functional interlayer alternates with an interlayer which is capable of osmotic swelling. Therefore, the latter can be considered as a predetermined slipping plane for a gentle and controlled exfoliation into bilayers.

Due to the structural anisotropy of the bilayers platelet texturing is straightforward which can be used for the self assembly to complex functional systems. Anisotropic coatings, mechanically reinforced nanofillers for polymer-nanocomposites and the synthesis of Janus-platelets are given as just a small selection of examples in a much broader range of potential applications.

In order to realize this concept, a novel synthetic clay was investigated which was made by melt synthesis followed by a long term annealing procedure. The characterization of this novel material proofed increased phase purity, high intracrystalline reactivity and superior layer charge homogeneity. Furthermore the low and homogeneous layer charge enables osmotic swelling which results for highly diluted suspensions in a complete delamination into individual layers. Osmotic swellability and charge homogeneity are both essential ingredients for formation of ordered interstratifications and their controlled exfoliation.

Next the synthesis and mechanism of formation of ordered interstratified structures were investigated. Two differently sized organic cations were used. It was found that the organic cations form a close packed organic interlayer structure in the ordered interstratified phase. Close packing was in both cases achieved by a deviation of the interlayer cation density from the average host charge density. This variation causes the alternating interlayer sequence.

The gained knowledge was then applied to investigate the properties of ordered interstratifications where a functional organic interlayer alternates with osmotically swellable sodium interlayers. A stilbazolium dye was chosen as a model functional compound. Upon addition of water to this interstratified material, double stacks are formed where a dye interlayer is localized between two silicate layers. It turned out that the encapsulation enables the dispersion of the hydrophobic dye in water, increases the thermal stability and improves the solid state photoluminescent quantum yield as compared to the solid dye salt.

Another interesting feature of the functional bilayers results from the preferred orientation of the encapsulated molecules. Due to the high aspect ratio, polymer based nanocomposite coatings are perfectly textured and show optical anisotropy. The preferred molecule orientation in combination with an improved chemical and thermal stability is an important feature which is expected to increase the performances of optoelectronic applications, for example in light emitting devices.

Finally bilayers were synthesized where the central interlayer species is ammonium. The size of the ammonium cation fits well to the size of the hexagonal cavities located at the silicate surface. As a consequence the interlayer space irreversibly collapse upon drying and the ammonium cations protrude into the upper and lower hexagonal cavities. An improved stiffness was verified with a wrinkling procedure which was recently published by Kunz et al. The ammonium-bilayer showed an increased in-plane modulus compared to the monolayer.

Another advantage of the ammonium functionality arises from the possibility of bilayer cleavage. Addition of bases with counterions of high hydration enthalpy, like lithium hydroxide, completely removes the ammonium from the interlayer, inducing osmotic swelling. This way the platelet symmetry can be easily broken if bilayers are externally modified with polycations. After cleaving Janus-platelets are formed which feature two different clay surfaces. One platelet side is completely modified with the cationic polymer while the cleaved one is covered with lithium cations.

A novel analytical method was established to proof the Janus-character. In this approach the distinct adsorption characteristics of cationic dendrimers to the two different surfaces were utilized. Nearly no dendrimers adsorb to the polymer covered surface, while the silicate surface is highly attractive for adsorption. The topographical and adhesion properties of the dendrimer covered surface are distinctly different from the dendrimer-free polymer surface.

The novel and versatile concept can be easily transferred to other types of bilayers made with protonated organic interlayer cations and arbitrary modifiers. Consequently, the novel Janus-synthesis could be interesting for all applications where interfacial as well as mechanical properties have to be considered. Possible fields of applications are coatings, emulsions and polymer blends.

### 3. Einleitung

#### 3.1 Herausforderungen an die Materialchemie

Die globale Herausforderung im 21. Jahrhundert besteht im alternativlosen Wechsel von fossilen Energieträgern, wie Öl, Gas und Kohle zu regenerativen Energieträgern auf Basis von Sonnenlicht, Windkraft und Wärme.<sup>1-3</sup> Diese technische Revolution schließt neben der Gewinnung von regenerativen Energien, deren Speicherung und der gleichzeitigen Verringerung des Energieverbrauchs, auch die Synthese von chemischen Verbindungen aus nichtfossilen Energieträgern und CO<sub>2</sub> ein.<sup>2-4</sup>

Für diese epochale Aufgabe muss die Festkörpermaterialforschung mit neuen Materialien einen entscheidenden Beitrag leisten. Ein zentraler Entwicklungsansatz besteht dabei in der Manipulation von Materialien und Strukturen auf der Nanoebene.

Ein Beispiel für das enorme Potential, welches sich durch eine kontrollierte Nanostrukturierung eröffnet, stellen natürliche Nano-Kompositmaterialien dar. Strukturen, die ähnlich wie Perlmutt von der Nano- bis auf die Mesoebene organisiert sind, ermöglichen einzigartige Materialeigenschaften.<sup>5</sup> Auf diese Weise könnten mechanisch stabilere und dennoch leichtere Werkstoffe erzeugt werden. Diese neuartigen Werkstoffe könnten beispielsweise Stähle in Kraftfahrzeugen ersetzen, was das Gewicht reduzieren und dadurch den Kraftstoffverbrauch senken würde.

Nanostrukturierung von Materie ist aber auch für photokatalytische Systeme wichtig. Dabei steht gegenwärtig die Verwendung von Sonnenlicht als Energiequelle und die Umsetzung von CO<sub>2</sub> als Kohlenstoffquelle im Vordergrund der Forschungsanstrengungen.<sup>3,6</sup>

Die Nanostrukturierung der katalytischen Materialien ist ein wichtiger Ansatz zur Verbesserung der katalytischen Effizienz. Könnten sich Materialien nach dem Baukastenprinzip auf der Nanoebene gezielt „designen“ lassen, so ließen sich ihre chemischen und physikalischen Eigenschaften für die Katalyse leichter optimieren.

Ein solcher „Nanobaukasten“ ist theoretisch am einfachsten mittels atomar-definierter Nanoschichten zu erreichen. Werden z.B. 1 nm dünne Silicatschichten in einer Polymermatrix definiert eingebettet, entstehen texturierte Materialien, in denen bis auf die Mesoskala anorganische Nanoschichten mit der Polymermatrix alternieren. Diese Nanokompositssysteme besitzen eine Transparenz und Flexibilität von Polymeren, weisen aber gleichzeitig eine überragende Gasbarriere und mechanische Eigenschaften auf.<sup>7,8</sup>

In ähnlicher Weise könnte ein hierarchischer Aufbau aus atomar-definierten Schichten von Materialien für die Katalyse erfolgen, so dass sich im Idealfall die elektronischen Bandstrukturen und damit die katalytischen Eigenschaften gezielt tunen lassen.<sup>9,10</sup>

Besonders erfolgsversprechend scheint hierbei die Verwendung von exfolierten Schichtmaterialien zu sein. Mit Dreier-, Zweier- oder vollständig delaminierten Schichten könnte die maßgeschneiderte Herstellung neuer Materialien relativ einfach durch gezielte Anordnung nach dem „LEGO-Prinzip“ erfolgen (Abbildung 1).<sup>9</sup>

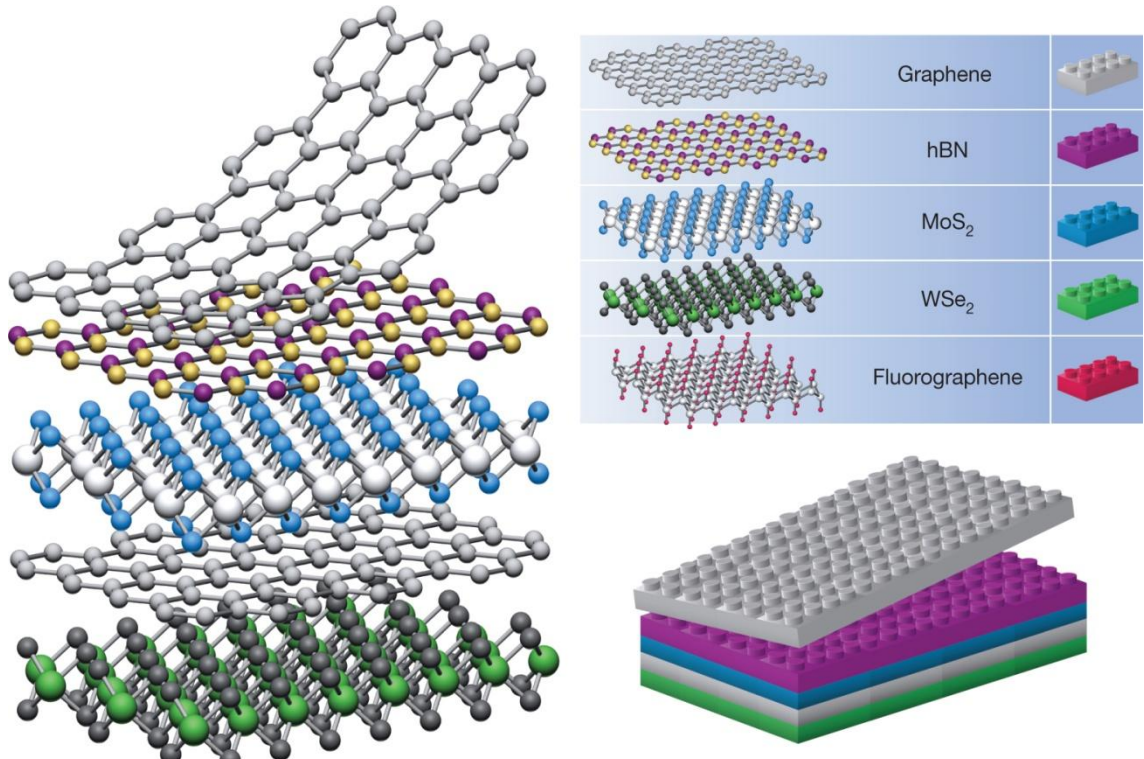


**Abbildung 1:** Das Konstruktionsprinzip von maßgeschneiderten Schichtmaterialien lässt sich mit dem LEGO-Baukastenprinzip vergleichen. Die einzelnen LEGO-Bausteine entsprechen zweidimensionalen Schichtmaterialien, die je nach benötigtem Eigenschaftsprofil gezielt aufgebaut werden.<sup>9</sup> Reproduced with permission from Reference 9. Copyright 2013, Nature Publishing Group.

Es handelt sich hierbei um eine Kombination eines Top-down und Bottom-up-Verfahrens, d.h. der Exfolierung eines Bulk-Kristalls in dünnere zweidimensionale Schichten (Top-down) und dem Aufbau der synthetischen schichtförmigen Heterostruktur (Bottom-up-Verfahren).

Der Physiker Andre Konstantin Geim, der den Nobelpreis für die Erforschung von Graphen innehat, sieht solche maßgeschneiderten Heterostrukturen in greifbare Nähe gekommen: „*Such artificial materials engineered with one-atomic-plane accuracy would have been science fiction a few years ago but are within the grasp of today’s technology.*“<sup>9</sup>

Bisher wurden streng alternierende Heterostrukturen aus unterschiedlichen Schichtverbindungen mittels aufwendiger mechanischer Trennverfahren (Scotch-Tape Methode) hergestellt.<sup>9</sup>

Für die großtechnische Materialsynthese ist dieser Syntheseansatz natürlich nicht praktikabel. Aus diesem Grund wird gegenwärtig intensiv nach Top-down-Verfahren zur kontrollierten Exfolierung von Schichtmaterialien gesucht, die großtechnisch skalierbar und ökonomisch attraktiv sind.<sup>11,12</sup>

Über die Möglichkeiten zur Exfolierung von Schichtverbindungen und die Vorteile, die sich dadurch ergeben, soll im Folgenden detailliert eingegangen werden.

## 3.2 Maßgeschneiderte Materialien durch Exfolierung von Schichtverbindungen

Das große Potential, welches schichtförmige Heterostrukturen bieten, ist auf die besondere Eigenschaft von zweidimensionalen Materialien zurückzuführen: Bei anorganischen Schichtmaterialien hängen die physikalischen Eigenschaften in großem Maße von der Translationssymmetrie entlang der Stapelrichtung ab. Durch die anisotropen Bindungsverhältnisse innerhalb einer Schichtverbindung, d.h. starken Bindungen innerhalb der Schichten (v.a. kovalente und ionische Bindungen) und meist schwachen Wechselwirkungen zwischen den einzelnen Schichten (van der Waals-Wechselwirkungen und Wasserstoffbrückenbindungen), kann die Ordnung und damit die Translationssymmetrie relativ leicht beeinflusst werden. Die physikalischen Eigenschaften der Schichtverbindung werden dadurch stark verändert.

Ein eindrucksvolles Beispiel für einen solchen Effekt ist die 30 fache Verringerung der Wärmeleitfähigkeit von WSe<sub>2</sub>-Schichten gegenüber eines perfekt geordneten WSe<sub>2</sub>-Einkristalls nach Einführung von turbostratischen Fehlordnungen.<sup>13</sup> Durch die Stapelfehler wird die Ausbreitung von kollektiven Gitterschwingungen (Phononen) extrem gestört und damit der Wärmetransport entlang der Stapelrichtung stark verringert.

Durch eine vollständige Delaminierung in einzelne Schichten wird die Translationssymmetrie entlang der Stapelrichtung komplett aufgehoben. Durch die damit einhergehende Veränderung der Bandstruktur unterscheiden sich die elektronischen, magnetischen und mechanischen Eigenschaften von der Volumenphase erheblich.<sup>14-17</sup> Beispielsweise zeigen einzelne MoS<sub>2</sub>-Schichten Piezoelektrizität, während die Volumenphase keinen Piezoeffekt aufweist.<sup>16</sup>

Durch eine zunehmende Exfolierung werden auch die mechanischen Eigenschaften gegenüber dem Bulkmaterial geändert. Beispielsweise sind Graphitoxid und Schichtsilicate (z.B. Hectorit) als mikrometerdicke Takoide vergleichsweise spröde. Nach einer vollständigen Delaminierung weisen jedoch einzelne Hectorit- und Graphitoxidschichten eine signifikante Zunahme der Flexibilität auf, wie durch kontrollierte Faltungsexperimente gezeigt werden konnte.<sup>18,19</sup> Neben der Flexibilität steigt auch die morphologische Anisotropie der Plättchen, was durch das Aspektverhältnis, d.h. Durchmesser ( $L$ ) dividiert durch die Dicke der Plättchen ( $h$ ), beschrieben wird (Abbildung 2).

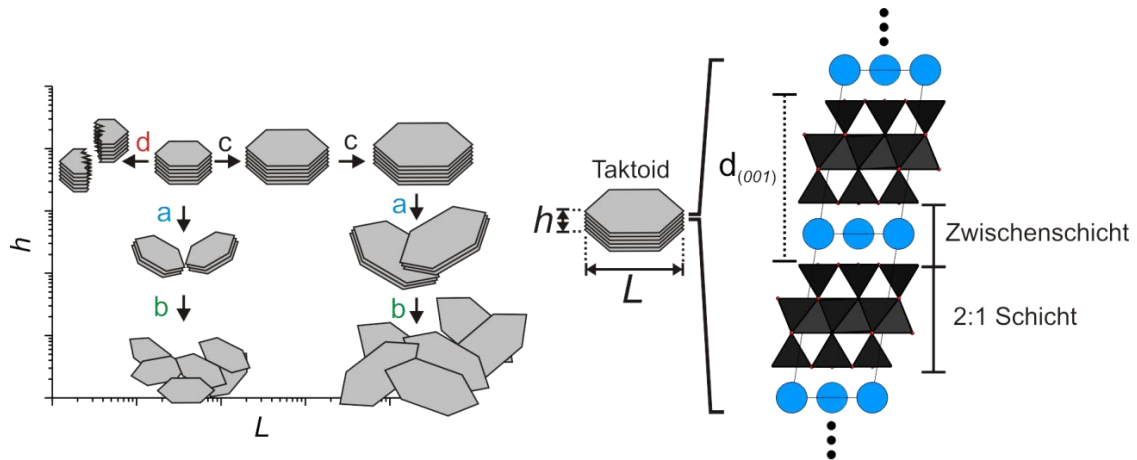


**Abbildung 2:** (Links) Die Verringerung der Taktoidhöhe ( $h$ ) durch Exfolierung (a) bzw. Delaminierung (b) erhöht das Aspektverhältnis während der Bruch der Plättchen (d) dieses verringert. Extrem hohe Aspektverhältnisse können dadurch erreicht werden, dass der Taktoiddurchmesser ( $L$ ) durch verbesserte Synthesebedingungen erhöht wird (c) und danach eine vollständige Delaminierung (b) erfolgt.<sup>20</sup> (Rechts) Struktur eines 2:1 Schichtsilicates. Adapted from Reference 20 with permission from The Royal Society of Chemistry.

Extrem hohe Aspektverhältnisse können durch die Kombination von erhöhtem Taktoiddurchmesser (Abbildung 2, c) und einer vollständigen Delaminierung in einzelne Schichten (Abbildung 2, b) generiert werden.<sup>20</sup> Durch die Wahl der geeigneten Synthesebedingungen (z.B. Schmelzsynthese) können sehr große Taktoiddurchmesser erreicht werden (siehe **Kapitel 3.5**).<sup>21,22</sup> Die Verwendung solcher plättchenartigen Füllstoffe mit extrem hohen Aspektverhältnissen verbessern beispielsweise die Gasbarriereeigenschaften von Polymer納kompositen bei gleichem Füllstoffanteil deutlich.<sup>7,8,23</sup>

Eine vollständige Delaminierung in einzelne Schichten ist jedoch keineswegs trivial. Die anziehenden Wechselwirkungen (z.B. Coulombanziehung, van-der-Waals-Wechselwirkungen und Wasserstoffbrückenbindungen) müssen durch entsprechende abstoßend wirkende Kräfte überwunden werden. Bei neutralen Schichtverbindungen (z.B.

Graphit,  $\text{MoS}_2$ ) ist eine komplette Delaminierung in einzelne Schichten schwierig, da als energetische Triebkraft für die Expansion nur relativ schwache Wasserstoffbrückenbindungen oder  $\pi$ - $\pi$ -Wechselwirkungen vorliegen. In Lösungsmitteln weiten die neutralen Schichten daher nicht selbsttätig auf. Selbst nach Intercalation benötigt man zur Scherung mechanische Verfahren (Mahlen, Ultraschall, thermische Schockexpansion). Diese mechanischen Ansätze führen allerdings meist in gewissem Maße zu einem Bruch der Plättchen und damit zu einer Abnahme des Aspektverhältnisses (Abbildung 2, d).<sup>24-27</sup>

Materialien, die geladene Schichten aufweisen, (z.B. Layered Double Hydroxides (LDH) und Schichtsilicate) besitzen zur Ladungskompensation ein- oder mehrwertige Zwischenschichtionen. In Abbildung 2 ist rechts die Struktur eines 2:1-Schichtsilicates gezeigt. Bei 2:1-Schichtsilikaten wird die negative Schichtladung durch isomorphe Substitution in der Oktaederschicht (z.B. Hectorit) oder in den Tetraederschichten (z.B. Saponit) generiert. Gegenüber neutralen Verbindungen bietet sich dadurch der Vorteil, dass die Expansion der Schichten durch die Solvatation, bzw. Hydratation der Zwischenschichtionen beeinflusst werden kann. Die Hydrationsenthalpie ist unter bestimmten Bedingungen ausreichend hoch, so dass durch eine Quellung die anziehenden Wechselwirkungen vollständig überwunden werden.

Für Schichtsilicate sind die Rahmenbedingungen diesbezüglich besonders günstig: Einwertige Kationen, wie  $\text{Li}^+$  und  $\text{Na}^+$ , weisen im Gegensatz zu Anionen, die in den Zwischenschichträumen in LDHs vorliegen, eine relativ hohe Hydrationsenthalpie auf.<sup>28</sup> Gleichzeitig sind die anziehenden Wechselwirkungen, welche vor allem durch die Höhe der Schichtladung bestimmt werden, durch die vergleichsweise niedrige Schichtladung besonders gering.<sup>29</sup> In günstigsten Fall tritt eine osmotische Quellung ein, d.h. der Abstand der Schichten wird nur durch das Verhältnis von Feststoff zu flüssigem Medium bestimmt. Bei höheren Verdünnungen delaminieren die Schichtpakete spontan zu einzelnen Schichten.<sup>30-33</sup> In **Kapitel 5.1** dieser Arbeit wird die Synthese und Charakterisierung eines quellfähigen Hectorits mit Schichtladung 0.5 beschrieben, mit dem sich nach Delaminierung Aspektverhältnisse von fast 20000 realisieren lassen.

Vollständig delamierte Einzelschichten könnten, ähnlich wie in Abbildung 1 schematisch gezeigt, zum Aufbau von Strukturen mit mehreren gleichen, oder unterschiedlichen Schichten nach dem Bottom-up-Prinzip verwendet werden. Eine weitere Möglichkeit ist die gezielte Synthese von Doppel- oder Dreischichtstrukturen nach dem Top-down-Prinzip, auf die im Folgenden näher eingegangen werden soll.

### 3.3 Optimierung der Materialeigenschaften durch Kontrolle der Schichtanzahl

Durch die Kombination von zwei oder mehreren Schichten des gleichen Schichtmaterials lassen sich Materialeigenschaften erreichen, die vollständig delamierte Schichten nicht bieten.

Werden beispielweise schichtförmige Füllstoffe für die Verwendung in Polymernanokompositen vollständig delaminiert, steigt zwar auf der einen Seite das Aspektverhältnis und damit die Grenzfläche zwischen Füllstoff und Polymer, aber andererseits nimmt die Biegesteifigkeit der Plättchen stark ab.<sup>34</sup> Stehen bei der Materialoptimierung nicht nur die Barriereeigenschaften, sondern auch die mechanischen Kenndaten des Polymernanokomposites (z.B. Kerbschlagzähigkeit) im Vordergrund, sind steifere Plättchen, die aus mehreren Schichten aufgebaut sind, gegenüber vollständig delamierten Schichten zu bevorzugen.<sup>25,34-36</sup> Das Optimum der gewünschten Materialeigenschaft, die von der Grenzfläche und Steifigkeit bestimmt wird, hängt deshalb von der exakten Anzahl der gestapelten Schichten ab.<sup>34</sup>

Nicht nur die mechanischen, sondern auch die elektronischen Eigenschaften werden durch die Schichtanzahl beeinflusst. Ein eindrucksvolles Beispiel ist die Hochtemperatursupraleitung von Cupraten (z.B. Yttrium-Barium-Kupferoxid-Supraleitern  $\text{YBa}_2\text{Cu}_3\text{O}_7$ ). In dieser Materialklasse alternieren die für die Supraleitfähigkeit verantwortlichen  $\text{CuO}_2$ -Schichten mit isolierenden Schichten. Die Höhe der kritischen Supraleitungstemperatur ( $T_c$ ) hängt, bei gleicher Materialzusammensetzung und Dicke der isolierenden Zwischenschicht, vor allem von der Anzahl der alternierenden  $\text{CuO}_2$ -Schichten in der Elementarzelle ab. Für verschiedenen Materialklassen wurde beobachtet, dass  $T_c$  stets mit der Anzahl der Schichten steigt und ein Temperaturmaximum erreicht ist, wenn genau drei alternierende  $\text{CuO}_2$ -Schichten in der Elementarzelle vorliegen.<sup>37</sup>

Eine Abhängigkeit der elektronischen Eigenschaften von der Stapelanzahl ist auch für exfolierte, zweidimensionale Leiter und Isolatoren bekannt. Gegenüber einzelnen Graphenschichten zeigen beispielsweise Drei- und Zweischichtgraphen durch die veränderte Bandstruktur vielversprechende Eigenschaften für zukünftige optoelektronische Anwendungen.<sup>38-41</sup> Interessante elektronische Effekte wurden ebenfalls für Doppelschichten eines natürlichen Glimmers berichtet, der laut einer kürzlich erschienenen Studie halbleitende Eigenschaften nach Exfolierung aufwies.<sup>42</sup>

Aus diesem Grund ist die Entwicklung eines simplen Verfahrens zur direkten Exfolierung einer Schichtverbindung in definierte Zwei- und Dreischichtstrukturen mittels eines

ökonomischen Top-down-Ansatzes sehr erstrebenswert. Eine vielversprechende Synthesemöglichkeit besteht in der Verwendung von geordneten Heterostrukturen, die durch simple Intercalationsreaktionen hergestellt werden. Auf diesen Ansatz zur Synthese von Doppelschichtstrukturen soll im Folgenden näher eingegangen werden.

### **3.4 Synthese alternierender Schichtstrukturen mittels Intercalationsreaktionen**

Eine einfache, skalierbare und kostengünstige Form der Bildung von geordneten Heterostrukturen stellt die Synthese mittels Intercalationsreaktionen dar. So ist beispielsweise von Graphitintercalationsverbindungen bekannt, dass sich während der Intercalation, alternierende Strukturen ausbilden können, die als geordnete Wechsellagerungen, bzw. „Stages“ bezeichnet werden.<sup>43,44</sup>

Bei diesen geordneten Strukturen können zwei, drei oder sogar vier Graphenschichten mit intercalierten Schichten alternieren.<sup>45</sup> Kürzlich wurde ein Verfahren vorgestellt, bei dem die intercalierten Schichten einer geordneten Wechsellagerung als Sollbruchstellen für die kontrollierte Trennung in Schichten mit definierter Anzahl dienen.<sup>40</sup>

Die Exfolierung dieser geordnet wechselgelagerten Graphitintercalationsverbindungen mittels thermischer Expansion bei 800°C, führt je nach Stage-Typ der Ausgangsverbindung zur Bildung von Zweischicht- oder Dreischichtgraphen.<sup>40</sup> Allerdings besteht bei diesem Syntheseansatz gegenwärtig noch das Problem, dass die synthetisierten Wechsellagerungen starke Stapelfehlordnungen aufweisen. Hierdurch entstehen Defekte, welche zu Nebenphasen mit anderer Schichtanzahl führen, oder die expandierten Schichten teilweise zusammenhalten. Aus diesem Grund muss die expandierte Intercalationsverbindung mittels Ultraschall aufgebrochen und dispergiert werden.<sup>40</sup> Die extrem starke mechanische Einwirkung durch die abrupte thermische Expansion als auch durch die nachfolgende Ultraschallbehandlung führt unweigerlich zu einer Verringerung des Plättchendurchmessers.

Die Synthese muss daher sowohl hinsichtlich der Qualität der geordneten Wechsellagerung als auch hinsichtlich der Exfolierungsmethode optimiert werden. Am schonendsten könnte die Exfolierung durch eine osmotische Quellung, wie in **Kapitel 5.3** beschrieben, erfolgen. Für eine verbesserte Synthese von geordneten Wechsellagerungen ist des Weiteren ein tieferes Verständnis der Bildungsmechanismen erforderlich. Auf diese Weise könnte die Ausordnung und damit die Ausbeute der angestrebten Schichtstrukturen verbessert werden. Aus dem Bereich der Graphitintercalationsverbindungen gibt es als Erklärung für die

Ursache der Bildung bisher nur recht spekulative Erklärungsansätze. Eine These sieht die Ursache in der Minimierung von Spannungen im Festkörper.<sup>40,43</sup> Angesichts der hohen Flexibilität einzelner Schichten erscheint dieser Erklärungsansatz etwas spekulativ.

Im Bereich der Schichtsilicatforschung ist das Phänomen der Ausbildung von geordneten Wechsellsagerungen ebenfalls schon länger bekannt und wurde bei natürlichen Vermiculiten und Hectoriten nach partieller Intercalation beobachtet.<sup>46</sup> Aufgrund der symmetrischen Struktur der 2:1-Schichtsilicate und der homogenen Ladungsverteilung entlang der Stapelrichtung war die Ausbildung einer solch geordneten Struktur überraschend und wurde daher intensiv experimentell untersucht.<sup>47-49</sup>

Dabei konnte gezeigt werden, dass eine Ursache für die Ausbildung dieser Strukturen in der Coulomb-Anziehung besteht, die eine Segregation der Kationen unter Bildung von minimierten Schichtabständen bewirkt.<sup>50</sup>

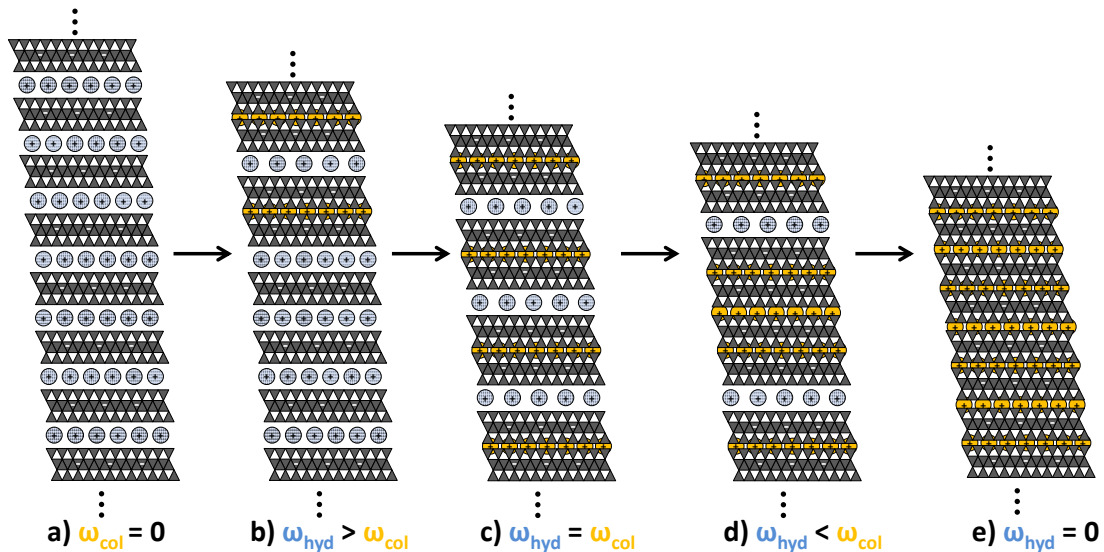


**Abbildung 3:** Partielle Intercalation von Kalium-Ionen (orange) in einen Hectorit mit hydratisierten Natriumzwischenschichten (blau) führt zur Separierung der Kalium-Ionen in kollabierte (col) Kaliumzwischenschichten und hydratisierte (hyd) Natriumzwischenschichten, wobei sich abhängig vom relativen Anteil  $\omega$  eine geordnete Wechsellsagerung ausbildet: (a) reiner Natriumhectorit ( $\omega_{\text{col}} = 0$ ), (b) geordnete Wechsellsagerung neben ursprünglicher Natriumphase ( $\omega_{\text{hyd}} > \omega_{\text{col}}$ ), (c) geordnet wechselgelagerte Phase mit gleicher Anzahl an hydratisierten und kollabierten Zwischenschichten ( $\omega_{\text{hyd}} = \omega_{\text{col}}$ ), (d) weiterer Austausch ( $\omega_{\text{hyd}} < \omega_{\text{col}}$ ) führt zu statistischer Wechsellsagerung und schließlich zu (e) einphasigem Kaliumhectorit ( $\omega_{\text{hyd}} = 0$ ).<sup>49</sup>

Bei partieller Intercalation in Schichtsilicaten führt die Coulomb-Anziehung dazu, dass sich im thermodynamischen Gleichgewicht stets vollständig ausgetauschte und unausgetauschte Schichten ausbilden (Abbildung 3).

Die Gruppe um *Pinnavaia et al.* untersuchte in zahlreichen Arbeiten die Bildung von gemischten anorganisch-organischen Wechsellagerungen nach Einlagerung verschiedener kationischer amphiphiler Moleküle.<sup>48,51-55</sup> Eine Ursache für die Ausbildung der geordneten Wechsellagerung sahen *Pinnavaia et al.* in der Größe und dem Platzbedarf der Kopfgruppe des organischen Kations begründet, welche nach Meinung der Autoren zur Bildung der Wechsellagerung benötigt werde.<sup>51,53</sup> *Pinnavaia et al.* gingen in ihrem Modell der Bildung von geordneten Wechsellagerung aufgrund verschiedener Untersuchungsergebnisse von einer homogenen Kationenverteilung innerhalb der verschiedenen Zwischenschichten aus.<sup>53</sup> Anzumerken ist, dass in diesen Studien das Schichtsilicat in vollentsalztem Wasser zunächst delaminiert wurde, so dass für die Ausbildung der Wechsellagerung ein Restacking notwendig war. Zusätzlich wurde die Intercalation in reinem Wasser durchgeführt. Für Alkylammonium-Ionen ist allerdings aus verschiedenen Intercalationsstudien bekannt, dass die Selektivität für die Intercalation in Wasser mit zunehmender Kettenlänge stark zunimmt.<sup>56-58</sup> Aus diesem Grund könnte es sein, dass die Bildung der verschiedenen Intercalationsverbindungen, welche von *Pinnavaia et al.* untersucht wurden, zum Teil kinetisch kontrolliert war und sich einige der untersuchten Intercalationsverbindungen nicht im thermodynamischen Gleichgewicht befunden haben könnten.

Das Modell von *Pinnavaia et al.* steht vielleicht auch deshalb im Widerspruch zu den Ergebnissen einer Arbeit von *Möller et al.*, in der eine unterschiedliche Kationendichteverteilung in den Zwischenschichten als Ursache für die Ausbildung von geordneten Wechsellagerung vermutet wurde.<sup>59</sup> *Möller et al.* konnten eine synthetische, rectorit-ähnliche Intercalationsverbindung unter Verwendung eines mit Schmelzsynthese hergestellten Hectorits herstellen, in der kollabierte, glimmerähnliche Kaliumzwischenschichten mit hydratisierten Natriumzwischenschichten alternieren (Abbildung 3).<sup>49</sup> Mittels verschiedener analytischer Methoden konnte dargelegt werden, dass in der untersuchten Intercalationsverbindung unterschiedliche Kationendichten in den kollabierten Kalium- bzw. Natriumzwischenschichten vorlagen.<sup>49</sup>

Wenn der Mechanismus für die Ausordnung der geordneten Wechsellagerung tatsächlich auf einer Modulation der Zwischenschichtkationendichten zurückgeht, sollte es sich hierbei um ein generelles Prinzip handeln, welches auch die Ausbildung von geordneten Wechsellagerungen von *Pinnavaia et al.* mit organischen Kationen erklären könnte.

Eine wichtige Voraussetzung für die Untersuchung dieser These, die in **Kapitel 5.2** dieser Arbeit beschrieben wird, ist die Verwendung von ladungshomogenen Schichtsilikaten auf die im Folgenden näher eingegangen werden soll.

### 3.5 Schmelzsynthese zur Herstellung ladungshomogener Schichtsilicate

Natürliche Schichtsilikate, wie beispielsweise Montmorillonite, sind zwar kostengünstig und ubiquitär in großen Vorkommen verfügbar, weisen allerdings eine sehr geringe Partikelgröße (typischerweise < 200 nm) und eine heterogene LadungsdichteVerteilung auf.<sup>29</sup> Aufgrund dieser Ladungsheterogenität liegen innerhalb und zwischen den verschiedenen Schichten unterschiedliche intrakristalline Reaktivitäten vor. Dies könnte ein Grund sein, warum mit natürlichen Montmorilloniten durch Intercalationsreaktionen keine geordneten Wechsellsagerungen hergestellt werden konnten.

Um eine homogene Ladungsdichte mit homogener intrakristalliner Reaktivität zu erreichen, muss die isomorphe Substitution in der Oktaeder, bzw. Tetraederschicht, welche die negative Schichtladung herbeiführt, absolut statistisch im Sinne einer festen Lösung sein. Mit Hilfe von Monte Carlo Simulationen wurde die Ausordnung der Oktaederkationen in Abhängigkeit von der Temperatur für verschiedene Zusammensetzungen untersucht.<sup>60</sup> Bei niedrigen Temperaturen (< 400 K) beginnen die Oktaederkationen für manche Zusammensetzungen Inseln zu bilden und damit zu segregieren, so dass lokale Ladungsinhomogenitäten zwischen und innerhalb einzelner Schichten entstehen. Um eine vollständig statistische Verteilung der Oktaederkationen zu erreichen, ist eine Synthesetemperatur von über 1000 K nötig.<sup>60</sup> Dies erklärt, warum hydrothermal gebildete Schichtsilikate, wie synthetischer Laponit und die oben genannten natürlichen Montmorillonite, die zum Beispiel durch hydrothermale Umkristallisation von Vulkangestein gebildet werden, starke Ladungsinhomogenitäten aufweisen.<sup>29</sup>

Natürliche Vermiculite werden dagegen aus Glimmern, vor allem aus Biotiten durch Magnesiumaustausch und Oxidation des strukturellen Eisens gebildet. Biotite entstehen wiederum in den tieferen Erdschichten bei hohen Temperaturen und Drücken. Dies erklärt die gute Ladungshomogenität mancher Vermiculite und die verschiedenen Berichte über das Auftreten geordneter Wechsellsagerungen nach partiellem Austausch.<sup>46</sup>

In der Gruppe von *Breu et al.* wurden verschiedene Verfahren der Schmelzsynthese mit Synthesetemperaturen oberhalb 1000 K entwickelt, bei denen große Takoide mit einer homogenen LadungsdichteVerteilung entstehen.<sup>20,21,61-63</sup> Dadurch können

ladungshomogene Schichtsilicate hergestellt werden, mit denen sich hohe Aspektverhältnisse realisieren lassen und die zugleich frei von Übergangsmetallen sind. Übergangsmetalle, wie beispielsweise Eisen, sind bei natürlichen Schichtsilikaten, wie Vermiculiten, als akzessorische Verunreinigungen oder strukturell in der Oktaederschicht vorhanden. Durch die damit einhergehende Farbigkeit des Materials sind natürliche Schichtsilicate für technisch anspruchsvolle, optoelektronische Anwendungen nicht geeignet. Farblose, synthetische Schichtsilicate, wie beispielsweise synthetische Hectorite, eröffnen durch ihre Reinheit und hohe optische Transparenz neue Anwendungsmöglichkeiten. Diese neuen Einsatzbereiche bestehen in der Verwendung als hochtransparente Füllstoffe zur Erhöhung der Gasbarriere,<sup>7,8,64</sup> oder als struktureller Bestandteil funktionaler optischer Materialien.<sup>65</sup>

In **Kapitel 5.1** und **Kapitel 5.6** wird ein osmotisch quellfähiger synthetischer Hectorit beschrieben. Durch seine Phasenreinheit, osmotische Quellfähigkeit und Ladungshomogenität ist dieser für die Synthese geordneter Wechsellagerungen ideal geeignet (**Kapitel 5.2**). Die Verwendung dieses wechselgelagerten Hectorits für die Synthese von Doppelschichten zur Herstellung von optisch anisotropen Systemen wird in **Kapitel 5.3** beschrieben.

### 3.6 Synthese von Janus-Partikeln mittels geordneter Wechsellagerung

Ein spezieller Fall von Heterostrukturen stellen Janus-Partikel dar. Der Name stammt von der römischen Gottheit Janus, der als Gott des Anfangs und des Endes für die Dualität des Lebens stand. Bildlich wurde diese Dualität durch zwei unterschiedliche Gesichter dargestellt, auf welche die Bezeichnung Janus-Partikel anspielt.<sup>66,67</sup> Es handelt sich um asymmetrische Partikel, bei denen zwei unterschiedliche Oberflächen räumlich getrennt vorliegen. Durch die räumliche Trennung zweier Oberflächen mit unterschiedlichen physikalischen und chemischen Eigenschaften liegen auf dem Janus-Partikel unterschiedliche Grenzflächeneigenschaften vor, welche eine Selbstorganisation dieser Partikel zu komplexen Strukturen ermöglichen.<sup>68-71</sup> Die Grenzflächenaktivität hängt dabei von der Größe der beiden Oberflächen ab und steigt bei plättchenförmigen Partikeln mit zunehmendem Aspektverhältnis.<sup>72</sup> Aufgrund der hohen Grenzflächenaktivität ergeben sich vielfältige Anwendungsbereiche für Januspartikel, die beispielsweise in der Verwendung als Emulgatoren, für funktionale Beschichtungen<sup>73</sup> oder im Einsatz als spezifische Adsorbenzien in der Biosensorik liegen.<sup>68,74,75</sup>

Für die Synthese von Janus-Partikeln wurden in der Forschung verschiedene Ansätze verfolgt, bei denen gegenwärtig vor allem hohe Ausbeuten und die Monodispersität im Fokus der Bemühungen stehen.<sup>68</sup> Im einfachsten Fall geht man von anorganischen Partikeln aus, die bereits aufgrund ihrer Kristallstruktur unterschiedliche Oberflächen aufweisen. So weisen anorganische Schichtmaterialien, wie z.B. Kaolinite, eine polare Struktur auf. Dieser intrinsische Janus-Charakter kann durch eine selektive Modifikation der Oberflächen zur Synthese anorganisch-organischer Janus-Partikel ausgenutzt werden.<sup>76-78</sup> Allerdings ist man bei diesem Ansatz auf die Verwendung von wenigen Materialklassen mit intrinsischem Janus-Charakter eingeschränkt.

Es wurden deshalb verschiedene Synthesestrategien entwickelt mit denen der Symmetriebruch auch von symmetrischen Ausgangsverbindungen erreicht werden kann. Generell lassen sich diese Syntheseansätze in *Maskierung*, *Phasenseparation* und *Selbstassemblierung* unterteilen.

Bei der *Maskierung* wird eine Oberfläche des Partikels durch Anlagerung an eine Grenzfläche (z.B. an Template) geschützt, oder eine der Oberflächen durch den Fluss in einem Kanal (Mikrofluidik) blockiert.<sup>68,74,79-81</sup> Nach der Maskierung der Oberfläche folgt eine irreversible Modifikation der freien Seite. Dieser Ansatz wurde beispielsweise für Laponit, einem synthetischen Hectorit mit Partikelgrößen im Bereich von 20-30 nm, verwendet. Zunächst erfolgt die Anlagerung der Nanoplättchen an Styrolatexpartikel, die in der Dispersion als Templat fungieren und eine Seite des Laponitplättchens maskieren. Danach erfolgte die Modifikation der freien Laponitoberfläche mit einem kationischen Polymer (Poly(2-(trimethylamino)-ethylmethacrylat).<sup>71</sup> Ein Nachteil der Maskierungsmethode liegt in den hohen Kosten durch die aufwendige Herstellung der Template begründet, welche wohldefinierte Blocklängen aufweisen müssen. Außerdem besteht bei diesem Verfahren die Gefahr, dass es durch die Anlagerung an die Grenzflächen zu einer Überlappung der Partikel und damit zu einer unvollständigen Modifikation der freien Seite bzw. einer irreversiblen Aggregation der adsorbierten Plättchen kommt. Gerade bei Verwendung von Schichtverbindungen mit hohen Aspektverhältnissen ist die Wahrscheinlichkeit einer Überlappung an der Grenzfläche besonders groß.

Eine Möglichkeit wie dieses Problem umgangen werden kann, besteht in der Synthese von Janus-Partikeln mittels *Phasenseparation* zweier nichtmischbarer Phasen. Hierbei werden meist Polymerblends oder Blockterpolymere verwendet, die im Dispersionsmedium aufgrund unterschiedlicher Polaritäten der Polymereinheiten phasenseparieren.<sup>74</sup>

Bei der verfeinerten Synthesemethode, der *Selbstassemblierung*, wird diese Phasenseparation verwendet, um exakt definierte Strukturen zu generieren und diese dauerhaft zu fixieren.<sup>68</sup> *Walther et al.* nutzten ein Triblockcopolymer auf Basis von Polystyrol (PS), Polymethylmethacrylat (PMMA) und Polybutadien (PB). Der PB-Block diente hierbei zur Fixierung. Je nach Blocklängen phasenseparieren die PS-b-PB-b-PMMA-Terpolymere zu unterschiedlichen geordneten Strukturen. So lassen sich auch lamellare Dreischichtstrukturen, aus geordnet wechselgelagerten Schichten herstellen. *Walther et al.* verwendete diese geordnete Wechsellagerung, um nach der Fixierung, d.h. der Vernetzung des PB-Blocks, stark anisotrope Janusscheibchen zu erzeugen (Abbildung 3).<sup>67</sup>

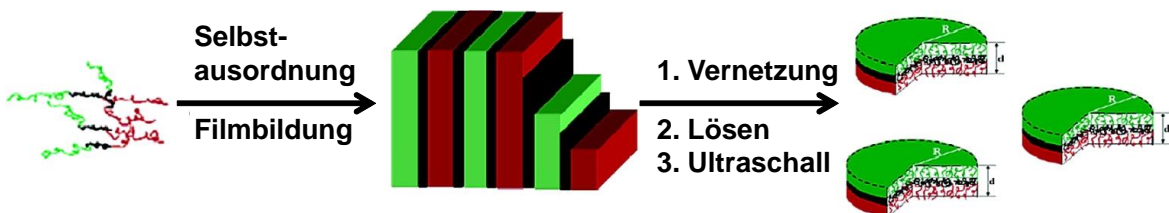


**Abbildung 3.** Bildung einer wechselgelagerten Schichtstruktur mittels Selbstassemblierung eines PS-b-PB-b-PMMA-Terpolymers. Nach der Filmbildung erfolgt die Vernetzung des PB-Blockes (schwarz). Durch Lösen und Ultraschallbehandlung entstehen Janus-Scheiben mit einer PS- (rot) und PMMA-Oberfläche (grün). Verändert nach Walter et al.<sup>67</sup> (Adapted with permission from Ref. 67. Copyright 2007, American Chemical Society)

Ein Nachteil dieser Methode liegt in der engen Blocklängenverteilung und der benötigten Polaritätsunterschiede der Polymere begründet, welche zur exakten Selbstassemblierung in die alternierende Dreischichtstruktur benötigt wird. Auch ist die Herstellung durch den Trocknungsschritt bei der Filmbildung und die benötigte Vernetzung sehr zeitaufwendig. Das Lösen und Spalten der Polymere mittels Ultraschalls führt außerdem zu einer Verringerung des Aspektverhältnisses der Scheibchen, welches die Grenzflächenaktivität verringert. Für eine großtechnische Verwendung erscheint das Verfahren von *Walter et al.* aufgrund der aufwendigen Synthese der Terpolymere zu aufwändig und teuer.

Die Methode veranschaulicht aber anschaulich, dass geordnete Wechsellagerungen als strukturdirigierende Funktion für die Synthese von plättchenförmigen Janus-Partikeln vorteilhaft sind.

In **Kapitel 5.4** wird ein neuartiges Syntheseverfahren unter Verwendung von geordneten Wechsellagerungen in Schichtsilicaten vorgestellt, mit dem sich Janus-Partikel mit hohem Aspektverhältnis unter Verwendung von preiswerten und kommerziell verfügbaren, statistischen Copolymeren ohne einen Trocknungs- und Vernetzungsschritt und mit beliebigen Funktionalitäten herstellen lassen.

### 3.7 Literatur

- (1) Kudo, A.; Miseki, Y. Heterogeneous photocatalyst materials for water splitting. *Chem. Soc. Rev.* **2009**, *38*, 253-278.
- (2) Yoon, T. P.; Ischay, M. A.; Du, J. N. Visible light photocatalysis as a greener approach to photochemical synthesis. *Nat. Chem.* **2010**, *2*, 527-532.
- (3) Ozin, G. A. You can't have an energy revolution without transforming advances in materials, chemistry and catalysis into policy change and action. *Energy Environ. Sci.* **2015**, *8*, 1682-1684.
- (4) Pera-Titus, M.; Leclercq, L.; Clacens, J. M.; De Campo, F.; Nardello-Rataj, V. Pickering interfacial catalysis for biphasic systems: From emulsion design to green reactions. *Angew. Chem. Int. Ed.* **2015**, *54*, 2006-2021.
- (5) Wang, J. F.; Cheng, Q. F.; Tang, Z. Y. Layered nanocomposites inspired by the structure and mechanical properties of nacre. *Chem. Soc. Rev.* **2012**, *41*, 1111-1129.
- (6) Luo, Y. H.; Li, D. M.; Meng, Q. B. Towards optimization of materials for dye-sensitized solar cells. *Adv. Mater.* **2009**, *21*, 4647-4651.
- (7) Kunz, D. A.; Schmid, J.; Feicht, P.; Erath, J.; Fery, A.; Breu, J. Clay-based nanocomposite coating for flexible optoelectronics applying commercial polymers. *ACS Nano.* **2013**, *7*, 4275-4280.
- (8) Möller, M. W.; Kunz, D. A.; Lunkenbein, T.; Sommer, S.; Nennemann, A.; Breu, J. UV-cured, flexible, and transparent nanocomposite coating with remarkable oxygen barrier. *Adv. Mater.* **2012**, *24*, 2142-2147.
- (9) Geim, A.; Grigorieva, I., Van der Waals heterostructures. *Nature.* **2013**, *499*, 419-425.
- (10) Gao, N.; Fang, X. S. Synthesis and development of graphene inorganic semiconductor nanocomposites. *Chem. Rev.* **2015**, *115*, 8294-8343.
- (11) Wan, X. J.; Huang, Y.; Chen, Y. S. Focusing on energy and optoelectronic applications: A journey for graphene and graphene oxide at large scale. *Acc. Chem. Res.* **2012**, *45*, 598-607.
- (12) Chen, L.; Hernandez, Y.; Feng, X. L.; Mullen, K. From nanographene and graphene nanoribbons to graphene sheets: chemical synthesis. *Angew. Chem. Int. Ed.* **2012**, *51*, 7640-7654.
- (13) Chiritescu, C.; Cahill, D. G.; Nguyen, N.; Johnson, D.; Bodapati, A.; Keblinski, P.; Zschack, P. Ultralow thermal conductivity in disordered, layered WSe<sub>2</sub> crystals. *Science.* **2007**, *315*, 351-353.
- (14) Novoselov, K. S.; Jiang, D.; Schedin, F.; Booth, T. J.; Khotkevich, V. V.; Morozov, S. V.; Geim, A. K. Two-dimensional atomic crystals. *Proc. Natl. Acad. Sci. USA.* **2005**, *102*, 10451-10453.
- (15) Rao, C.; Matte, H.; Maitra, U. Graphene analogues of inorganic layered materials. *Angew. Chem. Int. Ed.* **2013**, *52*, 13162-13185.
- (16) Wu, W.; Wang, L.; Li, Y.; Zhang, F.; Lin, L.; Niu, S.; Chenet, D.; Zhang, X.; Hao, Y.; Heinz, T. F.; Hone, J.; Wang, Z. L. Piezoelectricity of single-atomic-layer MoS<sub>2</sub> for energy conversion and piezotronics. *Nature.* **2014**, *514*, 470-474.

- (17) Kunz, D.; Max, E.; Weinkamer, R.; Lunkenbein, T.; Fery, A.; Breu, J. Deformation measurements on thin clay tactoids. *Small*. **2009**, *5*, 1816-1820.
- (18) Kunz, D. A.; Erath, J.; Kluge, D.; Thurn, H.; Putz, B.; Fery, A.; Breu, J. In-plane modulus of singular 2:1 clay lamellae applying a simple wrinkling technique. *ACS Appl. Mater. Interfaces*. **2013**, *5*, 5851-5855.
- (19) Kunz, D. A.; Feicht, P.; Goedrich, S.; Thurn, H.; Papastavrou, G.; Fery, A.; Breu, J. Space-resolved in-plane moduli of graphene oxide and chemically derived graphene applying a simple wrinkling procedure. *Adv. Mater.* **2013**, *25*, 1337-1341.
- (20) Kalo, H.; Möller, M. W.; Kunz, D. A.; Breu, J. How to maximize the aspect ratio of clay nanoplatelets. *Nanoscale*. **2012**, *4*, 5633-5639.
- (21) Breu, J.; Seidl, W.; Stoll, A. J.; Lange, K. G.; Probst, T. U. Charge homogeneity in synthetic fluorohectorite. *Chem. Mater.* **2001**, *13*, 4213-4220.
- (22) Kalo, H.; Möller, M. W.; Ziadeh, M.; Dolejs, D.; Breu, J. Large scale melt synthesis in an open crucible of Na-fluorohectorite with superb charge homogeneity and particle size. *Appl. Clay Sci.* **2010**, *48*, 39-45.
- (23) Cussler, E. L.; Hughes, S. E.; Ward, W. J.; Aris, R. Barrier membranes. *J. Membrane Sci.* **1988**, *38*, 161-174.
- (24) Singh, V.; Bosman, S.; Schneider, B.; Blanter, Y.; Castellanos-Gomez, A.; Steele, G. Optomechanical coupling between a multilayer graphene mechanical resonator and a superconducting microwave cavity. *Nat. Nanotech.* **2014**, *9*, 820-824.
- (25) Fischer, B.; Ziadeh, M.; Pfaff, A.; Breu, J.; Altstädt, V. Impact of large aspect ratio, shear-stiff, mica-like clay on mechanical behaviour of PMMA/clay nanocomposites. *Polymer*. **2012**, *53*, 3230-3237.
- (26) Obut, A.; Girgin, I. Hydrogen peroxide exfoliation of vermiculite and phlogopite. *Minerals Engineering*. **2002**, *15*, 683-687.
- (27) Weiss, Z.; Valaskova, M.; Seidlerova, J.; Supkova-Kristkova, M.; Sustai, O.; Matejka, V.; Capkova, P. Preparation of vermiculite nanoparticles using thermal hydrogen peroxide treatment. *J. Nanosci. Nanotechno.* **2006**, *6*, 726-730.
- (28) Smith, D. W. Ionic hydration enthalpies. *J. Chem. Educ.* **1977**, *54*, 540-542.
- (29) *Tonminerale und Tone - Struktur, Eigenschaften, Anwendungen und Einsatz in Industrie und Umwelt*; Jasmund K.; Lagaly G. Eds. Steinkopff Verlag: Darmstadt, **1993**.
- (30) Diar-Bakerly, B.; Beyer, G.; Schobert, R.; Breu, J. Significance of aspect ratio on efficiency of layered double hydroxide flame retardants. *Fire and Polymers VI: New Advances in Flame Retardant Chemistry and Science*; American Chemical Society: **2012**; pp 407-425.
- (31) Norrish, K. The swelling of montmorillonite. *Discuss. Faraday Soc.* **1954**, *18*, 120-134.
- (32) Hou, X. Q.; Bish, D. L.; Wang, S. L.; Johnston, C. T.; Kirkpatrick, R. J. Hydration, expansion, structure, and dynamics of layered double hydroxides. *Amer. Mineral.* **2003**, *88*, 167-179.
- (33) Liu, Z. P.; Ma, R. Z.; Osada, M.; Iyi, N.; Ebina, Y.; Takada, K.; Sasaki, T. Synthesis, anion exchange, and delamination of Co-Al layered double hydroxide:

- Assembly of the exfoliated nanosheet/polyanion composite films and magneto-optical studies. *J. Am. Chem. Soc.* **2006**, *128*, 4872-4880.
- (34) Möller, M. W.; Handge, U. A.; Kunz, D. A.; Lunkenbein, T.; Altstädt, V.; Breu, J. Tailoring shear-stiff, mica-like nanoplatelets. *ACS Nano*. **2010**, *4*, 717-724.
- (35) Ziadeh, M.; Fischer, B.; Schmid, J.; Altstädt, V.; Breu, J. On the importance of specific interface area in clay nanocomposites of PMMA filled with synthetic nano-mica. *Polymer*. **2014**, *55*, 3770-3781.
- (36) Ziadeh, M.; Weiss, S.; Fischer, B.; Förster, S.; Altstädt, V.; Müller, A. H.; Breu, J. Towards completely miscible PMMA nanocomposites reinforced by shear-stiff, nano-mica. *J. Colloid Interface Sci.* **2014**, *425*, 143-151.
- (37) Chakravarty, S.; Kee, H. Y.; Volker, K. An explanation for a universality of transition temperatures in families of copper oxide superconductors. *Nature*. **2004**, *428*, 53-55.
- (38) Ohta, T.; Bostwick, A.; Seyller, T.; Horn, K.; Rotenberg, E. Controlling the electronic structure of bilayer graphene. *Science*. **2006**, *313*, 951-954.
- (39) Craciun, M.; Russo, S.; Yamamoto, M.; Oostinga, J.; Morpurgo, A.; Tarucha, S. Trilayer graphene is a semimetal with a gate-tunable band overlap. *Nat. Nanotech.* **2009**, *4*, 383-388.
- (40) Shih, C. J.; Vijayaraghavan, A.; Krishnan, R.; Sharma, R.; Han, J. H.; Ham, M. H.; Jin, Z.; Lin, S. C.; Paulus, G. L. C.; Reuel, N. F.; Wang, Q. H.; Blankschtein, D.; Strano, M. S. Bi- and trilayer graphene solutions. *Nat. Nanotech.* **2011**, *6*, 439-445.
- (41) Sui, M.; Chen, G.; Ma, L.; Shan, W. Y.; Tian, D.; Watanabe, K.; Taniguchi, T.; Jin, X.; Yao, W.; Xiao, D.; Zhang, Y. Gate-tunable topological valley transport in bilayer graphene. *Nat. Phys.* **2015**, *11*, 1027-1031.
- (42) Kim, S. S.; Van Khai, T.; Kulish, V.; Kim, Y. H.; Na, H. G.; Katoch, A.; Osada, M.; Wu, P.; Kim, H. W. Tunable Bandgap narrowing induced by controlled molecular thickness in 2D mica nanosheets. *Chem. Mater.* **2015**, *27*, 4222-4228.
- (43) Winter, M.; Besenhard, J. O.; Spahr, M. E.; Novak, P. Insertion electrode materials for rechargeable lithium batteries. *Adv. Mater.* **1998**, *10*, 725-763.
- (44) Feicht, P.; Breu, J. Gas-phase preparation of SO<sub>3</sub>-Graphite: Host-exchange and exfoliation. *Zeitschrift für anorganische und allgemeine Chemie*. **2015**, *641*, 1093-1098.
- (45) Besenhard, J. O.; Fritz, H. P. The electrochemistry of black carbons. *Angew. Chem. Int. Ed.* **1983**, *22*, 950-975.
- (46) Sawhney, B. L. Interstratification in vermiculite. *Clays Clay Miner.* **1967**, *15*, 75-84.
- (47) Bailey, S. W. Nomenclature for regular interstratifications. *Am. Mineral.* **1982**, *67*, 394-398.
- (48) Ijdo, W. L.; Lee, T.; Pinnavaia, T. J. Regularly interstratified layered silicate heterostructures: Precursors to pillared rectorite-like intercalates. *Adv. Mater.* **1996**, *8*, 79-83.
- (49) Möller, M. W.; Hirsemann, D.; Haarmann, F.; Senker, J.; Breu, J. Facile scalable synthesis of rectorites. *Chem. Mater.* **2010**, *22*, 186-196.

- (50) Theng, B. K. G.; Quirk, J. P.; Greenland, D. J. Adsorption of alkylammonium cations by montmorillonite. *Clay Miner.* **1967**, *7*, 1-17.
- (51) Ijdo, W. L.; Pinnavaia, T. J. Staging of organic and inorganic gallery cations in layered silicate heterostructures. *J. Solid State Chem.* **1998**, *139*, 281-289.
- (52) Ijdo, W. L.; Pinnavaia, T. J. Amphiphilic layered silicate clay for the efficient removal of organic pollutants from water. *Green Chem.* **2001**, *3*, 10-12.
- (53) Ijdo, W. L.; Pinnavaia, T. J. Solid solution formation in amphiphilic organic-inorganic clay heterostructures. *Chem. Mater.* **1999**, *11*, 3227-3231.
- (54) Ozsoz, M.; Erdem, A.; Ozkan, D.; Kerman, K.; Pinnavaia, T. J. Clay/sol-gel-modified electrodes for the selective electrochemical monitoring of 2,4-dichlorophenol. *Langmuir*. **2003**, *19*, 4728-4732.
- (55) Ozkan, D.; Kerman, K.; Meric, B.; Kara, P.; Demirkan, H.; Polverejan, M.; Pinnavaia, T. J.; Ozsoz, M. Heterostructured fluorohectorite clay as an electrochemical sensor for the detection of 2,4-dichlorophenol and the herbicide 2,4-D. *Chem. Mater.* **2002**, *14*, 1755-1761.
- (56) Teppen, B. J.; Miller, D. M. Hydration energy determines isovalent cation exchange selectivity by clay minerals. *Soil Sci. Soc. Am. J.* **2006**, *70*, 31-40.
- (57) Teppen, B. J.; Aggarwal, V. Thermodynamics of organic cation exchange selectivity in smectites. *Clays Clay Miner.* **2007**, *55*, 119-130.
- (58) Vansant, E. F.; Uytterho, J. B. Thermodynamics of exchange of N-alkylammonium ions on Na-Montmorillonite. *Clays Clay Miner.* **1972**, *20*, 47-54.
- (59) Brown, G. Crystal-structures of clay-minerals and related phyllosilicates. *Phil. Trans. R. Soc. A.* **1984**, *311*, 221-240.
- (60) Palin, E. J.; Dove, M. T.; Hernandez-Laguna, A.; Sainz-Diaz, C. I. A computational investigation of the Al/Fe/Mg order-disorder behavior in the dioctahedral sheet of phyllosilicates. *Amer. Mineral.* **2004**, *89*, 164-175.
- (61) Kalo, H.; Möller, M. W.; Ziadeh, M.; Dolejs, D.; Breu, J. Large scale melt synthesis in an open crucible of Na-fluorohectorite with superb charge homogeneity and particle size. *Appl. Clay Sci.* **2010**, *48*, 39-45.
- (62) Baumgartner, A.; Sattler, K.; Thun, J.; Breu, J. A route to microporous materials through oxidative pillaring of micas. *Angew. Chem. Int. Ed.* **2008**, *47*, 1640-1644.
- (63) Baumgartner, A.; Butterhof, C.; Koch, S.; Mariychuk, R.; Breu, J. Melt synthesis and characterization of synthetic Mn-rich tainiolite. *Clays Clay Miner.* **2009**, *57*, 271-277.
- (64) Möller, M. W.; Lunkenbein, T.; Kalo, H.; Schieder, M.; Kunz, D. A.; Breu, J. Barrier properties of synthetic clay with a kilo-aspect ratio. *Adv. Mater.* **2010**, *22*, 5245-5249.
- (65) Kunz, D. A.; Leitl, M. J.; Schade, L.; Schmid, J.; Bojer, B.; Schwarz, U. T.; Ozin, G. A.; Yersin, H.; Breu, J. Quasi epitaxial growth of  $[\text{Ru}(\text{bpy})_3]^{2+}$  by confinement in clay nanoplatelets yields polarized emission. *Small.* **2014**, *11*, 792-796.
- (66) Degennes, P. G. Soft Matter. *Science.* **1992**, *256*, 495-497.
- (67) Walther, A.; Andre, X.; Drechsler, M.; Abetz, V.; Müller, A. H. E. Janus discs. *J. Am. Chem. Soc.* **2007**, *129*, 6187-6198.

- (68) Walther, A.; Müller, A. H. E. Janus particles: Synthesis, self-assembly, physical properties, and applications. *Chem. Rev.* **2013**, *113*, 5194-5261.
- (69) Nonomura, Y.; Komura, S.; Tsujii, K. Adsorption of disk-shaped Janus beads at liquid-liquid interfaces. *Langmuir*. **2004**, *20*, 11821-11823.
- (70) Hirose, Y.; Komura, S.; Nonomura, Y. Adsorption of Janus particles to curved interfaces. *J. Chem. Phys.* **2007**, *127*.
- (71) Liu, J. H.; Liu, G. N.; Zhang, M. M.; Sun, P. C.; Zhao, H. Y. Synthesis and Self-assembly of amphiphilic Janus Laponite disks. *Macromolecules*. **2013**, *46*, 5974-5984.
- (72) Ruhland, T. M.; Groschel, A. H.; Ballard, N.; Skelhon, T. S.; Walther, A.; Müller, A. H. E.; Bon, S. A. F. Influence of Janus particle shape on their interfacial behavior at liquid-liquid interfaces. *Langmuir*. **2013**, *29*, 1388-1394.
- (73) Berger, S.; Ionov, L.; Synytska, A. Engineering of ultra-hydrophobic functional coatings using controlled aggregation of bicomponent core/shell Janus particles. *Adv. Funct. Mater.* **2011**, *21*, 2338-2344.
- (74) Lattuada, M.; Hatton, T. Synthesis, properties and applications of Janus nanoparticles. *Nano Today*. **2011**, *6*, 286-308.
- (75) Pang, X.; Wan, C.; Wang, M.; Lin, Z. Strictly biphasic soft and hard Janus structures: Synthesis, properties, and applications. *Angew. Chem. Int. Ed.* **2014**, *53*, 5524-5538.
- (76) Hirsemann, D.; Köster, T. K. J.; Wack, J.; van Wüllen, L.; Breu, J.; Senker, J. Covalent grafting to  $\mu$ -hydroxy-capped surfaces? A kaolinite case study. *Chem. Mater.* **2011**, *23*, 3152-3158.
- (77) Hirsemann, D.; Shylesh, S.; De Souza, R. A.; Diar-Bakerly, B.; Biersack, B.; Müller, D. N.; Martin, M.; Schobert, R.; Breu, J. Large-scale, low-cost fabrication of Janus-type emulsifiers by selective decoration of natural kaolinite platelets. *Angew. Chem. Int. Ed.* **2012**, *51*, 1348-1352.
- (78) Weiss, S.; Hirsemann, D.; Biersack, B.; Ziadeh, M.; Müller, A. H. E.; Breu, J. Hybrid Janus particles based on polymer-modified kaolinite. *Polymer*. **2013**, *54*, 1388-1396.
- (79) Andala, D. M.; Shin, S. H. R.; Lee, H. Y.; Bishop, K. J. M. Templated synthesis of amphiphilic nanoparticles at the liquid-liquid interface. *ACS Nano*. **2012**, *6*, 1044-1050.
- (80) Hu, J.; Zhou, S. X.; Sun, Y. Y.; Fang, X. S.; Wu, L. M. Fabrication, properties and applications of Janus particles. *Chem. Soc. Rev.* **2012**, *41*, 4356-4378.
- (81) Dendukuri, D.; Pregibon, D. C.; Collins, J.; Hatton, T. A.; Doyle, P. S. Continuous-flow lithography for high-throughput microparticle synthesis. *Nat. Mater.* **2006**, *5*, 365-369.

## 4. Synopsis

Die vorliegende Arbeit enthält sechs Publikationen, in denen ein allgemeines Verfahren zur Synthese funktionaler schichtförmiger Nanobausteine auf Basis von synthetischen Schichtsilicaten entwickelt wird. Die Herstellung dieser funktionalen Nanobausteine soll durch einen industriell skalierbaren und kostengünstigen Top-down Ansatz erfolgen.

Das in dieser Arbeit entwickelte Verfahren beruht auf der Synthese von geordneten Wechsellagerungen und deren kontrollierter Exfolierung zu funktionalen Nanobausteinchen.

Die Entwicklung dieses neuartigen Verfahrens gliedert sich in vier Schritte.

Zunächst wird die **Synthese eines geeigneten Schichtsilicates** vorgestellt. Diese anorganische Wirtsverbindung weist aufgrund ihrer herausragenden Homogenität und Phasenreinheit alle Voraussetzungen für die Bildung von geordneten Wechsellagerungen mit hoher Perfektion auf.

Im zweiten Schritt wird mit dieser Schichtverbindung die **Bildung von geordneten Wechsellagerungen** mittels Intercalationsreaktionen untersucht. Aus dem gewonnenen Verständnis über den Bildungsmechanismus dieser alternierenden Strukturen soll eine allgemeine Vorschrift zur gezielten Synthese von streng alternierenden Zwischenschichten entwickelt werden.

Auf dieser Basis werden im dritten Schritt geordnete Wechsellagerungen mit funktionalen, organischen Zwischenschichten und Natriumzwischenschichten hergestellt, wobei letztere spätere Sollbruchstellen darstellen. Diese Sollbruchstellen werden anschließend für die **kontrollierte Exfolierung zu funktionalen Nanobausteinchen** verwendet.

Im vierten und letzten Schritt wird die **Anwendung dieser Nanobausteine** als funktionale Füllstoffe in Polymernanokompositen und zur gezielten Synthese von Janus-Partikeln untersucht.

## 4.1 Ladungshomogener Natriumhectorit

Für eine aussagekräftige Untersuchung der Bildung von geordneten Wechsellagerungen und deren kontrollierter Exfolierung zu funktionalen Nanobausteinen wird ein Schichtsilicat benötigt, welches in jeder Zwischenschicht die gleiche intrakristalline Reaktivität besitzt. Diese wird vor allem durch die Homogenität der Ladungsdichteverteilung bestimmt.

Aus diesem Grund muss die isomorphe Substitution, welche die negative Schichtladung hervorruft, absolut homogen im Sinne einer festen Lösung sein. Es dürfen weder Inseln mit höherer und niedrigerer Ladungsdichte innerhalb einer Oktaederschicht vorliegen, noch dürfen Unterschiede in der Ladungsdichte der Schichten innerhalb eines Taktoids, sowie zwischen unterschiedlichen Taktoiden bestehen. Die intrakristalline Reaktivität sollte aber nicht nur homogen, sondern in wässrigen Dispersionen auch entsprechend hoch sein, damit eine kontrollierte Exfolierung der Schichtstapel mittels osmotischer Quellung erfolgen kann. Die anziehenden Wechselwirkungen (v.a. Coulomb- und Van der Waals-Wechselwirkungen) sollten deshalb so gering sein, dass die Schichten sich in Wasser durch die Quellung, d.h. durch abstoßende Wechselwirkungen, voneinander trennen.

In Wasser ist für diesen Prozess vor allem die Hydratationsenthalpie des jeweiligen Zwischenschichtkations von entscheidender Bedeutung. Von natürlichen Schichtsilicaten, wie beispielsweise von Montmorilloniten mit einer niedrigen Schichtladung (ca. 0.35 bis 0.5 pro Formeleinheit) ist bekannt, dass bei diesen Schichtladungen die Hydratationsenthalpie von Lithium und Natrium für die osmotische Quellung ausreicht.

Trotz dieser interessanten Eigenschaft ist die Verwendung dieser natürlichen Schichtsilicate für diese Studie ungeeignet, da bei natürlichen Montmorilloniten durch die Genese bei niedriger Temperatur eine stark inhomogene Ladungsdichteverteilung und damit inhomogene intrakristalline Reaktivität vorliegt. Außerdem werden Montmorillonite meist von akzessorischen Nebenphasen begleitet, die eine vollständige Delaminierung unterdrücken. Für eine angestrebte Verwendung der Nanobausteine für Gasbarriere- und Flammenschutzanwendungen werden zudem hohe Aspektverhältnisse benötigt, welche Montmorillonite aufgrund der geringen Partikelgrößen im Bereich von 200 nm nicht bieten. Für optische Anwendungen der Nanobausteine ist zudem die Farbigkeit der natürlichen Schichtsilicate, die durch strukturelle Übergangsmetalle hervorgerufen wird, äußerst nachteilig.

Für die angestrebte, kontrollierte Exfolierung von geordneten Wechsellagerungen kommen daher nur synthetische Schichtsilicate infrage. Schichtsilicate, welche mittels

Schmelzsynthese hergestellt werden, lassen aufgrund der hohen Synthesetemperatur ( $>1000^{\circ}\text{K}$ ) eine gute Ladungshomogenität und durch die Möglichkeit der Wahl der Edukte eine verbesserte Reinheit erwarten.

Von schmelzsynthetisierten Lithiumhectoriten verschiedener Schichtladungen ist bekannt, dass diese zwar osmotisch quellen, aber bei der Synthese verschiedene Nebenphasen gebildet werden, so dass der Lithiumhectorit einer aufwendigen Aufreinigung unterzogen werden muss. Dagegen sind ähnlich synthetisierte Natriumhectorite mit vergleichbaren Schichtladungen bis auf einen geringen Protoamphibolgehalt nahezu phasenrein. Allerdings quollen diese Schichtsilicate mit Natrium in der Zwischenschicht bisher leider nicht osmotisch. Selbst unter Anwendung von hohen mechanischen Scherkräften konnten diese Natriumhectorite in Wasser nicht effektiv exfoliert werden.

Durch Langzeittempern wurde nun ein schmelzsynthetisierter Natriumhectorit so weit aktiviert, dass dieser vollständig osmotisch delaminiert (**Kapitel 5.1** und **Kapitel 5.6**). Aufgrund der bei der Schmelzsynthese erhaltenen Taktoidgröße werden einzelne Schichten von extrem hohem Aspektverhältnis (Median  $\approx 20000$ ) gebildet. Mittels Röntgendiffraktometrie an Pulvern (PXRD) konnte gezeigt werden, dass durch das Langzeittempern die im ungetemperten Material vorhandene Protoamphibolnebenphase verschwindet. Die verbesserte Phasenreinheit belegen auch Festkörper-NMR Messungen: Ein Peak einer weiteren Phase, die im PXRD nicht identifizierbar ist, verschwindet nach dem Temperiern. Die hohe Reinheit und gute intrakristalline Reaktivität wird durch eine deutlich erhöhte Kationenaustauschkapazität (CEC), die nahezu mit dem theoretischen Wert übereinstimmt, bestätigt.

Eine homogene intrakristalline Reaktivität deutet sich durch die vollständige Hydratation des Hectorits zum Ein- und Zweischichthydrat bei verschiedenen Luftfeuchtigkeiten an. Die Ursache für diese homogene Reaktivität liegt in der hervorragend homogenen Ladungsdichteverteilung begründet, die mittels der Alkylammonium-Methode nach *Lagaly*, bei der Alkylammoniumionen mit steigender Kettenlänge intercaliert werden, bestimmt wurde.

Die sehr gute Phasenreinheit dieses neuen Schichtsilicates, die hohe und homogene intrakristalline Reaktivität sowie die damit verbundene osmotische Quellfähigkeit, ermöglicht die gezielte Synthese und Untersuchung von geordneten Wechsellagerungen, welche die Grundlage für eine kontrollierte Exfolierung bildet.

## 4.2 Bildung geordneter Wechsellagerungen

Alternierende Schichtstrukturen werden gewöhnlich mittels Bottom-up Verfahren beispielsweise nach dem Layer-by-Layer (LBL) Verfahren oder durch Heterokoagulation hergestellt. Ein deutlich einfacheres Verfahren, das zudem besser geordnete Strukturen liefert, stellt die Bildung von geordneten Wechsellagerungen durch partielle Intercalation in Schichtsilicate dar.

Die Ursache für die Bildung dieser geordneten Wechsellagerungen nach partieller Intercalation von organischen Kationen war bisher unklar. So deuten einige Intercalationsstudien mit organischen Kationen auf eine homogene Kationenverteilung in benachbarten Zwischenschichten hin. In einer anderen Intercalationsstudie, in der ein rein anorganisches System untersucht wurde, konnte dagegen bewiesen werden, dass in der geordneten Wechsellagerung unterschiedliche Kationendichten in benachbarten Zwischenschichten vorliegen.

Durch die partielle Intercalation eines kationischen organischen Stilbazoniumfarbstoffes (N-Hexadecyl-4-(3,4,5-trimethoxystyryl)-pyridinium) beziehungsweise eines deutlich kleineren Pentylammonium-Kations in den ladungshomogenen Natriumhectorit konnte nun endgültig bewiesen werden, dass eine alternierende Variation der Kationendichte von benachbarten Zwischenschichten für die Bildung der geordneten Wechsellagerung ursächlich ist (**Kapitel 5.2**).

Die vergleichende Auswertung der Schichtabstände einer komplett ausgetauschten Stilbazoniumprobe mit einer wechselgelagerten Stilbaziumzwischenschicht machte deutlich, dass in der geordneten Wechsellagerung der Schichtabstand der organischen Zwischenschicht deutlich kleiner ist. Die photometrische und elementaranalytische Bestimmung der eingelagerten Stilbazoniumstoffmenge erlaubte eine vergleichende Abschätzung der Packungsdichte der beiden unterschiedlichen organischen Zwischenschichten. Hierbei zeigte sich, dass in der geordneten Wechsellagerung die Anzahl an Stilbazoniumkationen pro Fläche kleiner als in der komplett ausgetauschten Probe ist, was den geringeren Schichtabstand der wechselgelagerten organischen Zwischenschicht erklärt. Durch den geringeren Schichtabstand der geordneten Wechsellagerung ist die Packungsdichte der Stilbazoniumkationen im Vergleich zu einer komplett ausgetauschten Probe, bei der die Verteilung der Stilbazoniumkationen exakt der negativen Ladungsverteilung des Schichtsilicates entspricht, höher.

Eine erhöhte Packungsdichte wurde ebenfalls für die organische Zwischenschicht der geordneten Wechsellagerung mit dem Pentylammonium-Kation festgestellt. Bei diesem

kleineren Kation bleibt zwar der Schichtabstand unverändert, aber durch eine Zunahme der Pentylammoniumstoffmenge innerhalb der geordnet wechselgelagerten Zwischenschicht wird ebenfalls eine höhere Packungsdichte generiert.

Die reduzierte Stilbazoniumkationendichte bzw. erhöhte Pentylammoniumkationendichte führt in beiden Fällen dazu, dass die negative Schichtladung durch die organischen Kationen lokal nicht vollständig ausgeglichen wird. Ergebnisse der Adsorptionsisothermen sowie Wasserdampfphysisorptionsmessungen lassen den Schluss zu, dass in den angrenzenden Natriumzwischenschichten die erzeugte Abweichung von der Ladungsdichte des Schichtsilicates lokal kompensiert wird.

Diese Variation der Kationendichte in den benachbarten organischen und anorganischen Zwischenschichten erklärt die thermodynamisch bevorzugte Ausbildung der streng alternierenden Struktur.

Weiterhin konnte für die Weiterentwicklung der Synthese von geordneten Wechsellagerungen gezeigt werden, dass die Anpassung der Löslichkeit der organischen Verbindung und der hydrophilen Natriumkationen im jeweiligen Lösungsmittelsystem entscheidenden Einfluss hat. Werden zur Intercalation von hydrophoben organischen Verbindungen stark hydrophile Lösungsmittelmischungen verwendet, so ist die Intercalation kinetisch kontrolliert und es bilden sich keine einphasigen, geordneten Wechsellagerungen aus. Die Intercalationsbedingungen müssen daher stets so gewählt werden, dass sich die geordnete Wechsellagerung als thermodynamische Gleichgewichtsphase im gewählten Lösungsmittelsystem mittels De- und Reintercalation ausbilden kann.

Basierend auf den Erkenntnissen dieser Studie sollte es nun möglich sein, für beliebige funktionale Kationen geeignete Intercalationsbedingungen zur Ausbildung von geordneten Wechsellagerungen zu schaffen.

### 4.3 Synthese funktionaler Doppelschichten

Für viele industrielle Anwendungen ist die Verkapselung von funktionalen Molekülen von großer Bedeutung. Durch das Einbringen einer funktionalen Spezies in eine Wirtsverbindung kann die Löslichkeit sowie die thermische und photochemische Stabilität verbessert werden. Eine Verkapselung in strukturell anisotrope Verbindungen, wie z.B. Schichtsilicate, bringt zusätzlich den Vorteil, dass sich die verkapselte Gastverbindung innerhalb des räumlich begrenzten Zwischenschichtraumes in definierter Weise orientieren wird. Wie durch die Arbeit von Kunz et al. gezeigt wurde, hat diese Ausrichtung bei

Emittieren eine polarisierte Emission zur Folge. Dies könnte zur Effizienzsteigerung und Stabilisierung der Emitter in organischen Leuchtdioden (organic light emitting diode - OLED) beitragen.

Wie in **Kapitel 3.3** beschrieben, wäre ein Aufbau von Funktionsmaterialien aus exfolierten Doppelschichten, in denen die funktionale Spezies nur zwischen zwei einzelnen Schichten verkapselt ist, aus elektronischen Gründen besonders erstrebenswert. Solche Doppelschichtstrukturen sollten mittels einer kontrollierten Exfolierung einer geordneten Wechsellagerung herstellbar sein, wenn Zwischenschichten vorliegen, die osmotisch quellfähig sind.

Die prinzipielle Machbarkeit wurde in dieser Studie erstmals exemplarisch für eine geordnete Wechsellagerung demonstriert, bei der Zwischenschichten eines Stilbazonium-Farbstoffes mit Natriumzwischenschichten alternieren (siehe **Kapitel 4.2**). Bei dieser Synthese wurde die osmotische Quellung der Natriumzwischenschichten durch die Verwendung einer Ethanol-Wasser Mischung unterdrückt.

Nach Zugabe von Wasser zu dem geordnet wechselgelagerten Hectoritpulver konnte zunächst eine Gelbildung und bei weiterer Erhöhung der Wassermenge die Bildung einer stabilen, transparenten Dispersion beobachtet werden. Die erfolgreiche Dispergierung des stark hydrophoben Farbstoffes in Wasser deutet bereits auf eine erfolgreiche Verkapselung in das Schichtsilicat hin. Mittels SAXS, Rasterkraftmikroskopie (AFM) und Transmissionselektronenmikroskopie (TEM) konnte die spontane Exfolierung zu Doppelschichten bewiesen werden.

Die thermogravimetrische Analyse (TGA) der Intercalationsverbindung belegte, dass die Verkapselung des Farbstoffes zwischen die Schichtsilicatschichten zu einer deutlichen thermischen Stabilisierung im Vergleich zu dem unverkapselten Farbstoffsalz führt. Auch in den photophysikalischen Eigenschaften zeigten sich durch die räumliche Begrenzung des Emitters deutliche Verbesserungen. So verdoppelte sich die Emissionsquantenausbeute der Stilbazoniumverbindung durch die Intercalation.

Die interessanten optischen Eigenschaften wurden auch mittels eines Polymer-Nanokompositfilms auf Basis von Polyvinylalkohol (PVOH) demonstriert. Durch das hohe Aspektverhältnis der Plättchen besitzt der gerakelte PVOH-Nanokompositfilm eine fast perfekte Textur. Dies äußert sich in einer deutlich verbesserten Gasbarriere gegenüber Sauerstoff und in anisotropen optischen Eigenschaften. Dieser optische Effekt wird durch die bevorzugte Ausrichtung der anisotropen Farbstoffmoleküle in den Zwischenschichten hervorgerufen. Auf diese Weise kann mittels der Verkapselung in das Schichtsilicat die

anisotrope Eigenschaft der funktionalen Moleküle von der Nanoebene auf die makroskopische Ebene übertragen werden.

Die weiteren besonderen Eigenschaften von Doppelschichten sollen im Folgenden mittels einer Synthese von mechanisch verstärkten Füllstoffen und durch den Symmetriebruch von Schichtverbindungen demonstriert werden.

## 4.4 Mechanisch verstärkte Doppelschichten zur Synthese von Janus-Plättchen

Die beschriebene Synthese von geordneten Wechsellagerungen (**Kapitel 4.2**) und deren Exfolierung zu Doppelschichten (**Kapitel 4.3**) kann auf weitere Systeme übertragen werden, so dass die Herstellung von Füllstoffen mit verbesserten mechanischen Eigenschaften oder die Synthese von Janus-Plättchen ermöglicht werden.

Exemplarisch wurde für die Synthese der geordneten Wechsellagerung das Ammonium-Kation als funktionales Zwischenschichtkation und der bereits beschriebene ladungshomogene Natriumhectorit (**Kapitel 4.1**) ausgewählt.

Da Ammonium-Ionen eine ähnliche Größe wie Kalium-Ionen aufweisen, ähnelt das System der Rectorit-ähnlichen Wechsellagerung, die in der Studie von Möller et al. untersucht wurde. Aus diesem Grund zeigen sich nach Intercalation von Ammonium-Ionen Eigenschaften (siehe **Kapitel 5.4**), die auch bei der Intercalation von Kaliumionen auftreten. So kollabierten auch die Ammoniumzwischenschichten beim Trocknen irreversibel und hydratisieren an Luft nicht mehr. PXRD-Messungen zeigten, dass die Bildung einer geordneten Wechsellagerung auch nach der Intercalation von Ammonium-Ionen in den Natriumhectorit erfolgt. Mittels SAXS und AFM-Untersuchungen wurde die erfolgreiche Exfolierung der geordneten Wechsellagerung in Doppelschichten nachgewiesen.

Die mechanische Charakterisierung der Ammonium-Doppelschichten erfolgte mittels der von *Kunz et al.* entwickelten Wrinkling-Methode. Hierbei wurden die Doppelschichten zunächst auf ein vorgespanntes Elastomer aus Polydimethylsiloxan (PDMS) abgeschieden. Nach dem Trocknen wurde das PDMS-Substrat wieder entspannt. Durch den unterschiedlichen Elastizitätsmodul von Substrat und Doppelschichten bilden sich sinusoidale Faltungen, deren Wellenlänge proportional zum in-plane Elastizitätsmodul der Plättchen ist.

Für die Doppelschichten wurde mit dieser Methode ein in-plane Elastizitätsmodul von  $171 \pm 16$  GPa ermittelt. Dieses Ergebnis ist deutlich höher als der entsprechende Wert,

welcher für ein vollständig delaminiertes, d.h. einzelnes Natriumhectorit-Plättchen auf die gleiche Weise bestimmt wurde ( $146 \pm 21$  GPa). Die Zunahme des Elastizitätsmoduls von 15% lässt sich mit der kollabierten Zwischenschichtstruktur der Doppelschichten erklären. Im kollabierten Zustand sind die Ammonium-Ionen in den hexagonalen Kavitäten der oberen und unteren Silicatschicht positioniert. Auf diese Weise werden beide Silicatschichten miteinander verzahnt, so dass Änderungen der Bindungswinkel der  $\text{SiO}_4$ -Tetraeder stark eingeschränkt werden. Die signifikante Versteifung in Kombination mit einer hohen theoretischen externen Oberfläche von ca.  $400 \text{ m}^2/\text{g}$  macht die Verwendung der Doppelschichten als Füllstoff zur mechanischen Versteifung in Polymernanokompositen attraktiv.

Ein weiterer Vorteil der Ammonium-Doppelschichten ist der einfache Austausch gegen osmotisch quellfähige Kationen wie Natrium- und Lithiumionen. Durch leichtes Anbasen und Austreiben des gebildeten Ammoniaks kann das Gleichgewicht vollständig auf die Seite der Intercalation der angebotenen Kationen verschoben werden. Nach einer Zugabe von LiOH konnte die Spaltung von Doppelschichten unter Bildung von Einzelschichten durch SAXS-Messungen belegt werden.

Diese kontrollierte Spaltbarkeit der Doppelschichten kann für die Synthese von Janus-Plättchen (siehe **Kapitel 3.6**) verwendet werden. Dafür wurde zunächst die Oberfläche der Doppelschichten mit einem geeigneten wasserlöslichen Polykation (Polyethylenoxid-co-polyethylenimin - PEI-EO) irreversibel modifiziert. Anschließend wurden die PEI-EO-modifizierten Doppelschichten durch LiOH-Zugabe gespalten, wodurch Janus-Plättchen erhalten wurden.

Mittels Neutronenkleinwinkelstreuung (Small angle neutron scattering - SANS) konnte die Reduzierung der Plättchendicke, die durch eine Spaltung der Doppelschicht zu erwarten ist, belegt werden. Zum Nachweis des Januscharakters wurde die freie Oberfläche mit einem dendritischen Polykation (Polyamidoamin - PAMAM) modifiziert. Nach Abscheiden auf einem Mikroporenfilter konnten im AFM zwei unterschiedliche Plättchenoberflächen nachgewiesen werden: Eine Oberfläche war vollständig mit PAMAM-Dendrimer belegt, während die andere Oberfläche durch die Belegung mit dem PEI-EO-Copolymer nahezu Dendrimer-frei war, was den Januscharakter bestätigt.

Die hier entwickelte Synthese von Plättchen mit Janus-Charakter ist nicht auf Ammonium-Wechsellagerungen begrenzt. Wie anhand der Strategie zur Synthese von geordneten Wechsellagerungen (siehe **Kapitel 4.2**) deutlich wird, ist die Verwendung vieler

deprotonierbarer Kationen, wie z.B. langkettiger Alkylammonium-Ionen denkbar, mit denen sich die Bildung der geordneten Wechsellagerung sehr gut kontrollieren lässt.

Das allgemeine Konzept zur Herstellung der spaltbaren Doppelschichten, sowie die vielfältigen Möglichkeiten der Verwendung von kommerziell verfügbaren und kostengünstigen statistischen Polymeren, eröffnen vielfältige Anwendungsmöglichkeiten. Diese könnten vor allem in Bereichen liegen, in denen die Beeinflussung der Grenzflächeneigenschaften und gleichzeitig eine Verkapselung bzw. mechanische Verstärkung der Grenzfläche wichtig wären, wie beispielsweise in Lackemulsionen, in Polymerblends oder Polymerschäumen.

## 4.5 Kontrollierte Exfolierung von Schichtsilicaten

In einem Übersichtsartikel wurden die unterschiedlichen Strategien zur kontrollierten Exfolierung von Schichtverbindungen und die vielfältigen Einsatzmöglichkeiten, die sich dadurch ergeben, zusammengefasst. Dabei wurden vor allem die Erkenntnisse zur Exfolierung und Anwendung von synthetischen Hectoriten, die am Lehrstuhl Anorganische Chemie I in Bayreuth von Herrn *Prof. Breu* entwickelt wurden, exemplarisch ausgeführt.

Nach einem kurzen Überblick über die Eigenschaftsänderungen von exfolierten Schichtverbindungen wurde die Voraussetzung zur effizienten Exfolierung anhand beispielhafter Schichtverbindungen ausgearbeitet. Die Schwächung der interlamellaren Bindungskräfte durch eine Erhöhung des Zwischenschichtabstandes ist als ein zentrales Konzept zur erfolgreichen Exfolierung aufzufassen.

Für geladene Schichtverbindungen, die zum Ladungsausgleich Gegenionen im Zwischenschichtraum aufweisen, könnte prinzipiell der Schichtabstand und damit die Scherlabilität, durch Wahl der Zwischenschichtionen beeinflusst werden. Dies setzt allerdings voraus, dass die intrakristalline Reaktivität der Intercalationsverbindung ausreichend hoch ist. Eine hohe intrakristalline Reaktivität liegt dann vor, wenn eine geladene Schichtverbindung mit geringer Ladungsdichte mit Zwischenschichtionen mit hoher Solvatationsenthalpie kombiniert wird.

Diese Voraussetzung trifft insbesondere für niedrig geladene, synthetische Hectorite zu, welche aufgrund ihrer hervorragenden Ladungshomogenität definierte Quellungsstufen, sowohl an feuchter Luft als auch in Wasser ausbilden. Synthetische Hectorite können aus diesem Grund als Modellverbindungen betrachtet werden, anhand derer sich allgemeine Konzepte zur Exfolierung von Schichtverbindungen ableiten lassen.

In Arbeiten von *Möller et al.* und *Ziadeh et al.* konnte gezeigt werden, dass für eine effiziente Exfolierung die Kombination von Zwischenschichtkationen, die hohe Quellungszustände generieren (z.B. das Dreischichthydrat des Magnesium-Ions) mit mechanischen Verfahren, bei denen starke unidirektionale Scherkräfte erzeugt werden (z.B. Microfluidizer®, Rührwerkskugelmühle) ein besonders effizientes Abscheren der Takoide ermöglicht. Auf diese Weise kann der nachteilige Bruch der Plättchen, der das Aspektverhältnis beim Exfolierungsprozess nicht vergrößern sondern verringern würde, deutlich reduziert werden.

Soll das maximal mögliche Aspektverhältnis erreicht, das heißt das Brechen von Plättchen beim Exfolierungsprozess möglichst vollständig vermieden werden, bietet sich als besonders sanfte Exfolierungsmethode die osmotische Quellung an. Von niedrig geladenen, natürlichen Smectiten mit Natrium- und Lithiumionen als Zwischenschichtkationen, sowie synthetischen Lithiumhectoriten und dem getemperten, ladungshomogenen Natriumhectorit (**Kapitel 4.1**) ist ein osmotisches Quellverhalten bereits bekannt. Wie SAXS-Messungen des osmotisch gequollenen Natriumhectorits zeigen, bilden sich aufgrund der homogenen LadungsdichteVerteilung exakt definierte Schichtabstände aus, wenn der Quellungszustand innerhalb der Reichweite der elektrostatischen Abstoßung liegt. Erst wenn der Schichtabstand oberhalb der elektrostatischen Reichweite (Debye Länge) liegt, beginnen sich die einzelnen Schichten mit zunehmendem Schichtabstand stärker individuell zu orientieren. Von einer echten Delaminierung sollte man daher erst beim Schmelzen des Wigner Kristalls, d.h. oberhalb der Debye Länge, sprechen. (siehe **Kapitel 5.6**).

Die entwickelten Konzepte zur kontrollierten Exfolierung von Hectoriten, d.h. die Verwendung von geordneten Wechsllagerungen (**Kapitel 4.2**) und deren anschließende Exfolierung (**Kapitel 4.3**), sowie die Kombination einer mechanischen Exfolierung eines magnesiumausgetauschten Hectorits mit einem anschließenden Kollabieren der Zwischenschichträume (vgl. dazu **Kapitel 4.4**) durch Austauschreaktionen mit Kationen niedrigerer Solvatationsenthalpie werden ebenfalls vorgestellt.

Abschließend wird der Einfluss der kontrollierten Exfolierung von synthetischen Hectoriten auf die mechanischen Eigenschaften, auf die Gasbarriere und das Brandverhalten von Polymer-Nanokompositen erläutert.

## 5. Ergebnisse

### 5.1 Ladungshomogener Natriumhectorit

Matthias Stöter,<sup>[a]</sup> Daniel A. Kunz,<sup>[a]</sup> Marko Schmidt,<sup>[b]</sup> Dunja Hirsemann,<sup>[a]</sup> Hussein Kalo,<sup>[a]</sup> Bernd Putz,<sup>[a]</sup> Jürgen Senker,<sup>[b]</sup> und Josef Breu<sup>[a]</sup>

**Nanoplatelets of sodium hectorite showing aspect ratios of  $\approx 20000$  and superior purity**

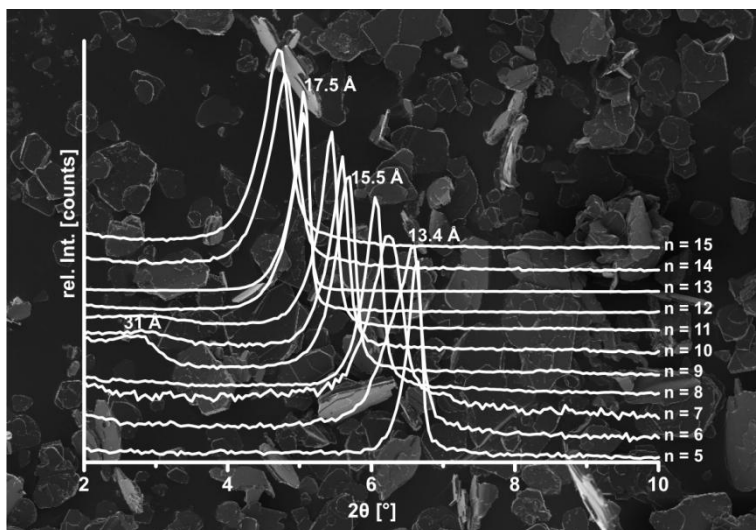
Erschienen in: Langmuir **2013**, 29, 1280-1285.

Reprinted with permission, Copyright (2013) American Chemical Society.

Impact Factor (2014) Langmuir: 4.457

<sup>[a]</sup> Lehrstuhl für Anorganische Chemie I, Universität Bayreuth, D-95440 Bayreuth, Germany

<sup>[b]</sup> Lehrstuhl für Anorganische Chemie III, Universität Bayreuth, D-95440 Bayreuth, Germany



#### Darstellung des Eigenanteils:

Diese Publikation stellt ein Gemeinschaftsprojekt zur Verbesserung der Synthese der Schichtsilicate am Lehrstuhl der Anorganischen Chemie I dar. Die Idee zur Nachbehandlung wurde von Herrn Prof. Dr. Josef Breu, Daniel Kunz und Bernd Putz entwickelt. Die Temperversuche wurden von Bernd Putz und Dr. Hussein Kalo durchgeführt. Die Festkörper-NMR-Messungen erfolgten durch Marko Schmidt, Dunja Hirsemann und Prof. Dr. Jürgen Senker. Daniel Kunz fertigte die AFM Messung an. Die experimentelle Untersuchung der Ladungshomogenität, der unterschiedlichen Hydratationszustände, der osmotischen Quellfähigkeit, der CEC, sowie die vergleichende Bestimmung der Partikelgrößenverteilung wurden von mir durchgeführt. Verfasst wurde diese Publikation hauptsächlich von Prof. Dr. Josef Breu, Daniel Kunz und mir. Daniel Kunz und ich haben zu einem Anteil von je 45 % beigetragen.

## 5.1.1 Nanoplatelets of sodium hectorite showing aspect ratios of $\approx 20000$ and superior purity

# Langmuir

Article

pubs.acs.org/Langmuir

## Nanoplatelets of Sodium Hectorite Showing Aspect Ratios of $\approx 20\,000$ and Superior Purity

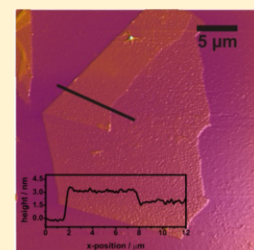
Matthias Stöter,<sup>†,§</sup> Daniel A. Kunz,<sup>†,§</sup> Marko Schmidt,<sup>‡</sup> Dunja Hirsemann,<sup>†</sup> Hussein Kalo,<sup>†</sup> Bernd Putz,<sup>†</sup> Jürgen Senker,<sup>‡</sup> and Josef Breu<sup>\*†</sup>

<sup>†</sup>Lehrstuhl für Anorganische Chemie I, Universität Bayreuth, D-95440 Bayreuth, Germany

<sup>‡</sup>Lehrstuhl für Anorganische Chemie III, Universität Bayreuth, D-95440 Bayreuth, Germany

 Supporting Information

**ABSTRACT:** Applying a combination of melt synthesis followed by long-term annealing a fluorohectorite is obtained which is unique with respect to homogeneity, purity, and particle size. Counterintuitively, the hectorite undergoes a disorder-to-order transition upon swelling to the level of the bilayer hydrate. Alkylammonium-exchanged samples show at any chain length only a single basal spacing corroborating a nicely homogeneous layer charge density. Its intracrystalline reactivity improves greatly upon annealing, making it capable to spontaneously and completely disintegrate into single clay lamellae of 1 nm thickness. Realizing exceptional aspect ratios of around 20 000 upon delamination, this synthetic clay will offer unprecedented potential as functional filler in highly transparent nanocomposites with superior gas barrier and mechanical properties.



### INTRODUCTION

Plenty of polymer nanocomposites contain platy nanofillers like clays as functional compounds for improvement in gas barrier activity, fire retardancy, and mechanical properties.<sup>1–8</sup> In order to exploit the full potential of these composite materials, it is especially important to optimize the performance of the clay filler, which in turn is mainly determined by its aspect ratio (ratio of particle size and height), textured orientation, mechanical properties, and compatibilization with the polymeric matrix. While texture and aspect ratio are strongly related to the filler's lateral extension, mechanical properties and interface management are crucially dependent on the homogeneity of the charge density of the clay layers which correlates with a uniform intracrystalline reactivity. Applicability of commercially available, natural swelling clays like montmorillonite is severely restricted by both small particle size (<200 nm) and a heterogeneous charge density. Additionally, all natural clays suffer from accessory minerals and poor optical quality due to colored transition metal ions incorporated into the structure. The latter drawbacks are particularly detrimental when aiming at flexible, transparent high-barrier films for optoelectronic packaging. Any globular impurities will act as defects and increase permeability significantly while the color reduces transmission.

Over the past decade we have developed melt synthesis protocols that yield platelets with particularly large lateral extensions and homogeneous charge density.<sup>6–8</sup> The intracrystalline reactivity was found to vary with charge<sup>9,10</sup> and the type of interlayer cation.<sup>11</sup> For instance, while Na-hectorite as obtained by melt synthesis<sup>7</sup> requires large shear forces in order to be exfoliated into thinner platelets,<sup>12</sup> Li-hectorite so far was the only material that spontaneously delaminates into single lamellae of 1 nm thickness by osmotic swelling when immersed

in deionized water.<sup>8</sup> Since in this gentle anisotropic top down process the particle diameter is preserved, such a fully delaminated material exhibits the maximum aspect ratio that may be obtained with given initial lateral dimension of the platelets which is determined by the synthesis conditions. While the Li-hectorite shows huge aspect ratios,<sup>8</sup> it lacks phase purity and needs to be purified before being applied as filler in nanocomposite films.<sup>3,13</sup>

Clearly, for high-barrier applications suitable for flexible optoelectronic packaging there still is a need for perfectly phase pure, transparent clay materials with huge lateral dimensions that spontaneously delaminate into nanoplatelets with aspect ratios >10 000.

Here we show that, surprisingly, a melt synthesized Na-fluorohectorite of medium charge density may be greatly activated in respect to swelling by long-term annealing. While the pristine material, as mentioned above, cannot be delaminated even when applying strong shearing forces, e.g. applying a ball mill, the annealed material spontaneously and completely delaminates. Since by annealing concomitantly the lateral extension of the material is increased, hydrodynamic suspensions of nanoplatelets of huge aspect ratios are obtained. In this paper, changes in respect to structure, phase, and chemical composition are revealed and related to rationalizing the observed unexpected activation.

### RESULTS AND DISCUSSION

**Synthesis of  $\text{Na}_{0.5}\text{-Hec}$ .**  $\text{Na}_{0.5}$ -fluorohectorite with nominal composition of  $[\text{Na}_{0.5}]_{\text{inter}}[\text{Mg}_{2.5}\text{Li}_{0.5}]^{\text{oct}}[\text{Si}_4]^{\text{tet}}\text{O}_{10}\text{F}_2$  ( $\text{Na}_{0.5}$

Received: November 8, 2012

Revised: December 14, 2012

Published: January 3, 2013

Hec) was synthesized by melt synthesis in a gastight molybdenum crucible according to an already published procedure.<sup>7</sup> 45 g of the as-synthesized dry Na<sub>0.5</sub>-Hec was milled with a planetary ball mill (Retsch PM 100) for 20 min at 250 rpm using a ZrO<sub>2</sub> grinding beaker with 15 ZrO<sub>2</sub> balls. By milling, the particle (aggregates) size was reduced to less than 250 µm. In order to remove the adsorbed humidity, the material was first dried overnight at 150 °C in a drying chamber, then dried under vacuum (10<sup>-2</sup> mbar) at 250 °C for 14 h to remove traces of water, and finally was stored in a glovebox. 35 g of the milled Na<sub>0.5</sub>-Hec was filled into a molybdenum crucible and then sealed under high vacuum (10<sup>-5</sup> mbar) with a molybdenum cap by a high-frequency furnace. In order to prevent the molybdenum from oxidation during the annealing procedure, the crucible was enclosed under vacuum into a quartz glass tube and heated in a chamber furnace (Thermal Technology) at 1045 °C (heating rate 2 °C/min). After annealing for 6 weeks the oven was switched off, and the sample was kept in the oven until the crucible cooled down to room temperature. Analysis by inductively coupled-plasma atomic emission spectroscopy (ICP-AES) and wavelength dispersive X-ray spectroscopy (WDX) (Supporting Information) confirmed that for the annealed material the compositions of both the bulk and individual clay tactoids were close to the target composition, [Na<sub>0.5</sub>]<sub>inter</sub>[Mg<sub>2.5</sub>Li<sub>0.5</sub>]<sup>oct</sup>[Si<sub>4</sub>]<sup>tet</sup>O<sub>10</sub>F<sub>2</sub> (Na<sub>0.5</sub>-Hec, x = 0.5 per formula unit (pfu)). Since WDX is incapable to determine Li, the analytical results were converted into the formula by normalizing to Si = 4 and gave [Na<sub>0.48(1)</sub>]<sub>inter</sub>[Mg<sub>2.57(3)</sub>Li<sub>x</sub>]<sup>oct</sup>[Si<sub>4</sub>] for the composition of cations. Additionally, Li and Na contents were determined by ICP-AES, and the Li content was derived by normalizing to the Na content found with WDX. This way the cation composition was found to be [Na<sub>0.48</sub>]<sub>inter</sub>[Mg<sub>2.57(3)</sub>Li<sub>0.47</sub>]<sup>oct</sup>[Si<sub>4</sub>]. The cation exchange capacity (CEC) was determined to be 126 mequiv/100 g with the barium method and 125 mequiv/100 g with the [Cu(trien)]<sup>2+</sup> method (see Supporting Information for details), which again is very close to the value expected for the target composition (130 mequiv/100 g). Usually for synthetic clays deviations from expectations are found to be much larger due to impurities. For instance, the CEC of the pristine sample is much lower (113 mequiv/100 g determined with the [Cu(trien)]<sup>2+</sup> method). Thus, the good agreement is a first indication for a high-purity material. The small residual difference is most likely due to the still limited size of the tactoids since in melt synthesis some sodium cations are consumed to neutralize tangling bonds at the edges.

Powder X-ray diffraction (PXRD) analysis confirmed a single phase material (Figure 2) while the pristine material, as obtained in the initial melt synthesis, by contrast contained small but detectable amounts of protoamphibole as side phase (Figure 1).<sup>7</sup>

Please note that PXRD is rather insensitive to amorphous materials that only show up in a broad background around 18°–28° 2θ. It is also obvious that by annealing the PXRD pattern develops additional peaks as compared to the pristine material. While the pristine material is almost turbostratically disordered,<sup>14</sup> these extra features are already pinpointing to a less disordered material with fewer stacking faults. The much improved stacking order becomes even more obvious upon hydration of the material. At relative humidities (RH) of 0%, 43%, and 93% well-defined hydration states of zero (0 WL), one (1 WL), and two layer hydrate (2 WL) are obtained. For

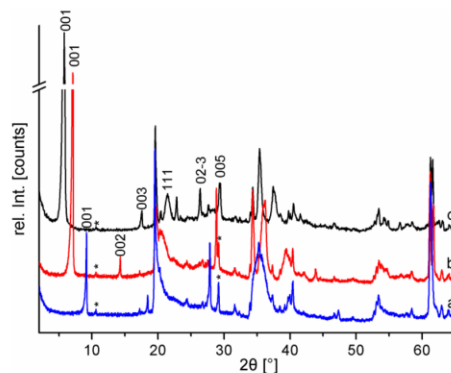


**Figure 1.** PXRD profiles of the nonannealed, pristine Na<sub>0.5</sub>-Hec at different relative humidities (RH): (a) sample heated at 120 °C, resulting in a nonhydrated state (0% RH, 0 WL); (b) sample equilibrated at 43% RH, resulting in a one-layer hydrate (1 WL); (c) swelling with water (*m*(water):*m*(pristine Na<sub>0.5</sub>-Hec) = 700:1), resulting in a two-layer hydrate (2 WL). Detectable reflexes of the protoamphibole side phase are marked with an asterisk.

all hydration states rational 001 series are observed. No signs for interstratifications of differently hydrated interlayers within the same stack were seen, and this unusual uniform intracrystalline reactivity in turn again indicates a superb homogeneous charge density.

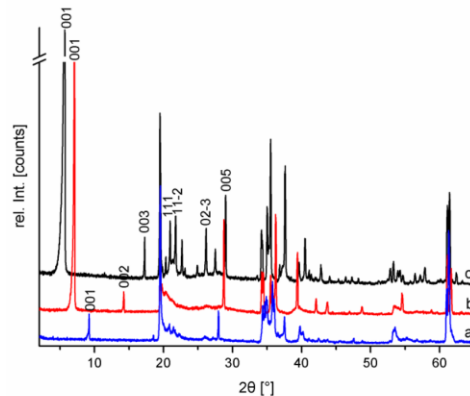


**Figure 2.** PXRD profiles of annealed Na<sub>0.5</sub>-Hec at different relative humidities (RH): (a) sample heated at 120 °C, resulting in a nonhydrated state (0% RH, 0 WL); (b) sample equilibrated at 43% RH, resulting in a one-layer hydrate (1 WL); (c) equilibrated at 93% RH, resulting in a two-layer hydrate (2 WL).

The nonhydrated structure (0 water layer = 0 WL) of Na<sub>0.5</sub>-Hec shows a *d*-spacing of 9.6 Å with a nearly perfect rational 001 series (coefficient of variation = 0.16%; see Supporting Information for details). Although the λ-shaped 11/02-band at around 20°2θ, indicates stacking faults, some peak maxima are visible and the PXRD pattern of the 0 WL can be indexed with a unit cell of *a* = 5.25 Å, *b* = 9.08 Å, *c* = 9.82 Å, and β = 94.5°. The *d*-spacing increases uniformly to 12.4 Å (coefficient of variation = 0.19%) at 43% RH. The PXRD pattern of the 1 WL can be indexed with a unit cell of *a* = 5.24 Å, *b* = 9.09 Å, *c* = 12.47 Å, and β = 96.0°. Finally swelling at a higher relative

humidity of 93% yields the 2 WL with  $d_{001} = 15.5 \text{ \AA}$  (coefficient of variation = 0.21%). As seen before for much higher charged swelling clays, e.g.,  $[\text{Na}_{0.7}]_{\text{inter}}[\text{Mg}_{2.3}\text{Li}_{0.7}]^{\text{oct}}[\text{Si}_4]^{\text{tet}}\text{O}_{10}\text{F}_2$ ,<sup>9</sup> for the 2 WL phase the number and the intensity of peaks in the range of the 11/02-band increased significantly. This is related to a disorder-to-order transition which is mediated by specific well-defined hydrogen-bonding networks to basal oxygens by the water molecules involved in octahedral coordination of  $\text{Na}^+$ . Evidently, the occurrence of this disorder-to-order transition is not crucially dependent on high charge densities. The PXRD pattern of the 2 WL can be indexed with the following unit cell:  $a = 5.248 \text{ \AA}$ ,  $b = 9.093 \text{ \AA}$ ,  $c = 15.483 \text{ \AA}$ , and  $\beta = 96.67^\circ$ .

Since PXRD is insensitive to amorphous phases, additionally, the purity of the material was investigated by solid-state NMR spectroscopy. Comparing the  $^{19}\text{F}$  MAS spectra of the pristine material and the annealed  $\text{Na}_{0.5}\text{-Hec}$  (Figure 3), clear

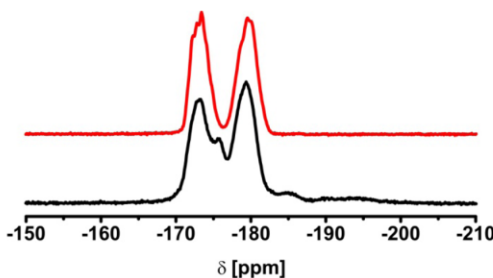


Figure 3.  $^{19}\text{F}$ -MAS spectra of  $\text{Na}_{0.5}\text{-Hec}$  (red line) in comparison with the nonannealed sample (black line).

differences in the environment of the  $^{19}\text{F}$  nuclei become evident. Two main types of fluorine sites with shifts at about  $-172$  and  $-180$  ppm were found. This is in good agreement with shifts reported in the literature for a hectorite of similar composition at  $-176.2$  and  $-182.8$  ppm, which were assigned to  $\text{Mg}-\text{Mg}-\text{Mg}$  and  $\text{Mg}-\text{Mg}-\text{Li}$  environments, respectively.<sup>15</sup> In the case of the pristine sample, however, an additional peak arises at ca.  $-175$  ppm. This signal cannot be attributed to protoamphibole, which would be expected at about  $-169$  ppm (Figure S1). Therefore, we propose that the pristine material, in addition to protoamphibole, contains a second, amorphous impurity phase. Clearly, this fluorine containing glass disappears during annealing, most likely by crystallization into  $\text{Na}$ -hectorite.

The high purity and homogeneity of this single phase material also became apparent applying the layer charge density determination by the alkylammonium method, which is demonstrated in Figure 4. Upon exchange of the interlayer  $\text{Na}^+$  ions with alkylammonium ions of increasing chain length ( $[\text{C}_n\text{H}_{2n+1}\text{NH}_3]^+$ ), the homogeneity of the layer charge can be easily checked by simply measuring the  $d$ -spacing of the intercalation compound. Because of the high selectivity of the alkylammonium ions, the interlayer cations are displaced completely and the negative layer charge is fully neutralized by alkylammonium ions. Depending on the charge density of the clay and the chain length of the alkylammonium ions different interlayer structures are formed. Monolayers ( $d_{001} = 13.4-13.6 \text{ \AA}$ ) will be realized as long as the charge density of flat-lying alkylammonium ions are higher than the charge density of the clay. At a certain critical chain length, these monolayers will be closely packed and with the next longer

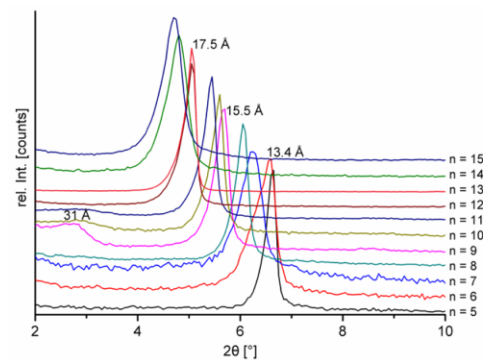


Figure 4. PXRD pattern of annealed  $\text{Na}_{0.5}\text{-Hec}$  exchanged with alkylammonium cations of different chain length ranging from pentyl ( $n = 5$ ) to pentadecylammonium ( $n = 15$ ).

chain lengths, some bilayers with a basal spacing of typically  $17.6 \text{ \AA}$  must be formed to neutralize the charge density of the clay. As already discussed with respect to hydration, heterogeneity in the charge density of clay sample will inevitably result in varying packing densities of the alkylammonium chains in different scattering domains. Consequently, the onset of bilayers being incorporated in the stack will occur at different chain length. This would cause the observation of more than one basal spacing at a given chain length as seen with the pristine material.<sup>7</sup> Contrary to this, for the annealed  $\text{Na}_{0.5}\text{-Hec}$  the basal spacing shifted gradually with increasing chain length, and at any chain length only a single basal spacing was observed, corroborating a nicely homogeneous layer charge density.

Please note that the smooth transition from mono- to bilayer with alkylammonium cations of increasing chain length is an artifact of interstratification. The X-ray beam averages over mono- and bilayer basal spacings in a volume weighted manner and while these basal spacings are fixed, the ratio of mono- and bilayers is varied to meet charge neutrality. This is because the strong coulomb interaction between positively charged interlayers and negatively charged silicate layers strongly favors minimization of the average basal spacing and therefore drives a strict segregation into densely packed mono- and bilayers.

The charge density ( $x$ ) of the clay corresponds directly to the longest alkylammonium ion (chain length  $n$ ) that still is capable to satisfy the charge density of the clay by a monolayer arrangement and can be calculated with a formula defined by Lagaly et al.:<sup>16-18</sup>

$$x = \frac{0.5a \cdot b}{5.67n + 14} \quad (1)$$

where  $a$  and  $b$  are the unit cell axes. Given unit cell parameters of  $a = 5.248 \text{ \AA}$  and  $b = 9.093 \text{ \AA}$  (e.g., for the 2WL state) a layer charge of  $x = 0.5$  should allow a monolayer arrangement up to a chain length of  $n = 5.95$ . The chain lengths must of course be an integer, and consequently charge neutrality with  $n = 6$  already requires very few bilayers. And indeed with  $n = 6$  the basal peak started to shift and the peak width broadens (Figure 4), both signs of beginning interstratification of some bilayers in the predominantly monolayer stacking.

Assuming the same packing density of mono- and bilayer arrangement, the critical chain length should be  $n = 14$  (more precisely 14.36) for the latter. However, uniform bilayer

arrangement is observed only up to tridecylammonium ( $n = 13$ , corresponding to  $x < 0.54$ ), while with  $n = 14$ , the basal peak already started to shift and broaden, indicating interstratification. Thus, with the Lagaly method, the layer charge can be narrowed down to  $\approx 0.5 < x < 0.54$ , which within the limits of the method is in excellent agreement with results from chemical analysis and determination of CEC.

As previously pointed out, with homogenously charged synthetic clays an ordered interstratification of bilayer and monolayers with Reichweite ( $R = 1$ ) is found to be the thermodynamically stable state. With some intermediate chain length, moreover, the ratio of mono- and bilayer will be close to 1:1, and indeed with nonadecylammonium ( $n = 9$ ) a superstructure reflection at 31 Å was observed (Figure 4). The plot of basal distance as a function of alkylammonium chain length (Figure S2) for this synthetic clay is therefore not linear but shows a plateau at  $d_{002}^*$  of the superstructure basal series of the ordered interstratification where the probability for a monolayer  $w_1$  is approximately equal to the probability for the bilayer  $w_2$  ( $w_1 = w_2$ ). Please note that the continuous shift of the  $d$ -spacing going from mono- to bilayer with alkylammonium cations of increasing chain length, which was observed by Lagaly and Weiss for a natural montmorillonite,<sup>18</sup> is due to random interstratification ( $R = 0$ ) caused by layer charge heterogeneity. Thus, the reason underlying interstratifications is different; for natural montmorillonites it is charge heterogeneity while for our synthetic clays it is observed for chain lengths where  $w_1 \ll w_2$  or  $w_1 \gg w_2$ .

In summary, both experimental facts—the observations of just one basal spacing with any alkylammonium intercalate and the formation of an ordered interstratification at an intermediate chain length—corroborate an unprecedented homogeneous distribution of the layer charge density.

The osmotic swelling behavior of  $\text{Na}_{0.5}\text{-Hec}$  was investigated in more detail by mixing the  $\text{Na}_{0.5}\text{-Hec}$  with different amounts of deionized water. Similar to what has been reported for synthetic Li-hectorite,<sup>8</sup> with increasing amounts of water the 00l peaks are continuously shifted to lower diffraction angle (higher  $d$ -values, Figure S3). The 001 reflection could, however, only be observed up to a weight ratio of  $m(\text{water}):m(\text{Na}_{0.5}\text{-Hec}) = 4:1$ ; even higher  $d_{001}$  values were out of the measurement range of our instrument. The  $d_{001}$  series for the mixture of 4:1 was rational ( $d_{001} = 115.4 \text{ \AA}$ ,  $d_{002} = 58.8 \text{ \AA}$ ,  $d_{003} = 38.8 \text{ \AA}$ , and  $d_{004} = 28.8 \text{ \AA}$ ). Larger basal spacings realized at higher water contents, could, however, still be calculated using higher order reflections. This way a linear increase of the  $d_{001}$ -spacing was obtained as a function of growing amounts of water being added (Figure 5). This linear characteristic resembles swelling of alkylammonium exchanged clays in organic liquids and organic liquid mixtures<sup>19–22</sup> and osmotic swelling of natural montmorillonites with sodium as an interlayer cation.<sup>23,24</sup>

Please note that the pristine  $\text{Na}_{0.5}\text{-Hec}$  shows no osmotic swelling. Even with a much higher water to pristine  $\text{Na}_{0.5}\text{-Hec}$  ratio of 700:1 only swelling to the two-layer hydrate (15.1 Å) was observed (curve c in Figure 1). The linear swelling characteristic, together with the broadening of the reflexes, as compared to “air” measurements, indicate that the tactoids of  $\text{Na}_{0.5}\text{-Hec}$  may delaminate in highly diluted dispersions. A proof for this suggestion could be delivered with AFM. For this, drops of a highly diluted dispersion (0.02 g/L,  $m(\text{water}):m(\text{Na}_{0.5}\text{-Hec}) = 50\,000:1$ ) were deposited and dried on a silicon wafer. Individual, delaminated platelets with a height of about 1 nm and a size between 10 and 20  $\mu\text{m}$  can be seen in the AFM

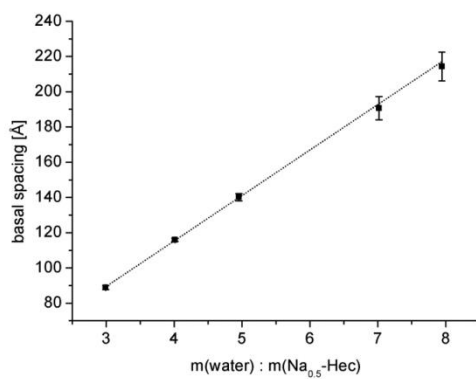


Figure 5. Relation between average  $d_{001}$  and mass ratio of water to  $\text{Na}_{0.5}\text{-Hec}$ .

image, as illustrated in Figure 6. Please note that due to the ambient conditions during measurement a water layer may exist

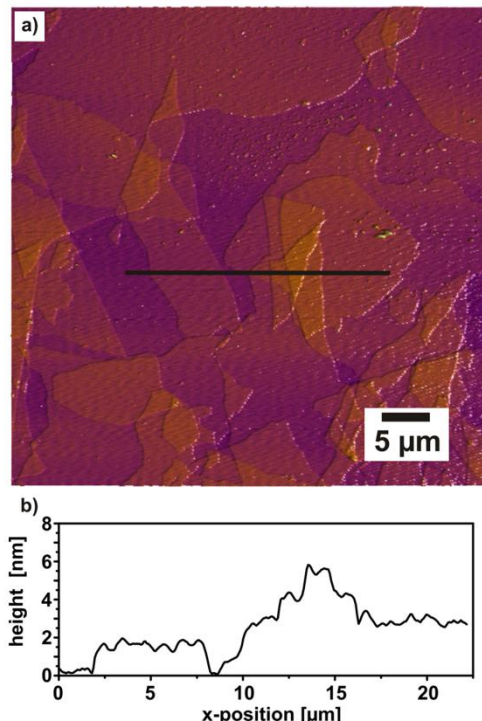


Figure 6. (a) Topographical AFM image of a typical sample of annealed  $\text{Na}_{0.5}\text{-Hec}$  showing the huge lateral extensions. (b) Height profile showing singular lamellae that are partially stacked above each other upon drying yielding discrete steps of about 1 nm height.

between substrate and platelets, causing an apparently larger height. Regardless of this systematic error, since the height of multilayer stacks increases in discrete steps of about 1 nm, all platelets with a thickness thinner than 2 nm can be safely assigned to be monolayers.

Although Figure 6 is a typical representative of many more images recorded, AFM is not a bulk method. In order to obtain

more information about the lateral extension of the platelets, the particle size distribution was measured with static light scattering (SLS) of an aqueous dispersion. The number weighted results show a relatively narrow size distribution of the platelets with a mean particle size of about 18  $\mu\text{m}$  (Figure S4). The SLS measurements were performed in aqueous dispersions; the particle size distribution therefore is representative for the bulk material. Moreover, it has been shown by Goossens<sup>25</sup> that the lateral extensions of clay tactoids correlate well with the hydrodynamical radius obtained from SLS. We are, however, aware that the absolute values might be somewhat in error because of the large size and the floppy nature of the nanoplatelets. To account for this high anisotropy of the particles, we therefore cross-checked the value by determining the chord lengths distribution by focused beam reflectance measurement (FBRM) (17  $\mu\text{m}$ ) and by assessing a large number of particles of Na<sub>0.5</sub>-Hec powders as seen in SEM micrographs (Figure S5) giving a mean tactoid size of 18  $\mu\text{m}$ . Considering a platelet thickness of about 1 nm and a median lateral extension of the clay particles of 18  $\mu\text{m}$  and assuming complete delamination by osmotic swelling as indicated by AFM and PXRD (Figure 5), Na<sub>0.5</sub>-Hec offers a mean aspect ratio of 18 000.

## CONCLUSIONS

Long-term annealing of melt-synthesized Na<sub>0.5</sub>-Hec induces crystallization of an amorphous impurity. We propose that this impurity acts as binder in the pristine material and limits its intracrystalline reactivity. As indicated by <sup>19</sup>F MAS solid-state NMR a highly phase pure fluorohectorite is obtained by the additional annealing step. Dispersing this activated Na<sub>0.5</sub>-Hec in water induces osmotic swelling and finally complete delamination into 1 nm thick platelets with medium aspect ratios of 18 000 as determined by AFM and particle size distributions. Moreover, annealing also results in superb charge characteristics. Both swelling with water and cation exchange with alkylammonium cations suggest a perfectly uniform intracrystalline reactivity corresponding to a degree of homogeneous charge density of the clay platelets not seen before. At last, stacking faults are diminished a great deal by annealing and the highly ordered material can be used for the synthesis of ordered microporous pillared or interstratified inorganic/organic hybrid materials. Most importantly, the combination of high optical transparency, ultrahigh aspect ratio, and the absence of impurities renders this clay the perfect filler for high gas barrier applications and mechanical improvement of nanocomposites which will be studied in future work.

## ASSOCIATED CONTENT

### Supporting Information

All experimental details and the following supporting data: <sup>19</sup>F-MAS spectra of a sample enriched in protoamphibole, plot of *d*-spacings as a function of alkylammonium chain length *n*, PXRD traces of osmotic swelling, particle size distributions, and SEM micrographs. This material is available free of charge via the Internet at <http://pubs.acs.org>.

## AUTHOR INFORMATION

### Corresponding Author

\*Phone +49 921 55 2531; Fax +49 921 55 2788; e-mail Josef.Breu@uni-bayreuth.de.

## Author Contributions

<sup>§</sup>These authors contributed equally. The manuscript was written through contributions of all authors. All authors have given approval to the final version of the manuscript.

## Notes

The authors declare no competing financial interest.

## ACKNOWLEDGMENTS

This work was supported by the Deutsche Forschungsgemeinschaft (SFB 840). D.A.K. thanks the elite study program “Macromolecular Science” as well as the International Graduate School “Structure, Reactivity and Properties of Oxide Materials” within the Elite Network of Bavaria (ENB) for ongoing support. The authors thank the Bayerisches Geoinstitut, Bayreuth, Germany for the WDX measurements. We also thank Prof. A. Fery, Physikalische Chemie II, Universität Bayreuth, for making AFM equipment available.

## REFERENCES

- (1) Schütz, M. R.; Kalo, H.; Lunkenbein, T.; Gröschel, A. H.; Müller, A. H. E.; Wilkie, C. A.; Breu, J. Shear Stiff, Surface Modified, Mica-Like Nanoplatelets: a Novel Filler for Polymer Nanocomposites. *J. Mater. Chem.* 2011, 21, 12110–12116.
- (2) Tang, Z. Y.; Kotov, N. A.; Magonov, S.; Ozturk, B. Nanostructured Artificial Nacre. *Nat. Mater.* 2003, 2, 413–418.
- (3) Möller, M. W.; Kunz, D. A.; Lunkenbein, T.; Sommer, S.; Nennemann, A.; Breu, J. UV-Cured, Flexible, and Transparent Nanocomposite Coating with Remarkable Oxygen Barrier. *Adv. Mater.* 2012, 24, 2142–2147.
- (4) Podsiadlo, P.; Kaushik, A. K.; Arruda, E. M.; Waas, A. M.; Shim, B. S.; Xu, J. D.; Nandivada, H.; Pumpkin, B. G.; Lahann, J.; Ramamoorthy, A.; Kotov, N. A. Ultrastrong and Stiff Layered Polymer Nanocomposites. *Science* 2007, 318, 80–83.
- (5) Schütz, M. R.; Kalo, H.; Lunkenbein, T.; Breu, J.; Wilkie, C. A. Intumescent-like Behavior of Polystyrene Synthetic Clay Nanocomposites. *Polymer* 2011, 52, 3288–3294.
- (6) Kalo, H.; Möller, M. W.; Ziadeh, M.; Dolejs, D.; Breu, J. Large Scale Melt Synthesis in an Open Crucible of Na-Fluorohectorite with Superb Charge Homogeneity and Particle Size. *Appl. Clay Sci.* 2010, 48, 39–45.
- (7) Breu, J.; Seidl, W.; Stoll, A. J.; Lange, K. G.; Probst, T. U. Charge Homogeneity in Synthetic Fluorohectorite. *Chem. Mater.* 2001, 13, 4213–4220.
- (8) Kalo, H.; Möller, M. W.; Kunz, D. A.; Breu, J. How to Maximize the Aspect Ratio of Clay Nanoplatelets. *Nanoscale* 2012, 4, 5633–5639.
- (9) Kalo, H.; Milius, W.; Breu, J. Single Crystal Structure Refinement of One- and Two-Layer Hydrate of Sodium-Fluorohectorite. *RSC Adv.* 2012, 2, 8452–8459.
- (10) Kalo, H.; Milius, W.; Bräu, M.; Breu, J. Synthesis and Single Crystal Structure Refinement of the One-Layer Hydrate of Sodium Brittle Mica. *J. Solid State Chem.* 2013, 198, 57–64.
- (11) Möller, M. W.; Handge, U. A.; Kunz, D. A.; Lunkenbein, T.; Altstadt, V.; Breu, J. Tailoring Shear-Stiff, Mica-Like Nanoplatelets. *ACS Nano* 2010, 4, 717–724.
- (12) Ziadeh, M.; Chwalka, B.; Kalo, H.; Schütz, M. R.; Breu, J. A Simple Approach for Producing High Aspect Ratio Fluorohectorite Nanoplatelets Utilizing a Stirred Media Mill (Ball Mill). *Clay Miner.* 2012, 47, 341–353.
- (13) Möller, M. W.; Lunkenbein, T.; Kalo, H.; Schieder, M.; Kunz, D. A.; Breu, J. Barrier Properties of Synthetic Clay with a Kilo-Aspect Ratio. *Adv. Mater.* 2010, 22, 5245–5249.
- (14) Breu, J.; Seidl, W.; Stoll, A. Disorder in Smectites in Dependence of the Interlayer Cation. *Z. Anorg. Allg. Chem.* 2003, 629, 503–515.

- (15) Huve, L.; Delmotte, L.; Martin, P.; LeDred, R.; Baron, J.; Saehr, D. F-19 MAS-NMR study of structural fluorine in some natural and synthetic 2:1 layer silicates. *Clays Clay Miner.* **1992**, *40*, 186–191.
- (16) Mermut, A. R.; Lagaly, G. Baseline studies of The Clay Minerals Society source clays: Layer-charge determination and characteristics of those minerals containing 2: 1 layers. *Clays Clay Miner.* **2001**, *49*, 393–397.
- (17) Lagaly, G. Characterization of Clays by Organic-Compounds. *Clay Miner.* **1981**, *16*, 1–21.
- (18) Lagaly, G.; Weiss, A. Arrangement and Orientation of Cationic Tensides on Silicate Surfaces 0.4. Arrangement of Alkylammonium Ions in Low-Charged Silicates of Films. *Kolloid Z. Z. Polym.* **1971**, *243*, 48–55.
- (19) Dekany, I.; Szanto, F.; Nagy, L. G. Sorption and Immersional Wetting on Clay-Minerals Having Modified Surface 0.2. Interlamellar Sorption and Wetting on Organic Montmorillonites. *J. Colloid Interface Sci.* **1986**, *109*, 376–384.
- (20) Kotov, N. A.; Meldrum, F. C.; Fendler, J. H.; Tombacz, E.; Dekany, I. Spreading of Clay Organocomplexes on Aqueous-Solutions - Construction of Langmuir-Blodgett Clay Organocomplex Multilayer Films. *Langmuir* **1994**, *10*, 3797–3804.
- (21) Dekany, I.; Szanto, F.; Weiss, A.; Lagaly, G. Interactions of Hydrophobic Layer Silicates with Alcohol-Benzene Mixtures 0.1. Adsorption-Isotherms. *Ber. Bunsenges. Phys. Chem.* **1986**, *90*, 422–427.
- (22) Dekany, I.; Szanto, F.; Weiss, A.; Lagaly, G. Interactions of Hydrophobic Layer Silicates with Alcohol-Benzene Mixtures 0.2. Structure and Composition of the Adsorption Layer. *Ber. Bunsenges. Phys. Chem.* **1986**, *90*, 427–431.
- (23) Norrish, K. The Swelling of Montmorillonite. *Discuss. Faraday Soc.* **1954**, *120*–134.
- (24) Segad, M.; Hanski, S.; Olsson, U.; Ruokolainen, J.; Akesson, T.; Jonsson, B. Microstructural and Swelling Properties of Ca and Na Montmorillonites (In Situ) Observations with Cryo-TEM and SAXS. *J. Phys. Chem. C* **2012**, *116*, 7596–7601.
- (25) Goossens, D. Techniques to Measure Grain-Size Distributions of Loamy Sediments: a Comparative Study of Ten Instruments for Wet Analysis. *Sedimentology* **2008**, *55*, 65–96.

### 5.1.2 Supporting information

## Nanoplatelets of sodium hectorite showing aspect ratios of $\approx 20000$ and superior purity

*Matthias Stöter,<sup>†,§</sup> Daniel A. Kunz,<sup>†,§</sup> Marko Schmidt,<sup>‡</sup> Dunja Hirsemann,<sup>†</sup> Hussein Kalo,<sup>†</sup> Bernd Putz,<sup>†</sup> Jürgen Senker,<sup>‡</sup> and Josef Breu<sup>†,\*</sup>*

<sup>†</sup> Lehrstuhl für Anorganische Chemie I, Universität Bayreuth, D-95440 Bayreuth, Germany

<sup>‡</sup> Lehrstuhl für Anorganische Chemie III, Universität Bayreuth, D-95440 Bayreuth, Germany

## Supporting Information

### Content:

1. Experimental Details
2. Supporting Data
3. Supporting References

## 1. Experimental Details

### Cation exchange capacity

The cation exchange capacity (CEC) of the non-annealed, pristine hectorite and the annealed material was determined with the  $[\text{Cu}(\text{trien})]^{2+}$  method.<sup>1</sup> A control measurement was done by a threefold exchange of the annealed  $\text{Na}_{0.5}\text{-Hec}$  with excess of a  $\text{BaCl}_2$  solution (0.1 mol/L) according to the DIN ISO 11260 standard procedure. The collected washing solutions were analyzed for Na using a Varian SpectrAA-100 atomic absorption spectrometer.

### WDX

The composition of the annealed  $\text{Na}_{0.5}\text{-Hec}$  was determined by wavelength dispersive X-ray spectroscopy (WDX) on a Joel JXA 8200 spectrometer, with acceleration voltage 15 kV and 15 nA with a beam spot diameter of 1  $\mu\text{m}$ . Calibration was done using andradite  $\text{Ca}_3\text{Fe}_2\text{Si}_3\text{O}_{12}$  as silicon standard, synthetic enstatite  $\text{Mg}_2[\text{Si}_2\text{O}_6]$  as magnesium standard and albite  $\text{NaAlSi}_3\text{O}_8$  as sodium standard. After polishing only particles with smooth surfaces were chosen for the WDX measurement. The counting time was 20 s at every peak position. The composition was normalized to  $\text{Si}_{4.00}$  because lithium is not detectable with this method.

### ICP-AES

The lithium and sodium content of the bulk material was determined by inductive-coupled-plasma atomic emission spectroscopy (ICP-AES). Two samples of about 20 mg of dry synthetic  $\text{Na}_{0.5}\text{-Hec}$  were weighed into clean Teflon flasks of 150 mL volume. After addition of 1.5 mL 30 wt. % HCl (Merck), 0.5 mL of 85 wt. %  $\text{H}_3\text{PO}_4$  (Merck), 0.5 mL 65 wt. %  $\text{HNO}_3$  (Merck) and 1 mL of 48 wt. %  $\text{HBF}_4$  (Merck) the sample was digested in a MLS 1200 Mega microwave digestion apparatus for 6.5 min and heated at 600W (MLS GmbH, Mikrowellen-Labor-Systeme, Leutkirch, Germany). The closed sample container was cooled to room temperature and the clear solution was diluted to 100 mL in a volumetric flask and analyzed.

### Layer charge determination

The layer charge was determined by the alkylammonium method.<sup>2</sup> The alkylammonium salts were prepared by acidification of amines ( $[C_nH_{2n+1}NH_3]^+$ ; n = 5-15) dissolved in ethanol by adding aqueous formic acid (2 mol/L). The solutions were adjusted to a pH of 8 and filled up with water to achieve a concentration of 2 mol/L for the pentyl- and hexylamine, 0.5 mol/L for the pentyl- to decylamines and 0.1 mol/L for the corresponding longer chain alkylamines. 90 mg of the annealed Na<sub>0.5</sub>-Hec was exchanged 3 times with 3 ml of the different amines in small glass vessels closed with screw caps at 60 °C in an overhead shaker. The products were removed from the solution by centrifugation and washed 6 times with ethanol-water mixture (1:1), 4 times with pure ethanol and finally dried at 60°C.

### Powder X-ray diffraction

Powder X-ray diffraction (PXRD) was measured in transmission geometry on a STOE Stadi P powder diffractometer equipped with a MYTHEN1K detector using Cu K $\alpha_1$  radiation ( $\lambda = 1.54056\text{\AA}$ ). For investigation of the different hydration states the Na<sub>0.5</sub>-Hec powder was filled into fused silica capillaries (0.7 mm Hilgenberg) and equilibrated for 30 days in a desiccator at 43% and 93% relative humidity using saturated K<sub>2</sub>CO<sub>3</sub> and KNO<sub>3</sub> solutions, respectively. To prevent evaporation of water during the PXRD measurement the capillaries were sealed with high vacuum silicone grease (Merck) immediately after being removing from the selected water vapor atmosphere. For the non-hydrated (0% RH) sample the capillary was stored at 120°C overnight and sealed by melting the top of the capillary.

The osmotic swelling experiments were completed in small glass vessels by mixing a weighted mass of deionized water with a corresponding mass of hectorite powder. After an equilibration time of 48 hours, the resulting gels were mixed with a spatula, placed between two mylar foils using a flat sample holder and then were immediately measured on the XRD within 15 minutes.

### Atomic Force Microscopy

Atomic Force Microscopy was done by using a MFP3D<sup>TM</sup> Atomic Force Microscope (Asylum Research, Santa Barbara, California) equipped with silicon cantilevers (silicon tip, type NSC15/AlBS,  $\mu$ mash, Tallin, Estonia) with a scan rate of 1 Hz. The samples were prepared by slowly evaporation of a few drops of a diluted suspension (0.02 g/L) on a Si-wafer under ambient conditions.

### Particle size distribution

Particle size distribution was recorded by static light scattering (SLS) of aqueous dispersions using a Retsch Horiba LA-950 SLS instrument. The refractive index of the solid phase was set to a value of 1.5. A measurement routine called “mica in water” supplied by the manufacturer (Horiba) was applied. Micas have similar lateral extensions as the synthetic hectorites studied here. The routine determines transmission rates and optimizes the concentration of the suspensions.

For comparison the chord length distribution of an aqueous dispersion was additionally investigated by focused beam reflectance measurement (FBRM) with a Mettler Toledo LASENTEC FBRM model D600L-HC22-K. Finally, the crystal size of the solid material was also measured by assessing a large number of hectorite particles as imaged with a LEO 1530 FE-SEM at an operating voltage of 3 kV.

### NMR MAS Measurement

The  $^{19}\text{F}$  shifts are reported with respect to  $\text{CFCl}_3$ . The 1D- $^{19}\text{F}$  MAS NMR spectra were recorded on a Bruker Avance II spectrometer using triple resonance probes ( $\text{ZrO}_2$ , diameter 2.5 mm) at a MAS frequency of 30 kHz. A direct excitation on the  $^{19}\text{F}$  channel with a  $90^\circ$  pulse length of 2  $\mu\text{s}$  was applied. The recycle delay was 20 s, the number of experiments was set to 16. For all experiments, no proton decoupling was used.

## 2. Supporting Data

**Coefficient of variation (CV)**

The coefficient of variation was calculated according to Bailey:<sup>3</sup>

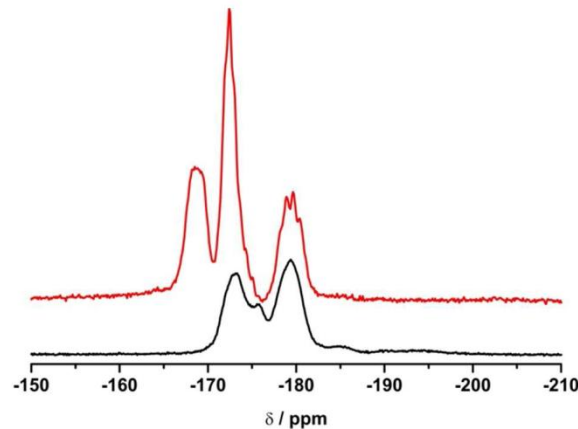
$$CV = \frac{100s}{X}$$

where s = standard deviation and X = mean of the observed  $l * d_{00l}$  values. Due to overlap, we were only able to unambiguously determine the positions of the  $00l$ -series where  $l_{\max} = 7$  in case of zero-layer hydrate,  $l_{\max} = 9$  in case of one layer hydrate, and  $l_{\max} = 10$  in case of the two-layer hydrate.

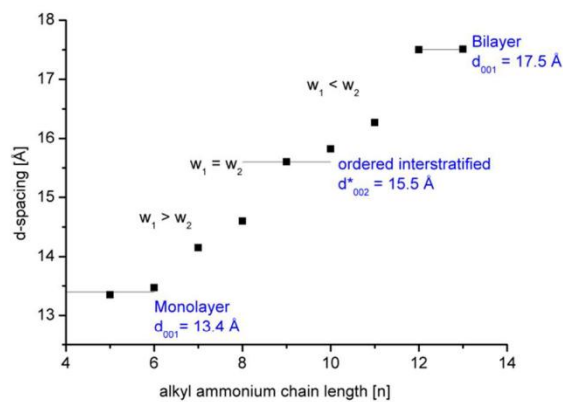
The 2WL gives a basal spacing of  $d_{001} = 15.4 \text{ \AA}$  (coefficient of variation = 0.21 %).

Example 2WL:

<i>l</i>	<i>d</i>	<i>l</i> * <i>d</i> (001)
1	15.459	15.46
3	5.130	15.39
4	3.848	15.39
5	3.073	15.36
6	2.563	15.38
7	2.195	15.37
8	1.920	15.36
10	1.537	15.37
Mean		15.39
CV		0.21%

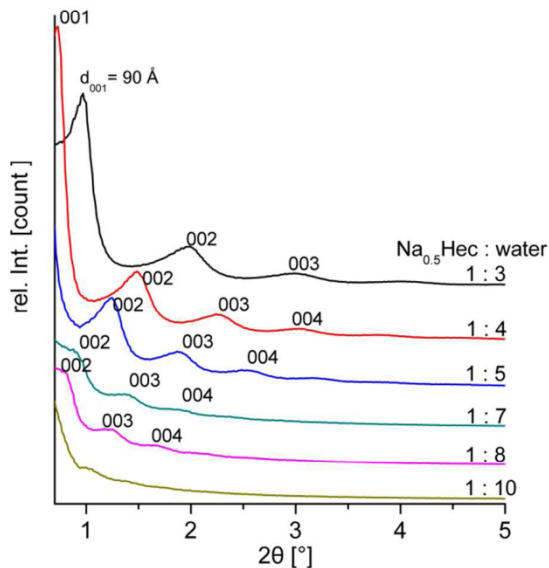
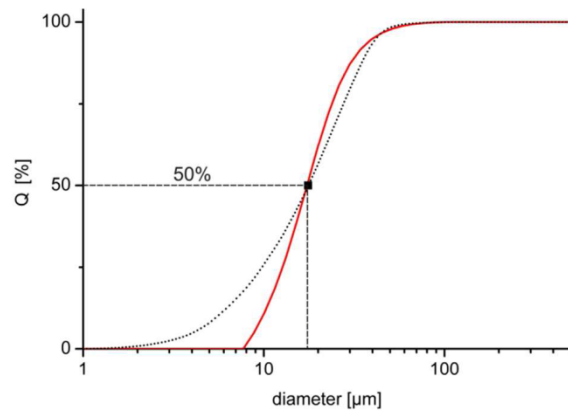


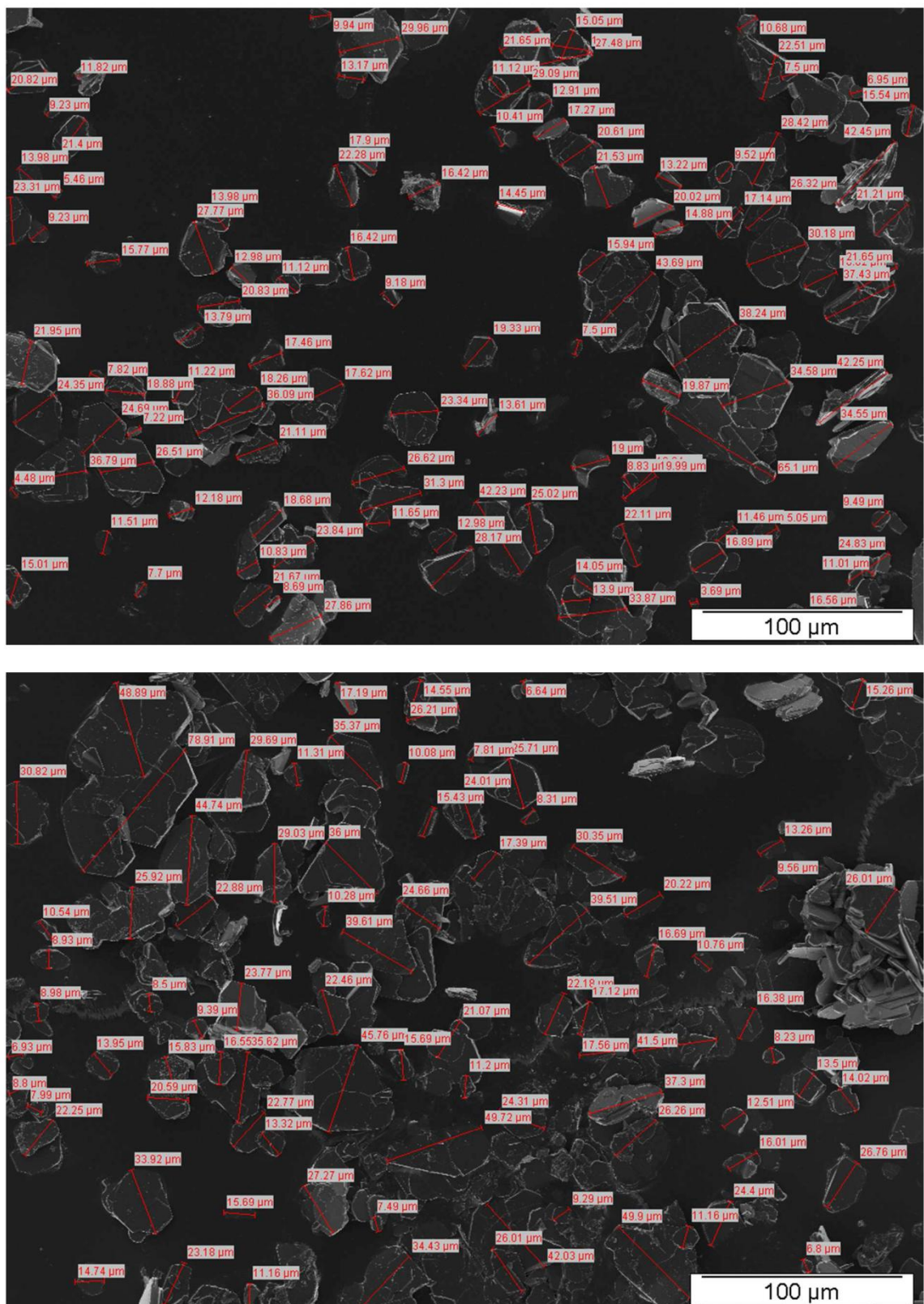
**Figure S1:** <sup>19</sup>F-MAS spectra of a Na<sub>0.5</sub>-Hec sample containing a much increased volume ratio of protoamphibole<sup>4,5</sup> sidephase (red line) as compared to the pristine Na<sub>0.5</sub>-Hec sample. The additional peak at about -169 ppm can be assigned to protoamphibole.



**Figure S2:** Plot of  $d$ -spacings as function of alkylammonium chain length  $n$  ( $[C_nH_{2n+1}NH_3]^+$ ).

A plateau for the ordered interstratification where the probability of the monolayer  $w_1$  is approximately equal to the probability of the bilayer  $w_2$  ( $w_1 = w_2$ ) is indicated.

**Figure S3:** PXRD measurement of the osmotic swelling of the  $Na_{0.5}$ -Hec as function of the mass ratio  $Na_{0.5}$ -Hec : water.**Figure S4.** Number weighted particle size distribution as determined by SLS measurement of a  $Na_{0.5}$ -Hec dispersion in water (solid red line) and corresponding unweighted FBRM measurement (dotted black line). Both results agree well with the mean tactoid size of  $Na_{0.5}$ -Hec powder as seen in SEM micrographs (black square).



### 3. Supporting References

- (1) Ammann, L.; Bergaya, F.; Lagaly, G. Determination of the cation exchange capacity of clays with copper complexes revisited. *Clay Miner.* **2005**, *40*, 441-453.
- (2) Mermut, A. R.; Lagaly, G. Baseline studies of The Clay Minerals Society Source Clays: Layer-charge determination and characteristics of those minerals containing 2 : 1 layers. *Clays Clay Miner.* **2001**, *49*, 393-397.
- (3) Bailey, S. W. Nomenclature for Regular Interstratifications. *Am. Mineral.* **1982**, *67*, 394-398.
- (4) Delevoye, L.; Liu, S. X.; Welch, M. D.; Fernandez, C.; Amoureaux, J. P.; Klinowski, J. Triple-quantum Al-27 and Na-23 MAS NMR study of amphiboles. *J. Chem. Soc. Faraday Trans.* **1997**, *93*, 2591-2595.
- (5) Möller, M.; Hirsemann, D.; Haarmann, F.; Senker, J.; Breu, J. Facile Scalable Synthesis of Rectorites. *Chem. Mater.* **2010**, *22*, 186-196.

## 5.2 Bildung geordneter Wechsellagerungen

Matthias Stöter,<sup>[a]</sup> Bernhard Biersack,<sup>[b]</sup> Nele Reimer,<sup>[c]</sup> Markus Herling,<sup>[a]</sup> Norbert Stock,<sup>[c]</sup> Rainer Schobert,<sup>[b]</sup> und Josef Breu<sup>[a]</sup>

### Ordered heterostructures of two strictly alternating types of nanoreactors

Erschienen in: Chemistry of Materials **2014**, 26, 5412–5419.

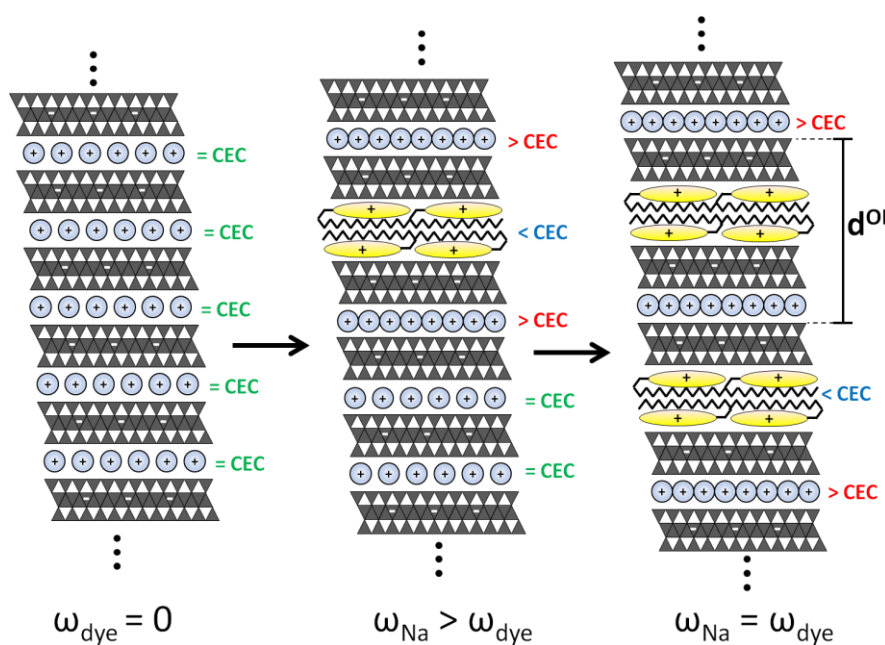
Reprinted with permission, Copyright (2014) American Chemical Society.

Impact Factor (2014) Chemistry of Materials: 8.354

<sup>[a]</sup> Lehrstuhl für Anorganische Chemie I, Universität Bayreuth, D-95440 Bayreuth, Germany

<sup>[b]</sup> Lehrstuhl für Organische Chemie I, Universität Bayreuth, D-95440 Bayreuth, Germany

<sup>[c]</sup> Institut für Anorganische Chemie, Universität Kiel, D-24118 Kiel, Germany



### Darstellung des Eigenanteils:

Das Konzept für diese Publikation wurde von Prof. Dr. Josef Breu und mir entwickelt. Die Synthese der Stilbazoniumverbindung erfolgte in der Organischen Chemie I, Universität Bayreuth durch Dr. Bernhard Biersack und Prof. Dr. Rainer Schobert. Die Wasserdampfphysisorption wurde am Institut der Anorganischen Chemie, Universität Kiel von Nele Reimer und Prof. Dr. Norbert Stock gemessen. Markus Herling führte einen Teil der CHN-Analytik und den Anionenaustausch des DABCO-Salzes durch.

Die experimentelle Entwicklung der Synthesen und Charakterisierungen der Intercalationsverbindungen sowie die Bestimmung der Adsorptionsisothermen wurden von mir selbst durchgeführt. Verfasst wurde diese Publikation hauptsächlich von Prof. Dr. Josef Breu und mir. Mein Eigenanteil beträgt ca. 80 %.

## 5.2.1 Ordered heterostructures of two strictly alternating types of nanoreactors



Article

pubs.acs.org/cm

### Ordered Heterostructures of Two Strictly Alternating Types of Nanoreactors

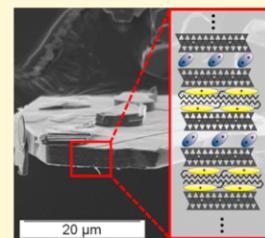
Matthias Stöter,<sup>†</sup> Bernhard Biersack,<sup>‡</sup> Nele Reimer,<sup>§</sup> Markus Herling,<sup>†</sup> Norbert Stock,<sup>§</sup> Rainer Schobert,<sup>‡</sup> and Josef Breu\*,<sup>†</sup>

<sup>†</sup>Lehrstuhl für Anorganische Chemie I and <sup>‡</sup>Lehrstuhl für Organische Chemie I, Universität Bayreuth, D-95440 Bayreuth, Germany

<sup>§</sup>Institut für Anorganische Chemie, Universität Kiel, D-24118 Kiel, Germany

#### Supporting Information

**ABSTRACT:** One-dimensional crystalline heterostructures of two types of nanoreactors strictly alternating along the stacking direction are obtained by partial ion exchange into a synthetic clay mineral distinguished by an outstandingly homogeneous charge density. The driving force for the formation of these high interface architectures is proven to be founded in densely packed cationic molecules in the interlayer with a charge density deviating from the charge density of the host clay mineral. The established mechanism renders the approach generally applicable and will allow for synthesis of ordered heterostructures of any desired combination of functional molecules that moreover are separated by exactly 1 nm thick silicate walls. The ordered heterostructures were furthermore shown to represent the thermodynamic equilibrium suggesting the mechanism of formation to be robust.



#### INTRODUCTION

Materials with alternating functional layered nanostructures have shown great potential for energy transfer and conversion, sensoring, and catalysis.<sup>1–4</sup> Main advantages of such regularly alternating two-dimensional heterostructures are a huge interface area allowing for effective energy or electron transfer which require proximity in nanometer architectures i.e. Foerster resonance energy transfer (FRET).<sup>3</sup> Most frequently such architectures have been manufactured in a bottom up process like layer-by-layer (LBL) assembly.<sup>5,6</sup> For instance, an alternating heterostructure of a negatively charged semiconductive layered perovskite and a positively charged layered double hydroxide could be obtained by using the LBL approach.<sup>7,8</sup> However, this LBL method is a time and cost intensive procedure and difficult to scale. Alternatively, such regularly ordered nanostructures may be achieved by self-assembly of oppositely charged layers (heterocoagulation). For instance, after restacking of a negatively charged layered titanate and a positively charged layered double hydroxide a highly effective visible photocatalyst for water splitting could be obtained.<sup>1</sup> However, both LBL and heterocoagulation methods require a complete delamination of the two types of layered materials in order to obtain structures with defined periodicity. Suitable delaminated nanostructures may for instance be obtained by surfactant-mediated synthesis of nanosheets.<sup>9</sup>

Here we present a robust and scalable alternative route to arrive at strictly alternating architectures which are referred to as staging or ordered interstratification in the intercalation community. Ordered interstratifications were first investigated for different 2:1 clay minerals like hectorites and vermiculites.<sup>10,11</sup> Within these regular interstratified materials, two distinct nanoreactors are exactly separated by a 1 nm-thick insulating layer and therefore are arranged in a much more

regular, one-dimensional crystalline, manner as compared to materials assembled by LBL or heterocoagulation. Pinnavaia described the formation of a mixed inorganic–organic layered material using cationic amphiphiles and explored numerous potential applications of these materials.<sup>11–14</sup> For instance, in a proof of principle study the potential of such regular interstratifications for electrochemical sensing of herbicides was shown.<sup>2,15</sup>

While in these initial studies a first synthesis protocol was established, a general mechanism could not be established. Consequently, transfer to any functional heterostructures of interest was not possible. The structure of 2:1 layered silicates is symmetrical along the stacking direction, and it is therefore anything but trivial that this symmetry may be broken in such a regular manner. A deeper insight into the ordering mechanism is, however, required to broaden the synthesis protocol to arbitrary functional interstratified materials.

Ijdo et al. suggested a model with homogeneous interlayer cation occupation.<sup>14</sup> Later Möller et al. showed that for synthetic rectorite-type structures, where nonhydrated, mica-like potassium interlayers alternate with hydrated sodium interlayers, the symmetry is broken by a modulation of the interlayer cation density.<sup>16</sup> Upon formation of the regular interstratification, the charge density of the interlayers changes from homogeneous to regularly alternating from interlayer to interlayer in the stacking direction. For these synthetic rectorites, the higher selectivity of  $K^+$  as compared to  $Na^+$  was shown to be the driving force for the redistribution of exchangeable interlayer cations. The cation exchange capacity

Received: July 30, 2014

Revised: August 19, 2014

Published: September 2, 2014

## Chemistry of Materials

## Article

(CEC) of the collapsed interlayers is higher than the average CEC, while the CEC of the hydrated interlayers was found to be correspondingly lower. If this mechanism based on regular charge density modulations is generally true, the formation of ordered interstratified materials upon partial cation exchange with organocations might be related to dense packed interlayer structures of organocations that do not satisfy the average charge density of the silicate layers. Consequently, the local charge balance will be accomplished by surrounding this layer by two interlayers occupied by hydrated  $\text{Na}^+$ .

In the present work the proposed mechanism for the formation of ordered interstratification will be verified by a detailed study of the partial cation exchange of a synthetic Na-fluorohectorite with largely differing organic cations, a stilbazolium dye (*N*-Hexadecyl-4-(3,4,5-trimethoxystyryl)-pyridinium (dye), and a simple alkylammonium cation. Based on the deeper insight gained a generally applicable synthesis protocol for one-dimensionally ordered functional heterostructures is established.

## ■ EXPERIMENTAL SECTION

**Synthesis of Na-hec.** Sodium-fluorohectorite with the composition  $[\text{Na}_{0.5}]_{\text{inter}}^{+} [\text{Mg}_{2.5}\text{Li}_{0.5}]^{0\alpha} [\text{Si}_4]^{1\alpha} \text{O}_{10}\text{F}_2$  (Na-hec) was synthesized by melt synthesis in a closed molybdenum crucible according to a published procedure.<sup>17</sup> After synthesis the material was annealed for 6 weeks at 1045 °C to improve intracrystalline reactivity, charge homogeneity, and phase purity as recently described.<sup>18</sup>

**Synthesis of *N*-Hexadecyl-4-(3,4,5-trimethoxystyryl)-pyridinium Bromide (dye).** *N*-Hexadecyl-4-methylpyridinium bromide (6.15 g, 15.45 mmol) and 3,4,5-trimethoxybenzaldehyde (3.03 g, 15.45 mmol) were mixed in ethanol (50 mL), and piperidine (1 mL) was added. The reaction mixture was stirred under reflux for 3 h. The reaction mixture was concentrated in vacuum until a yellow precipitate appeared, and the precipitated solid was collected, washed with ethanol, and dried in vacuum. Yield: 4.46 g (7.73 mmol, 50%); yellow solid of mp >135 °C (dec.);  $\nu_{\text{max}}$  (ATR)/cm<sup>-1</sup>: 2914, 2847, 1637, 1614, 1578, 1504, 1470, 1460, 1420, 1352, 1335, 1319, 1274, 1262, 1240, 1206, 1175, 1152, 1120, 1002, 982, 844, 718; <sup>1</sup>H NMR (300 MHz, DMSO-*d*<sub>6</sub>): δ: 0.8–0.9 (3 H, m), 1.1–1.3 (26 H, m), 1.8–2.0 (2 H, m), 3.72 (3 H, s), 3.86 (6 H, s), 4.50 (2 H, t, <sup>3</sup>J 7.3 Hz), 7.11 (2 H, s), 7.56 (1 H, d, <sup>3</sup>J 16.3 Hz), 8.00 (1 H, d, <sup>3</sup>J 16.3 Hz), 8.21 (2 H, d, <sup>3</sup>J 6.9 Hz), 8.97 (2 H, d, <sup>3</sup>J 6.9 Hz); <sup>13</sup>C NMR (75.5 MHz, DMSO-*d*<sub>6</sub>): δ 13.9, 22.1, 25.4, 28.4, 28.7, 28.9, 29.0, 30.5, 31.3, 59.7, 60.2, 105.8, 122.5, 123.6, 130.8, 141.1, 144.2, 153.0, 153.2; *m/z* (%): 496 (66) [M<sup>+</sup>], 482 (15), 452 (19), 391 (15), 317 (12), 284 (45), 271 (39), 257 (29), 181 (100), 135 (53), 57 (77), 41 (83). Melting points were determined with a Gallenkamp apparatus and are uncorrected. IR spectra were recorded on a PerkinElmer One FT-IR spectrophotometer. Magnetic resonance (NMR) spectra were recorded under conditions as indicated on a Bruker Avance 300 spectrometer. Chemical shifts (δ) are given in parts per million downfield from TMS as internal standard. Mass spectra were recorded using a Varian MAT 311A (EI). Elemental analyses were carried out with a PerkinElmer 2400 CHN elemental analyzer. Technical organic solvents were distilled prior to use. Reagents and solvents of analytical grade were purchased from the common sources and were used without further purification.

**Synthesis and Intercalation of Me<sub>2</sub>DABCO<sup>2+</sup>.** 1,4-Dimethyl-1,4-diazoniabicyclo[2.2.2]octane dichloride (Me<sub>2</sub>DABCO<sup>2+</sup> Cl<sub>2</sub>) was synthesized according to a literature procedure.<sup>19</sup> Residual Na<sup>+</sup> of an ordered interstratified material was exchanged by a stoichiometric amount of an aqueous Me<sub>2</sub>DABCO<sup>2+</sup>-solution.

## ■ ANALYTICS

**Cation Exchange Capacity.** The cation exchange capacity (CEC) of Na-hec was determined with the [Cu(trien)] method.<sup>20</sup> Since the Na-hec is hygroscopic weighing was generally performed at 43%

relative humidity (RH, saturated K<sub>2</sub>CO<sub>3</sub>-solution) in the middle of the stability range of the monohydrate<sup>21,22</sup> (see Figure 5). Since this RH is also close to typical laboratory conditions, errors due to changes in the water content during weighing are minimized.

**Powder X-ray Diffraction.** Powder X-ray diffraction (PXRD) was performed in Bragg–Brentano-geometry on a Panalytical XPERT-PRO diffractometer. Textured samples were prepared by drying a few drops of the fluorohectorite dispersion on microscope slides (Menzel Gläser). The glass slides were dried at 110 °C for 12 h and then equilibrated at 43% RH (saturated K<sub>2</sub>CO<sub>3</sub>-solution) at room temperature prior to measurement.

**SEM.** SEM images were taken with a LEO 1530 FE-SEM at an operating voltage of 3 kV.

**Intercalation of Dye and Adsorption Isotherms.** For intercalation and determination of the adsorption isotherms of dye the samples were equilibrated at 80 °C for 24 h using a temperature-controlled oven equipped with a self-made overhead shaker. The intercalation was performed in glass vessels with screw caps with varied amounts of dye dissolved in different ethanol–water volume ratios (4:1 and 1:1). The amount of solvent was adjusted concomitantly with the variation of the dye amount in order to keep the dye concentration constant at 2 mmol/L. For instance, 28.9 mg of Na-hec was immersed in 1.17 mL of an ethanol–water mixture (4:1) for 12 h at room temperature using an overhead shaker. After adding 3.94 mL (10.2 μmol) of dye solution (ethanol–water mixture 4:1 with c = 2.594 mmol/L) the dispersion was mixed at 80 °C for 24 h. The solid was separated by sedimentation followed by centrifugation at 3800 rpm for 5 min. The remaining dye concentration was then determined photometrically using an Agilent CARY 300 UV–vis spectrophotometer.

**Amount of Organic Cations Adsorbed.** Dye or pentylammonium exchanged into the Na-hec was quantified by determination of the carbon content using CHN elemental analysis (Elementar vario el III).<sup>23</sup> Prior to analysis the samples were thoroughly washed 7-fold with a water–ethanol mixture (1:1) and 2-fold with pure ethanol in order to remove the remaining salts. For weighting, all samples were heated at 110 °C for 2 days and transferred into a glovebox with argon atmosphere. For complete oxidation of the intercalated dye the combustion temperature was set to 1150 °C using a combustion tube filled with tungsten(VI)-oxide-granules.

**Water Vapor Sorption Isotherms.** Isotherms were measured with a Belsorp-max (BEL JAPAN INC.) at 25 °C. All samples were dried prior to measurement at 120 °C under vacuum (0.1 mbar) for 12 h.

**Argon Physisorption Measurements.** Physisorption measurements of the Me<sub>2</sub>DABCO<sup>2+</sup> exchanged ordered interstratified materials were performed using a Quantachrome Autosorb 1 at a temperature of 87.35 K with Ar according to the literature.<sup>19</sup> Prior to measurement, the samples were dried for 24 h at 100 °C under high vacuum.

## ■ RESULTS AND DISCUSSION

High purity, charge homogeneity, and uniform intracrystalline reactivity for each individual interlayer space are essential ingredients for a quantitative investigation of the ordered interstratification phenomenon. Therefore, a 2:1 layered silicate, a sodium fluorohectorite synthesized from melt with a composition of  $[\text{Na}_{0.5}]_{\text{inter}}^{+} [\text{Mg}_{2.5}\text{Li}_{0.5}]^{0\alpha} [\text{Si}_4]^{1\alpha} \text{O}_{10}\text{F}_2$  (Na-hec), was used. The permanent negative layer charge  $\alpha$  ( $\alpha = 0.5$ ) of this fluorohectorite is a consequence of an isomorphous substitution of magnesium with lithium within the octahedral sheet. Because of the high synthesis temperature followed by long-term annealing the charge density of Na-hec is homogeneous both within the layer and all layers in the stack.<sup>17</sup>

The cation exchange capacity (CEC) of the one-layer hydrate is 118 mequiv/100 g as determined by the [Cu(trien)]<sup>2+</sup> method. This is in good agreement with the value of 121 mequiv/100 g expected from the composition of Na-hec.<sup>22</sup>

## Chemistry of Materials

## Article

The intracrystalline reactivity of Na-hec is very high. When dispersed in deionized water it swells osmotically leading eventually to spontaneous delamination at low solid contents.<sup>18</sup> Delamination can, however, be suppressed, and the pristine thickness of the stacks can be preserved during intercalation reactions when working in solvents of lower dielectric constant. Different solvent mixtures were tested, and suspensions of Na-hec in ethanol–water mixtures with higher ethanol content than  $V_{\text{ethanol}}:V_{\text{water}} = 1:4$  showed no gel formation even with an excess of solvent ( $m(\text{solvent}):m(\text{Na-hec}) \gg 100$ ). PXRD measurement (Figure S1) proved that swelling of Na-hec dispersed in these solvent mixtures is limited to the two-layer hydrate ( $d_{001} = 15.3 \text{ \AA}$ ). A narrow full width at half-maximum (fwhm) of  $0.04^\circ$  and a coefficient of variation (CV)<sup>24</sup> of 0.03% corroborates a perfect one-dimensional crystallinity in turn indicating a uniform intracrystalline reactivity.

As a generic model for a functional organic cation a stilbazolium dye was chosen, because this class of organic dyes exhibits a high affinity toward clay minerals<sup>25</sup> and features high extinction coefficients in the visible spectral region.<sup>26</sup> The stilbazolium moiety was further functionalized by an alkyl chain. This hexadecylammonium chain increases the hydrophobicity of the *N*-hexadecyl-4-(3,4,5-trimethoxystyryl)pyridinium cation (Figure 1, dye) and thus should further improve selectivity.<sup>27,28</sup>

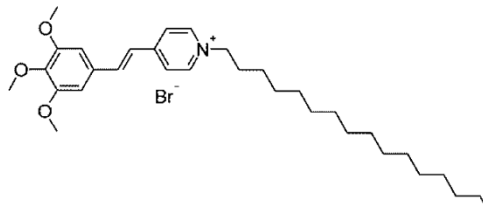


**Figure 1.** *N*-Hexadecyl-4-(3,4,5-trimethoxystyryl)pyridinium cation (dye) which features a hydrophobic hexadecyl chain and a fluorescent chromophoric stilbazolium headgroup.

The dye possesses an extinction coefficient of  $2 \times 10^4 \text{ L}^*\text{mol}^{-1}\text{cm}^{-1}$  ( $\lambda = 380 \text{ nm}$ ) in ethanol–water mixtures. Thus, even very small amounts of dye remaining in solution can be accurately detected by UV–vis spectroscopy. Due to the pronounced differences in basal spacing of hydrated  $\text{Na}^+$ - and dye-interlayers, the strong Coulomb attraction between positive interlayer and negative silicate layer strongly favors segregation of the organic cations into separate, highly hydrophobic interlayers.<sup>29</sup>

Upon incremental addition of dye to Na-hec in a mixture of  $V_{\text{ethanol}}:V_{\text{water}} = 4:1$ , even at a partial cation exchange as low as 9% of the total CEC ordered interstratified domains ( $d^{\text{OI}}(001) = 34.4 \text{ \AA}$  consisting of alternating  $\text{Na}^+$ -layers ( $d^{\text{Na}}(001) = 12.3 \text{ \AA}$ ) and dye layers ( $d^{\text{dye OI}}(001) = 22.1 \text{ \AA}$ ) were formed (Figure 2).

A complete cation exchange is possible but requires a large excess and high concentrations (HC) of dye ( $d^{\text{dye HC}}(001) = 27.2 \text{ \AA}$ ). The exact degree of cation exchange was determined by UV–vis spectroscopy. All values were furthermore cross-checked by elementary analysis, and the results were found to be in good agreement (Table S1).

The formation of a perfectly one-dimensionally crystalline ordered interstratification (OI) requires both a strong tendency for strictly alternating stacking and equal numbers of the two distinct interlayer species, in this case hydrated  $\text{Na}^+$ - and dye-

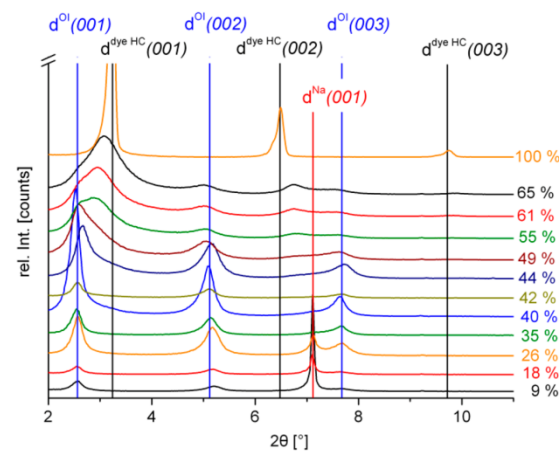


**Figure 2.** Evolution of PXRD patterns with increasing partial exchange of dye in  $V_{\text{ethanol}}:V_{\text{water}} = 4:1$ . Reflection positions are marked ( $d^{\text{OI}}(001)$  blue line,  $d^{\text{Na}}(001)$  red line,  $d^{\text{dye HC}}(001)$  black line).

interlayers ( $\omega_{\text{Na}} = \omega_{\text{dye}}$ ). The system has three different modes to adjust to the stoichiometry as defined by the partial exchange: 1. Two phases may be formed, unmodified Na-hec and the OI. 2. Statistical interstratification of the majority component into the OI (e.g.,  $\omega_{\text{Na}} > \omega_{\text{dye}}$ ) 3. The packing density of the dye-interlayers may be adjusted to meet  $\omega_{\text{Na}} = \omega_{\text{dye}}$ .

The basal series of the one water layer hydrate of Na-hec with  $d^{\text{Na}}(001) = 12.3 \text{ \AA}$  is clearly visible up to 35% exchange of the total CEC. This concomitant occurrence of two phases at  $\omega_{\text{Na}} \neq \omega_{\text{dye}}$  suggests that mechanism 1 is preferred. Once the first dye-interlayer is formed it acts as nuclei from which the OI domains grow. For the sake of completeness it shall be mentioned that a more detailed analysis of the basal series of OI suggests a random incorporation of very few ‘wrong’ basal spacings into OI at exchange levels where  $\omega_{\text{Na}} \neq \omega_{\text{dye}}$  (see the Supporting Information).

At this point it is unclear whether the formation of the OI is a kinetic or thermodynamic phenomenon. A first hint is obtained from the comparison of PXRD traces of materials made from solvent mixtures of different polarity. The selectivity of the organocation for the interlayer is high; nevertheless the partition equilibrium can be shifted toward the solution by increasing the hydrophobicity of the solvent. The higher the solubility of the organocation in the solvent, the more reversible is the character of the ion exchange. Thus, the exchange experiment at 40% CEC was repeated in a much more polar solvent ( $V_{\text{ethanol}}:V_{\text{water}} = 1:3$ ). At this polarity, the solubility of dye is very low, and, consequently, the equilibrium is shifted toward the intercalated state with 99.9% of dye being intercalated in equilibrium. Shifting the partition equilibrium toward the intercalated phase then hinders the system to reach thermodynamic equilibrium and to remedy defects like wrong stacking sequences caused by fast kinetics. Consequently, at a dye concentration where only the OI phase is expected actually three phases were formed concomitantly (OI-domains, domains with mostly hydrated  $\text{Na}^+$ -interlayers, and dye HC domains, Figure 3).

Nevertheless, by equilibration at elevated temperatures ( $80^\circ\text{C}$ ) in more hydrophobic solvents like  $V_{\text{ethanol}}:V_{\text{water}} = 4:1$  this phase-segregated material may be converted within 12 h to its

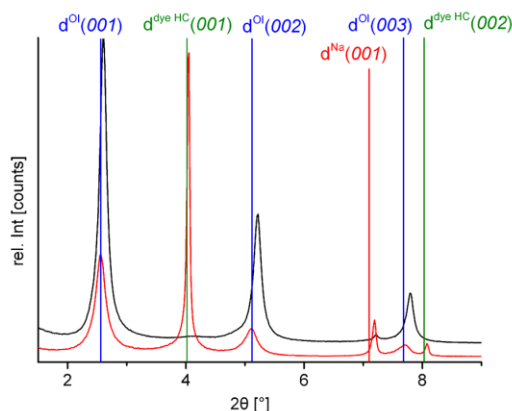


**Figure 3.** Evolvement of PXRD of a three phase sample after intercalation in  $V_{\text{ethanol}}:V_{\text{water}} = 1:3$  (red pattern) and subsequent thermal equilibration in  $V_{\text{ethanol}}:V_{\text{water}} = 4:1$  at  $80^\circ\text{C}$  (black pattern) to produce OI.

thermodynamic equilibrium which is a well-ordered OI (Figure 3). In summary, these results suggest that at appropriate levels of partial cation exchange ( $\approx 40\%$ ) the OI phase represents indeed a thermodynamic equilibrium.

#### ■ WHY WOULD THE OI PHASE BE THERMODYNAMICALLY PREFERRED OVER A STATISTICAL (RANDOM) INTERSTRATIFICATION?

The occurrence of the best-ordered OI with  $\omega_{\text{Na}} = \omega_{\text{dye}}$  at levels of  $\approx 40\%$  exchange can only be explained if dye-interlayers realize densely packed structures that represent a charge density of the interlayer that is slightly below the charge density of the host layers. According to Pauling's rules, in ionic crystals (and an intercalation compound represents a one-dimensional ionic crystal) electroneutrality has to be achieved by local charge compensation. Thus, once nucleation has started with a densely packing dye-interlayer (Figure 4, middle), a local charge balance can only be realized by arranging a higher cation density in both adjacent interlayers. This higher cation density cannot be realized by dye OI-interlayers, while hydrated  $\text{Na}^+$  can easily be redistributed into higher charged interlayers. In

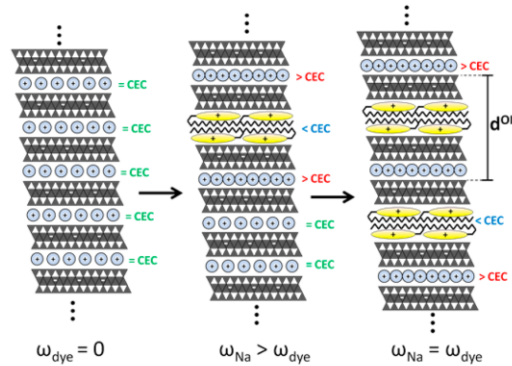


**Figure 4.** Scheme explaining the nucleation of an OI domain by intercalation of a single densely packed interlayer with lower interlayer cation densities (< CEC, yellow) into initially homogeneously distributed hydrated Na-interlayers.

this way a single exchanged interlayer can act as a nucleus for an OI domain eventually stretching over the complete stack. The nucleation rate will depend on the supersaturation of the organocation which in turn can be influenced by the solvent polarity. The higher the nucleation rate, the more antiphase boundaries where two domains meet with the wrong type of interlayer will be generated. The lower the solubility of dye in a given solvent mixture, the higher the nucleation rate will be, and, consequently, the more defects will be included.

This regular alteration of charge densities of adjacent interlayers is of course highly sensitive to heterogeneities in the charge density of the pristine clay mineral. If such charge density variations in the host layers are in the same order as the modulations induced by the nucleation of the organocation, the one-dimensional growth of the OI will be stopped. This might explain why for natural clay minerals like montmorillonite to the best of our knowledge only random interstratifications were reported.<sup>30</sup> In order to produce a homogeneous charge density, isomorphous substitution must be strictly statistical which requires higher synthesis temperatures.<sup>31</sup>

The building mechanism proposes distinctly different  $\text{Na}^+$  cation densities in pristine Na-hec and OI which in turn should induce a different hydration behavior of these interlayers as evidenced by hydration isotherms.<sup>16</sup> Different studies of clay minerals with  $\text{Na}^+$  as an interlayer cation showed that increasing layer charge causes decreased swelling capability.<sup>32–34</sup> Additionally, at any given hydration state, with an increasing number of interlayer cations that need to be accommodated, more noncoordinating water molecules need to be replaced, and, consequently, the total number of interlayer water molecules decreases with increasing layer charge.<sup>22</sup>

Consequently, if the number of  $\text{Na}^+$  in the hydrated interlayers of the OI is indeed higher than in the pristine Na-hec as proposed by the mechanism, the transition to the next higher hydration should be shifted toward higher RH and the amount of interlayer water should be reduced.<sup>33</sup> The latter needs to be corrected by the number of hydrated interlayers, which is reduced by 50% in the OI and the water adsorbed in the dye-interlayers.

The pristine Na-hec showed two sharp hydration steps (Figure 5).

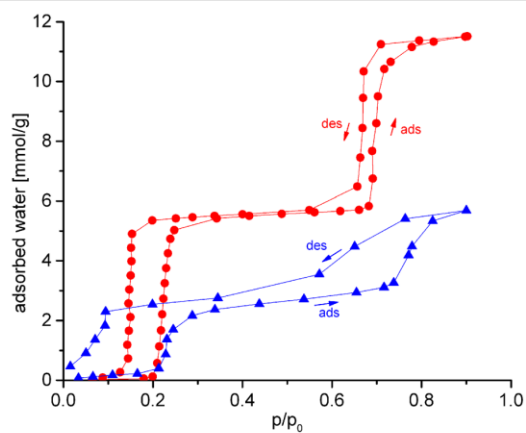


**Figure 5.** Water vapor sorption isotherms of Na-hec (red circle) and OI (blue triangle).

## Chemistry of Materials

## Article

During adsorption, the points of inflection for the transition from a zero- to a one-layer hydrate and from a one-layer hydrate to a two-layer hydrate were found at 22% RH and 70% RH, respectively. The completely dye exchanged sample showed a relatively small continuous water uptake. As expected for interlayers with differing  $\text{Na}^+$ -concentration, the hydration isotherm of the OI sample is distinctly different from the isotherm observed for pristine Na-hec.

While still two well-defined hydration stages are observed, the hysteresis involved is much broader, the transition steps are somewhat more sluggish, and the adsorption steps are shifted. The points of inflection for the transition from a zero- to a one-layer hydrate and from a one-layer hydrate to a two-layer hydrate are shifted in the expected direction to 23% RH and 77% RH, respectively. A detailed discussion including quantification of adsorption capacities is included in the Supporting Information.

While in the previous paragraphs pieces of evidence were presented that consistently corroborate the reshuffling of interlayer cations leading to a strict alternation of charge densities of subsequent interlayers, next the driving force for this mechanism shall be carved out. Why does the system favor interlayer structures with reduced dye OI occupation ( $\approx 40\%$  of CEC) over a dye HC interlayer structure where the dye packing matches the charge density of the host?

While the Coulomb attraction between negative clay mineral host and positive interlayers thrives to minimize the basal spacing, the lateral van der Waals interactions between adjacent dye molecules as well as the van der Waals interactions with the surface oxygens of the clay mineral are another significant contribution to the total energy of the organic interlayers. Both these contributions create a very strong bias for the most densely packed organic interlayers. Thus, if the HC interlayer structure would indeed be less densely packed as compared to the OI interlayer structure, a strong driving force to realize the latter for partial ion exchange would arise.

Please note that dye features a flexible *n*-hexadecyl chain, and it is well-known that flexible *n*-alkylammonium cations are able to form different interlayer structures depending on the charge density of the clay mineral and the chain length of the *n*-alkylammonium ions.<sup>35,36</sup>

At 0% RH *d*-spacings of 26.4 Å, 31.7 Å, and 9.6 Å were found for dye HC, OI, and pristine Na<sup>+</sup>-hec, respectively (Figure 6).

Please note that the *d*<sup>OI</sup> spacing of 31.7 Å consists of two interlayers of different height and two silicate layers of the same height (Figure 4 right). The *d*-spacing of the Na<sup>+</sup>/silicate layer stack in the dried state is 9.6 Å as shown for pristine Na-hec (Figure 6). Consequently, the *d*-spacing of an individual dye/silicate layer (gallery height of the dye interlayer and the 2:1-silicate layer) in OI can be assigned to be 22.1 Å = 31.7 Å – 9.6 Å. This value is much lower than the measured *d*-spacing of 26.4 Å for the dye HC sample which was proven to be completely exchanged by CHN analysis (Table S1). The difference of 4.3 Å already creates a significant electrostatic bias for OI-type interlayers. Since the number of dye molecules in OI- and HC-type interlayers is known from cation exchange experiments, derivation of packing densities is straightforward (see the Supporting Information for calculation details). For a single dye cation in OI- and HC-type interlayers a volume of 788 Å<sup>3</sup> and 802 Å<sup>3</sup>, respectively, is occupied. Thus, OI-type interlayer structures not only allow for a smaller basal spacing, but concomitantly the dye cations realize a significantly denser packing which most likely will correspond to a higher lateral

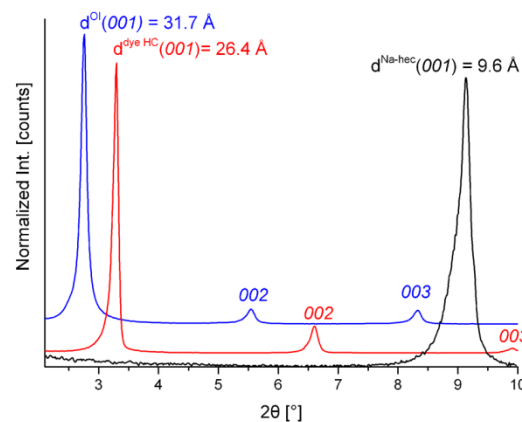


Figure 6. PXRD patterns of dye HC (red trace), OI (blue trace), and pristine Na-hec (black trace) measured at 0% RH.

van der Waals energy as compared with HC-type interlayers. This line of argumentation ignores changes in the hydration enthalpy of the hydrated interlayers due to lower water content and a possible reduction of overall Coulomb interaction due to the asymmetric distribution of the cations in the OI.

According to Laird and Shang interlayer structures with different *d*-spacings should be considered as different solid phases.<sup>37</sup> Consequently, after formation of the OI (Figure 7

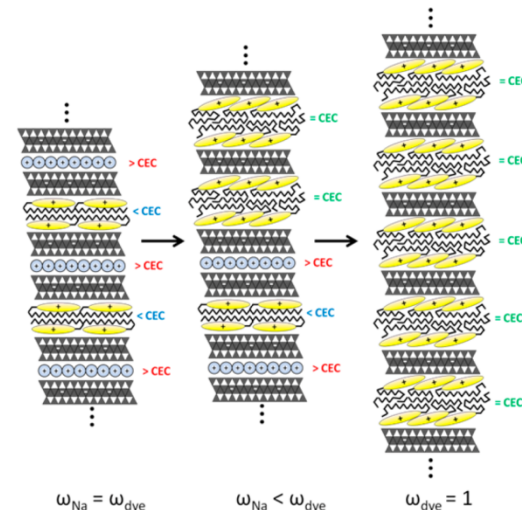


Figure 7. Scheme for a progressing exchange of an OI structure.

left) further dye uptake has to involve necessarily a structural change from an OI-type to a HC-type interlayer with significantly higher *d*-spacing (Figure 7 middle). For reasons of local charge balance, the phase transition is expected to be coupled to a concomitant cation exchange of adjacent hydrated Na<sup>+</sup>-interlayers.

The phase transition from OI-type to HC-type interlayers will involve an activation barrier which is expected to manifest itself by a change in selectivity of dye adsorption. This assumption was verified by the measurement of an adsorption

## Chemistry of Materials

## Article

isotherm of dye in that regime where up to 70% of the total CEC is occupied by dye.

As expected, at low dye loadings (10%–40% CEC) where only the OI phase is formed, the part of dye remaining in solution is nearly constant (Figure 8).

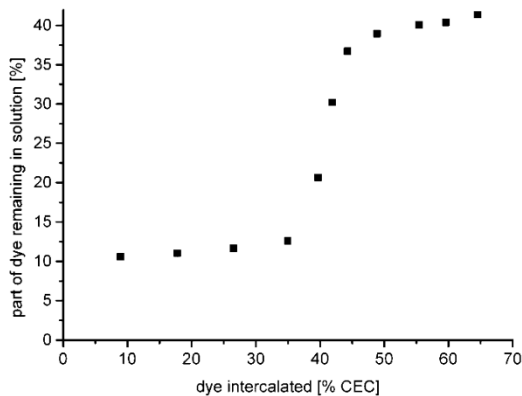


**Figure 8.** Adsorption isotherm of dye and Na-hec at 80 °C in  $V_{\text{ethanol}}:V_{\text{water}} = 4:1$ .

The partition coefficient changes abruptly as soon as about 40% of the CEC is occupied by dye. The discontinuity corresponds well with conditions where an OI phase with  $\omega_{\text{Na}} = \omega_{\text{dye}}$  was observed (Figure 2). Since OI- and HC-type interlayers represent two different phases due to different structures, such a discontinuity in partition coefficients is not surprising but is actually expected for two distinct phases.

The influence of different solvent mixtures on the partition equilibrium can be utilized to further improve the regularity of the OI. The stoichiometry to ensure  $\omega_{\text{Na}} = \omega_{\text{dye}}$  can be better controlled at conditions where the equilibrium is completely shifted in favor of the intercalated phase. Hence, first 38% CEC of dye is applied in  $V_{\text{ethanol}}:V_{\text{water}} = 1:1$  where it is quantitatively intercalated (99.6%). The defects in the regular stacking produced are then remedied by equilibration in  $V_{\text{ethanol}}:V_{\text{water}} = 4:1$ , where the differences in partition coefficients between OI- and HC-type interlayers are more pronounced and the kinetics for de- and reintercalation are faster. This way a rational series with a CV as low as 0.11% and a fwhm of 001 of 0.12° is obtained (Figure 9).

#### ■ IS THE ESTABLISHED SYNTHESIS REGIME FOR ONE-DIMENSIONAL HETEROSTRUCTURES GENERALLY APPLICABLE?

The proposed mechanism should provide maximum flexibility and make the approach generally applicable for a wide variety of functional materials since the OI phase represents a thermodynamic equilibrium. The regular alteration of interlayer cation density only requires a dense packing of interlayer cations in the OI that deviates from the average charge density corresponding to the CEC.

In the sample discussed so far a clay mineral with a particular charge density was applied, and an organic cation was identified that realizes a dense packing with a charge density < CEC. In order to demonstrate the general validity of the mechanism, an OI phase was synthesized with a cation that realizes dense packing > CEC. According to the equivalent areas proposed by

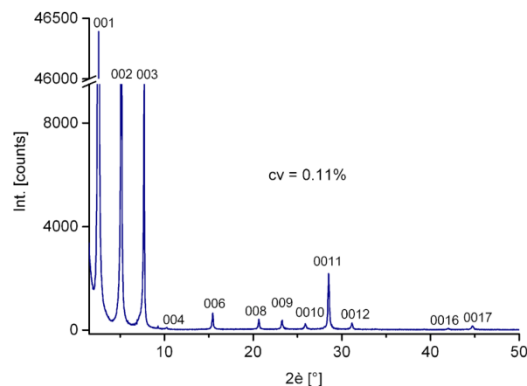


**Figure 9.** PXRD pattern of the ordered interstratified sample after exchanging 38% CEC with dye in  $V_{\text{ethanol}}:V_{\text{water}} = 1:1$  and annealing in  $V_{\text{ethanol}}:V_{\text{water}} = 4:1$  ( $\text{CV} = 0.11\%$ ).

Lagaly et al. in combination with the unit cell parameters of the Na-hec,<sup>18</sup> for pentylammonium (C5) a densely packed monolayer is expected with a layer charge  $x = 0.56$ .<sup>35</sup> Since Na-hec features a slightly lower layer charge ( $x = 0.5$ ), such a densely packed monolayer structure would then be expected to have a positive charge density exceeding the negative charge density of this host. According to the proposed mechanism, for this very simple organic cation a perfect OI should be achieved at a partial exchange of 56% of CEC. The best OI was obtained in a more polar solvent mixture,  $V_{\text{ethanol}}:V_{\text{water}} = 1:1$ , due to the largely reduced hydrophobicity of the C5 molecule as compared with dye. The optimum amount of C5 giving the most regular OI was identified empirically. Increasing amounts of C5 (30% to 100% of the CEC) were offered in solution for cation exchange, and PXRD traces were measured to judge the regularity of the OI obtained (Figure 10).

With  $d$ -spacings for the one-layer hydrate of  $\text{Na}^+$ -interlayers and densely packed C5 monolayers of 12.3 and 13.3 Å, respectively, the  $d$ -spacing of the OI phase is expected at 25.6 Å. PXRD showed a superstructure at about 3.5°  $2\theta$  corresponding to the  $d^{\text{OI}}$ -spacing of 25.6 Å which can be observed even with additions of C5 as low as 30% CEC where

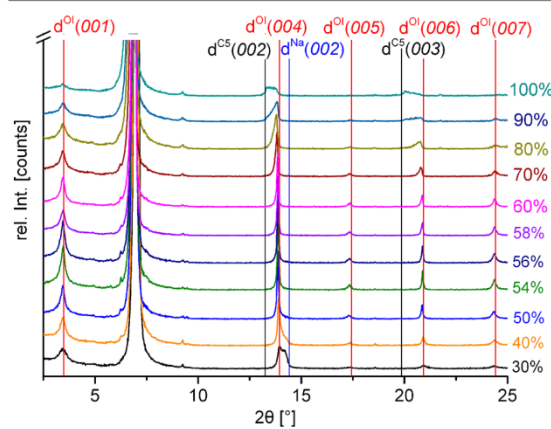


**Figure 10.** Evolution of PXRD patterns with increasing addition of *n*-pentylammonium (C5) in  $V_{\text{ethanol}}:V_{\text{water}} = 1:1$ . Reflection positions are marked ( $d^{\text{OI}}(001)$  red line,  $d^{\text{Na}}(001)$  blue line,  $d^{\text{C5}}(001)$  black line).

## Chemistry of Materials

Article

still  $\text{Na}^+$ -domains must be and are present ( $\omega_{\text{Na}} > \omega_{\text{Cs}}$ ). Higher amounts of C5 form more OI and reduce the remaining  $\text{Na}^+$ -phase until it completely vanished with addition of 58% CEC ( $\omega_{\text{Na}} \approx \omega_{\text{Cs}}$ ). At this point of exchange the most regular OI was obtained (Table S2). CHN analysis gave a C5 content corresponding to 52% of the CEC (Table S3). Addition of 70% CEC already leads to a small shift of the  $d^{\text{OI}}(00l)$  series toward the *d*-spacing of the C5 end member, indicating that at this point of exchange more C5 interlayer phase is formed ( $\omega_{\text{Na}} < \omega_{\text{Cs}}$ ). The CHN analysis of this material showed an increased C5 content (56% of the CEC) as compared to the best OI sample. The adsorption isotherm obtained for C5 reveals again a discontinuity in the range where the best OIs were found (Figure S2).

In the previous paragraphs OIs were shown where an organic interlayer strictly alternates with a sodium interlayer. For many functional materials, however, two different alternating organic functionalities would be advantageous. Generally, all OIs can be further functionalized by cation exchange of the remaining inorganic cations to obtain two alternating functional nanoreactors. As a preliminary proof of principle, the remaining  $\text{Na}^+$ -interlayers of the best OI were selectively replaced by 1,4-dimethyl-1,4-diazoniabicyclo[2.2.2]octane ( $\text{Me}_2\text{DABCO}^{2+}$ ) (Figure S3). Ar-physisorption measurements proofed microporosity of the obtained OI (Figure S4).

## CONCLUSION

A generally applicable mechanism was established that allows the synthesis of materials with alternating functional nanoreactors separated by 1 nm silicate walls. While such heteroarchitectures most frequently have been manufactured in a bottom up process like layer-by-layer assembly, this mechanism is based on thermodynamic equilibrium and yields micron sized one-dimensional crystals (Figure S5).

The driving force for the formation of the regularly interstratified architectures is founded in densely packed interlayers of functional cationic molecules with a charge density deviating from the charge density of the host clay mineral. The material may be further functionalized by cation exchange of the remaining inorganic cations. For instance by pillaring, microporous hybrid interlayers may be obtained alternating with a photoactive antenna in the adjacent interlayer allowing for size and shape selective photochemistry.<sup>38,39</sup>

This example shows that any combination of two different, strictly alternating functionalities will be accessible. Moreover, transfer of the mechanism to other layered materials appears feasible as long as a homogeneous charge density is warranted.

## ASSOCIATED CONTENT

## Supporting Information

CHN results of the dye OI and C5 OI samples, the swelling of Na-hec in  $V_{\text{ethanol}}:V_{\text{water}} = 1:1$  as well as an SEM image of the dye OI crystals are provided. Furthermore, a more detailed PXRD analysis of the  $d^{\text{OI}}(00l)$ -series, short explanations of the water content calculation and dye density calculations are included. This material is available free of charge via the Internet at <http://pubs.acs.org>.<sup>\*</sup>

## AUTHOR INFORMATION

## Corresponding Author

\*Phone: +49 921 55 2531. Fax: +49 921 55 2788. E-mail: Josef.Breu@uni-bayreuth.de.

## Notes

The authors declare no competing financial interest.

## ACKNOWLEDGMENTS

This work was financially supported by the Deutsche Forschungsgemeinschaft (SFB 840).

## REFERENCES

- (1) Gunjakar, J. L.; Kim, T. W.; Kim, H. N.; Kim, I. Y.; Hwang, S. J. *J. Am. Chem. Soc.* **2011**, *133*, 14998–15007.
- (2) Ozkan, D.; Kerman, K.; Meric, B.; Kara, P.; Demirkhan, H.; Polverejan, M.; Pinnavaia, T. J.; Ozsoz, M. *Chem. Mater.* **2002**, *14*, 1755–1761.
- (3) Zhang, Q.; Atay, T.; Tischler, J. R.; Bradley, M. S.; Bulovic, V.; Nurmiikko, A. V. *Nat. Nanotechnol.* **2007**, *2*, 555–559.
- (4) Ariga, K.; Ji, Q. M.; Hill, J. P.; Bando, Y.; Aono, M. *NPG Asia Mater.* **2012**, *4*, e17.
- (5) Fang, M. M.; Kaschak, D. M.; Sutorik, A. C.; Mallouk, T. E. *J. Am. Chem. Soc.* **1997**, *119*, 12184–12191.
- (6) Keller, S. W.; Kim, H. N.; Mallouk, T. E. *J. Am. Chem. Soc.* **1994**, *116*, 8817–8818.
- (7) Ziegler, C.; Werner, S.; Bugnet, M.; Worschling, M.; Duppel, V.; Botton, G. A.; Scheu, C.; Lotsch, B. V. *Chem. Mater.* **2013**, *25*, 4892–4900.
- (8) Virdi, K. S.; Kauffmann, Y.; Ziegler, C.; Ganter, P.; Lotsch, B. V.; Kaplan, W. D.; Blaha, P.; Scheu, C. *Phys. Rev. B* **2013**, *87*, 115108.
- (9) Junggeburth, S. C.; Diehl, L.; Werner, S.; Duppel, V.; Sigle, W.; Lotsch, B. V. *J. Am. Chem. Soc.* **2013**, *135*, 6157–6164.
- (10) Sawhney, B. L. *Clays Clay Miner.* **1972**, *20*, 93–100.
- (11) Ijdo, W. L.; Lee, T.; Pinnavaia, T. J. *Adv. Mater.* **1996**, *8*, 79–83.
- (12) Ijdo, W. L.; Pinnavaia, T. J. *J. Solid State Chem.* **1998**, *139*, 281–289.
- (13) Ijdo, W. L.; Pinnavaia, T. J. *Green Chem.* **2001**, *3*, 10–12.
- (14) Ijdo, W. L.; Pinnavaia, T. J. *Chem. Mater.* **1999**, *11*, 3227–3231.
- (15) Ozsoz, M.; Erdem, A.; Ozkan, D.; Kerman, K.; Pinnavaia, T. J. *Langmuir* **2003**, *19*, 4728–4732.
- (16) Möller, M. W.; Hirsemann, D.; Haarmann, F.; Senker, J.; Breu, J. *Chem. Mater.* **2010**, *22*, 186–196.
- (17) Breu, J.; Seidl, W.; Stoll, A. J.; Lange, K. G.; Probst, T. U. *Chem. Mater.* **2001**, *13*, 4213–4220.
- (18) Stöter, M.; Kunz, D. A.; Schmidt, M.; Hirsemann, D.; Kalo, H.; Putz, B.; Senker, J.; Breu, J. *Langmuir* **2013**, *29*, 1280–1285.
- (19) Baumgartner, A.; Sattler, K.; Thun, J.; Breu, J. *Angew. Chem., Int. Ed.* **2008**, *47*, 1640–1644.
- (20) Ammann, L.; Bergaya, F.; Lagaly, G. *Clay Miner.* **2005**, *40*, 441–453.
- (21) Beyer, J.; von Reichenbach, H. G. *Clay Miner.* **2002**, *37*, 157–168.
- (22) Kalo, H.; Milius, W.; Breu, J. *RSC Adv.* **2012**, *2*, 8452–8459.
- (23) Stocker, M.; Seyfarth, L.; Hirsemann, D.; Senker, J.; Breu, J. *Appl. Clay Sci.* **2010**, *48*, 146–153.
- (24) Bailey, S. W. *Am. Mineral.* **1982**, *67*, 394–398.
- (25) Usami, H.; Takagi, K.; Sawaki, Y. *J. Chem. Soc., Faraday Trans. 1* **1992**, *88*, 77–81.
- (26) Gorner, H. *J. Photochem. Photobiol., A* **2011**, *218*, 199–203.
- (27) Cowan, C. T.; White, D. *Trans. Faraday Soc.* **1958**, *54*, 691–697.
- (28) Vansant, E. F.; Uytterhoe, J. B. *Clays Clay Miner.* **1972**, *20*, 47–54.
- (29) Theng, B. K. G.; Quirk, J. P.; Greenland, D. J. *Clay Miner.* **1967**, *7*, 1–17.
- (30) Solin, S. A. *Annu. Rev. Mater. Sci.* **1997**, *27*, 89–115.
- (31) Palin, E. J.; Dove, M. T.; Hernandez-Laguna, A.; Sainz-Diaz, C. *L. Am. Mineral.* **2004**, *89*, 164–175.
- (32) Laird, D. A. *Appl. Clay Sci.* **2006**, *34*, 74–87.
- (33) Suquet, H.; Pezerat, H. *Clays Clay Miner.* **1987**, *35*, 353–362.
- (34) Laird, D. A.; Shang, C.; Thompson, M. L. *J. Colloid Interface Sci.* **1995**, *171*, 240–245.

## Chemistry of Materials

## Article

- (35) Mermut, A. R.; Lagaly, G. *Clays Clay Miner.* **2001**, *49*, 393–397.  
(36) Lagaly, G. *Clay Miner.* **1981**, *16*, 1–21.  
(37) Laird, D. A.; Shang, C. *Clays Clay Miner.* **1997**, *45*, 681–689.  
(38) Herling, M. M.; Breu, J. Z. *Anorg. Allg. Chem.* **2014**, *640*, 547–560.  
(39) Herling, M. M.; Kalo, H.; Seibt, S.; Schobert, R.; Breu, J. *Langmuir* **2012**, *28*, 14713–14719.

## 5.2.2 Supporting Information

### Supporting Information

#### Ordered Heterostructures of Two Strictly Alternating Types of Nanoreactors

*Matthias Stöter, Bernhard Biersack, Nele Reimer, Markus Herling, Norbert Stock, Rainer Schobert, Josef Breu \**

### Content

1. Swelling in ethanol-water mixture
2. Crosschecking of the intercalated amount of dye by CHN analysis
3. Detailed analysis of the PXRD basal series of OI
4. Calculation of the water content of OI
5. Calculation of the packing density of dye in OI and HC interlayers
6. Calculation of the cv for C5 intercalates
7. Determination of the amount of intercalated C5 using CHN analysis
8. Pillaring of  $\text{Na}^+$ -interlayers of OI with  $\text{Me}_2\text{DABCO}^{2+}$
9. Macroscopic structure of dye OI stacks

#### 1. Swelling in ethanol-water mixture

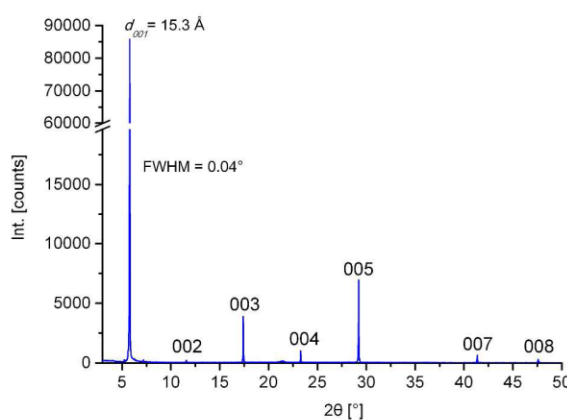


**Figure S1.** PXRD profile of  $\text{V}_{\text{ethanol}}:\text{V}_{\text{water}} = 4:1$  Na-hec suspension on a glass slide covered by a polyethylene foil to prevent evaporation (wet conditions). A  $d$ -spacing of  $15.3 \text{ \AA}$  with a FWHM of  $0.04^\circ$  and a very low cv of  $0.03\%$  proofs a complete swelling to the two layer hydrate.

## 2. Crosschecking of the intercalated amount of dye by CHN analysis

The dye concentration remaining in solution after equilibrating for 24 hours with Na-hec was detected by UV-VIS measurement. The intercalated amount of dye was calculated by subtracting the detected amount of dye in solution from the total amount of added dye. For example:

*28.9 mg of Na-hec (CEC = 118 meq/100 g) has a total amount of exchangeable sodium cations of 34.1 µmol. Consequently, for the equilibration with 30 % CEC 10.2 µmol of dye were added. UV-VIS measurement showed that 1.2 µmol of dye remains in solution. Therefore the intercalated amount is 9.0 µmol corresponding to a total dye intercalation of 26.5 % CEC.*

With dye intercalation concomitantly the same amount of sodium cations are released into the supernatant. With the known formula of Na-hec ( $[Na_{0.5}]^{inter}[Mg_{2.5}Li_{0.5}]^{oct}[Si_4]^{tet}O_{10}F_2$ ) the chemical composition of the partially exchanged sample can be calculated.

*After intercalation of dye with 26.5 % CEC the interlayer composition has changed to  $\{Na_{0.368}dye_{0.132}\}$  yielding a chemical composition of  $[Na_{0.368}dye_{0.132}]^{inter}[Mg_{2.5}Li_{0.5}]^{oct}[Si_4]^{tet}O_{10}F_2$  and a molar mass ( $M_w$ ) of 448.6 g/mol.*

The molar mass obviously changes with the degree of exchange. The carbon content of the exchanged sample can be calculated by using the molecular weight and the carbon content of dye ( $C_{32}H_{50}NO_3$ ).

*For  $[Na_{0.368}dye_{0.132}]^{inter}[Mg_{2.5}Li_{0.5}]^{oct}[Si_4]^{tet}O_{10}F_2$  the carbon content can be calculated to be 50.7 g/mol. With the molar mass of the intercalation compound of 448.6 g/mol a carbon content of 11.3% has to be expected. This value is in good agreement with the carbon content of 11.5% as obtained by CHN elemental analysis.*

Within the experimental errors the compositions as determined by colorimetry and by CHN analysis are in good agreement (Table S1)

**Table S1.** CHN-results after intercalation in a solution of  $V_{\text{ethanol}} : V_{\text{water}} = 4:1$ 

dye added [% CEC]	dye intercalated [% CEC]	interlayer composition	molar mass [g/mol]	expected carbon content [%]	carbon content by CHN analysis [%]
10	8.9	{Na <sub>0.455</sub> dye <sub>0.045</sub> }	407.4	4.2	4.1
20	17.8	{Na <sub>0.411</sub> dye <sub>0.089</sub> }	428.2	8.0	7.9
30	26.5	{Na <sub>0.368</sub> dye <sub>0.132</sub> }	448.6	11.3	11.5
40	35.0	{Na <sub>0.325</sub> dye <sub>0.175</sub> }	469.0	14.3	14.4
50	39.7	{Na <sub>0.302</sub> dye <sub>0.198</sub> }	479.9	15.9	16.0
60	41.9	{Na <sub>0.291</sub> dye <sub>0.209</sub> }	485.1	16.6	17.2
70	44.3	{Na <sub>0.279</sub> dye <sub>0.221</sub> }	490.8	17.3	17.9
80	48.8	{Na <sub>0.256</sub> dye <sub>0.244</sub> }	501.7	18.7	19.5
90	55.4	{Na <sub>0.223</sub> dye <sub>0.277</sub> }	517.3	20.6	20.7
100	59.6	{Na <sub>0.197</sub> dye <sub>0.303</sub> }	529.6	22.0	22.9
110	64.5	{Na <sub>0.177</sub> dye <sub>0.323</sub> }	539.1	23.0	22.5
excess	100	{dye <sub>0.5</sub> }	622.9	30.8	30.6

### 3. Detailed analysis of the PXRD basal series of OI

According to Mering's principles, the quality of the ordering in OI domains can be judged mainly by two criteria: The rationality of the basal series as expressed by the coefficient of variation (cv)<sup>1</sup> and the full width at half maximum (FWHM) of the basal reflections.<sup>2,3</sup> Any statistical interstratification will increase both FWHM and cv. The pristine Na-hec has a cv of 0.08% and a narrow FWHM of the *001*-reflection of 0.05°. For lower degrees of exchange (18% to 30%) both FWHM (> 0.24° for *001*) and cv (> 0.6 %) of the OI domains are considerably higher than for the pristine material indicating some degree of random interstratifications. Most likely a surplus of hydrated Na<sup>+</sup>-interlayers ( $\omega_{\text{Na}} > \omega_{\text{dye}}$ ) will be incorporated randomly into the OI domains. According to these criteria, the best OI was found with 40 % exchange of the total CEC (FWHM of *001* = 0.20°, cv = 0.2%) suggesting that at this point the probability of the two types of interlayers is close to equal ( $\omega_{\text{Na}} = \omega_{\text{dye}}$ ).

FWHM and cv of the OI increased again beyond 40 % exchange, indicating that increasing numbers of additional dye-interlayers are present ( $\omega_{\text{Na}} < \omega_{\text{dye}}$ ). The broadening of the  $d^{OI}$ -reflexion together with a continuous shifting to higher 2θ angles can only be explained with a statistical insertion, most likely, of dye HC-interlayers into the OI-phase resulting in a random interstratification.

#### 4. Calculation of the water content of OI

The adsorption capacities were taken at the inflection point of the “plateaus”. The inflection point of the plateau for the pristine Na-hec was found at a relative humidity (RH) of 54.6%.

Since the molecular weight of OI and pristine Na-hec are obviously quite different, for comparison the absolute capacities need to be normalized to the number of water molecules per  $\text{Na}^+$  to allow comparison. The corresponding water uptake at this humidity is 5.61 mmol/g which gives a value of  $2.17 \text{ H}_2\text{O / per formula unit (pfu)}$  ( $M_w = 386.1 \text{ g/mol}$ ) and therefore  $4.33 \text{ H}_2\text{O / Na}^+$ . However, for OI with an interlayer composition of  $\{\text{Na}_{0.311}\text{dye}_{0.189}\}$  (37.8% intercalated) the point of inflection changes to 50.7% RH. The amount of water at this point is 2.67 mmol/g corresponding to  $1.27 \text{ H}_2\text{O / pfu}$  ( $M_w = 475.7 \text{ g/mol}$ ) or  $4.09 \text{ H}_2\text{O / Na}^+$ -cation.

Please note, that the smaller value for the OI sample is definitely not an artefact of inflection points occurring at different RHs. The water uptake of Na-hec at the RH of 50.7% ( $4.31 \text{ H}_2\text{O / Na}^+$ ) is almost the same as at 54.6% RH. Furthermore, the real water content of the hydrated  $\text{Na}^+$  interlayers might indeed be lower than  $4.09 \text{ H}_2\text{O / Na}^+$  because any possible water adsorption of the dye interlayers is ignored in this calculation.

## 5. Calculation of the packing density of dye in OI and HC interlayers

The packing density was calculated as the volume (V) occupied by one dye molecule in the two different dye occupied interlayer structures OI and HC.

The area available in the *ab-plane* pfu ( $[\text{Mg}_{2.5}\text{Li}_{0.5}]^{\text{oct}}[\text{Si}_4]^{\text{tet}}\text{O}_{10}\text{F}_2$ ) is  $(0.5 \cdot a \cdot b)$ , for hectorites with the given composition this is 0.5 ( $5.248 \text{ \AA} \times 9.093 \text{ \AA} = 23.86 \text{ \AA}^2$ ).<sup>4</sup> The d-spacing for dye-occupied interlayers in OI is  $22.1 \text{ \AA}$ . The gallery height is obtained by subtracting the silicate layer thickness ( $9.6 \text{ \AA}$ ) from this value:  $22.1 \text{ \AA} - 9.6 \text{ \AA} = 12.5 \text{ \AA}$ . Therefore the interlayer volume available pfu for OI interlayer regions is:  $23.86 \text{ \AA}^2 \times 12.5 \text{ \AA} = 298 \text{ \AA}^3$ . In case of HC interlayer structures, the d-spacing was found to be considerably higher ( $26.4 \text{ \AA}$ ) and therefore the volume available pfu is considerably larger:  $23.86 \text{ \AA}^2 \times (26.4 \text{ \AA} - 9.6 \text{ \AA}) = 401 \text{ \AA}^3$ .

The number of dye molecules pfu for dye-occupied interlayers in OI and HC is 0.378 and 0.5 respectively. Consequently, the volume occupied by one dye molecule in OI and HC interlayer structures is  $788 \text{ \AA}^3$  and  $802 \text{ \AA}^3$ , corroborating a significantly higher packing density of dye in OI.

## 6. Calculation of the cv for C5 intercalates

Table S2.  $d^{0l}(00l)$ -series and calculated cv after intercalation of C5

	54% CEC		56% CEC		58% CEC		60% CEC		70% CEC	
<i>l</i>	<i>d</i>	$I^*d(00l)$								
1	25.652	25.652	25.584	25.584	25.587	25.587	25.666	25.666	25.647	25.647
2	12.746	25.492	12.760	25.519	12.759	25.517	12.764	25.528	12.825	25.649
3	-	-	-	-	-	-	-	-	-	-
4	6.375	25.501	6.379	25.516	6.382	25.529	6.386	25.546	6.403	25.613
5	5.113	25.565	5.116	25.579	5.111	25.555	5.109	25.545	5.110	25.549
6	4.252	25.510	4.252	25.514	4.255	25.529	4.257	25.541	4.265	25.589
7	3.651	25.560	3.651	25.554	3.650	25.549	3.649	25.543	3.645	25.517
8	3.188	25.506	3.189	25.510	3.190	25.522	3.192	25.537	3.198	25.582
9	2.839	25.555	2.840	25.558	2.838	25.543	2.839	25.547	2.836	25.526
10	2.550	25.502	2.551	25.515	2.553	25.534	2.553	25.526	2.563	25.635
11	2.322	25.547	2.323	25.551	2.323	25.551	2.321	25.535	2.320	25.520
12	2.126	25.509	2.126	25.514	2.127	25.520	2.128	25.536	2.131	25.568
13	1.966	25.552	1.965	25.539	1.965	25.542	1.965	25.542	1.964	25.528
14	1.822	25.510	1.823	25.516	1.823	25.517	1.824	25.532	1.827	25.574
15	-	-	-	-	-	-	-	-	-	-
16	1.594	25.501	1.594	25.509	1.595	25.521	1.596	25.532	1.597	25.550
17	1.503	25.547	1.503	25.551	1.502	25.539	1.502	25.539	1.502	25.532
18	1.418	25.520	1.418	25.518	1.418	25.517	1.418	25.527	1.420	25.557
19	1.344	25.545	1.344	25.541	1.344	25.540	1.344	25.544	1.344	25.534
20	1.276	25.529	1.276	25.511	1.276	25.524	-	-	-	-
Mean		<b>25.533</b>		<b>25.533</b>		<b>25.535</b>		<b>25.545</b>		<b>25.569</b>
cv		0.148		0.096		0.070		0.125		0.174

## 7. Determination of the amount of intercalated C5 using CHN analysis

C5 is colourless and therefore, the carbon content of partially exchanged samples can only be obtained by elemental analysis. The degree of C5 intercalated at different amounts of C5 offered and hence the partition equilibrium needed for the adsorption isotherm (Figure S4) was determined from the composition of the clay samples. However, during intercalation each C5 cation intercalated replaces one sodium cation and consequently the molar mass of the intercalation compound changes with the degree of C5 uptake. Thus, the chemical composition must be derived from the carbon content measured in an iterative way. The value (y) for the C5 content of the general composition  $[C5_yNa_{0.5-y}]^{inter}[Mg_{2.5}Li_{0.5}]^{oct}[Si_4]^{tet}O_{10}F_2$  and hence the concomitantly changing molecular weight was varied iteratively to meet the experimentally determined carbon contents. The part of C5 which remains in solution was then obtained by subtracting the intercalated amount of C5 from the total added amount of C5.

*For example: CHN analysis gave a carbon content of 3.84 wt% corresponding to a chemical composition of  $[Na_{0.24}C5_{0.26}]^{inter}[Mg_{2.5}Li_{0.5}]^{oct}[Si_4]^{tet}O_{10}F_2$ . In this composition 52% of sodium is exchanged by C5. The added amount of C5 was 58% of the total CEC. Therefore, 11% of the added dye remains in solution.*

The errors of the CHN analysis are much higher as compared to colorimetric analysis used to determine the adsorption isotherm of dye. In particular at low degrees of cation exchange the errors are large and this explains why as an artifact for two samples even negative values for C5 remaining in solution are calculated. While due to restrictions in analysis the C5 adsorption isotherm is less precisely defined as compared to the dye adsorption isotherm, the steep change in partition equilibrium between solid phase and solution around 50 % exchange is in good agreement with PXRD results that suggest the best OI at 52 % exchange.

**Table S3. CHN-results after intercalation of C5 in V<sub>ethanol</sub> : V<sub>water</sub> = 1:1**

C5 added % CEC	experimental carbon content [%]	interlayer composition	C5 intercalated [% CEC]	part of C5 remaining in solution [%]
30	2.46	{Na <sub>0.34</sub> C5 <sub>0.16</sub> }	33	-8
40	3.10	{Na <sub>0.29</sub> C5 <sub>0.21</sub> }	41	-3
50	3.29	{Na <sub>0.28</sub> C5 <sub>0.22</sub> }	44	12
54	3.57	{Na <sub>0.26</sub> C5 <sub>0.24</sub> }	48	11
56	3.65	{Na <sub>0.26</sub> C5 <sub>0.24</sub> }	49	13
58	3.84	{Na <sub>0.24</sub> C5 <sub>0.26</sub> }	52	11
60	3.90	{Na <sub>0.24</sub> C5 <sub>0.26</sub> }	52	13
70	4.13	{Na <sub>0.22</sub> C5 <sub>0.28</sub> }	56	21
80	4.46	{Na <sub>0.20</sub> C5 <sub>0.30</sub> }	60	25
90	5.15	{Na <sub>0.15</sub> C5 <sub>0.35</sub> }	70	22
100	5.68	{Na <sub>0.11</sub> C5 <sub>0.39</sub> }	78	22

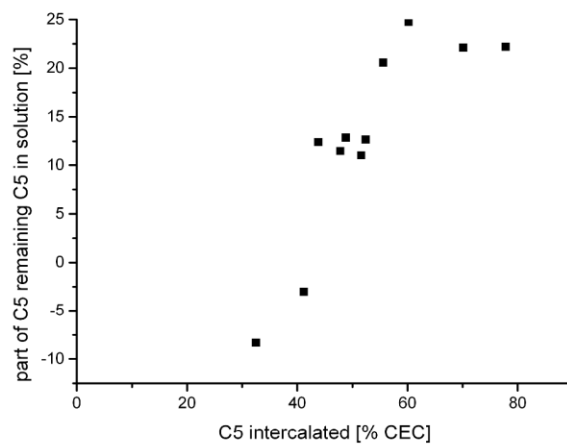


**Figure S2.** Adsorption isotherm of C5 and Na-hec at room temperature intercalated in V<sub>ethanol</sub>:V<sub>water</sub> = 1:1 using results of CHN analysis. The C5 amount remaining in solution was calculated as the difference of total C5 offered to C5 adsorbed.

### 8. Pillaring of $\text{Na}^+$ -interlayers of OI with $\text{Me}_2\text{DABCO}^{2+}$

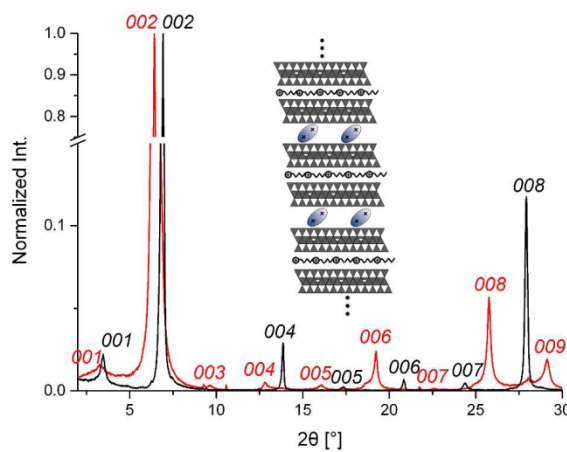


**Figure S3.** PXRD patterns of OI C5 (black trace) showing a  $d^{\text{OI}}(001)$  of 25.6 Å (cv = 0.06%) and after pillarizing into a microporous heterostructure (see inset) by exchanging the remaining sodium interlayers with  $\text{Me}_2\text{DABCO}^{2+}$  (red trace). Upon pillarizing the *d*-spacing increases to 27.6 Å (cv = 0.20%).

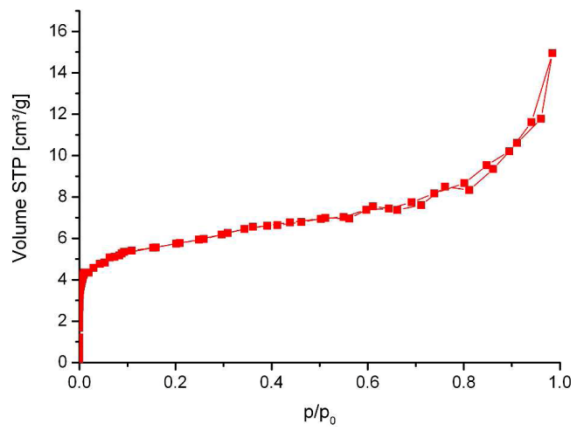


**Figure S4.** Physisorption isotherm (Ar/Ar(l)) of the pillared microporous heterostructure. The calculated micropore volume (< 10 Å) is 0.008 cm<sup>3</sup>/g and the BET surface is 21 m<sup>2</sup>/g.

## 9. Macroscopic structure of dye OI stacks

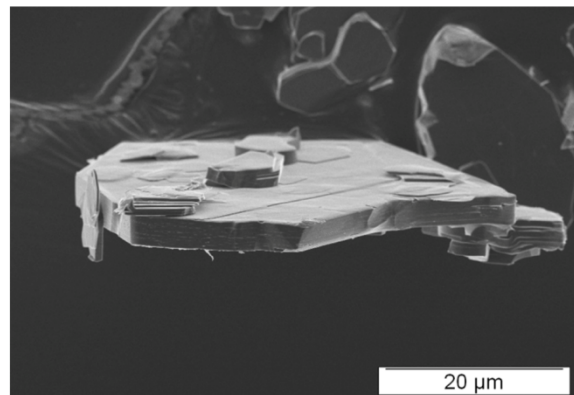


**Figure S5.** SEM image showing intact stacks of the dye OI sample after intercalation of 38% CEC.

## References

- (1) Bailey, S. W. *Am. Mineral.* **1982**, *67*, 394-398.
- (2) Reynolds, R. C.; Distefano, M. P.; Lahann, R. W. *Clays Clay Miner.* **1992**, *40*, 262-267.
- (3) Reynolds, R. C.; Hower, J. *Clays Clay Miner.* **1970**, *18*, 25-&.
- (4) Stöter, M.; Kunz, D. A.; Schmidt, M.; Hirsemann, D.; Kalo, H.; Putz, B.; Senker, J.; Breu, J. *Langmuir* **2013**, *29*, 1280-1285.

### 5.3 Synthese funktionaler Doppelschichten

Matthias Stöter,<sup>[a]</sup> Dr. Bernhard Biersack,<sup>[b]</sup> Dr. Sabine Rosenfeldt,<sup>[c]</sup> Markus J. Leitl,<sup>[d]</sup> Dr. Hussein Kalo,<sup>[a]</sup> Prof. Dr. Rainer Schobert,<sup>[b]</sup> Prof. Dr. Hartmut Yersin,<sup>[d]</sup> Prof. Geoffrey A. Ozin,<sup>[e]</sup> Prof. Dr. Stephan Förster,<sup>[c]</sup> Prof. Dr. Josef Breu<sup>[a]</sup>

#### Encapsulation of Functional Organic Compounds in Nanoglass for Optically Anisotropic Coatings

Erschienen in: Angewandte Chemie International **2015**, *54*, 4963-4967.

Angewandte Chemie, **2015**, *127*, 5047-5051

Reprinted with permission. Copyright 2015, Wiley.

Impact Factor (2014) Angewandte Chemie International: 11.261

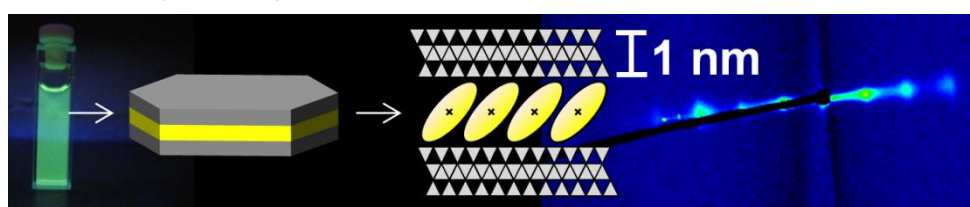
<sup>[a]</sup> Lehrstuhl für Anorganische Chemie I, Universität Bayreuth, D-95440 Bayreuth, Germany

<sup>[b]</sup> Lehrstuhl für Organische Chemie I, Universität Bayreuth, D-95440 Bayreuth, Germany

<sup>[c]</sup> Physikalische Chemie I, Universität Bayreuth, 95440 Bayreuth (Germany)

<sup>[d]</sup> Lehrstuhl für Physikalische Chemie, Universität Regensburg, 93053 Regensburg (Germany)

<sup>[e]</sup> Department of Chemistry, University of Toronto, Toronto, M5S 3H6 (Canada)



#### Darstellung des Eigenanteils:

Das Konzept für diese Publikation wurde von Prof. Dr. Josef Breu, Prof. Dr. Geoffrey A. Ozin und mir entwickelt. Die Synthese der Stilbazoliumverbindung erfolgte in der Organischen Chemie I, Universität Bayreuth durch Dr. Bernhard Biersack und Prof. Dr. Rainer Schobert. Die SAXS-Messungen und Simulationen wurden in der Physikalischen Chemie I, Universität Bayreuth durch Dr. Sabine Rosenfeldt und Prof. Dr. Stephan Förster durchgeführt. Die Emissionsquantenausbeute und die Fluoreszenzspektren wurden am Lehrstuhl für Physikalische Chemie der Universität Regensburg von Markus J. Leitl und Prof. Dr. Hartmut Yersin gemessen. Dr. Hussein Kalo führte die Gasbarriermessungen durch.

Die experimentelle Durchführung, Charakterisierung der Doppelschichten, die Herstellung der Nanokompositfilme sowie die optische Charakterisierung mittels polarisierten UV-VIS Messungen wurden von mir selbst durchgeführt. Verfasst wurde diese Publikation hauptsächlich von Prof. Dr. Josef Breu und mir. Mein Eigenanteil beträgt ca. 70 %.

### 5.3.1 Encapsulation of functional organic compounds in nanoglass for optically anisotropic coatings



**Layered Materials**

International Edition: DOI: 10.1002/anie.201411137  
 German Edition: DOI: 10.1002/ange.201411137

## Encapsulation of Functional Organic Compounds in Nanoglass for Optically Anisotropic Coatings\*\*

Matthias Stöter, Bernhard Biersack, Sabine Rosenfeldt, Markus J. Leitl, Hussein Kalo, Rainer Schobert, Hartmut Yersin, Geoffrey A. Ozin, Stephan Förster, and Josef Breu\*

**Abstract:** A novel approach is presented for the encapsulation of organic functional molecules between two sheets of 1 nm thin silicate layers, which like glass are transparent and chemically stable. An ordered heterostructure with organic interlayers strictly alternating with osmotically swelling sodium interlayers can be spontaneously delaminated into double stacks with the organic interlayers sandwiched between two silicate layers. The double stacks show high aspect ratios of >1000 (typical lateral extension 5000 nm, thickness 4.5 nm). This newly developed technique can be used to mask hydrophobic functional molecules and render them completely dispersible in water. The combination of the structural anisotropy of the silicate layers and a preferred orientation of molecules confined in the interlayer space allows polymer nanocomposite films to be cast with a well-defined orientation of the encapsulated molecules, thus rendering the optical properties of the nanocoatings anisotropic.

The industrial application of many functional organic molecules is often hampered by thermal and/or oxidative instability. Frequently, their processability may also be hampered by limited water solubility, while the masking and targeting of biologically active compounds is sought for many pharmaceuticals.<sup>[1]</sup>

It is well-known in the case of various clathrates that encapsulation is capable of stabilizing even highly reactive species, such as of S<sub>3</sub> ions in ultramarine. Moreover, intercalation results in the functional species no longer being in direct contact with the solvent. Instead, the dispersibility is determined by the surface properties of the hybrid material. A large surface potential, for example, allows for robust electrostatic stabilization of aqueous suspensions.<sup>[2]</sup>

A layered host may offer the additional advantage of pronounced inherent structural anisotropy. Consequently, the interlayer structure formed by the intercalation of organic compounds between a sandwich of two layers ensures a well-defined orientation in the confined space.<sup>[3,4]</sup> Such a controlled arrangement of molecules is of key importance for efficient light absorption in organic solar cells and for spintronics.<sup>[5,6]</sup> In this regard, Kunz et al. have shown that the intercalation of [Ru(bpy)<sub>3</sub>]<sup>2+</sup> (bpy=2,2'-bipyridine) into a synthetic clay mineral leads to the polarized emission of light.<sup>[7]</sup>

Recently, we established a general synthetic procedure for the synthesis of ordered functional heterostructures, where interlayers with a functional molecular moiety strictly alternate with hydrated inorganic Na<sup>+</sup> interlayers.<sup>[8]</sup> Surprisingly, we now succeeded in spontaneously delaminating this material into double stacks of two highly transparent, flexible silicate layers that encapsulate a central organic layer of oriented functional molecules. Moreover, the large aspect ratio of these delaminated double stacks inevitably leads to perfectly textured films upon casting suspensions on flat substrates, which in turn results in a pseudoepitaxial orientation of the encapsulated functional moiety.

A melt-synthesized sodium hectorite ([Na<sub>0.5</sub>]<sub>inter</sub>[Mg<sub>2.5</sub>Li<sub>0.5</sub>]<sup>tot</sup>[Si<sub>4</sub>]<sup>tot</sup>O<sub>10</sub>F<sub>2</sub>; Na-hec) can be synthesized with perfectly homogeneous charge density.<sup>[9]</sup> Any molecular interlayer cation that assembles into densely packed structures that show a charge density significantly higher or lower than that of the layered silicate host allows for formation of ordered interstratified heterostructures.<sup>[8]</sup>

For example, intercalation of the fluorescent stilbazolium dye N-hexadecyl-4-(3,4,5-trimethoxystyryl)-pyridinium (subsequently shortened to dye) into well-characterized Na-hec<sup>[9]</sup> at a level whereby 38 % of the pristine interlayer cation (Na<sup>+</sup>) is exchanged by dye leads to a perfectly ordered interstratified heterostructure<sup>[8]</sup> with strictly alternating layers of hydrated Na<sup>+</sup> and dye. The formation of the heterostructures is based on the partition equilibrium between the intercalated dye and the dye in solution. Although the dye will prefer the intercalated state and thus must have certain hydrophobicity, it still needs to show a reasonable solubility. Ethanol/water ratios of 4:1 were therefore used for the partial ion exchange.

\*\*] M. Stöter, Dr. H. Kalo, Prof. Dr. J. Breu  
 Lehrstuhl für Anorganische Chemie I, Universität Bayreuth  
 Universitätsstrasse 30, 95440 Bayreuth (Germany)  
 E-mail: Josef.Breu@uni-bayreuth.de  
 Dr. B. Biersack, Prof. Dr. R. Schobert  
 Organische Chemie I, Universität Bayreuth  
 Universitätsstrasse 30, 95440 Bayreuth (Germany)  
 Dr. S. Rosenfeldt, Prof. Dr. S. Förster  
 Physikalische Chemie I, Universität Bayreuth  
 Universitätsstrasse 30, 95440 Bayreuth (Germany)  
 M. J. Leitl, Prof. Dr. H. Yersin  
 Lehrstuhl für Physikalische Chemie, Universität Regensburg  
 Universitätsstrasse 31, 93053 Regensburg (Germany)  
 Prof. G. A. Ozin  
 Department of Chemistry, University of Toronto  
 80, St George Street, Toronto, M5S 3H6 (Canada)

[\*\*] This work was financially supported by the Deutsche Forschungsgemeinschaft (SFB 840). We thank Prof. A. Fery, Physikalische Chemie II, University of Bayreuth, for making AFM equipment available. G.A.O. is the Governor of Canada Research Chair in Materials Chemistry and Nanochemistry. He is deeply grateful to the Natural Sciences and Engineering Research Council of Canada for strong and sustained support of his work.

Supporting information for this article (including Experimental Details) is available on the WWW under <http://dx.doi.org/10.1002/anie.201411137>.

For other dyes, the solubility needs to be adjusted. In the mixture used here, the swelling of the  $\text{Na}^+$  interlayers is restricted to the two-layer hydrate and no exfoliation is observed at the stage where the heterostructure is formed.<sup>[8]</sup> Surprisingly, we now find that immersing the microcrystalline powder of the ordered interstratified heterostructure into deionized water results in the material swelling (Figure 1) into

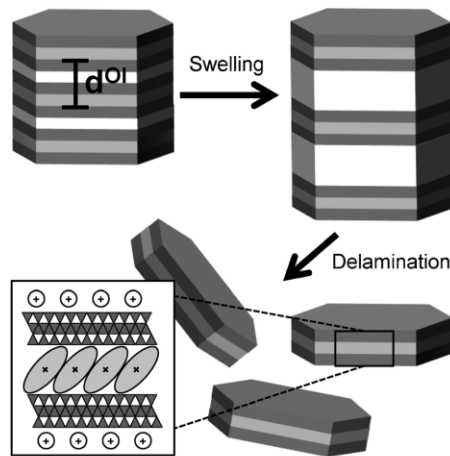


**Figure 1.** Delamination of the ordered interstratified heterostructured powder along swollen sodium interlayers (white) to produce water-dispersible double stacks with an oriented interlayer of encapsulated hydrophobic dye (gray).

a yellow gel with a high viscosity. A concomitant huge increase in sample volume (Figure S1) is observed, which indicates a delamination of the one-dimensional crystals into thinner nanoplatelets. Stable suspensions are formed at higher dilution, and a “Schlieren” texture implies a high stability of the suspension in water (Figure S2). Drying the diluted suspension on a flat substrate leads to a film that shows a good wettability for  $\text{H}_2\text{O}$ , comparable to the wettability of the pristine Na-hec. This finding suggests that the hydrophobic dye is not released upon swelling, but is irreversibly immobilized by intercalation (Figure S3). This is further supported by the high negative streaming potential of the double stacks that resembles the potential of the delaminated unmodified layered silicate, thus suggesting a similar surface charge.

Apparently, the hydration enthalpy of the  $\text{Na}^+$  interlayers is still sufficient to trigger osmotic swelling, where the distance between individual platelets is determined simply by the silicate/water ratio. Upon swelling, the hydrophobic dye remains encapsulated between two 1 nm thick silicate layers. The diluted suspensions are transparent (Figure S4, right). The scattering of green laser light and a strong and homogeneous fluorescence under UV irradiation at 366 nm demonstrate that the double stacks are highly dispersed with the fluorescent dye molecules sandwiched between the silicate layers (Figure S4, left).

Final proof of the existence of double stacks comes from small-angle X-ray scattering (SAXS) studies. The SAXS pattern of the ordered interstratified heterostructured powder scales in the low  $q$  range ( $q < 0.7 \text{ nm}^{-1}$ ) according to  $q^{-4}$ , which is typical for bulk 3D objects such as crystals, and confirms the mesoscopic length scale of the one-dimensional crystalline stacks (Figure 2d). The scaling of  $q$  for the most

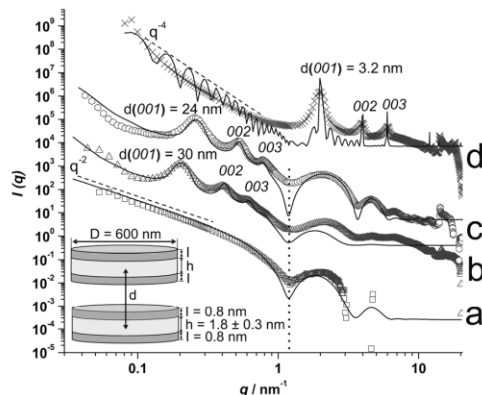


**Figure 2.** Experimental SAXS patterns (symbols) for aqueous suspensions of a) 2.5 wt% (square), b) 15 wt% (triangle), c) 20 wt% (hexagon), and d) the pristine ordered interstratified heterostructured powder (cross). The continuous lines correspond to calculated intensities based on a model of stacked “hamburgers” (see the Supporting Information for further details). The dotted line represents the position of the first minimum of the form factor, which is correlated to the thickness of one “hamburger” ( $h+2l$ ). The scaling of  $q$  is indicated by dashed lines (only shown for the 2.5 wt% suspension and the ordered interstratified heterostructured powder).

diluted (2.5 wt%) suspension, however, changes to  $q^{-2}$ , which is typically observed for platelet-like objects (Figure 2a). The change in the scaling indicates a huge increase in aspect ratio, most probably because of delamination into thinner nanoplatelets upon swelling. This is further supported by a continuous shift of the average distance between double stacks ( $d$ ) to lower  $q$  values as the water content is increased. The  $d$  spacing increases from 3.2 nm in the dry powder to 24 nm at 20 wt% and finally to 30 nm at 15 wt% suspension. The disappearance of the  $00l$  series for the most diluted 2.5 wt% suspension indicates a loss of positional correlation in the 2D SAXS pattern (Figures S5 and S6). At this stage, the material is swollen to a degree where the double stacks are separated far enough ( $>60 \text{ nm}$ ) to realize an apparently isotropic orientation of the platelets. It is noteworthy that the intensity minima of the form factor oscillation at  $q = 1.2 \text{ nm}^{-1}$  is the same for all suspensions of various concentrations. This value corresponds to a platelet thickness of 3.4 nm, which again corroborates the delamination into double stacks. The formation of individual double stacks was further verified by atomic force microscopy (AFM) of samples obtained from a highly diluted delaminated suspension. AFM confirms double stacks with a height of 4.5 nm (Figure 3), a value corresponding to the sum of the heights of two hydrated

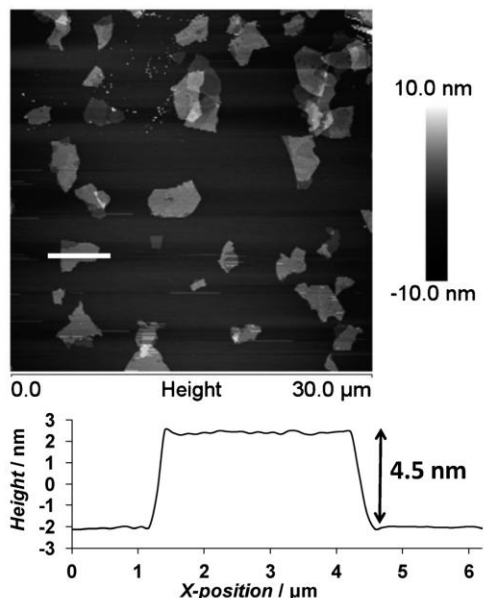


**Figure 3.** AFM image of a diluted aqueous suspension ( $0.01 \text{ mg mL}^{-1}$ ) dried on a silicon wafer illustrating the presence of double stacks with a height of 4.5 nm. The height profile of a platelet (white bar) is included.

silicate layers with a monolayer of dye encapsulated in between. The van der Waals thickness of one silicate layer is 0.96 nm.<sup>[9]</sup> The thickness of the dye interlayer can be deduced from a powder X-ray diffractogram (PXRD) recorded on a film of restacked double stacks dried at 0% relative humidity (r.h.; Figure S7) to be approximately 1.6 nm (3.52 nm –  $2 \times 0.96 \text{ nm}$ ). It is noteworthy that the AFM measurement is performed under ambient conditions at approximately 50% r.h. Consequently, the  $\text{Na}^+$  ions on both surfaces of the double stack are expected to be octahedrally coordinated by water (0.54 nm<sup>[10]</sup> on each side), summing to a total height of the double stack of 4.6 nm ( $2 \times 0.96 \text{ nm} + 1.6 \text{ nm} + 2 \times 0.54 \text{ nm}$ ).

Encapsulation of the hydrophobic dye between two silicate layers not only allows its dispersion in water but also significantly influences the solid-state optical properties of the fluorophore. Compared to the bromide salt of the dye, the intercalated dye no longer shows the additional absorption and emission bands at higher wavelengths (Figures S8 and S9), which are usually attributed to J-type dimers.<sup>[4]</sup> While such a change in structure might be expected as a consequence of the confinement between the layers, the increase in the emission quantum yield is somewhat surprising. The dye bromide salt shows a photoluminescence quantum yield (QY) of 3%, while the QY for the crystalline ordered interstratified heterostructured powder and the delaminated double stacks increases to 11% and 7%, respectively. Comparable improvement of the QY was obtained for a similar stilbazolium compound after microencapsulation in micelles, where tor-

sional motions and nonradiative relaxation from the excited to the ground state are reduced.<sup>[11]</sup> Indeed, the confinement between the silicate layers might well impose restrictions on changes in the geometry of the luminescent molecule upon a transition between these states. These restrictions might be responsible for the increased QY observed.

When casting films of the delaminated suspension, the huge aspect ratio of double stacks of  $> 1000$  (typical diameter 5000 nm, thickness 4.5 nm, Figure 3) will inevitably produce texture, as already indicated by the well-defined  $00l$  series observed by PXRD (Figure S7). Additionally, 2D SAXS measurements of the films were performed to judge the quality of the platelet texture (Figure 4).

In the transmission geometry, only a continuous ring of the  $hk$  band is visible, which is caused by a random, statistically isotropic orientational distribution of restacked double stacks within the film plane (Figure 4, top, and Figure S10). In the parallel geometry, mainly one  $00l$  series running along a fixed reciprocal direction can be observed, which indicates

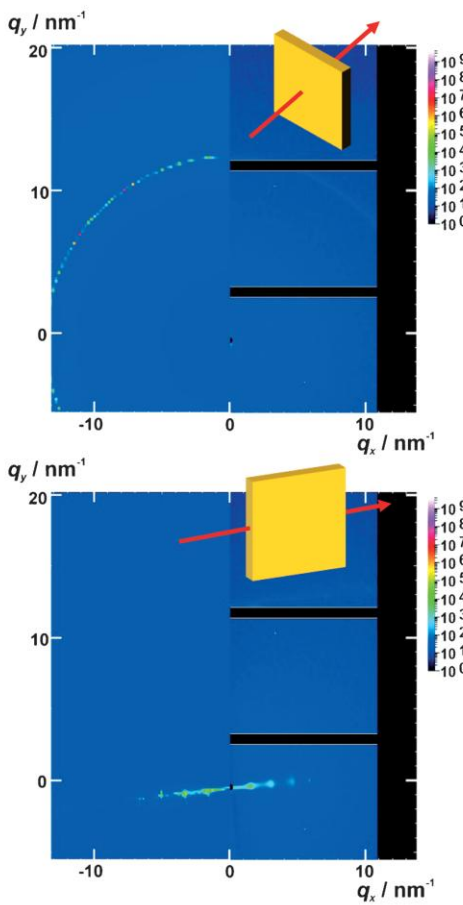


**Figure 4.** Measured (right) and calculated (left) 2-dimensional SAXS patterns of a textured film of delaminated and restacked double stacks in the transmission (top) and parallel geometry (bottom).

an anisotropic (textured) stacking of the double stacks orthogonally to the film plane (Figure 4, bottom, and Figure S10). From the coherence length in the azimuthal direction and the *d* spacing, an angle derivation of about 2° is found, which indicates a nearly perfect texture (see the Supporting Information for details).

The double stacks can be easily compounded into any polymer matrices of choice. The external Na<sup>+</sup> ions might have to be replaced by appropriate organic cations in the case of more hydrophobic matrices. As a proof of principle, we produced nanocomposite films with 50 wt % inorganic content by solution-casting delaminated double stacks mixed with an aqueous solution of polyvinyl alcohol (PVOH). SAXS patterns confirmed a highly anisotropic structure, thus corroborating the efficient texturing also in polymer matrices (Figure S11). TEM and SEM images of a cross-section of the nanocomposite film illustrate the layered structure and the presence of double stacks (Figures S12 and S13). The good texture is also reflected by a significantly improved oxygen barrier. The transmission rate of the nanocomposite film is four times lower than the unfilled PVOH film (Table S1), which indicates that the encapsulated dye will be protected from oxygen attack. Thermal analysis, moreover, indicates that the thermal stability of the encapsulated dye is improved by as much as 100°C compared to the dye bromide salt (Figure S14). The decomposition temperature of the nanocomposite increases by approximately 30°C compared to the neat PVOH matrix (Figure S15).

As indicated by the changes in the UV spectra, and as recently shown for a bulk layered silicate crystal intercalated with [Ru(bpy)<sub>3</sub>]<sup>2+</sup>,<sup>[7]</sup> the surface corrugation of the layered silicate will orientate molecules when confined between silicate layers. Consequently, a well-textured film of delaminated and restacked double stacks is expected to feature optical anisotropy with respect to absorption and emission of linearly polarized light.<sup>[4, 12]</sup>

*x*- and *y*-polarized UV/Vis spectra of the textured film of delaminated and restacked double stacks and the nanocomposite film are shown in Figure 5 and Figure S17, respectively. The *y*-polarized UV/Vis spectra do not change as the  $\delta$  angle increases, thus indicating a statistically isotropic orientation of the transition moments within the film surface, as a result of a random orientation within the *xy* plane. However, the *x*-polarized UV/Vis spectra show a linear reduction of the absorption as the  $\delta$  angle increases, thus indicating optical anisotropy (see Figure S18 and the Supporting Information for more details) because of a fixed orientation of the transition moments along the *z* direction. Similar results were obtained for the nanocomposite film (Figure S19).

In conclusion, a general strategy is reported for the synthesis of nanosized layered hybrid materials where a functional organic cation is encapsulated between two transparent 1 nm thin silicate layers. Encapsulation assists dispersion of hydrophobic organic compounds in water, which bodes well for their use in medical applications such as photodynamic therapy and drug delivery. Additionally, the structural anisotropy of the clay mineral host in combination with the preferred orientation of the guest facilitates the production of

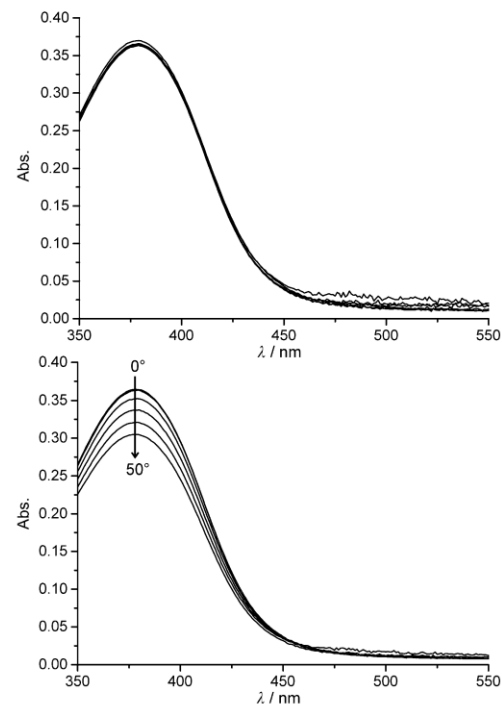


**Figure 5.** Corrected *y* (top) and *x*-polarized (bottom) absorption spectra of a textured film of delaminated and then restacked double stacks. Both sets of spectra were obtained at different  $\delta$  angles by turning the textured film around its *y* axis in 10° steps (arrow). The observed *x* polarization indicates orientation of the dye monolayer.

(polymer-based) nanocoatings with anisotropic physical properties. The concept should be transferable to other charged swelling inorganic layered materials, such as titanates<sup>[13]</sup> and niobates,<sup>[14]</sup> as long as an absolutely homogeneous charge density is warranted, which is essential to form ordered interstratifications.

**Keywords:** delamination · encapsulation · host compounds · layered materials · organic-inorganic hybrid composites

**How to cite:** *Angew. Chem. Int. Ed.* **2015**, *54*, 4963–4967  
*Angew. Chem.* **2015**, *127*, 5047–5051

- [1] Y. Chen, H. R. Chen, J. L. Shi, *Adv. Mater.* **2013**, *25*, 3144–3176.
- [2] L. Li, L. Harnau, S. Rosenfeldt, M. Ballauff, *Phys. Rev. E* **2005**, *72*, 051504.
- [3] S. Takagi, T. Shimada, Y. Ishida, T. Fujimura, D. Masui, H. Tachibana, M. Eguchi, H. Inoue, *Langmuir* **2013**, *29*, 2108–2119.
- [4] V. Martínez Martínez, F. L. Arbeloa, J. B. Prieto, I. L. Arbeloa, *Chem. Mater.* **2005**, *17*, 4134–4141.
- [5] O. Guskova, C. Schünemann, K. J. Eichhorn, K. Walzer, M. Levichkova, S. Grundmann, J. U. Sommer, *J. Phys. Chem. C* **2013**, *117*, 17285–17293.
- [6] M. A. Niño, I. A. Kowalik, F. J. Luque, D. Arvanitis, R. Miranda, J. J. de Miguel, *Adv. Mater.* **2014**, *26*, 7474–7479.

- [7] D. A. Kunz, M. J. Leitl, L. Schade, J. Schmid, B. Bojer, U. T. Schwarz, G. A. Ozin, H. Yersin, J. Breu, *Small* **2015**, *11*, 792–796.
- [8] M. Stöter, B. Biersack, N. Reimer, M. Herling, N. Stock, R. Schobert, J. Breu, *Chem. Mater.* **2014**, *26*, 5412–5419.
- [9] M. Stöter, D. A. Kunz, M. Schmidt, D. Hirsemann, H. Kalo, B. Putz, J. Senker, J. Breu, *Langmuir* **2013**, *29*, 1280–1285.
- [10] H. Kalo, W. Milius, J. Breu, *RSC Adv.* **2012**, *2*, 8452–8459.
- [11] L. F. M. Ismail, *J. Lumin.* **2012**, *132*, 2512–2520.
- [12] V. Martínez, S. Salleres, J. Banuelos, F. L. Arbeloa, *J. Fluoresc.* **2006**, *16*, 233–240.
- [13] F. Geng, R. Ma, A. Nakamura, K. Akatsuka, Y. Ebina, Y. Yamauchi, N. Miyamoto, Y. Tateyama, T. Sasaki, *Nat. Commun.* **2013**, *4*, 1632.
- [14] M. M. Fang, C. H. Kim, G. B. Saupe, H. N. Kim, C. C. Waraksa, T. Miwa, A. Fujishima, T. E. Mallouk, *Chem. Mater.* **1999**, *11*, 1526–1532.

Received: November 17, 2014

Published online: February 20, 2015

## 5.3.2 Nanoglas-Verkapselung funktionaler organischer Verbindungen für optisch anisotrope Beschichtungen



### Schichtmaterialien

Deutsche Ausgabe: DOI: 10.1002/ange.201411137  
 Internationale Ausgabe: DOI: 10.1002/anie.201411137

## Nanoglas-Verkapselung funktionaler organischer Verbindungen für optisch anisotrope Beschichtungen\*\*

Matthias Stöter, Bernhard Biersack, Sabine Rosenfeldt, Markus J. Leitl, Hussein Kalo, Rainer Schobert, Hartmut Yersin, Geoffrey A. Ozin, Stephan Förster und Josef Breu\*

**Abstract:** Funktionale Moleküle lassen sich mit einem neuen Verfahren zwischen zwei 1 nm dünnen Schichten verkapseln, die ähnlich wie Glas transparent und chemisch inert sind. Geordnete Wechsellagerungen von alternierenden organischen und osmotisch quellfähigen  $\text{Na}^+$ -Zwischenschichten delaminieren spontan zu Doppelschichten bestehend aus zwei Silicatschichten, welche die organische Zwischenschicht einschließen. Die neue Technik ist geeignet, um hydrophobe, funktionale Moleküle zu maskieren und vollständig in Wasser dispergierbar zu machen. Die Doppelschichten besitzen durch die laterale Ausdehnung von 5000 nm und die Dicke von 4.5 nm ein Aspektverhältnis von > 1000. Die Kombination aus strukturimmanenter Anisotropie der Silicatschichten und der aus dem begrenzten Raum zwischen den Schichten resultierenden Vorzugsorientierung eingelagelter Moleküle erlaubt es, Nanokompositfilme mit einer definierten Orientierung der eingekapselten Moleküle herzustellen, die sich in der Folge durch anisotrope optische Eigenschaften auszeichnen.

Die industrielle Anwendung funktionaler organischer Verbindungen wird häufig durch thermische und/oder oxidative Labilität eingeschränkt. Auch ihre Prozessierbarkeit ist vielfach durch eine begrenzte Wasserlöslichkeit limitiert. Bei Arzneimitteln ist oft eine Maskierung von Vorteil, und eine möglichst gezielte Wirkstofffreisetzung wird angestrebt.<sup>[1]</sup>

Durch Verkapselung lassen sich selbst hoch reaktive  $\text{S}_3^-$ -Anionen dauerhaft stabilisieren, wie am Beispiel der Ultramarine deutlich wird. Bei Einlagerungsverbindungen kommt außerdem hinzu, dass sich die funktionale Spezies nicht länger in direktem Kontakt zum umgebenden Lösungsmittel befindet. Dadurch wird die Dispergierbarkeit einzig und allein durch die Oberflächeneigenschaften des Hybridmaterials bestimmt. Mit einem hohen Oberflächenpotential kann sogar eine stabile Dispergierung erreicht werden.<sup>[2]</sup>

Schichtförmige Wirtverbindungen bieten von Natur aus den Vorteil einer ausgeprägten strukturimmanenten Anisotropie. Deshalb werden im Zwischenschichtraum eingelagerte organische Verbindungen durch die umgebenden Schichten ausgerichtet.<sup>[3,4]</sup> Diese kontrollierte Molekülorientierung ist z.B. für eine effizientere Lichtabsorption in organischen Solarzellen oder für Spintronics wichtig.<sup>[5,6]</sup> In diesem Zusammenhang wurde kürzlich von Kunz et al. über eine polarisierte Lichemission nach Einlagerung von  $[\text{Ru}(\text{bpy})_3]^{2+}$  ( $\text{bpy} = 2,2'-\text{Bipyridin}$ ) in ein synthetisches Tonmineral berichtet.<sup>[7]</sup>

Vor kurzem haben wir einen Weg zur Synthese von geordneten, funktionalen Wechsellagerungen vorgestellt, bei denen organische mit anorganischen  $\text{Na}^+$ -Zwischenschichten streng alternieren.<sup>[8]</sup> Überraschenderweise ist es uns nun gelungen, diese geordneten Strukturen spontan zu Doppelschichten zu delaminieren, bei denen eine zentrale organische Schicht aus orientierten, fluoreszierenden Molekülen durch zwei hochtransparente, flexible Silicatschichten eingekapselt wird. Durch das hohe Aspektverhältnis der delaminierten Doppelschichten lassen sich durch Aufstreichen auf plane Substrate Filme mit perfekter Textur herstellen, wodurch es dann zu einer pseudo-epitaxialen Orientierung der funktionalen Einheit kommt.

Wird Natrium-Hectorit ( $[\text{Na}_{0.5}]^{\text{inter}}[\text{Mg}_{2.5}\text{Li}_{0.5}]^{\text{oxt}}[\text{Si}_4]^{\text{tet}}\text{O}_{10}\text{F}_2$ ) (Na-hec) aus der Schmelze synthetisiert, weist er eine nahezu perfekt homogene Schichtladungsdichte auf.<sup>[9]</sup> Wenn dann im Zwischenschichtraum eingelagerte molekulare Kationen dichtgepackte Strukturen ausbilden, die eine vom Schichtsilicat abweichende Ladungsdichte besitzen, kommt es in der Folge zur Ausbildung geordneter Wechsellagerungen.<sup>[8]</sup>

Wird beispielsweise die fluoreszierende Stilbazoniumverbindung (*N*-Hexadecyl-4-(3,4,5-trimethoxystyryl)-pyridinium (in der Folge mit Farbstoff abgekürzt) in den in vorangegangenen Arbeiten eingehend charakterisierten Na-hec<sup>[9]</sup> eingelegt, und zwar mit einem Anteil von genau 38 % der ursprünglichen  $\text{Na}^+$ -Ionen, wird eine perfekt geordnete Wechsellagerung ausgebildet.<sup>[8]</sup> Diese ist aufgebaut aus einer strikt alternierenden Abfolge von hydratisierten  $\text{Na}^+$ - und Farbstoff-

[\*] M. Stöter, Dr. H. Kalo, Prof. Dr. J. Breu  
 Lehrstuhl für Anorganische Chemie I, Universität Bayreuth  
 Universitätsstraße 30, 95440 Bayreuth (Deutschland)  
 E-Mail: Josef.Breu@uni-bayreuth.de  
 Dr. B. Biersack, Prof. Dr. R. Schobert  
 Organische Chemie I, Universität Bayreuth  
 Universitätsstraße 30, 95440 Bayreuth (Deutschland)  
 Dr. S. Rosenfeldt, Prof. Dr. S. Förster  
 Physikalische Chemie I, Universität Bayreuth  
 Universitätsstraße 30, 95440 Bayreuth (Deutschland)  
 M. J. Leitl, Prof. Dr. H. Yersin  
 Lehrstuhl für Physikalische Chemie, Universität Regensburg  
 Universitätstr. 31, 93053 Regensburg (Deutschland)  
 Prof. G. A. Ozin  
 Department of Chemistry, University of Toronto  
 80, St George Street, Toronto, M5S 3H6 (Kanada)

[\*\*] Diese Arbeit wurde von der Deutschen Forschungsgemeinschaft (SFB 840) finanziell unterstützt. Wir danken Prof. A. Fery, Physikalische Chemie II, Universität Bayreuth, für die Möglichkeit der Nutzung des AFM-Gerätes. G.A.O. ist Government of Canada Research Chair in Materials Chemistry and Nanochemistry. Er dankt dem Natural Sciences and Engineering Research Council of Canada für die Unterstützung seiner Arbeit.

Hintergrundinformationen zu diesem Beitrag sind im WWW unter <http://dx.doi.org/10.1002/ange.201411137> zu finden.

## Angewandte Zuschriften

stoff-Schichten. Die Bildung dieser eindimensional kristallinen Heterostruktur basiert auf der Einstellung des Verteilungsgleichgewichtes zwischen interkaliertem und in Lösung verbleibendem Anteil an Farbstoff. Einerseits sollte der Farbstoff den Zwischenschichtraum bevorzugen, wofür eine bestimmte Hydrophobie essentiell ist, andererseits ist für die Gleichgewichtseinstellung eine gewisse Löslichkeit nötig. Für den gegebenen Farbstoff wurde diese Balance durch den partiellen Austausch in einer Ethanol-Wasser-Mischung im Verhältnis von 4:1 gewährleistet. Bei anderen Farbstoffen muss die Löslichkeit entsprechend angepasst werden. In dem verwendeten Lösungsmittelgemisch bleibt die Quellung der  $\text{Na}^+$ -Zwischenschichten auf das Zweischichthydrat beschränkt, weshalb bei der Synthese der Wechsellagerung keinerlei Exfolierung beobachtet wurde.<sup>[8]</sup> Zu unserer Überraschung haben wir nun entdeckt, dass das mikrokristalline Pulver in entionisiertem Wasser quillt (Abbildung 1). Unter

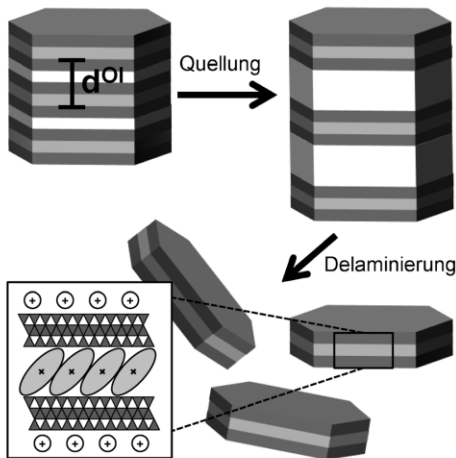


**Abbildung 1.** Die Delaminierung von geordnet wechselgelagerten Pulvern entlang gequollener  $\text{Na}^+$ -Zwischenschichten (weiß) führt zu wasserdispergierbaren Doppelschichten mit eingekapselten und orientierten, hydrophoben Farbstoffzwischenschichten (grau).

großem Volumenzuwachs wird ein gelbes Gel hoher Viskosität gebildet (Abbildung S1 in den Hintergrundinformationen), was auf eine Delaminierung der eindimensionalen Kristalle in dünnere Nanoplättchen hindeutet. Bei höheren Verdünnungen entstehen stabile Suspensionen, die eine „Schlierentextur“ aufweisen, was die gute Stabilität in Wasser belegt (Abbildung S2). Wird eine verdünnte Suspension auf einer flachen Unterlage getrocknet, bildet sich ein Film, der gegenüber Wasser eine ähnlich gute Benetzbarkeit zeigt wie Na-hec (Abbildung S3). Dies deutet darauf hin, dass der hydrophobe Farbstoff beim Quellen nicht freigesetzt wird, sondern durch die Interkalation irreversibel immobilisiert wurde. Das wird durch die Messung des Strömungspotentials der verdünnten Suspension bestätigt. Die Doppelschichten zeigen ein stark negatives Potential in der Größenordnung des Potentials von vollständig delaminierten Na-hec, was auf eine ähnliche Oberflächenladung hindeutet.

Offensichtlich reicht die Hydrationsenthalpie der  $\text{Na}^+$ -Zwischenschichten aus, um osmotisches Quellen, bei dem der Abstand zwischen den Schichten nur vom Verhältnis Schichtsilicat/Wasser abhängt, zu gewährleisten. Während des Quellens verbleibt der Farbstoff zwischen den 1 nm dünnen Silcatschichten. Die verdünnten Suspensionen sind transparent (Abbildung S4, rechts). Die Streuung des grünen Laserstrahls und eine homogene Fluoreszenz unter UV-Licht (366 nm) deuten auf eine homogene Dispergierung der eingekapselten Farbstoffmoleküle hin (Abbildung S4, links).

Den endgültigen Beweis für die Bildung von Doppelschichten liefert die Röntgenkleinwinkelstreuung (SAXS). Das SAXS-Streubild der geordnet wechselgelagerten Kristalle skaliert im vorderen  $q$ -Bereich ( $q < 0.7 \text{ nm}^{-1}$ ) mit  $q^{-4}$ , wie es typischerweise bei voluminösen dreidimensionalen Objekten, wie Kristallen, beobachtet wird. Dies bestätigt die mesoskopische Längenskala der eindimensionalen Kristallite (Abbildung 2d). Bei der höchstverdünnnten (2.5 Gew.-%)

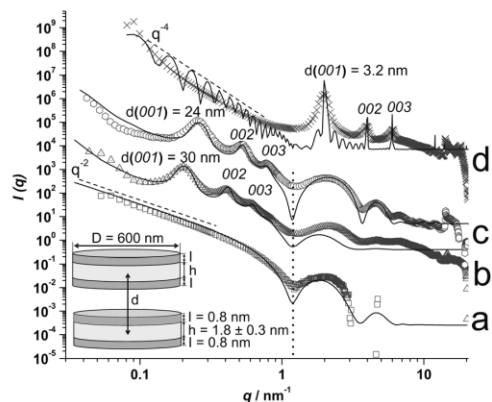


**Abbildung 2.** Experimentell bestimmte SAXS-Intensitäten (Symbole) von wässrigen Suspensionen mit a) 2.5 Gew.-% (Quadrat), b) 15 Gew.-% (Dreieck), c) 20 Gew.-% (Sechsecke), sowie d) von geordnet wechselgelagertem Pulver (Kreuz). Die durchgezogenen Linien beziehen sich auf berechnete Intensitäten basierend auf dem „Hamburger-Modell“ (vgl. Hintergrundinformationen). Die gepunktete Linie kennzeichnet die Position des ersten Formfaktorminimums, welches mit der Dicke der „Hamburger“ korreliert ( $h+2$ ). Die Skalierungsgesetze sind durch gestrichelte Linien für die Suspension mit 2.5 Gew.-% und für das geordnet wechselgelagerte Pulver angegeben.

Suspension ändert sich die Steigung zu  $q^{-2}$ , was eher bei plättchenförmigen Objekten typisch ist (Abbildung 2a). Diese Änderung des Abfallverhaltens deutet auf ein starkes Ansteigen des Aspektverhältnisses hin und ist auf eine Delaminierung unter Bildung dünnerer Plättchen beim Quellen zurückzuführen. Dies wird durch die kontinuierliche Verschiebung des durchschnittlichen Abstandes zwischen den Doppelschichten ( $d$ ) (kleinere  $q$ -Werte) mit zunehmendem Wassergehalt bestätigt. Der  $d$ -Wert von 3.2 nm des geordnet wechselgelagerten Pulvers steigt bei der Suspension mit 20 Gew.-% auf 24 nm und bei derjenigen mit 15 Gew.-% auf 30 nm an. Das Verschwinden der  $00l$ -Serie im zweidimensionalen SAXS-Streubild bei der höchstverdünnnten Suspen-

sion mit 2.5 Gew.-% deutet auf einen Verlust der Positions-korrelation hin (Abbildungen S5 und S6). Bei diesem Grad der Quellung sind die Doppelschichten weit genug ( $>60$  nm) entfernt, um eine im SAXS isotrop erscheinende Plättchen-verteilung zu realisieren. Es fällt auf, dass das erste Formfaktorminimum bei  $q=1.2\text{ nm}^{-1}$  für alle Suspensionen unterschiedlicher Konzentration identisch ist. Dieser Wert entspricht einer Plättchendicke von 3.4 nm, was für eine Delamination zu Doppelschichten spricht. Dies wird durch die Rasterkraftmikroskopie (AFM) einer hochverdünnten delaminierten Suspension bestätigt. Die im AFM gemessene Höhe der Doppelschichten von 4.5 nm (Abbildung 3) ent-

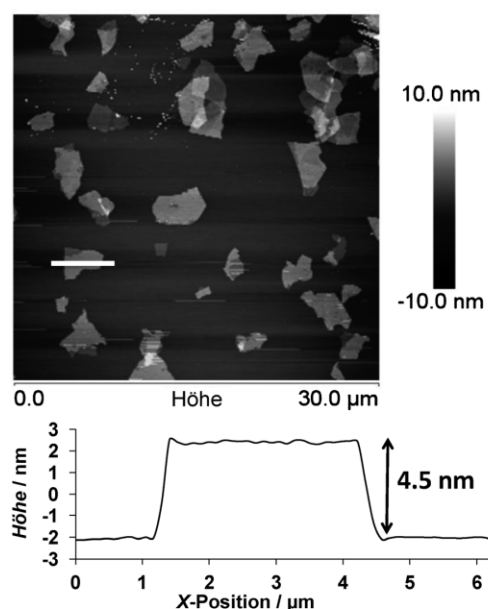


**Abbildung 3.** AFM-Aufnahme einer verdünnten, wässrigen Suspension ( $0.01\text{ mg mL}^{-1}$ ) nach Eintrocknen auf einem Silicium-Wafer verdeutlicht das Vorliegen von Doppelschichten mit einer Höhe von 4.5 nm. Das Höhenprofil eines Plättchens (weißer Balken) ist darunter angegeben.

spricht sehr gut der Summe von zwei hydratisierten Silicatschichten mit einer eingekapselten Farbstoffschicht. Die Van-der-Waals-Dicke einer Silicatschicht beträgt 0.96 nm.<sup>[9]</sup> Die Dicke der Farbstoffzwischenschicht kann aus dem Pulverdiffraktogramm (PXRD) eines Filmes von getrockneten Doppelschichten bei 0% relater Luftfeuchte (r.h.) entnommen werden (Abbildung S7) und beträgt ca. 1.6 nm ( $3.52\text{ nm}-2\times0.96\text{ nm}$ ). Da die AFM-Messung unter Umgebungsbedingungen, d.h. ca. 50% r.h. durchgeführt wurde, sind die  $\text{Na}^+$ -Kationen auf beiden Seiten oktaedrisch von Wasser koordiniert (je 0.54 nm<sup>[10]</sup> auf beiden Seiten), wodurch sich eine zu erwartende Höhe für eine Doppelschicht von  $4.6\text{ nm}$  ( $2\times0.96\text{ nm}+1.6\text{ nm}+2\times0.54\text{ nm}$ ) ergibt.

Die Verkapselung zwischen zwei Silicatschichten ermöglicht nicht nur die Dispergierung des hydrophoben Farbstoffs

in Wasser, sondern beeinflusst auch signifikant die optischen Eigenschaften des Luminophors im festen Zustand. Der interkalierte Farbstoff zeigt im Vergleich zum Farbstoffbromidsalz keine zusätzlichen Absorptions- und Emissionsbänder (Abbildungen S8 und S9), welche meist mit der Bildung von J-Typ-Dimeren erklärt werden.<sup>[4]</sup> Zwar ist durch die Einlagerung im Zwischenschichtraum eine Änderung in der räumlichen Struktur zu erwarten, aber es überrascht, dass dies mit einer Zunahme der Quantenausbeute (QA) einhergeht: Die QA steigt gegenüber dem Farbstoffbromidsalz von 3% beim geordnet wechselgelagerten Pulver auf 11% und bei den delaminierten Doppelschichten auf 7% an. Eine ähnliche Steigerung der QA wurde nach Mikroverkapselung eines vergleichbaren Stilbazolumfarbstoffs in Mizellen beobachtet, in denen Torsionsbewegungen behindert werden und damit die strahlungslose Relaxation vom Anregungs- in den Grundzustand eingeschränkt wird.<sup>[11]</sup> Auf ähnliche Weise könnte die Verkapselung des Farbstoffs zwischen den Silicatschichten wirken: Eine sterische Einschränkung von Strukturänderungen, die zwischen den unterschiedlichen Anregungszuständen auftreten, könnte den Anstieg der QA nach der Verkapselung erklären.

Wenn von einer Suspension delaminerter Doppelschichten Filme gerakelt werden, führt das hohe Aspektverhältnis der Doppelschichten von über 1000 (Durchmesser ca. 5000 nm, Dicke 4.5 nm, Abbildung 3) unweigerlich zur Texturierung. Dies zeigte bereits die gut ausgeprägte  $00l$ -Serie im PXRD (Abbildung S7). Um die Qualität der Textur zu beurteilen, werden zweidimensionale SAXS-Streubilder verwendet (Abbildung 4).

In Transmissionsgeometrie ist nur ein kontinuierlicher Ring der  $hk$ -Bande sichtbar, welcher durch eine zufällige, statistisch-isotrope räumliche Verteilung der in der Filmebene parallel übereinander liegenden Doppelschichten hervorgerufen wird (Abbildung 4, oben und Abbildung S10). In paralleler Geometrie ist hauptsächlich eine einzige  $00l$ -Serie, die entlang einer bestimmten reziproken Richtung verläuft, zu erkennen, was die anisotrope (texturierte) Stapelung der Doppelschichten rechtwinklig zur Filmoberfläche beweist (Abbildung 4, unten und Abbildung S10). Aus der Kohärenzlänge in azimuthaler Richtung und dem  $d$ -Wert lässt sich eine Winkelabweichung von etwa  $2^\circ$  abschätzen, was einer praktisch perfekten Texturierung entspricht (Näheres dazu in den Hintergrundinformationen).

Die Doppelschichten können sehr einfach in jede beliebige Polymermatrix eingebracht werden. Für stark hydrophobe Matrizen müssen die externen  $\text{Na}^+$ -Ionen gegen geeignete organische Kationen ausgetauscht werden. Als Beweis für die prinzipielle Machbarkeit wurde ein Nanokompositfilm mit 50 Gew.-% anorganischem Feststoffgehalt mittels Rakeln einer wässriger Suspension von delaminierten Doppelschichten in Polyvinylalkohol (PVOH) hergestellt. Im SAXS-Streubild ist eine stark anisotrope Struktur zu erkennen, die eine effiziente Texturierung auch in der Polymermatrix nahelegt (Abbildung S11). In TEM- und REM-Aufnahmen eines Querschnitts des Nanokompositfilms sind eine schichtförmige Struktur und einzelne Doppelschichten zu erkennen (Abbildung S12 und S13). Die gute Textur wird ferner durch eine signifikante Verbesserung der  $\text{O}_2$ -Gasbar-

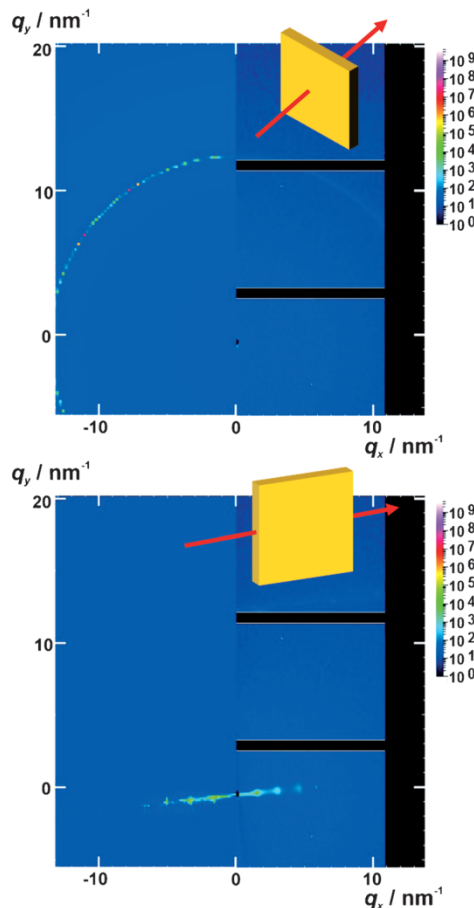


**Abbildung 4.** Gemessene (rechts) und berechnete (links) zweidimensionale SAXS-Streubilder eines texturierten Films von eingetrockneten Doppelschichten in Transmissions- (oben) und Parallelgeometrie (unten).

riere belegt: Die  $O_2$ -Transmissionsrate des Nanokompositfilms ist um einen Faktor 4 kleiner als die des ungefüllten PVOH-Films (Tabelle S1). In der thermischen Analyse an Luft wurde eine Stabilisierung des eingekapselten Farbstoffs im Vergleich zum Farbstoffbromidsalz von  $100^\circ\text{C}$  festgestellt (Abbildung S14). Für den Nanokompositfilm steigt die Zersetzungstemperatur gegenüber dem PVOH-Film um ca.  $30^\circ\text{C}$  an (Abbildung S15).

Wie bereits in den Veränderungen des UV/Vis-Spektrums deutlich wurde – und kürzlich für einen Schichtsilicatkristall mit  $[\text{Ru}(\text{bpy})_3]^{2+}$  gezeigt wurde –<sup>[7]</sup> führt die Oberflächenrauhigkeit der Silicatschichten zu einer Ausrichtung der eingelagerten Moleküle. Daher ist in gut texturierten Filmen von getrockneten Doppelschichten eine optische Anisotropie bezüglich der Absorption und Emission von polarisiertem Licht zu erwarten.<sup>[4,12]</sup>

x- und y-polarisierte UV/Vis-Absorptionsspektren der texturierten Filme aus getrockneten Doppelschichten und

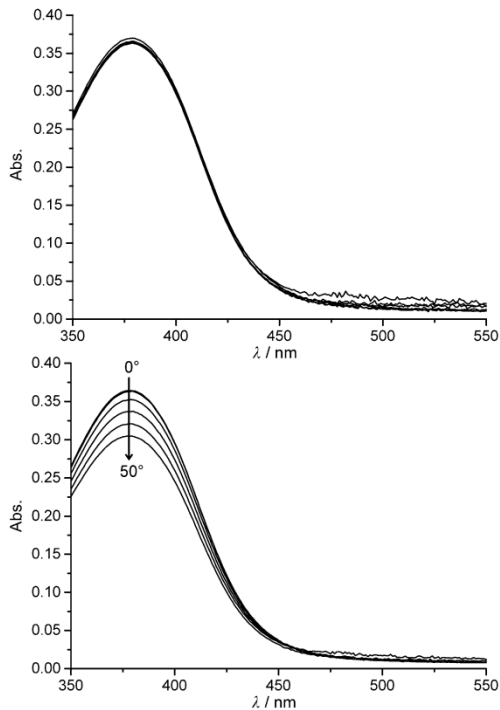


**Abbildung 5.** Korrigierte y- (oben) und x-polarisierte (unten) Absorptionspektren eines texturierten Films aus getrockneten Doppelschichten. Beide Reihen an Spektren wurden für unterschiedliche  $\delta$ -Winkel durch Drehung des Filmes entlang der y-Achse in  $10^\circ$ -Schritten (Pfeilrichtung) erhalten. Die bei den x-polarisierten Spektren auftretende Änderung beweist die Ausrichtung der eingekapselten Farbstoffe.

dem Nanokompositfilm sind in Abbildung 5 und Abbildung S17 gezeigt. Die y-polarisierten UV/Vis-Spektren zeigen keine Änderung mit ansteigendem  $\delta$ -Winkel, was auf eine statisch-isotrope Orientierung der Übergangsmomente innerhalb der Filmebene ( $xy$ -Ebene) hindeutet. Bei den x-polarisierten UV/Vis-Spektren tritt dagegen eine lineare Verringerung der Absorption mit zunehmendem  $\delta$ -Winkel auf. Diese optische Anisotropie wird durch eine Ausordnung der Übergangsmomente entlang der z-Richtung hervorgerufen (vgl. Abbildung S18 und weitere Hintergrundinformationen). Ähnliche Ergebnisse wurden für den Nanokompositfilm erhalten (Abbildung S19).

Zusammenfassend lässt sich festhalten, dass ein allgemeines Verfahren zur Synthese von schichtförmigen Nano-hybridmaterialien vorgestellt wurde, bei dem ein funktionales organisches Kation zwischen zwei transparenten, 1 nm dünne Silicatschichten eingekapselt wird. Die Verkapselung ermöglicht die Dispergierung von hydrophoben organischen Verbindungen in wässrigen Medien, was sich als vorteilhaft für medizinische Anwendungen, z.B. in der photodynamischen Therapie oder der gezielten Wirkstofffreisetzung herausstellen könnte. Zusätzlich wird durch die strukturimmameante Anisotropie des Schichtsilicats und der in Folge definierten Orientierung des eingelagerten Gastmoleküls die

Herstellung von polymerbasierten Nanobeschichtungen mit anisotropen physikalischen Eigenschaften möglich. Unser Konzept sollte sich auf andere quellfähige anorganische Schichtmaterialien, wie beispielsweise Titanate<sup>[13]</sup> und Niobate<sup>[14]</sup> übertragen lassen, soweit eine zur Bildung der geordneten Wechsellegerung notwendige, absolut homogene Ladungsdichte vorliegt.

**Stichwörter:** Delaminierung · Organisch-anorganische Nanokomposite · Schichtförmige Materialien · Verkapselung · Wirtverbindungen

**Zitierweise:** *Angew. Chem. Int. Ed.* **2015**, *54*, 4963–4967  
*Angew. Chem.* **2015**, *127*, 5047–5051

- [1] Y. Chen, H. R. Chen, J. L. Shi, *Adv. Mater.* **2013**, *25*, 3144–3176.
- [2] L. Li, L. Harnau, S. Rosenfeldt, M. Ballauff, *Phys. Rev. E* **2005**, *72*, 051504.
- [3] S. Takagi, T. Shimada, Y. Ishida, T. Fujimura, D. Masui, H. Tachibana, M. Eguchi, H. Inoue, *Langmuir* **2013**, *29*, 2108–2119.
- [4] V. Martínez Martínez, F. L. Arbeloa, J. B. Prieto, I. L. Arbeloa, *Chem. Mater.* **2005**, *17*, 4134–4141.

- [5] O. Guskova, C. Schünemann, K. J. Eichhorn, K. Walzer, M. Levichkova, S. Grundmann, J. U. Sommer, *J. Phys. Chem. C* **2013**, *117*, 17285–17293.
- [6] M. A. Niño, I. A. Kowalik, F. J. Luque, D. Arvanitis, R. Miranda, J. J. de Miguel, *Adv. Mater.* **2014**, *26*, 7474–7479.
- [7] D. A. Kunz, M. J. Leitl, L. Schade, J. Schmid, B. Bojer, U. T. Schwarz, G. A. Ozin, H. Yersin, J. Breu, *Small* **2015**, *11*, 792–796.
- [8] M. Stöter, B. Biersack, N. Reimer, M. Herling, N. Stock, R. Schobert, J. Breu, *Chem. Mater.* **2014**, *26*, 5412–5419.
- [9] M. Stöter, D. A. Kunz, M. Schmidt, D. Hirsemann, H. Kalo, B. Putz, J. Senker, J. Breu, *Langmuir* **2013**, *29*, 1280–1285.
- [10] H. Kalo, W. Milius, J. Breu, *RSC Adv.* **2012**, *2*, 8452–8459.
- [11] L. F. M. Ismail, *J. Lumin.* **2012**, *132*, 2512–2520.
- [12] V. Martínez, S. Salleres, J. Banuelos, F. L. Arbeloa, *J. Fluoresc.* **2006**, *16*, 233–240.
- [13] F. Geng, R. Ma, A. Nakamura, K. Akatsuka, Y. Ebina, Y. Yamauchi, N. Miyamoto, Y. Tateyama, T. Sasaki, *Nat. Commun.* **2013**, *4*, 1632.
- [14] M. M. Fang, C. H. Kim, G. B. Saupe, H. N. Kim, C. C. Waraksa, T. Miwa, A. Fujishima, T. E. Mallouk, *Chem. Mater.* **1999**, *11*, 1526–1532.

Eingegangen am 17. November 2014  
 Online veröffentlicht am 20. Februar 2015

### 5.3.3 Supporting information



### Supporting Information

#### **Encapsulation of Functional Organic Compounds in Nanoglass for Optically Anisotropic Coatings\*\***

*Matthias Stöter, Bernhard Biersack, Sabine Rosenfeldt, Markus J. Leitl, Hussein Kalo, Rainer Schobert, Hartmut Yersin, Geoffrey A. Ozin, Stephan Förster, and Josef Breu\**

anie\_201411137\_sm\_miscellaneous\_information.pdf

## Supporting Information

1. Experimental Section
2. UV-VIS measurement with polarized light

### 1. Experimental Section

#### Materials and methods

##### Synthesis of Na-hec

Na<sub>0.5</sub>-fluorohectorite with the composition [Na<sub>0.5</sub>]<sup>inter</sup>[Mg<sub>2.5</sub>Li<sub>0.5</sub>]<sup>oct</sup>[Si<sub>4</sub>]<sup>tet</sup>O<sub>10</sub>F<sub>2</sub> (Na-hec) was synthesized by melt synthesis in a closed molybdenum crucible according to a published procedure.<sup>[1]</sup> After synthesis the material was annealed for 6 weeks at 1045°C to improve intracrystalline reactivity, charge homogeneity and phase purity as recently described.<sup>[2]</sup>

##### Synthesis of N-hexadecyl-4-(3,4,5-trimethoxystyryl)-pyridinium bromide (dye)

N-hexadecyl-4-(3,4,5-trimethoxystyryl)-pyridinium bromide was synthesized according to the recently published procedure.<sup>[3]</sup>

##### Powder X-ray diffraction (PXRD)

Diffractograms were recorded in Bragg-Brentano-geometry on a Panalytical XPERT-PRO diffractometer. The textured film of restacked double stacks was prepared by drying a few drops of the suspension on microscope slides (Menzel Gläser). In order to remove adsorbed water, the glass slides were dried at 120 °C for 12 h (0 % r.h.).

##### SAXS

The small angle x-ray scattering (SAXS) samples were prepared at ambient conditions. All SAXS data were measured using the small-angle x-ray system “Double Ganesha AIR” (SAXSLAB, Denmark). The X-ray source of this laboratory-based system is a rotating anode (copper, MicoMax 007HF, Rigaku Corporation, Japan) providing a micro-focused beam. The data are recorded by a position sensitive detector (PILATUS 300K, Dectris). To cover the range of scattering vectors between 0.004-2.0 Å<sup>-1</sup> different detector positions were used. The measurements of the suspensions were done in 1 mm glass capillaries (Hilgenberg, code 4007610, Germany) at room temperature. As substrate for the films 15 µm thick mica crystals were used (provided by SAXSLAB, Denmark). The circularly averaged data were normalized to incident beam, sample thickness and measurement time before subtraction of the solvent. The data analysis was performed mainly with the software Scatter (version 2.5) which allows

the 2-dimensional modeling of scattering intensities with respect to the layer distance (d), of mean deviations from the ideal positions (displacement), and of mean sizes of crystal domains (coherence length in azimuthal and radial direction).<sup>[4]</sup> Further calculations were done using the software SASfit (version 0.94.1) written by J. Kohlbrecher and I. Bressler

### SAXS Modeling

The SAXS intensities were described applying a model of stacked hamburgers. For computational reasons (restrictions of the software) a platelet diameter of 600 nm was used. Please note, that there is no difference in SAXS patterns for  $R > 300$  nm. For the calculations of the SAXS patterns of the suspensions and of the ordered interstratified heterostructured powder a thickness of  $l = 0.8$  nm is used for the silicate layer which was experimentally deduced from the intensity minima of the form factor oscillation of SAXS patterns of the completely delaminated Na-hec. This value is in good agreement with the platelet thickness derived by SAXS measurements of delaminated natural montmorillonites.<sup>[5]</sup> The experimental platelet thickness of 0.8 nm is slightly higher than the distance between the planes formed by the basal oxygens of the two tetrahedral sheets (0.66 nm<sup>[6]</sup>) indicating a contribution to the scattering by sodium ions in the Helmholtz layer.

To account for a limited hydration of the dye interlayer in aqueous suspension and for some flexibility of the organic interlayer a small variation of the organic dye interlayer height (h) of  $1.8 \pm 0.3$  nm is applied. For the SAXS pattern of the ordered interstratified heterostructured powder a faultless stacking of 30 double stacks with a rigid dye gallery height of  $l = 1.4$  nm was applied.

The texture of the films was evaluated using the results of the modeling of the 2-dimensional data. The angular spread  $2\phi_s$  is calculated by the coherence length in azimuthal direction (azi) and the  $d$ -spacing according to equitation 1:<sup>[4]</sup>

$$azi = \frac{2d}{\tan(2\phi_s)} \quad (1)$$

### AFM

Atomic Force Microscopy was done by using a MFP3DTM Atomic Force Microscope (Asylum Research, Santa Barbara, California) equipped with silicon cantilevers (silicon tip, type NSC15/AIBS, Rmash, Tallinn, Estonia). The samples were prepared by slow evaporation of a few drops of a diluted suspension (0.01 g/L) on a silicon wafer under ambient conditions.

### Photoluminescence

For absolute measurements of photoluminescence quantum yields at ambient temperature, a Hamamatsu Photonics (C9920-02) system was used.

### Film preparation

Films for UV-VIS measurements were prepared on piranha treated glass slides by doctor blading (50.8 µm film applicator BYK, Altana Group). All films were dried at 120°C for 12 h. Textured films of delaminated and restacked double stacks were prepared applying a 2 wt% suspension, while for the nanocomposite film a 2.7 wt% suspension of polyvinyl alcohol (PVOH) (Mowiol® 20-98, SIGMA-ALDRICH,  $M_w = 125000$  g/mol) and clay in a 1:1 ratio was used.

Films for the barrier measurements of nanocomposite and PVOH were prepared with the same suspensions on a PET-foil (100 µm) using an automatic film applicator (ZAA 2300 with ZUA 2000 universal applicator, Zehntner GmbH) with a gap height of 100 µm and a speed of 18 mm/s. These casted films were stored at ambient conditions for 1 h and than dried at 60 °C for 24h prior to the barrier measurement.

### UV-VIS measurements

UV-VIS spectra of the powder samples were measured with a Varian Cary 300 spectrophotometer equipped with an integrating sphere (Labsphere DRA-CA-30I).

UV-VIS measurements of the films with polarised light were performed with an Agilent Cary 5. The coated glass slides were mounted on a goniometer (Brewster film holder, Harrick). Polarized spectra were obtained using a Glan-Taylor polarizer (PGT-S1V, Harrick) before and a depolarizer (DPS-R4V, Harrick) behind the sample (Figure S16).

### Streaming potential

The streaming potential was measured with a particle charge analyzer (Stabisizer®, Particle Metrix GmbH).

### Gas barrier properties

The oxygen transmission rate of the PET supported nanocomposite and PVOH film (100 µm) was determined with a Mocon OX-TRAN® Model 2/21 permeation testing instrument at 50% RH at 23°C.

### Scanning electron microscopy (SEM)

SEM images were taken with a LEO 1530 FE-SEM at an operating voltage of 3 kV.

**Transmission electron microscopy (TEM)**

TEM images were taken with a LEO 922 A EF-TEM at an operating voltage of 200 kV.

**Thermal gravimetric analysis (TGA)**

TGA was performed with a NETZSCH STA 449 C using synthetic air and a heating rate of 5 K/min.



**Figure S1.** 55 mg dried ordered interstratified heterostructured powder (left) and 55 mg of freeze dried gel (right).

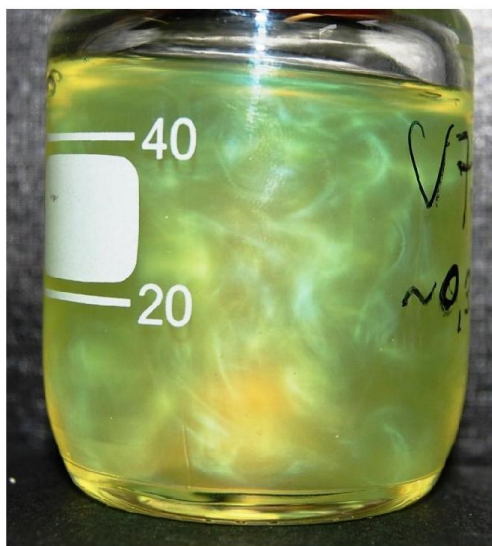


**Figure S2.** 0.3 wt% suspension in water. The “Schlieren” texture upon shearing illustrates good dispersibility in water and implies liquid crystalline behavior. While at this dilution the material is swollen to a degree where the double stacks are separated far enough ( $> 60$  nm) to realize an apparently isotropic platelet orientation, the lamellar flow generated for instance by simple stirring triggers scattering in the visible region even for such highly diluted suspensions. This observation implies that the double stacks are in a lyotropic liquid crystalline state and not yet capable of free rotation. The lateral extension of the platelets is much larger than the distance between them hampering free rotation.



**Figure S3.** When drying the diluted suspension of double stacks on a flat substrate a film is obtained that shows a good wettability for  $\text{H}_2\text{O}$ , very much comparable to the wettability of the pristine Na-hec, indicating a strongly hydrophilic film surface due to the presence of sodium cations at the platelet surface.

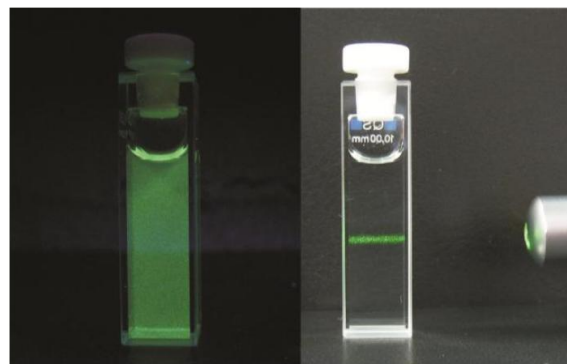


**Figure S4.** Diluted aqueous suspension (0.04 mg/ml) under UV irradiation of  $\lambda = 366 \text{ nm}$  (left) and under daylight (right). Well dispersed double stacks are visualized by the Tyndall-effect using a green light laser pointer (right).

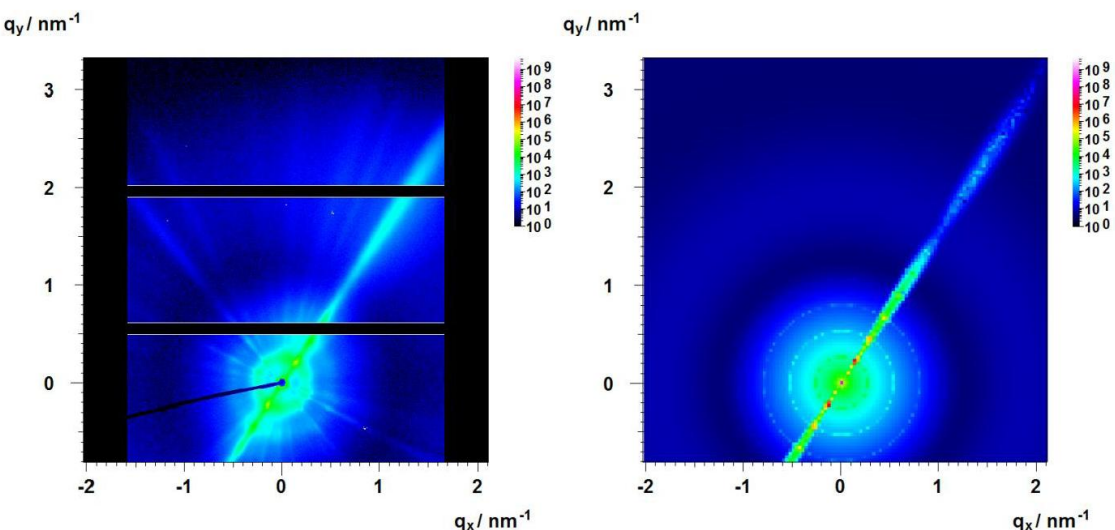


**Figure S5.** Representative 2-dimensional SAXS pattern of a 20 wt% suspension (left). The pattern illustrates the presence of oriented domains of double stacks with positional correlation. Calculated 2-dimensional SAXS pattern (right) based on the model of interacting “hamburgers” with a distance of  $d = 23.5 \text{ nm}$  and a crystalline domain size of 700 nm in radial and 100 nm in azimuthal direction with deviations of 2 nm. For computational reasons only one crystal with a tilt of  $57^\circ$  was calculated. The rest of the oriented domains were considered as isotropic background ( $I_{max} = 004$ ).

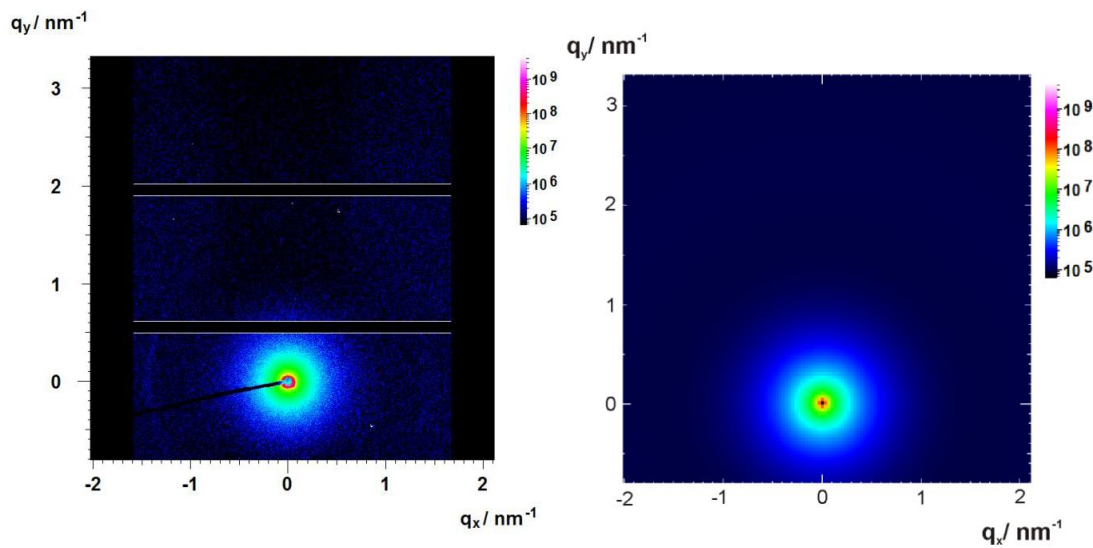


**Figure S6.** Representative 2-dimensional SAXS pattern of a 2.5 wt% delaminated suspension of double stacks (left). The isotropic pattern illustrates an apparently isotropic orientation of double stacks. Calculated (right) 2-dimensional SAXS pattern based on non-correlated double stacks.

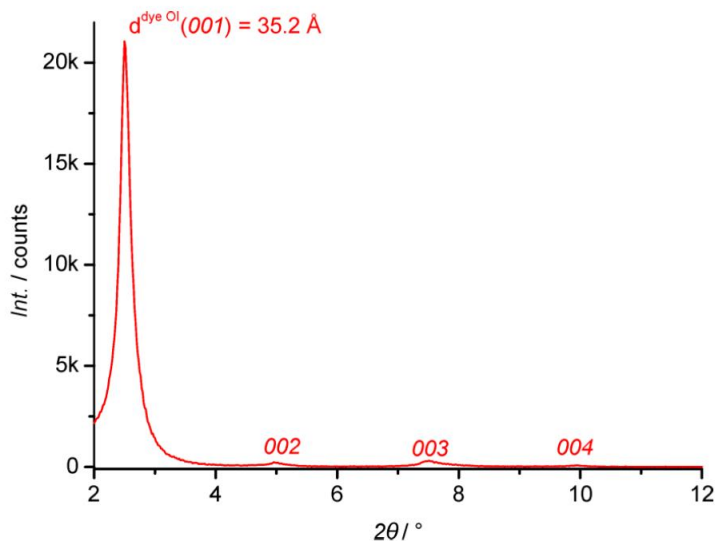


**Figure S7.** PXRD patterns of a film of restacked double stacks dried at 0% r.h. shows a superstructure at about  $2.5^\circ$   $2\theta$  with a narrow full width of half maximum of  $0.2^\circ$  and a low coefficient of variation<sup>[7]</sup> of 0.4%. Both values indicate a high ordering of alternating sodium and dye interlayers upon restacking the double stacks.

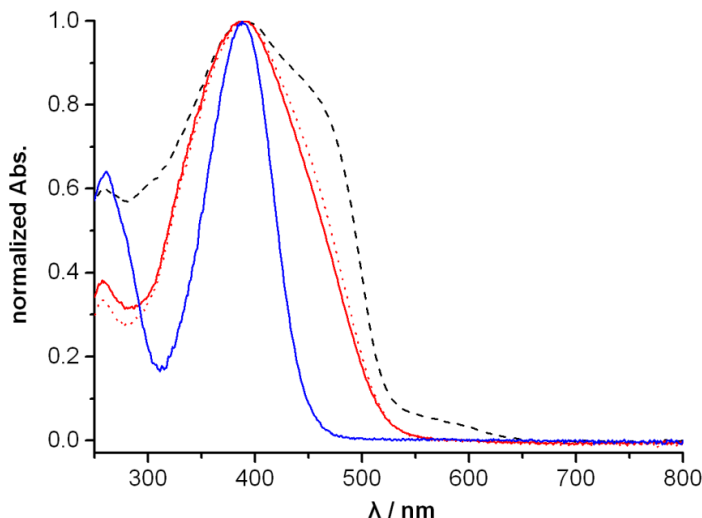


**Figure S8.** UV-VIS absorption spectra of the bromide salt of dye (black broken line), of the ordered interstratified heterostructured powder (red dotted line), and of a freeze dried delaminated suspension of double stacks (red solid line). An UV-VIS spectrum of an ethanolic solution of the bromide salt ( $10^{-4}$  M) is shown for comparison (blue solid line).

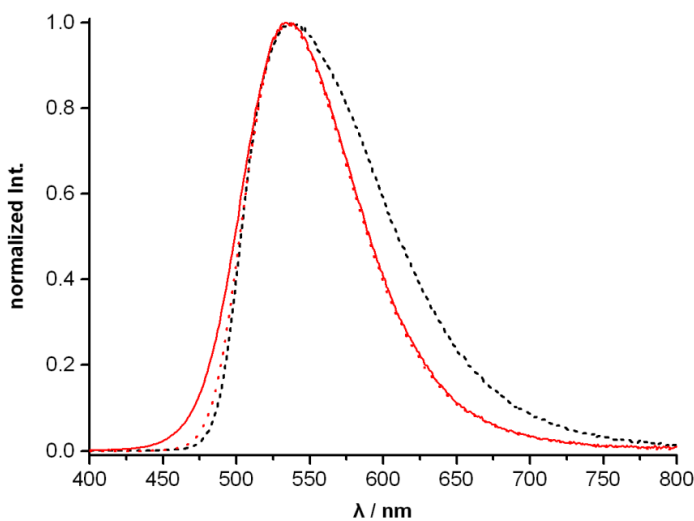


**Figure S9.** Emission spectra obtained after irradiation at 350 nm of the bromide salt of dye (black broken line), of the ordered interstratified heterostructured powder (red dotted line) and of a freeze dried delaminated suspension of double stacks (red solid line).

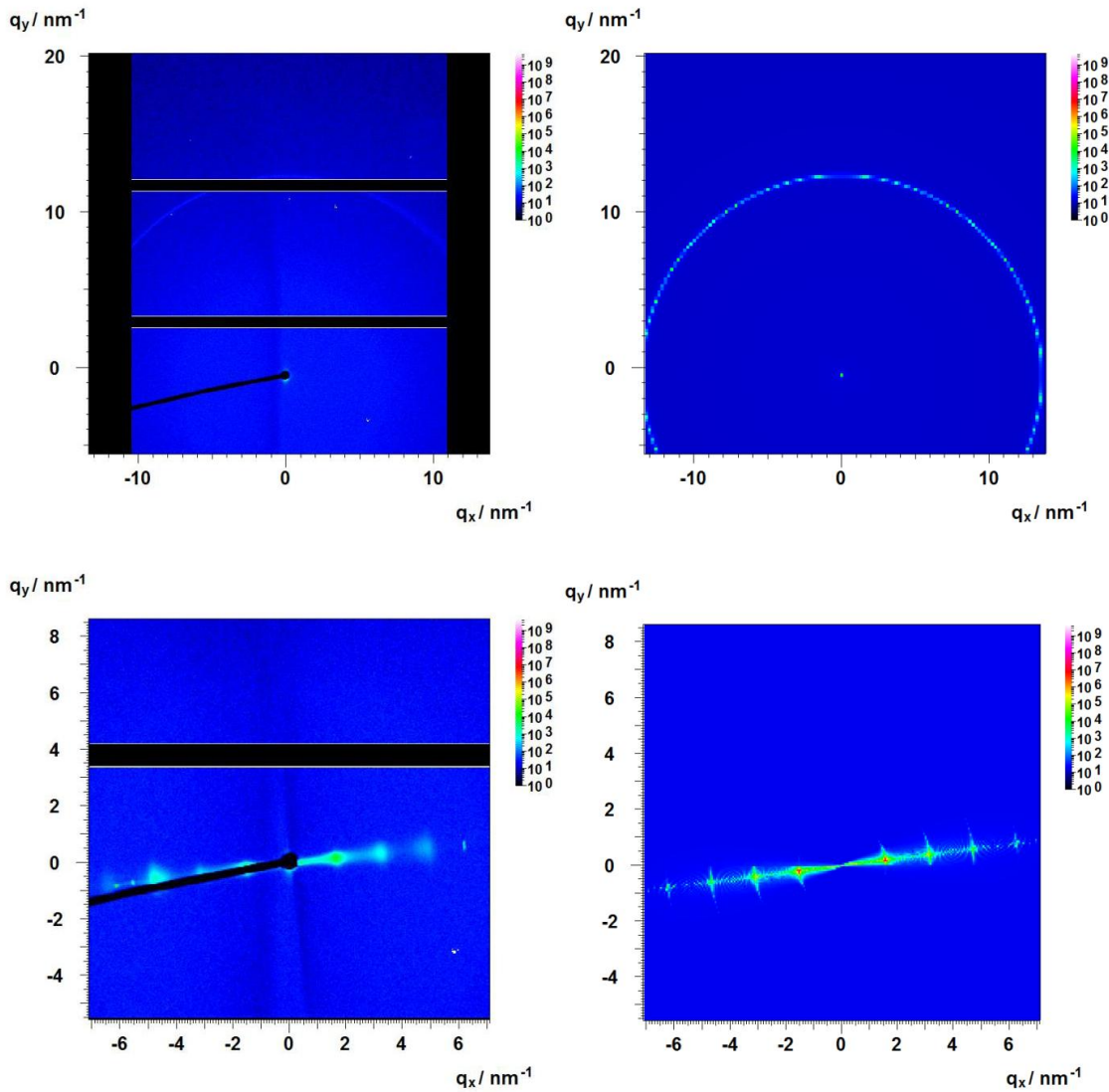


**Figure S10.** Comparison of the 2-dimensional-SAXS pattern of a measured textured film of delaminated and restacked double stacks (left) with the calculated pattern (right). The continuous ring of the  $hk$ -band observed in transmission geometry (top) is calculated as a Bragg peak with a spacing of 0.5 nm and a displacement of 0.05 nm. The  $00l$  series observed in parallel geometry (bottom) is calculated using double stacks with a diameter of 600 nm and a distance of  $d = 4$  nm with a deviation of 0.05 nm. The radial instrumental resolution was 400 nm with an azimuthal angular resolution of  $\sim 2^\circ$ .<sup>[4]</sup>

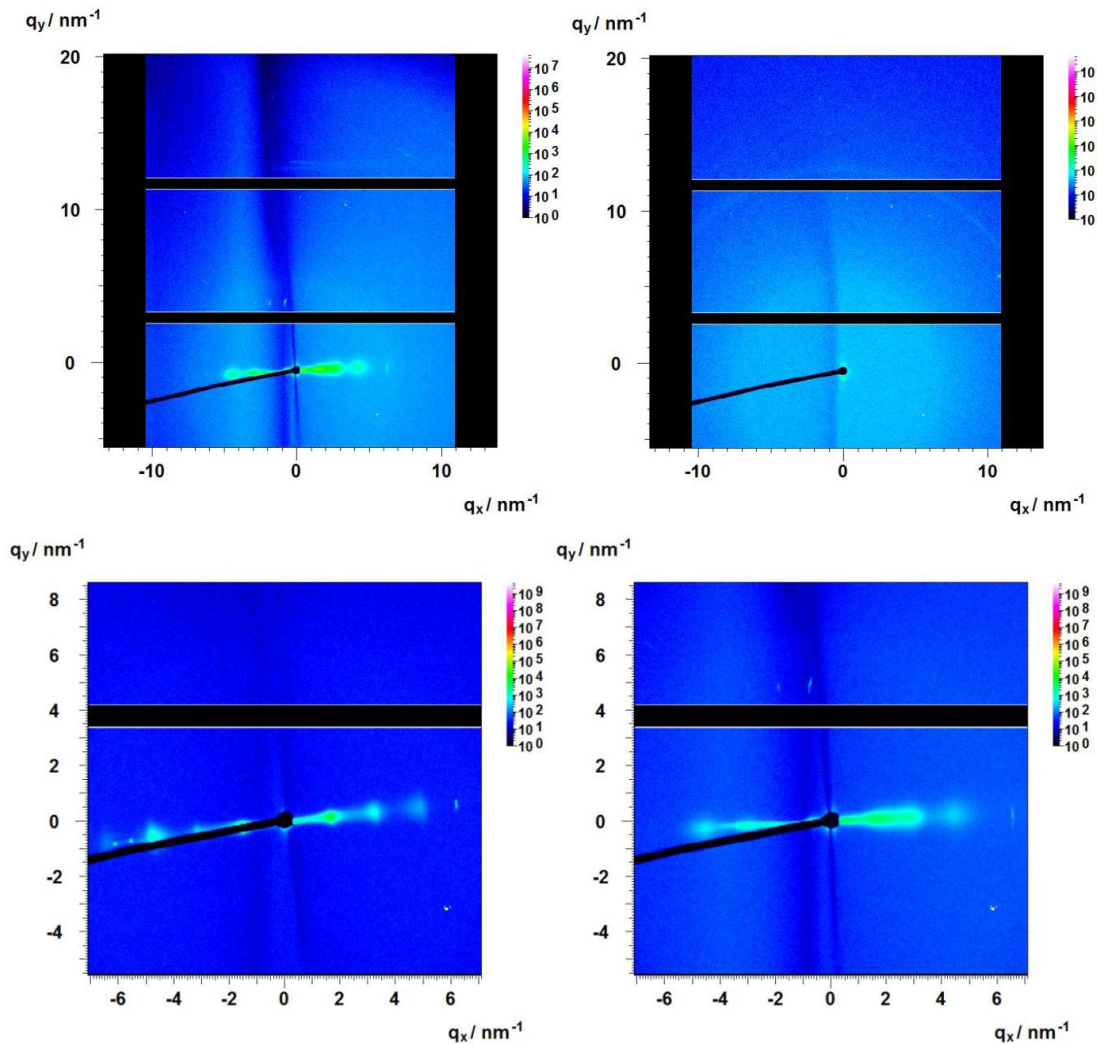


**Figure S11.** 2-dimensional-SAXS pattern measured in parallel geometry (top left) and in transmission geometry (top right) of a solution casted nanocomposite film. Zooms of the textured film of delaminated and restacked double stacks (bottom left) and the nanocomposite film (bottom right) are shown for comparison.

**Table S1 oxygen transmission rate (OTR) measured at 50% RH**

Film	inorganic content [wt%]	film thickness [μm]	OTR [cc*m <sup>-2</sup> *day <sup>-1</sup> ]
nanocomposite	50	≈1	0.48
PVOH	0	≈1	2.11

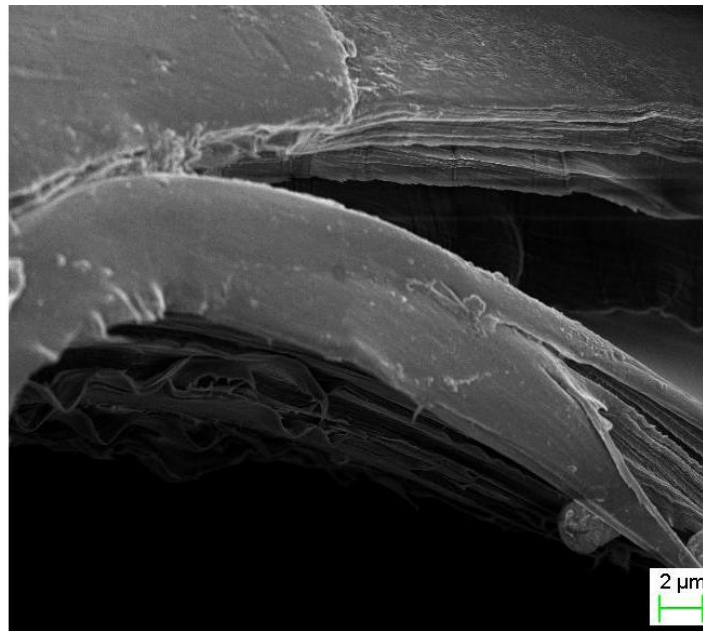


**Figure S12.** SEM image of a freeze fractured nanocomposite film illustrating the texture and the parallel arrangement of double stacks.

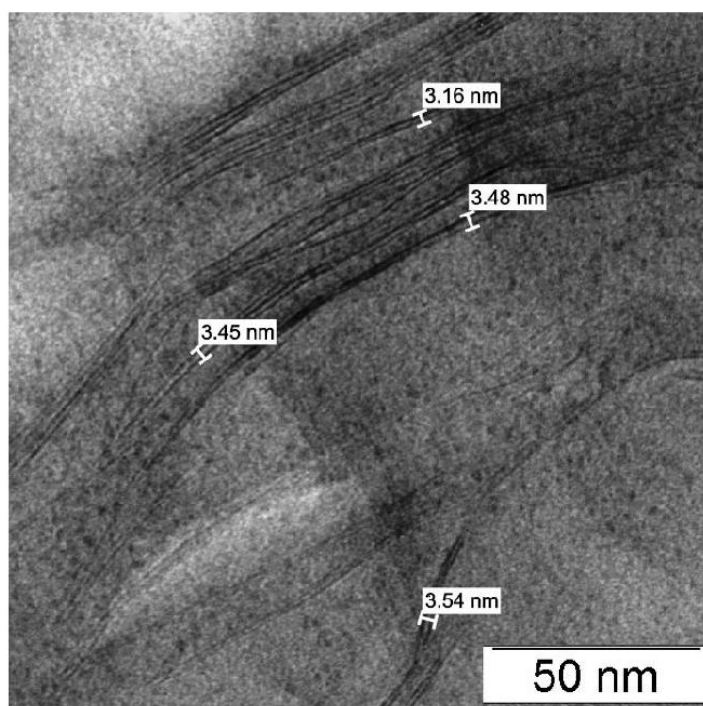


**Figure S13.** TEM images of a cross section of the nanocomposite film. Fracture occurs at the interface between textured double stacks and PVOH matrix during microtome sample preparation. Individual double stacks of about 3.5 nm separated by polymer can be identified.

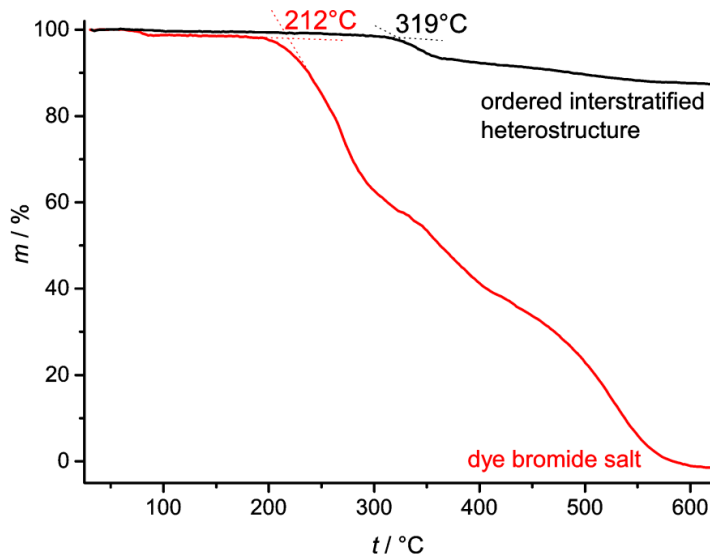


**Figure S14.** TGA results using synthetic air of the dye bromide salt (red line) and the ordered interstratified heterostructured powder (black line). For the intercalated dye the onset temperature for the dye decomposition is about 100°C higher.

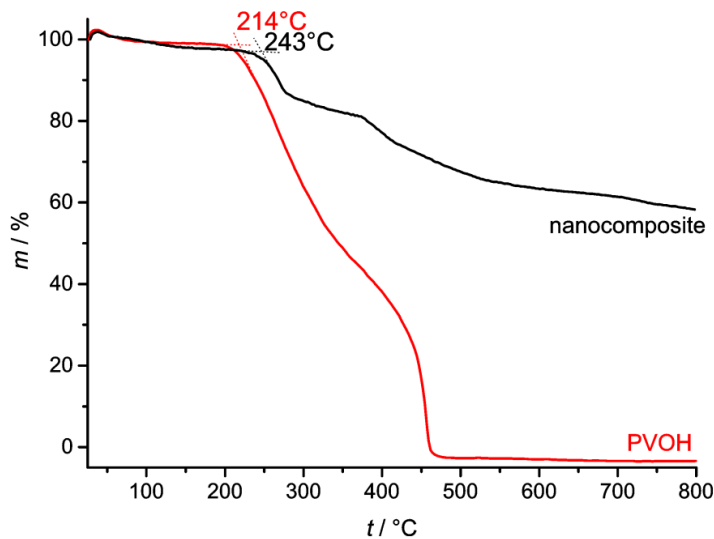


**Figure S15.** TGA results using synthetic air of a casted PVOH film (red line) and the nanocomposite film (black line). For the nanocomposite the onset temperature for the PVOH decomposition is appr. 30°C higher.

## 2. UV-VIS measurement with polarized light

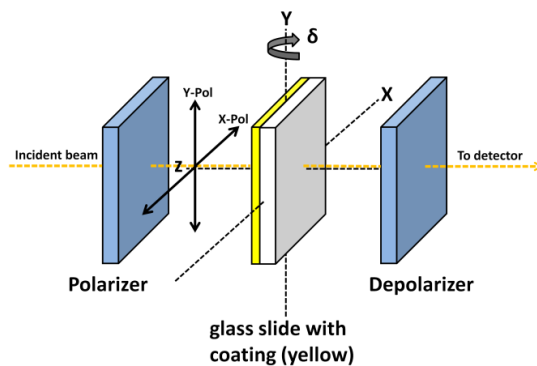


**Figure S16.** Set up for UV-VIS measurement with x- and y-polarized light. The textured coating (yellow) is facing towards the incident polarized beam.

The textured film of delaminated and restacked double stacks and the nanocomposite film were rotated around its y-axis in a range of  $\delta = 0^\circ\text{--}50^\circ$  (Figure S16). A depolarizer is used to minimize variations in beam intensity caused by the intrinsic polarization of the spectrophotometer.<sup>[8]</sup> UV-VIS spectra were baseline-corrected with spectra obtained for textured films of delaminated and restacked double stacks and nanocomposite films not loaded with dye. As described in the literature,<sup>[8]</sup> factors for correcting the spectra for varying path lengths as a function of  $\delta$ -angle were determined by measuring an isotropic sample (dye bromide ( $c = 10^{-4}$  M) dissolved in a 1:1-water-ethanol mixture) in a 1 mm quartz cuvette. These factors were then applied to correct the y- and x-polarized absorption spectra.

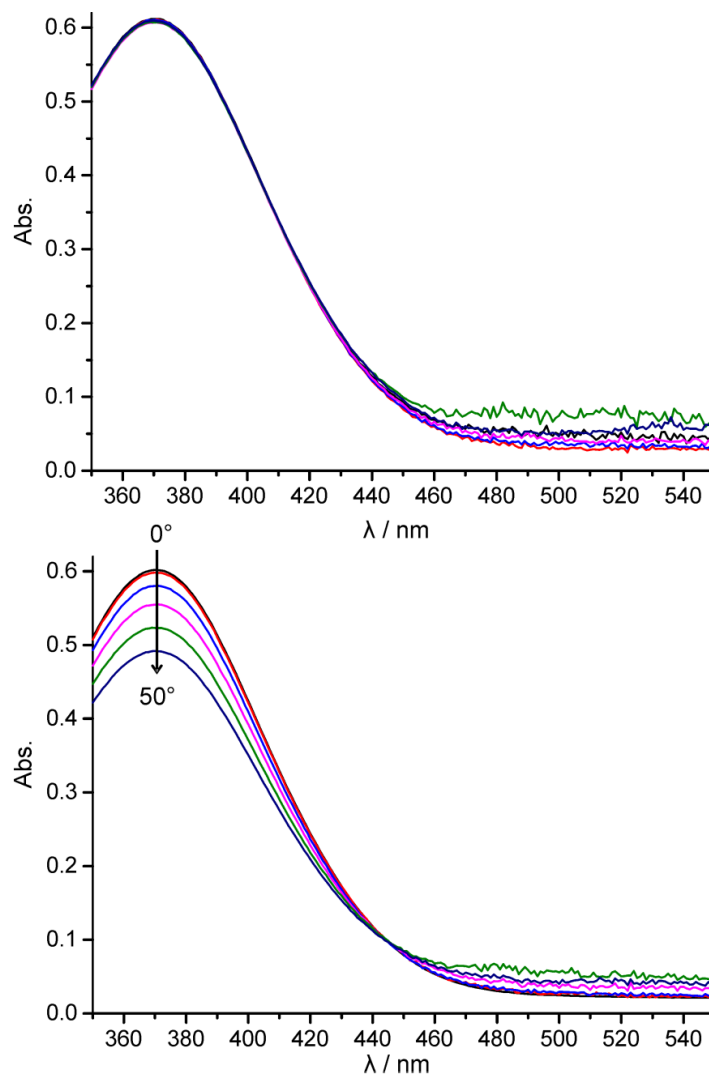


**Figure S17.** Corrected y- (top) and corrected x-polarized (bottom) absorption spectra of the nanocomposite film. Both sets of spectra were obtained at different  $\delta$ -angles by turning the film around its y-axis in  $10^\circ$  steps (arrow)

A plot of the dichroic ratio ( $D_{x/y}$ ), defined as the ratio of the absorption of x- ( $A_x$ ) and y-polarized light ( $A_y$ ) as a function of  $\sin^2 \delta$  yields a linear relationship for both the textured film of delaminated and restacked double stacks and the nanocomposite film (Figure S18 and Figure S19, respectively).

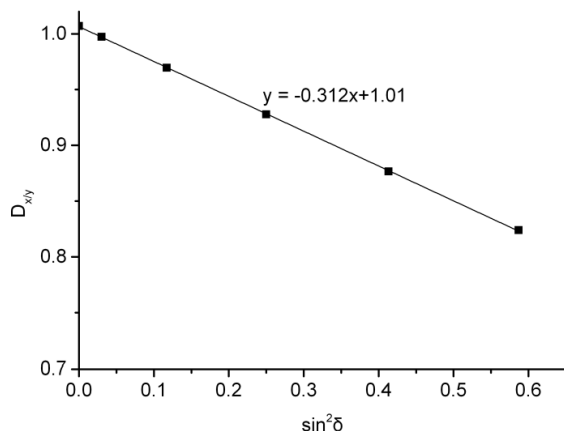


Figure S18. Linear relationship for the textured film of delaminated and restacked double stacks between  $D_{xy}$  measured at the absorption maximum of 378 nm and the  $\sin^2$  of twisting angle  $\delta$ .

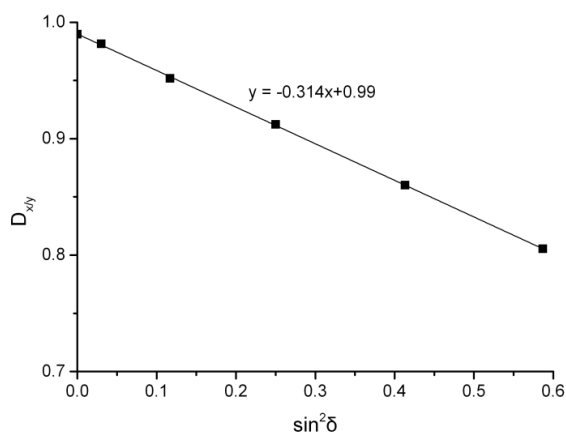


Figure S19. Linear relationship for the nanocomposite film between  $D_{xy}$  measured at the absorption maximum of 370 nm and the  $\sin^2$  of twisting angle  $\delta$ .

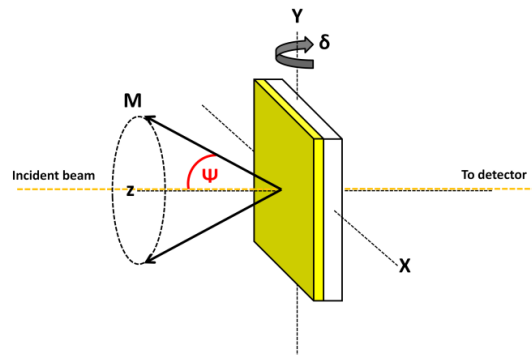


Figure S20. Angle  $\psi$  between the transition moment ( $\vec{M}$ ) and the normal of the film surface.

The angle  $\psi$  between the transition moment ( $\vec{M}$ ) and the normal of the film surface (Figure S20) was calculated from the slope of the linear regression of Figure S18 and Figure S19 according to equation 1<sup>[8]</sup>

$$D_{x,y} = \frac{A_x}{A_y} = 1 + \frac{2-3\sin^2\psi}{\sin^2\psi} \sin^2\delta \quad [1]$$

$\psi$  is calculated to be  $60^\circ$  for both the textured film of delaminated and restacked double stacks and the nanocomposite film, suggesting that the orientation of dye achieved by the preferred orientation is equally good.

#### References

- [1] J. Breu, W. Seidl, A. J. Stoll, K. G. Lange, T. U. Probst, *Chem. Mater.* **2001**, *13*, 4213-4220.
- [2] M. Stöter, D. A. Kunz, M. Schmidt, D. Hirsemann, H. Kalo, B. Putz, J. Senker, J. Breu, *Langmuir* **2013**, *29*, 1280-1285.
- [3] M. Stöter, B. Biersack, N. Reimer, M. Herling, N. Stock, R. Schobert, J. Breu, *Chem. Mater.* **2014**, *26*, 5412-5419.
- [4] S. Förster, S. Fischer, K. Zielske, C. Schellbach, M. Sztucki, P. Lindner, J. Perlich, *Adv. Colloid Interface Sci* **2011**, *163*, 53-83.
- [5] E. Paineau, I. Bihannic, C. Baravian, A. M. Philippe, P. Davidson, P. Levitz, S. S. Funari, C. Rochas, L. J. Michot, *Langmuir* **2011**, *27*, 5562-5573.
- [6] J. Breu, W. Seidl, A. Stoll, *Z. Anorg. Allg. Chem.* **2003**, *629*, 503-515.
- [7] S. W. Bailey, *Am. Mineral.* **1982**, *67*, 394-398.
- [8] V. M. Martinez, F. L. Arbeloa, J. B. Prieto, I. L. Arbeloa, *Chem. Mater.* **2005**, *17*, 4134-4141.

## 5.4 Mechanisch verstärkte Doppelschichten zur Synthese von Janus-Plättchen

Matthias Stöter<sup>[a]</sup>, Sebastian Gödrich<sup>[b]</sup>, Patrick Feicht<sup>[a]</sup>, Sabine Rosenfeldt<sup>[c]</sup>, Herbert Thurn<sup>[d]</sup>, Jens W. Neubauer<sup>[e]</sup>, Maximilian Seuss<sup>[e]</sup>, Peter Lindner<sup>[f]</sup>, Hussein Kalo<sup>[a]</sup>, Michael Möller<sup>[a]</sup>, Andreas Fery<sup>[e, g]</sup>, Stephan Förster<sup>[c]</sup>, Georg Papastavrou<sup>[b]</sup>, Josef Breu<sup>[a]</sup>

### Controlled Exfoliation of Layered Silicate Heterostructures into Bilayers and Their Conversion to Giant Janus Platelets

Angewandte Chemie International **2016**, DOI: 10.1002/anie.201601611

Angewandte Chemie, **2016**, DOI: 10.1002/ange.201601611

Reprinted with permission. Copyright 2016, Wiley.

Impact Factor (2014) Angewandte Chemie International: 11.261

<sup>[a]</sup> Lehrstuhl für Anorganische Chemie I, Universität Bayreuth, D-95440 Bayreuth, Germany

<sup>[b]</sup> Lehrstuhl für Physikalische Chemie II, Universität Bayreuth, D-95440 Bayreuth, Germany

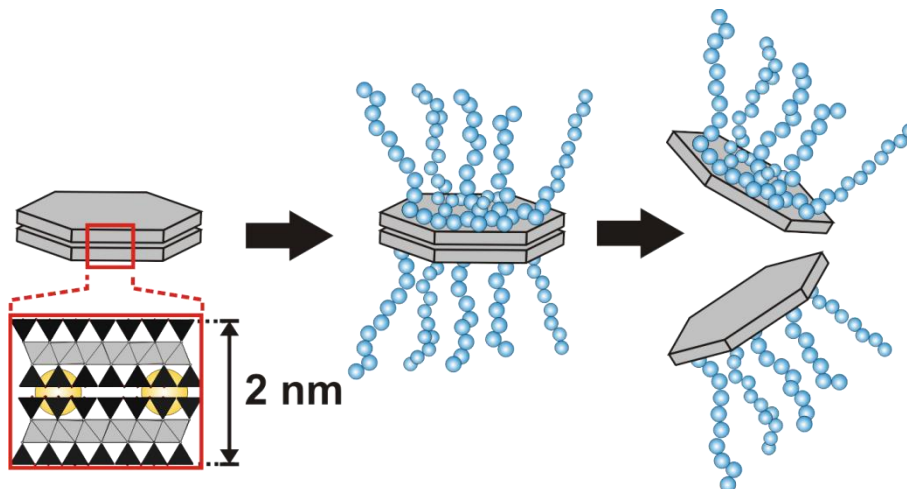
<sup>[c]</sup> Lehrstuhl für Physikalische Chemie I, Universität Bayreuth, 95440 Bayreuth (Germany)

<sup>[d]</sup> Computing Center, University of Bayreuth, D-95440 Bayreuth, Germany;

<sup>[e]</sup> Institute for Physical Chemistry and Polymer Physics, Leibniz-Institut für Polymerforschung Dresden e.V., D-01069 Dresden, Germany

<sup>[f]</sup> Institut Laue-Langevin, DS LSS, F-38042 Grenoble 9, France.

<sup>[g]</sup> Chair of Physical Chemistry of Polymeric Materials, Technical University Dresden, D-01069 Dresden, Germany



#### Darstellung des Eigenanteils:

Die Idee zur Verwendung von geordneten Wechsellagerungen in Schichtsilikaten zur Janus-Modifikationen wurde von Herrn Prof. Josef Breu und Michael Möller vorgeschlagen. Das hier vorgestellte Konzept zur kontrollierten Spaltung von modifizierten Doppelschichten wurde von mir entwickelt. Die Synthese der Doppelschichten sowie die verschiedenen Modifikationen wurden von mir entwickelt und durchgeführt. Die SAXS-

und SANS Messungen und Simulationen wurden in der Physikalischen Chemie I, Universität Bayreuth von Dr. Sabine Rosenfeldt und Herrn Prof. Stephan Förster angefertigt. Das Konzept der Verwendung eines AFM-Tracers wurde von Herrn Prof. Georg Papastavrou und Sebastian Gödrich (Physikalischen Chemie II, Universität Bayreuth) entwickelt. Patrick Feicht fertigte die Wrinkling-Experimente zur Bestimmung der mechanischen Eigenschaften an. Dr. Hussein Kalo führte erste Experimente zur Dispersionsstabilisierung von Hectoriten mit PEI-EO durch.

Verfasst wurde diese Publikation hauptsächlich von Prof. Dr. Josef Breu und mir. Mein Eigenanteil beträgt ca. 65 %.

## 5.4.1 Controlled Exfoliation of Layered Silicate Heterostructures into Bilayers and Their Conversion to Giant Janus Platelets



Hybrid Materials Hot Paper

International Edition: DOI: 10.1002/anie.201601611  
German Edition: DOI: 10.1002/ange.201601611

### Controlled Exfoliation of Layered Silicate Heterostructures into Bilayers and Their Conversion into Giant Janus Platelets

Matthias Stöter, Sebastian Gödrich, Patrick Feicht, Sabine Rosenfeldt, Herbert Thurn, Jens W. Neubauer, Maximilian Seuss, Peter Lindner, Hussein Kalo, Michael Möller, Andreas Fery, Stephan Förster, Georg Papastavrou,\* and Josef Breu\*

**Abstract:** Ordered heterostructures of layered materials where interlayers with different reactivities strictly alternate in stacks offer predetermined slippage planes that provide a precise route for the preparation of bilayer materials. We use this route for the synthesis of a novel type of reinforced layered silicate bilayer that is 15 % stiffer than the corresponding monolayer. Furthermore, we will demonstrate that triggering cleavage of bilayers by osmotic swelling gives access to a generic toolbox for an asymmetrical modification of the two vis-à-vis standing basal planes of monolayers. Only two simple steps applying arbitrary commercial polycations are needed to obtain such Janus-type monolayers. The generic synthesis route will be applicable to many other layered compounds capable of osmotic swelling, rendering this approach interesting for a variety of materials and applications.

**E**xfoliation of layered compounds into two-dimensional nanosheets allows the tuning of phononic,<sup>[1]</sup> electronic,<sup>[2–5]</sup> ferroic,<sup>[6]</sup> electrochemical,<sup>[7]</sup> and mechanical properties.<sup>[8,9]</sup> Modulation of these properties is strongly related to the destruction or limitation of translational symmetry and is thus dependent on accurate control over the number of layers in the stacks.<sup>[10–12]</sup> Mono-, bi-, tri-, and multilayers must con-

sequently be regarded as distinct phases. For example, bilayer phases of graphene and mica have been shown to have interesting electronic band structures.<sup>[4,13,14]</sup>

Various techniques ranging from epitaxial growth to mechanical exfoliation, potentially assisted by surface-active compounds or by rendering the starting material more shear labile by intercalation reactions, have been shown to yield two-dimensional (2D) materials. Established techniques, however, tend to produce broad distributions in the number of layers.<sup>[6,14–16]</sup>

Crystalline heterostructures with 1D-ordered structures along the stacking direction (also referred to as ordered or regularly interstratified compounds) are the thermodynamic equilibrium for many layered compounds intercalated with two different interlayer species that segregate into distinct interlayer spaces.<sup>[17–19]</sup> We recently established a general synthesis for such crystalline heterostructures composed of synthetic layered silicates (Figure 1a).<sup>[19,20]</sup>

Herein, we prepare ordered heterostructures of layered silicates where interlayers with different reactivities strictly alternate in stacks. Such heterostructures offer predetermined slippage planes that provide a precise, scalable, and quantitative preparation route for desired bilayer materials.<sup>[5,21]</sup> The

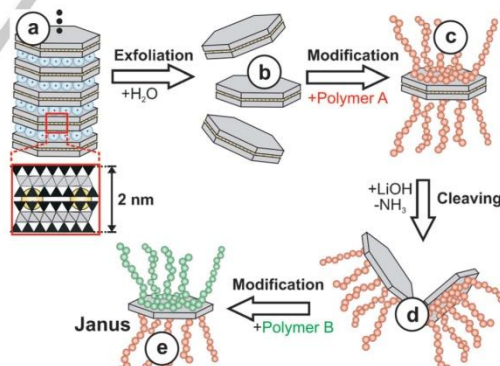


**Figure 1.** Selective swelling of a crystalline heterostructure (a) with  $\text{NH}_4^+$  interlayers (yellow) and hydrated  $\text{Na}^+$  interlayers (blue) induces highly selective exfoliation into bilayers (b). After external modification with a polycation A (red; c), modified bilayers can be cleaved under basic conditions using, for example,  $\text{LiOH}$  (d) while the symmetry is simultaneously broken at this stage. The platelets can be further modified (green) to form Janus-type platelets (e) with differently functionalized surfaces.

- [\*] M. Stöter, P. Feicht, Dr. H. Kalo, Dr. M. Möller, Prof. Dr. J. Breu  
Lehrstuhl für Anorganische Chemie I, University of Bayreuth  
Universitätsstraße 30, 95440 Bayreuth (Germany)  
E-mail: Josef.Breu@uni-bayreuth.de  
S. Gödrich, Prof. Dr. G. Papastavrou  
Lehrstuhl für Physikalische Chemie II, University of Bayreuth  
Universitätsstraße 30, 95440 Bayreuth (Germany)  
E-mail: georg.papastavrou@uni-bayreuth.de  
Dr. S. Rosenfeldt, Prof. Dr. S. Förster  
Lehrstuhl für Physikalische Chemie I, University of Bayreuth  
Universitätsstraße 30, 95440 Bayreuth (Germany)  
H. Thurn  
Computing Center, University of Bayreuth  
Universitätsstraße 30, 95440 Bayreuth (Germany)  
J. W. Neubauer, M. Seuss, Prof. Dr. A. Fery  
Institute for Physical Chemistry and Polymer Physics  
Leibniz-Institut für Polymerforschung Dresden e.V.  
01069 Dresden (Germany)  
Dr. P. Lindner  
Institut Laue-Langevin, DS LSS, 38042 Grenoble 9 (France)  
Prof. Dr. A. Fery  
Chair of Physical Chemistry of Polymeric Materials  
Technical University Dresden, 01069 Dresden (Germany)
- Supporting information for this article can be found under:  
<http://dx.doi.org/10.1002/anie.201601611>.

novel bilayers are significantly stiffer than monolayers, are at the same time easily cleavable and can be directly converted into Janus platelets.

Synthetic sodium fluorohectorite ( $\text{Na}_{0.5}^{\text{inter}}[\text{Mg}_{2.5}\text{Li}_{0.5}]^{\text{ext}}(\text{Si}_4)^{\text{tet}}\text{O}_{10}\text{F}_2$ ) with typical lateral dimensions in the range of several micrometers (median ca. 20  $\mu\text{m}$ )<sup>[24]</sup> is partially ion-exchanged with ammonium cations ( $\text{NH}_4^+$ ) to yield a crystalline heterostructure (Supporting Information, Figure S1).

When  $\text{NH}_4^+$  and  $\text{Na}^+$  are chosen as the segregated interlayer cation pair, alternating  $\text{NH}_4^+$  interlayers are formed, which do not hydrate, while adjacent  $\text{Na}^+$  interlayers readily hydrate (Supporting Information, Figures S1 and S2).

In an intercalation compound of charged host layers, interlayer cations of different size will always be forced to segregate into different interlayers with densely packed structures since this allows for minimizing the average d-spacing and therefore maximizing the Coulomb energy. The cation density in a particular type of interlayer does not necessarily have to match the charge density of the layered silicate host if a local charge balance is assured by adjusting the second type of interlayer accordingly.<sup>[19,20]</sup> In our case, the  $\text{NH}_4^+$  interlayers are significantly above while the  $\text{Na}^+$  interlayers are below the charge density of the host layers (Supporting Information, Figure S1). As evidenced by equilibration experiments, the formation of ordered heterostructures is thermodynamically favored.<sup>[19,20]</sup>

In deionized water,  $\text{Na}^+$  interlayers swell osmotically, which means that at the early swelling states all available water is drawn into the  $\text{Na}^+$  interlayers. In the obtained Wigner crystal phase, the distance between the  $\text{NH}_4^+$ -bridged bilayers corresponds to the silicate to water ratio (Supporting Information, Figure S3). By adding increasing amounts of water, the separation steadily increases (Figure 2) to the point where the bilayers gain rotational freedom and the layer separation is consequently no longer determined by the volume ratio of silicate layer to water.

Osmotic swelling is the most gentle exfoliation method, and therefore the large platelet diameters are preserved.<sup>[25]</sup> Thus, by simply suspending these crystalline heterostructures in water, bilayers with extremely high aspect ratios up to 8000 are produced with unprecedented precision (Figure 1b; Supporting Information, Figures S4, S9, S10).

Quantitative and selective bilayer formation is proven by small angle X-ray scattering (SAXS) studies of the highly swollen heterostructured sample (Figure 2, gray trace).

The SAXS pattern scales in the low  $q$  range as  $q^{-2}$ , which is typically observed for platelet shaped scattering objects. At a solid content of 4 wt %, for instance, the bilayers of the exfoliated heterostructure are uniformly separated to 59 nm. The first form factor minimum appears around  $q = 0.26 \text{ \AA}^{-1}$ , followed by a second minimum around  $q = 0.76 \text{ \AA}^{-1}$ . We use a very simplified SAXS model of discs with homogeneous electron density to fit the experimental data (see the Supporting Information for further details), rendering the minima somewhat shallow.

The best fit for the SAXS trace is obtained with a bilayer thickness of 2.1 nm. This value corresponds to the sum of two silicate layers of 0.85 nm and an interlayer height of 0.4 nm.

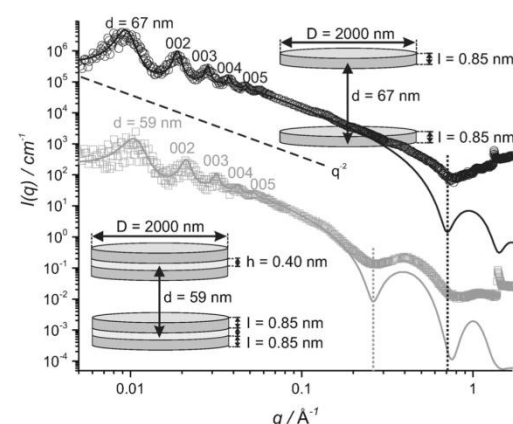


**Figure 2.** SAXS results of swollen gel samples (4 wt%): pristine bilayer sample (gray □) and a sample after cleaving with LiOH (black ○). The intensities of the cleaved sample are shifted by a factor of 10000 to avoid overlap. The corresponding solid lines are fits with a model of bilayer discs and single discs (see schemes and Supporting Information for further details). The dotted lines mark the position of the first minima of the form factors for bilayers (gray) and after cleavage to monolayers by the addition of LiOH (black). The scaling of  $q$  for the low  $q$ -range is indicated by a dashed line.

Bilayer formation is further confirmed by atomic force microscopy (AFM) of a sample obtained by drying a highly diluted, isotropic sol where platelets with a thickness of 2.6 nm are detected (Supporting Information, Figure S4).

Shih et al.<sup>[5]</sup> were the first to propose a route for the synthesis of bi- and trilayers of graphene starting with ionic stage-two and stage-three ICl or IBr intercalates of graphene. These graphite intercalates are popped by shock expansion, but they are unable to swell in solvents. Consequently, they lack an appropriate route for subsequent gentle and highly selective exfoliation. Moreover, the transformation of bilayers into Janus platelets, as described below, requires a second quantitative cleavage of bilayers via osmotic swelling.

Our novel silicate bilayers can easily be converted into monolayers by using bases to deprotonate the  $\text{NH}_4^+$  cations; these cations hold the silicate layers together. Treating the suspension of bilayers with LiOH initially exchanges  $\text{NH}_4^+$  with  $\text{Li}^+$ . Then, the bilayers are quantitatively cleaved by osmotic swelling of the resulting  $\text{Li}^+$  interlayers into singular silicate layers (Figure 2, black trace). In the SAXS pattern, the first form factor minimum of the single layer sample shifts from  $q = 0.26 \text{ \AA}^{-1}$ , as observed for the bilayer, to  $q = 0.73 \text{ \AA}^{-1}$  (Figure 2). The best fit for the SAXS trace is obtained with a single layer thickness of 0.85 nm.

Owing to the collapse of the  $\text{NH}_4^+$  interlayer, the structure of the bilayer is comparable to the bonding situation in potassium-rich micas: the  $\text{NH}_4^+$  cations inside the collapsed interlayer space will protrude on both sides into the hexagonal cavities of the Kagome-like silicate surface, cross-linking the two silicate layers encompassing this single interlayer space in the bilayer (Figure 3c). The bilayer may be regarded

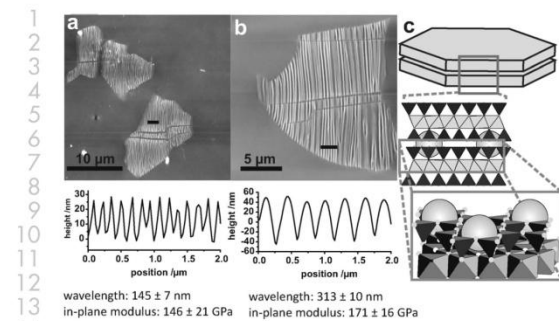


**Figure 3.** Determination of the in-plane bending moduli: Typical AFM topographical images of wrinkled a) monolayers and b) bilayers on PDMS substrates. The corresponding height profiles (black bars) are shown below. The resulting wavelength and in-plane modulus are obtained by Fourier transformation. c) the structure of a reinforced bilayer-sandwich. NH<sub>4</sub><sup>+</sup> cations (gray ○) protrude into the upper and lower hexagonal cavities of the silicate surface (additional details are shown in the Supporting Information, Figures S6, S7).

as a nanosandwich structure; therefore, it is expected to be stiffer than a single lamella.<sup>[26,27]</sup> When comparing the in-plane moduli of a single layer and a bilayer, the latter is indeed found to be 15% stiffer (Figure 3). The in-plane moduli of a single layer and a bilayer were determined by a supported metrology using a simple wrinkling technique in which the observed wavelength is directly related to the in-plane modulus of the platelet (see Figure S6 and Figure S7 and the more detailed explanation in the Supporting Information).<sup>[9,26]</sup> The in-plane modulus of a single lamellae is found to be 146 ± 21 GPa, which is in good agreement with previous results.<sup>[26]</sup> The average in-plane modulus of the bilayer, however, is significantly higher and was determined to be 171 ± 16 GPa. Interestingly, the value of the bilayer is already in the range of the in-plane moduli of bulk mica (178.5 ± 1.5 GPa) as determined by conventional methods.<sup>[26,28,29]</sup>

The base lability of the NH<sub>4</sub><sup>+</sup> interlayer allows for the quantitative conversion of bilayers into Janus-type nanoplatelets. The importance and prospective applications of Janus particles was first noted by de Gennes.<sup>[30]</sup> Distinct chemical and physical properties of the basal surfaces of Janus platelets offer directionality, allowing complex self-assembly.<sup>[23]</sup> Many approaches to synthesize inorganic-organic Janus particles were developed.<sup>[31–33]</sup> Typically the symmetry of inorganic particles is broken by immobilization of the particles at the surface of templates or interfaces followed by selective modification of one hemisphere of the particle.<sup>[34–36]</sup>

When starting with the bilayers described herein, breaking symmetry is beautifully simple (Figure 1d). Janus character can be directly realized by selectively coating the two surfaces of the monolayers with different polymers: Commercial polyethylenimine-ethyleneoxide (PEI-EO) and the dendritic poly(amidoamine) of generation G10 yield morphologically different monolayers that can be distinguished clearly by AFM imaging. Such Janus platelets are made by

first coating both surfaces of the bilayer by PEI-EO. Then, the bilayers are cleaved, and the produced Li<sup>+</sup>-decorated (Figure 1d) surfaces are “stained” with PAMAM G10 (Figure 1e), which does not adsorb to the PEI-EO-terminated surfaces. The irreversible exchange<sup>[37]</sup> of the Na<sup>+</sup> cations and the uniform coating of both surfaces of the bilayers with PEI-EO (Figure 1c) was probed by small-angle neutron scattering (SANS; Supporting Information, Figure S8). The overall thickness of the modified bilayer increases to 5.8 nm upon cation exchange with PEI-EO. As expected, after cleavage, SANS indicates a Janus platelet thickness of 3 nm (Figure 1d), which corresponds to a 1 nm-thick silicate layer coated on one side with an approximately 2 nm-thick monolayer of PEI-PEO (see the Supporting Information).

As already mentioned, the Li<sup>+</sup>-decorated surface is subsequently exchanged by PAMAM G10, which is known to bind quasi-irreversibly to negatively charged surfaces.<sup>[38,39]</sup> The adsorption process follows the random sequential adsorption (RSA) model and leads to a fractional surface coverage.<sup>[38]</sup> For sufficiently large dendrimers (> G5), single dendrimers can be readily resolved by AFM. Moreover, PAMAM G10 has a very narrow  $M_w$  distribution, which results in nearly identical heights and diameters of the adsorbed dendrimers. Hence, the surface morphology is easily distinguishable from the smooth PEI-EO covered surface (Figure 4a).

AFM samples were prepared by aspiration onto micro-pore filters (Figure 4a), which produces some degree of aggregation of individual platelets but suppresses any preferred orientation of the Janus platelets. The extremely high aspect ratios always force the platelets into orientations parallel to the substrate (Figure 4b and c), but the distinct surfaces are randomly exposed up or down.

The AFM signal corresponding to the adhesion shows two distinct types of surface morphologies for individual platelets: one with very high dendrimer coverage and one with negligible dendrimer coverage (Figure 4d and e). This difference in adhesion corresponds to the two different surface types of the Janus platelets: PAMAM or PEI-EO. The coverage of the platelets with very high dendrimer content (Figure 4e) resembles the level of dendrimer coverage of the bilayers that were modified with PAMAM for comparison (Supporting Information, Figure S9). As expected, dendrimer adsorption to the negatively charged silicate layers follows the RSA model.<sup>[38]</sup> The presence of two distinct surfaces in terms of dendrimer coverage unequivocally confirms the selective modification of the platelets in an asymmetric manner and thus the preparation of Janus-type platelets.

In conclusion, a novel approach for a quantitative, cost-effective, and robust fabrication of mechanically reinforced bilayers via osmotic exfoliation of ordered heterostructures is established. The synthesis route for bilayers will be generally applicable to other layered compounds capable of osmotic swelling, such as layered titanates, niobates, or perovskites.<sup>[40–44]</sup> By cleaving bilayers with appropriate reagents, in this case bases, the symmetry is broken in the simplest way, giving access to a general method for the synthesis of asymmetrically modified Janus nanoplatelets with tuneable functionalities.

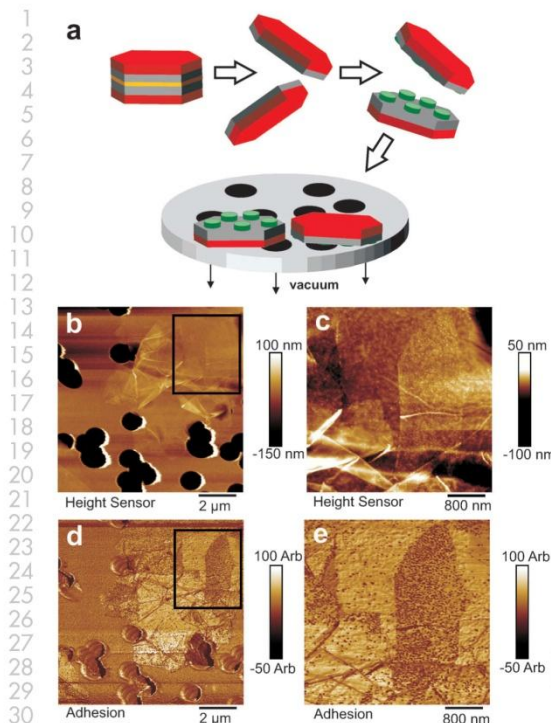


**Figure 4.** a) The Janus modification of the nanoplatelets. PEI-EO-modified bilayers were cleaved, and new Li<sup>+</sup>-decorated surfaces are subsequently modified with dendrimers, which serve as tracers for AFM imaging. The Janus platelets are immobilized onto a micropore filter by vacuum filtration. The AFM images of the topography (b, c) and adhesion (d, e) of the Janus platelets show different surface morphologies and adhesion properties. In particular, the adhesion signals unequivocally enable the identification of distinct surfaces with negligible and high dendrimer coverage, respectively. The Janus platelets are randomly oriented. Consequently, digital magnification (d, e) demonstrates that dendrimers are present only on such platelets, exposing this surface type to the AFM. More high-resolution images can be found in the Supporting Information, Figures S9–S11.

#### Acknowledgements

This work was financially supported by the Deutsche Forschungsgemeinschaft (SFB 840). Andreas Schedl is gratefully acknowledged for helping with the PDMS tensile tests.

**Keywords:** atomic force microscopy · hybrid materials · nanomaterials · silicate · thin layers

- [1] C. Chiritescu, D. G. Cahill, N. Nguyen, D. Johnson, A. Bodapati, P. Kebblinski, P. Zschack, *Science* **2007**, *315*, 351–353.  
[2] K. Takada, H. Sakurai, E. Takayama-Muromachi, F. Izumi, R. A. Dilanian, T. Sasaki, *Nature* **2003**, *422*, 53–55.

- [3] K. S. Novoselov, A. K. Geim, S. V. Morozov, D. Jiang, Y. Zhang, S. V. Dubonos, I. V. Grigorieva, A. A. Firsov, *Science* **2004**, *306*, 666–669.  
[4] M. Sui, G. Chen, L. Ma, W. Y. Shan, D. Tian, K. Watanabe, T. Taniguchi, X. Jin, W. Yao, D. Xiao, Y. Zhang, *Nat. Phys.* **2015**, *11*, 1027–1031.  
[5] C. J. Shih, A. Vijayaraghavan, R. Krishnan, R. Sharma, J. H. Han, M. H. Ham, Z. Jin, S. C. Lin, G. L. C. Paulus, N. F. Reuel, Q. H. Wang, D. Blankschtein, M. S. Strano, *Nat. Nanotechnol.* **2011**, *6*, 439–445.  
[6] W. Wu, L. Wang, Y. Li, F. Zhang, L. Lin, S. Niu, D. Chenet, X. Zhang, Y. Hao, T. F. Heinz, J. Hone, Z. L. Wang, *Nature* **2014**, *514*, 470–474.  
[7] O. Mashtalar, M. Naguib, V. N. Mochalin, Y. Dall'Agnese, M. Heon, M. W. Barsoum, Y. Gogotsi, *Nat. Commun.* **2013**, *4*, 1716.  
[8] J. W. Suk, R. D. Piner, J. An, R. S. Ruoff, *ACS Nano* **2010**, *4*, 6557–6564.  
[9] D. A. Kunz, P. Feicht, S. Goedrich, H. Thurn, G. Papastavrou, A. Fery, J. Breu, *Adv. Mater.* **2013**, *25*, 1337–1341.  
[10] B. Rasche, A. Isaeva, M. Ruck, S. Borisenko, V. Zabolotny, B. Buchner, K. Koepernik, C. Ortix, M. Richter, J. van den Brink, *Nat. Mater.* **2013**, *12*, 422–425.  
[11] B. V. Lotsch, G. A. Ozin, *Adv. Mater.* **2008**, *20*, 4079–4084.  
[12] S. H. Yu, M. Antonietti, H. Colfen, M. Giersig, *Angew. Chem. Int. Ed.* **2002**, *41*, 2356–2360; *Angew. Chem.* **2002**, *114*, 2462–2466.  
[13] T. Ohta, A. Bostwick, T. Seyller, K. Horn, E. Rotenberg, *Science* **2006**, *313*, 951–954.  
[14] S. S. Kim, T. Van Khai, V. Kulish, Y. H. Kim, H. G. Na, A. Katoch, M. Osada, P. Wu, H. W. Kim, *Chem. Mater.* **2015**, *27*, 4222–4228.  
[15] B. Butz, C. Dolle, F. Niekiel, K. Weber, D. Waldmann, H. B. Weber, B. Meyer, E. Speicher, *Nature* **2014**, *505*, 533–537.  
[16] M. Lotya, Y. Hernandez, P. J. King, R. J. Smith, V. Nicolosi, L. S. Karlsson, F. M. Blighe, S. De, Z. M. Wang, I. T. McGovern, G. S. Duesberg, J. N. Coleman, *J. Am. Chem. Soc.* **2009**, *131*, 3611–3620.  
[17] W. L. Ijdo, T. Lee, T. J. Pinnavaia, *Adv. Mater.* **1996**, *8*, 79–83.  
[18] W. L. Ijdo, T. J. Pinnavaia, *J. Solid State Chem.* **1998**, *139*, 281–289.  
[19] M. W. Möller, D. Hirsemann, F. Haarmann, J. Senker, J. Breu, *Chem. Mater.* **2010**, *22*, 186–196.  
[20] M. Stöter, B. Biersack, N. Reimer, M. Herling, N. Stock, R. Schobert, J. Breu, *Chem. Mater.* **2014**, *26*, 5412–5419.  
[21] M. Stöter, B. Biersack, S. Rosenfeldt, M. J. Leitl, H. Kalo, R. Schobert, H. Yersin, G. A. Ozin, S. Förster, J. Breu, *Angew. Chem. Int. Ed.* **2015**, *54*, 4963–4967; *Angew. Chem.* **2015**, *127*, 5047–5051.  
[22] A. Walther, X. Andre, M. Drechsler, V. Abetz, A. H. E. Müller, *J. Am. Chem. Soc.* **2007**, *129*, 6187–6198.  
[23] A. Walther, A. H. E. Müller, *Chem. Rev.* **2013**, *113*, 5194–5261.  
[24] M. Stöter, D. A. Kunz, M. Schmidt, D. Hirsemann, H. Kalo, B. Putz, J. Senker, J. Breu, *Langmuir* **2013**, *29*, 1280–1285.  
[25] M. Stöter, S. Rosenfeldt, J. Breu, *Annu. Rev. Mater. Res.* **2015**, *45*, 129–151.  
[26] D. A. Kunz, J. Erath, D. Kluge, H. Thurn, B. Putz, A. Fery, J. Breu, *ACS Appl. Mater. Interfaces* **2013**, *5*, 5851–5855.  
[27] M. W. Möller, U. A. Hande, D. A. Kunz, T. Lunkenbein, V. Altstadt, J. Breu, *ACS Nano* **2010**, *4*, 717–724.  
[28] G. D. Zartman, H. Liu, B. Akdim, R. Pachter, H. Heinz, *J. Phys. Chem. C* **2010**, *114*, 1763–1772.  
[29] A. Castellanos-Gomez, M. Poot, A. Amor-Amoros, G. A. Steele, H. S. J. van der Zant, N. Agrait, G. Rubio-Bollinger, *Nano Res.* **2012**, *5*, 550–557.  
[30] P. G. de Gennes, *Science* **1992**, *256*, 495–497.  
[31] D. Hirsemann, S. Shylesh, R. A. De Souza, B. Diar-Bakerly, B. Biersack, D. N. Müller, M. Martin, R. Schobert, J. Breu, *Angew.*

- 1      *Chem. Int. Ed.* **2012**, *51*, 1348–1352; *Angew. Chem.* **2012**, *124*,  
2      1376–1380.
- 3      [32] C. Ma, H. Wu, Z. H. Huang, R. H. Guo, M. B. Hu, C. Kubel,  
4      L. T. Yan, W. Wang, *Angew. Chem. Int. Ed.* **2015**, *54*, 15699–  
5      15704; *Angew. Chem.* **2015**, *127*, 15925–15930.
- 6      [33] W. O. Yah, A. Takahara, Y. M. Lvov, *J. Am. Chem. Soc.* **2012**,  
7      *134*, 1853–1859.
- 8      [34] J. H. Liu, G. N. Liu, M. M. Zhang, P. C. Sun, H. Y. Zhao,  
9      *Macromolecules* **2013**, *46*, 5974–5984.
- 10     [35] F. X. Liang, K. Shen, X. Z. Qu, C. L. Zhang, Q. A. Wang, J. L. Li,  
11     J. G. Liu, Z. Z. Yang, *Angew. Chem. Int. Ed.* **2011**, *50*, 2379–  
12     2382; *Angew. Chem.* **2011**, *123*, 2427–2430.
- 13     [36] L. M. Zhang, J. W. Yu, M. M. Yang, Q. Xie, H. L. Peng, Z. F. Liu,  
14     *Nat. Commun.* **2013**, *4*, 1443.
- 15     [37] M. Ziadeh, S. Weiss, B. Fischer, S. Förster, V. Altstädt, A. H.  
16     Müller, J. Breu, *J. Colloid Interface Sci.* **2014**, *425*, 143–151.
- 17     [38] R. Pericet-Camara, G. Papastavrou, M. Borkovec, *Langmuir*  
18     **2004**, *20*, 3264–3270.
- [39] B. P. Cahill, G. Papastavrou, G. J. M. Koper, M. Borkovec,  
[40] Y. Ebina, T. Sasaki, M. Watanabe, *Solid State Ionics* **2002**, *151*,  
[41] F. Geng, R. Ma, A. Nakamura, K. Akatsuka, Y. Ebina, Y.  
[42] M. Osada, G. Takanashi, B. W. Li, K. Akatsuka, Y. Ebina, K.  
[43] T. Sasaki, M. Watanabe, *J. Am. Chem. Soc.* **1998**, *120*, 4682–  
[44] Y. J. Song, N. Iyi, T. Hoshida, T. C. Ozawa, Y. Ebina, R. Z. Ma, N.  
Miyamoto, T. Sasaki, *Chem. Commun.* **2015**, *51*, 17068–17071.

Received: February 15, 2016

Revised: March 24, 2016

Published online: ■■■■■

- 1      *Chem. Int. Ed.* **2012**, *51*, 1348–1352; *Angew. Chem.* **2012**, *124*,  
2      1376–1380.
- 3      [32] C. Ma, H. Wu, Z. H. Huang, R. H. Guo, M. B. Hu, C. Kubel,  
4      L. T. Yan, W. Wang, *Angew. Chem. Int. Ed.* **2015**, *54*, 15699–  
5      15704; *Angew. Chem.* **2015**, *127*, 15925–15930.
- 6      [33] W. O. Yah, A. Takahara, Y. M. Lvov, *J. Am. Chem. Soc.* **2012**,  
7      *134*, 1853–1859.
- 8      [34] J. H. Liu, G. N. Liu, M. M. Zhang, P. C. Sun, H. Y. Zhao,  
9      *Macromolecules* **2013**, *46*, 5974–5984.
- 10     [35] F. X. Liang, K. Shen, X. Z. Qu, C. L. Zhang, Q. A. Wang, J. L. Li,  
11     J. G. Liu, Z. Z. Yang, *Angew. Chem. Int. Ed.* **2011**, *50*, 2379–  
12     2382; *Angew. Chem.* **2011**, *123*, 2427–2430.
- 13     [36] L. M. Zhang, J. W. Yu, M. M. Yang, Q. Xie, H. L. Peng, Z. F. Liu,  
14     *Nat. Commun.* **2013**, *4*, 1443.
- 15     [37] M. Ziadeh, S. Weiss, B. Fischer, S. Förster, V. Altstädt, A. H.  
16     Müller, J. Breu, *J. Colloid Interface Sci.* **2014**, *425*, 143–151.
- 17     [38] R. Pericet-Camara, G. Papastavrou, M. Borkovec, *Langmuir*  
18     **2004**, *20*, 3264–3270.
- [39] B. P. Cahill, G. Papastavrou, G. J. M. Koper, M. Borkovec,  
[40] Y. Ebina, T. Sasaki, M. Watanabe, *Solid State Ionics* **2002**, *151*,  
[41] F. Geng, R. Ma, A. Nakamura, K. Akatsuka, Y. Ebina, Y.  
[42] M. Osada, G. Takanashi, B. W. Li, K. Akatsuka, Y. Ebina, K.  
[43] T. Sasaki, M. Watanabe, *J. Am. Chem. Soc.* **1998**, *120*, 4682–  
[44] Y. J. Song, N. Iyi, T. Hoshida, T. C. Ozawa, Y. Ebina, R. Z. Ma, N.  
Miyamoto, T. Sasaki, *Chem. Commun.* **2015**, *51*, 17068–17071.

**GDCh**

**Communications**

**Angewandte Chemie International Edition**

**Communications**

**Hybrid Materials**

1 M. Stöter, S. Gödrich, P. Feicht,  
2 S. Rosenfeldt, H. Thurn, J. W. Neubauer,  
3 M. Seuss, P. Lindner, H. Kalo, M. Möller,  
4 A. Fery, S. Förster, G. Papastavrou,\*  
5 J. Breu\* **■■■■■**

6 Controlled Exfoliation of Layered Silicate  
7 Heterostructures into Bilayers and Their  
8 Conversion into Giant Janus Platelets

9

10

11

12

13

14

15

16

17

18

19

20

21

22

23

24

25

26

27

28

29

30

31

32

33

34

35

36

37

38

39

40

41

42

43

44

45

46

47

48

49

50

51

52

53

54

55

56

57

58

59

**Bilayer** → **Janus monolayer**

**Doppel-schicht** → **Janus-Monoschicht**

**Controlled exfoliation** of layered silicate heterostructures into bilayers with unprecedented precision by osmotic swelling gives access to a general method for asymmetrical modification of basal planes. Only two simple steps are needed to obtain Janus-type monolayers as bulk material.

**Die kontrollierte Exfolierung** schichtförmiger Silicat-Heterostrukturen unter Bildung von Doppelschichten durch osmotisches Quellen dient als allgemeine Methode für die unsymmetrische Modifizierung von Basalebenen. In zwei einfachen Schritten gelangt man zu Janus-Monoschichten.

**Exfoliation of #LayeredSilicate #heterostructures into a #bilayer for giant Janus platelets** **SPACE RESERVED FOR IMAGE AND LINK**

Share your work on social media! *Angewandte Chemie* has added Twitter as a means to promote your article. Twitter is an online microblogging service that enables its users to send and read text-based messages of up to 140 characters, known as "tweets". Please check the pre-written tweet in the galley proofs for accuracy. Should you or your institute have a Twitter account, please let us know the appropriate username (i.e., @accountname), and we will do our best to include this information in the tweet. This tweet will be posted to the journal's Twitter account @angew\_chem (follow us!) upon online publication of your article, and we recommend you to repost ("retweet") it to alert other researchers about your publication.

## 5.4.2 Supporting information

### Controlled Exfoliation of Layered Silicate Heterostructures into Bilayers and Their Conversion to Giant Janus Platelets

Matthias Stöter<sup>1</sup>, Sebastian Gödrich<sup>2</sup>, Patrick Feicht<sup>1</sup>, Sabine Rosenfeldt<sup>3</sup>, Herbert Thurn<sup>4</sup>, Jens W. Neubauer<sup>5</sup>, Maximilian Seuss<sup>5</sup>, Peter Lindner<sup>6</sup>, Hussein Kalo<sup>1</sup>, Michael Möller<sup>1</sup>, Andreas Fery<sup>5,7</sup>, Stephan Förster<sup>3</sup>, Georg Papastavrou<sup>2</sup>, Josef Breu<sup>1\*</sup>

<sup>1</sup>Lehrstuhl für Anorganische Chemie I, University of Bayreuth, D-95440 Bayreuth, Germany;

<sup>2</sup>Lehrstuhl für Physikalische Chemie II, University of Bayreuth, D-95440 Bayreuth, Germany;

<sup>3</sup>Lehrstuhl für Physikalische Chemie I, University of Bayreuth, D-95440 Bayreuth, Germany;

<sup>4</sup>Computing Center, University of Bayreuth, D-95440 Bayreuth, Germany;

<sup>5</sup>Institute for Physical Chemistry and Polymer Physics, Leibniz-Institut für Polymerforschung Dresden e.V., D-01069 Dresden, Germany

<sup>6</sup>Institut Laue-Langevin, DS LSS, F-38042 Grenoble 9, France.

<sup>7</sup>Chair of Physical Chemistry of Polymeric Materials, Technical University Dresden, D-01069 Dresden, Germany

## Supporting Information

### Methods

#### *Synthesis of the layered silicate:*

Sodium fluorohectorite, denoted as Na-hectorite ( $\text{Na}_{0.5}^{\text{inter}}[\text{Mg}_{2.5}\text{Li}_{0.5}]^{\text{oct}}<\text{Si}_4>^{\text{tet}}\text{O}_{10}\text{F}_2$ ) in the following, was obtained by melt synthesis in a closed molybdenum crucible according to a published procedure.<sup>[1]</sup> The raw material was annealed for 6 weeks at 1045 °C to improve intracrystalline reactivity, charge homogeneity and phase purity, as recently described.<sup>[2]</sup>

#### *Synthesis of bilayers*

First, 1.5 g of Na-hectorite was immersed in 200 ml of a water-ethanol mixture (33 vol% ethanol) for 12 h at room temperature in an overhead shaker. Then, 61.53 mg (65% CEC) of NH<sub>4</sub>Cl (Grüssing GmbH, Germany) dissolved in 200 ml of a water-ethanol mixture (33 vol% ethanol) was added dropwise to the stirred suspension. The suspension was mixed in a glass vessel with a screw cap at room temperature for 48 h. The solid was washed five times with a water-ethanol mixture (33 vol%) by centrifugation at 8000 rpm for 10 min. During washing and centrifugation, an iridescent gel is formed. After centrifugation at

3000 rpm for 5 min, the iridescent gel was decanted and washed three times with deionized water by centrifugation at 10000 rpm for 10 min and stored in a glass vessel.

#### *Modification of bilayers with polymers*

A 5 g/L solution of PEI-EO (PEI-EO 20, obtained from BASF) in water at pH = 5 was added to 10 mg of exfoliated Na-hectorite in 10 ml of water while monitoring the streaming potential (StabiSizer®, Particle Metrix GmbH). After the addition of 0.0175 g of PEI-EO, a streaming potential of zero was reached for 10 mg of Na-hectorite. The ratio of 0.822 g PEI-EO/1 g bilayer was applied in the following to prepare PEI-EO-modified bilayers. These suspensions were concentrated by centrifugation at 8000 rpm and were washed 5 times with water. Modification of the bilayers with polyamido amine (PAMAM) generation G10 dendrimers (purchased from Dendritech Inc.) was carried out with 13 ml of the bilayer suspension ( $c = 2.37 \text{ mg/L}$  at pH = 5) by adding 2.5 ml of the aqueous PAMAM G10 solution ( $c = 5 \text{ ppm}$  PAMAM G10 in 5 mM/L NaCl solution at pH = 5.5).

#### *Cleaving of bilayers*

Cleaving was performed at pH 9 using an aqueous solution of LiOH (Merck) as the base. The suspension was heated at 60 °C for 12 h while degassing with argon to quantitatively release ammonia. The cleaved bilayers were concentrated by centrifugation at 8000 rpm and were washed three times with water (pH = 5).

#### *Modification of $\text{Li}^+$ Janus platelets with PAMAM G10 dendrimers*

First, 13 ml of the bilayer suspension ( $c = 2.37 \text{ mg/L}$  at pH = 5) was added to 1.25 ml of an aqueous dendrimer solution ( $c = 5 \text{ ppm}$  PAMAM G10 from Dendritech, Inc. dissolved in a 5 mmol/L NaCl solution at pH = 5.5). The suspension was mixed at room temperature for 20 min using an overhead shaker (IKA Trayster digital). Janus-modified platelets were then immobilized onto a millipore filter (Isopore membrane filter, type RTTP; pore size = 1.2 µm; Merck Millipore) by applying vacuum to a miniature Büchner funnel. The filter disks were washed immediately by rinsing twice with 10 ml of water (pH = 5) while still

applying vacuum to remove the excess non-immobilized PAMAM dendrimers before drying the filter disks. After drying at ambient conditions, the filter disks were examined by AFM.

#### *Small angle X-ray scattering (SAXS)*

Suspensions of 4 wt% were concentrated by centrifugation at 10000 rpm for 1 h. Suspensions of 15 wt% were achieved by adding water to the freeze dried and at 120°C heated powder. Samples were equilibrated in the closed vessels for 4 days prior to measurement. All SAXS data were measured using the small-angle X-ray system “Double Ganesha AIR” (SAXSLAB, Denmark). The X-ray source of this laboratory-based system is a rotating anode (copper, MicroMax 007HF, Rigaku Corporation, Japan) providing a micro-focused beam. The data are recorded by a position sensitive detector (PILATUS 300K, Dectris). To cover the range of scattering vectors between 0.004-2.0 Å<sup>-1</sup>, different detector positions were used. The measurements of the suspensions were done in 1-mm glass capillaries (Hilgenberg, code 4007610, Germany) at room temperature. The circularly averaged data were normalized to the incident beam, sample thickness and measurement time before subtraction of the solvent. Calculations were done using the software SASfit (version 0.94.1) written by J. Kohlbrecher and I. Bressler and the software Scatter written by S. Förster.<sup>[3]</sup>

#### *Small angle neutron scattering (SANS)*

SANS experiments were performed in D<sub>2</sub>O (99%, Sigma Aldrich) in 1-mm-pathway cuvettes (QS-110, Hellma Analytics) at the instrument D11 at the Institut Laue-Langevin (ILL, Grenoble, France). To cover the range of scattering vectors between 0.0009-0.67 Å<sup>-1</sup>, different detector positions were used. All data were converted to an absolute scale using the standard software provided by ILL. The 1D data are corrected to contributions of the solvent and the cuvette.

#### *Wide angle X-ray diffraction (XRD)*

Diffractograms were recorded in Bragg-Brentano-geometry on a Panalytical XPERT-PRO. The textured film of restacked bilayers was prepared by drying a few drops of the suspension on microscope slides (Menzel-Gläser, Thermo Scientific). The glass slides were dried at 120 °C for 12 h and rehydrated at 43% r.h. for 24 h (in a desiccator with saturated K<sub>2</sub>CO<sub>3</sub>-solution).

#### *Preparation of wrinkled platelets on polydimethylsiloxane (PDMS) substrates*

Wrinkling metrology was performed according to a recently published procedure,<sup>[4,5]</sup> outlined here only briefly: the PDMS precursor (Dow Corning Sylgard 184) was mixed in a 10:1 mass ratio of oligomeric base to curing agent, degassed and poured into (60 x 10 x 2) mm<sup>3</sup> polytetrafluoroethylene moulds. After pre-hardening for 20 h at room temperature, all samples were post-treated for 2 h at 150 °C. The PDMS substrates were hydrophilized by immersing them in 10 vol% aqueous HCl solutions for 16 h, thoroughly washing with deionized water, and finally drying. Tensile tests were carried out on an Instron 5565 universal tester with pneumatic clamps and a 100-N load cell (clamping distance 30 mm, strain rate 200 mm min<sup>-1</sup>, see ISO 37:2005). Young's moduli were calculated from the initial slope and averaged over 16 different samples. The PDMS substrates were uniaxially stretched to a strain of 33% along their length in a custom made apparatus. In the stretched stage, a droplet of the nanoplatelet suspension was added to the centre and dried gently. Finally, the stress was released and the sample was investigated by AFM.

#### *Atomic force microscopy (AFM)*

All AFM measurements were performed on instruments with large sample stages. The topographic imaging of the bilayers was carried out on a Dimension 3100 with a Nanoscope IV controller (Bruker), while the imaging of the wrinkled platelets was carried out on an ICON with a Nanoscope V controller. The surface topographies were acquired in tapping mode using aluminium-coated cantilevers (OTESPA-R3, Bruker). Image processing and analysis was conducted with NanoScope Analysis v1.40. AFM

measurements of the PAMAM dendrimer-modified Janus-type single platelets were acquired in PeakForce mode using a Dimension ICON Microscope (Bruker). Aluminium-coated silicon nitride cantilevers (SCANASYST-AIR, Bruker) were used for these measurements. Image processing and data analysis were performed with NanoScope Analysis v1.50.

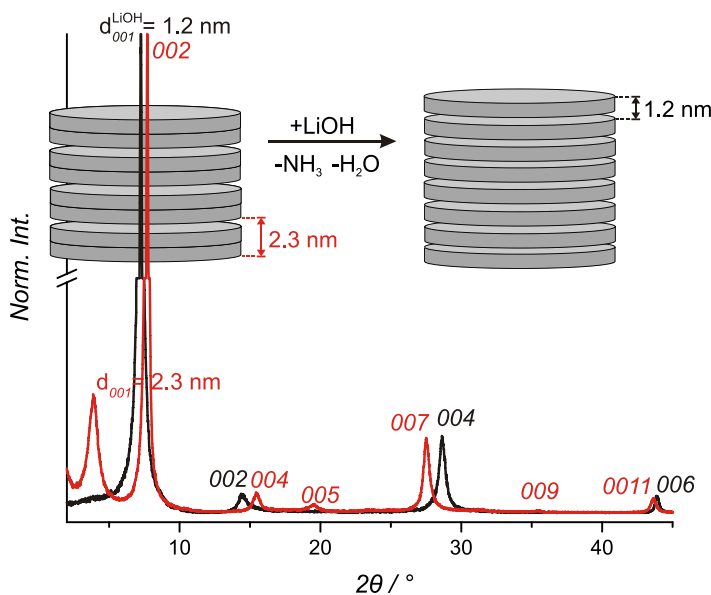


**Figure S1.** Powder X-ray diffraction (XRD) traces of the 1D ordered, crystalline heterostructure (red). To produce a perfect order with Reichweite 1 and equal weight of  $\text{Na}^+$ - and  $\text{NH}_4^+$ -interlayers<sup>[6]</sup> 62% of the interlayer cations need to be  $\text{NH}_4^+$ . The reason is that the  $\text{NH}_4^+$ -interlayers possess a higher density of interlayer cations as observed previously for synthetic rectorites.<sup>[7]</sup> When releasing the  $\text{NH}_4^+$  by treatment with excess LiOH (black line) the superstructure is lost. Both samples were equilibrated in an atmosphere with 43% relative humidity. The pattern of the ordered heterostructure shows a superstructure at around  $4^\circ 2\theta$ , corresponding to a  $d$ -spacing of 2.3 nm. The rational  $00l$ -series proofs the formation of a perfectly ordered heterostructure of strictly alternating hydrated  $\text{Na}^+$ - and collapsed  $\text{NH}_4^+$ -interlayers. After addition of LiOH (black line) the superstructure has vanished and a  $d$ -spacing of 1.2 nm, which is a typical value for a one-water layer hydrate<sup>[2,8]</sup>, is observed.

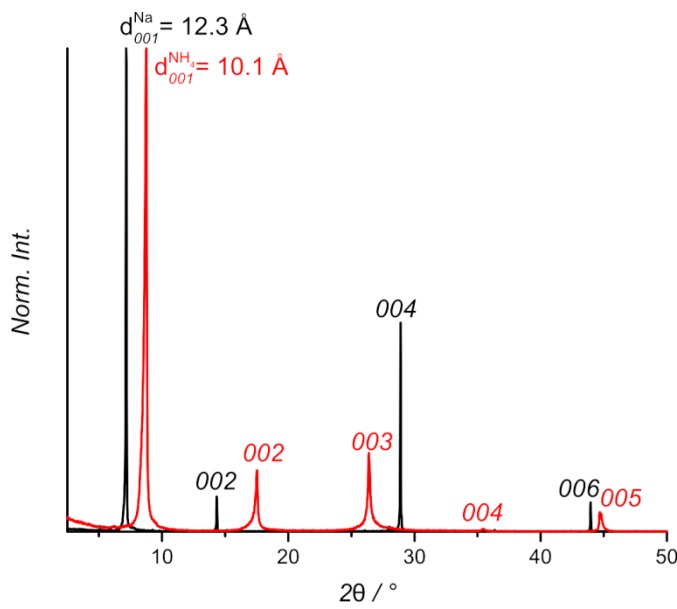


**Figure S2.** XRD traces of homoionic  $\text{Na}^+$ - and  $\text{NH}_4^+$ -hectorite, black and red trace, respectively. Both samples were equilibrated in an atmosphere with 43% relative humidity. The  $d$ -spacing for the sodium hectorite sample is 12.3 Å (black trace) which is a typical value for the one water-layer hydrate.<sup>[2,8]</sup> For the  $\text{NH}_4^+$ -exchanged sample a  $d$ -spacing of 10.1 Å which corresponds to  $d$ -spacings in micas and indicates non-swellable, collapsed  $\text{NH}_4^+$ -interlayers.<sup>[9]</sup>

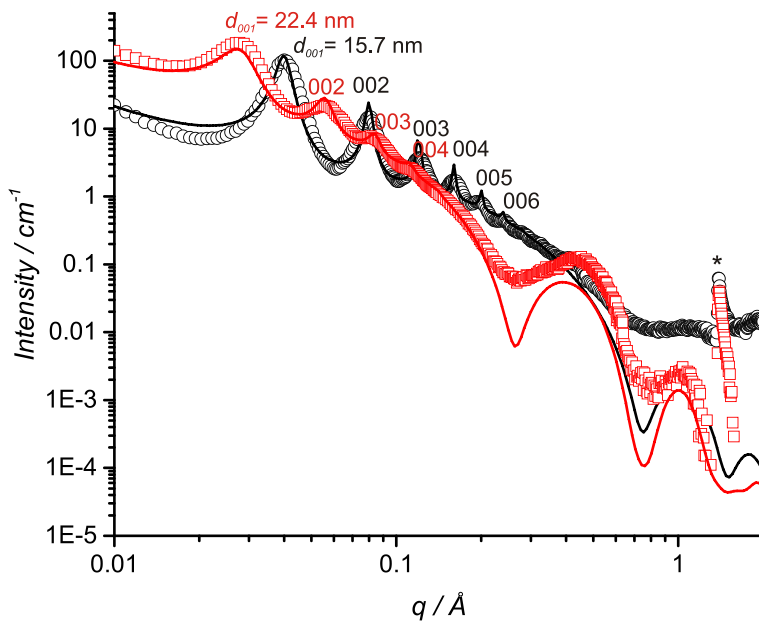


**Figure S3.** SAXS results of swollen gel samples at a high solid content of 15 wt%: pristine bilayer sample (red squares) and a sample after cleaving with LiOH (black circles). The corresponding solid lines are fits with a model of bilayer discs and single discs, respectively. The asterisk (\*) marks the position of the  $hk$ -Band of the TOT layered silicate structure, which cannot be fitted applying a homogeneous disc model.

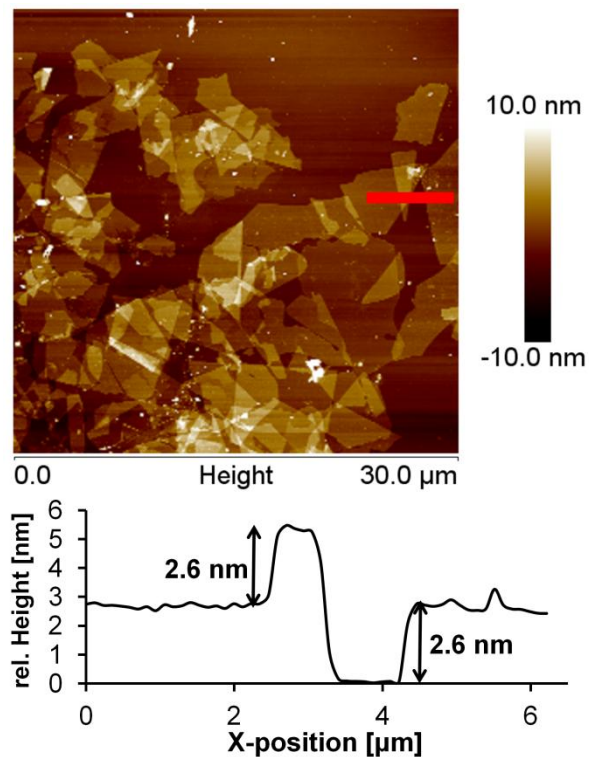


**Figure S4.** Representative, topographical AFM image of a suspension of bilayers (10 mg/L) dried on a silicon wafer. A height profile (red bar) shows a platelet thickness of 2.6 nm.

### SAXS Modeling

The SAXS intensities were described applying a model of stacked hamburgers.<sup>[10]</sup> For technical reasons a platelet radius of  $R = 1000$  nm was used in the model. Please note, that there is no difference in SAXS patterns for  $R > 1000$  nm. For the calculations of the SAXS patterns of the single platelets a thickness of  $l = 0.85$  nm is used, which is in good agreement with the platelet thickness derived by other SAXS measurements of delaminated natural montmorillonites.<sup>[11]</sup> The experimental monolayer thickness of 0.85 nm is slightly higher than the distance between the planes formed by the basal oxygens of the two tetrahedral sheets (0.66 nm<sup>[12]</sup>). This indicates a contribution to the scattering by sodium ions in the Helmholtz layer. For the calculation of the bilayer pattern the platelet thickness of 0.85 nm for the upper and lower layer and a interlayer height ( $h$ ) of 0.4 nm is applied. The separation distance ( $d$ -spacing) between the single platelets /

hamburgers which is the cause for the oscillations at low  $q$  are also included in the modeling ( $l = 8$ ).

Please note, that modeling of the layered silicate platelets as homogeneous discs with homogeneous electron density, is very simplified. At high  $q$ -values the real 2:1 tetrahedral-octahedral-tetrahedral (T-O-T) atomistic structure of the layered silicate becomes evident in the experimentally observed scattering. This is further corroborated by the appearance of the  $hk$ -band originating from the two-dimensional layer structure. The simplifications of the model and the limited experimental resolution of the SAXS instrument at high  $q$ -values may lead to the observed deviation between experimental and theoretical data.

When comparing bilayer samples and monolayer samples at very high solid content of 15 wt% (Wigner crystal regime), the bilayer sample swells to a higher  $d$ -spacing ( $d_{001} = 22.4$  nm) as compared to the monolayer sample ( $d_{001} = 15.7$  nm) corresponding to layer separations of about 20 nm and 15 nm, respectively (Figure S3). Since the number of independent bilayers is half of the number of monolayers, in a first approximation the separation of bilayers would be expected to show twice the monolayer separation. The observed separation is, however, modified by a limited water uptake of  $\text{NH}_4^+$ -interlayers by crystalline swelling.

### Wrinkling technique for determination of the in-plane modulus of nano-objects

The wrinkling technique is based on the planar compression of a thin and stiff nano-object on a thicker but softer substrate like poly(dimethylsiloxane) (PDMS).<sup>[4,5]</sup> A suspension of platelets (1 mg/L) is deposited onto a prestretched (33%) PDMS substrate. After drying, the strain is released and a topographical AFM image is measured.

The in-plane modulus of the nano-platelet  $E_p$  can be calculated from the characteristic wrinkling wavelength  $\lambda$ , the platelet thickness  $h$ , and the Young's modulus  $E_s$  of the substrate:

$$E_p = \frac{3E_s(1 - \nu_p^2)}{(1 - \nu_s^2)} \left( \frac{\lambda}{2\pi h} \right)^3$$

$\nu_p$  and  $\nu_s$  refer to Poisson's ratios of nano-platelet and substrate and are 0.5 and 0.3 for substrate and layer silicate, respectively.<sup>[4]</sup>  $E_s$  was measured by applying a standard tensile test and was found to be  $2.9 \pm 0.2$  MPa.

It is important to accurately determine the platelet thickness  $h$  of the platelets. The dependence of the in-plane modulus on the platelet thickness is illustrated in Figure S5.

Determination of the platelet thicknesses using SAXS form factor modeling is not accurate enough due to simplifications within the modeling (e.g. assumption of homogeneous electron density). Measured values of platelet thickness by AFM are often erroneous due to systematical errors like inclusion of adsorbed water layers. We therefore determined the platelet thickness by XRD measurement of unhydrated  $\text{Na}^+$ - and  $\text{NH}_4^+$ -samples. In consensus with previous publications, the platelet thicknesses  $h$  of 0.96 nm<sup>[2]</sup> and of 1.97 nm (0.96 nm + 1.01 nm = 1.97 nm, Figure S2) are applied for monolayer and bilayer, respectively.

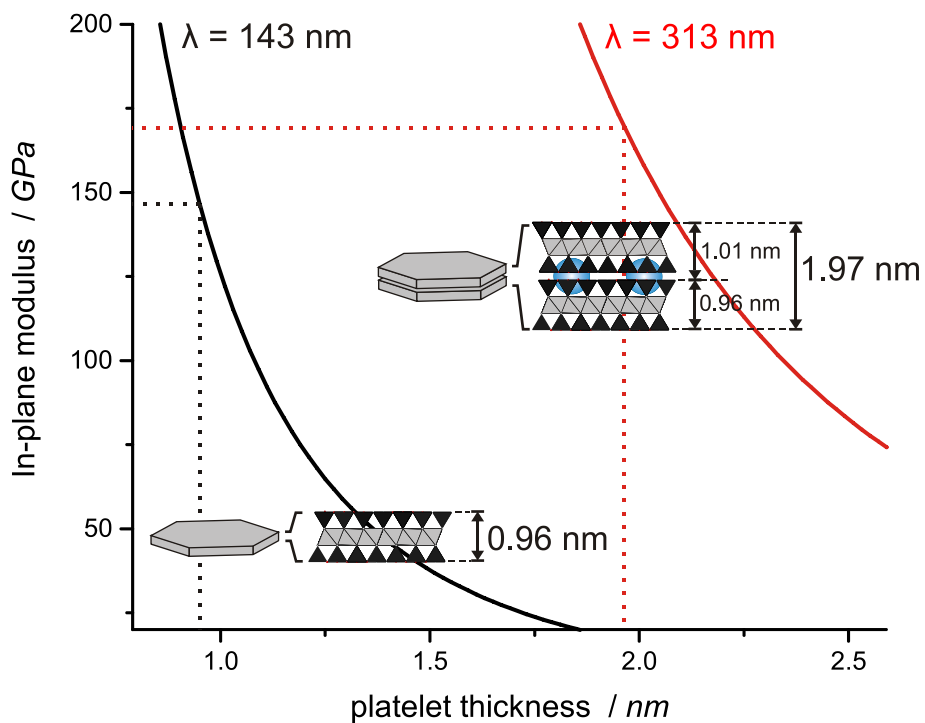


**Figure S5.** The dependence of the in-plane modulus on the platelet thickness is illustrated. The black solid line corresponds to a wavelength of 143 nm as observed for the monolayer, while the red solid line corresponds to the bilayer where a wavelength of 313 nm was determined. The dotted lines mark the platelet thickness measured by XRD of 0.96 nm and 1.97 nm for the monolayer and bilayer, respectively.

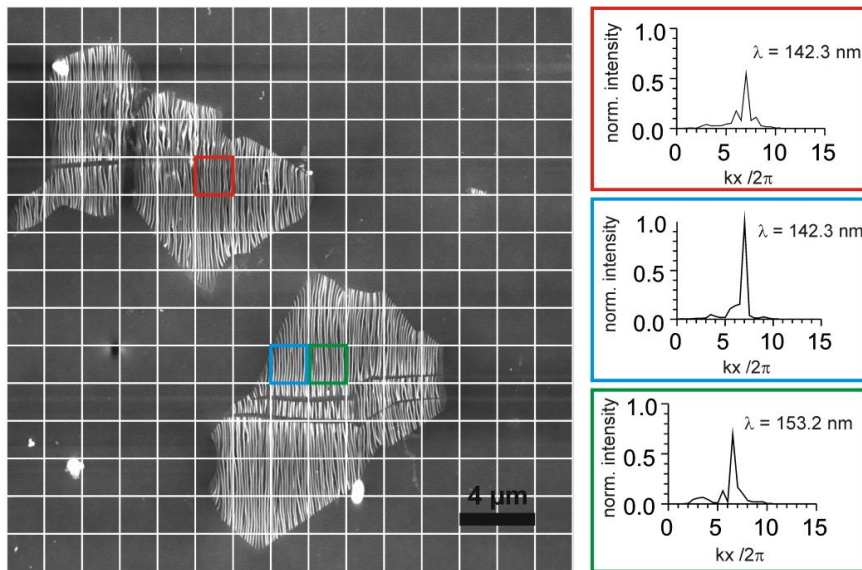


**Figure S6.** Monolayers: Normalized intensity profiles of 2D-fourier transformations (right) along  $k_x$  at different positions (left) of the wrinkling pattern in different  $2 \mu\text{m} \times 2 \mu\text{m}$  sections of monolayers. The values were integrated over a range of  $-5$  to  $+5$   $k_y$  values to consider also wrinkles that are slightly tilted away from  $90^\circ$ . The wrinkling wavelength of e.g. 142 nm corresponds to an in-plane modulus of 138 GPa. Averaging 70 sectors of four platelets gives a wavelength of  $145 \pm 7$  nm, corresponding to an in-plane modulus of  $146 \pm 21$  GPa.

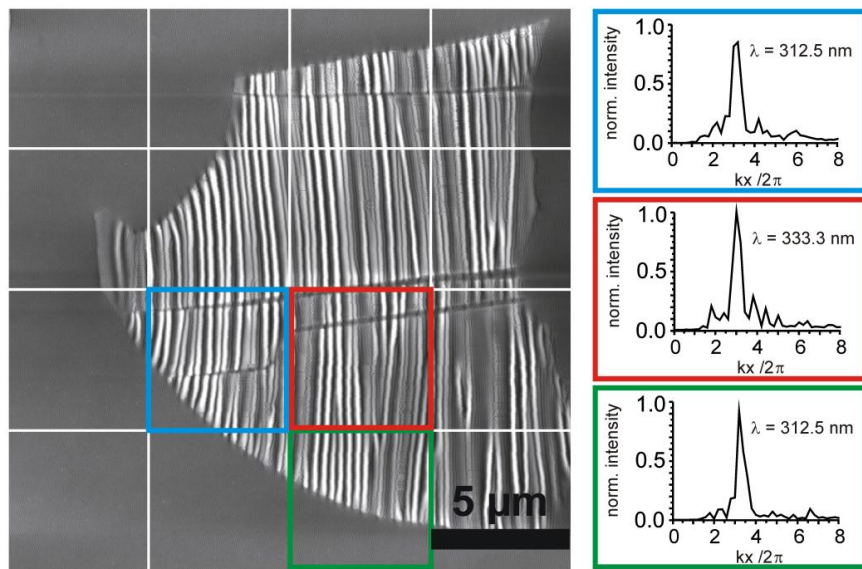


**Figure S7.** Bilayer: Normalized intensity profiles of 2D-fourier transformations (right) along  $k_x$  at different positions (left) of the wrinkling pattern in different  $5 \mu\text{m} \times 5 \mu\text{m}$  sections of bilayers. The values were integrated over a range of  $-5$  to  $+5$   $k_y$  values to consider also wrinkles that are slightly tilted away from  $90^\circ$ . The wrinkling wavelength of e.g. 313 nm corresponds, considering the bilayer thickness of 1.97 nm, to an in-plane modulus of 171 GPa. Averaging all 35 sectors on three platelets gives a wavelength of  $313 \pm 10$  nm, corresponding to an in-plane modulus of  $171 \text{ GPa} \pm 16$  GPa.

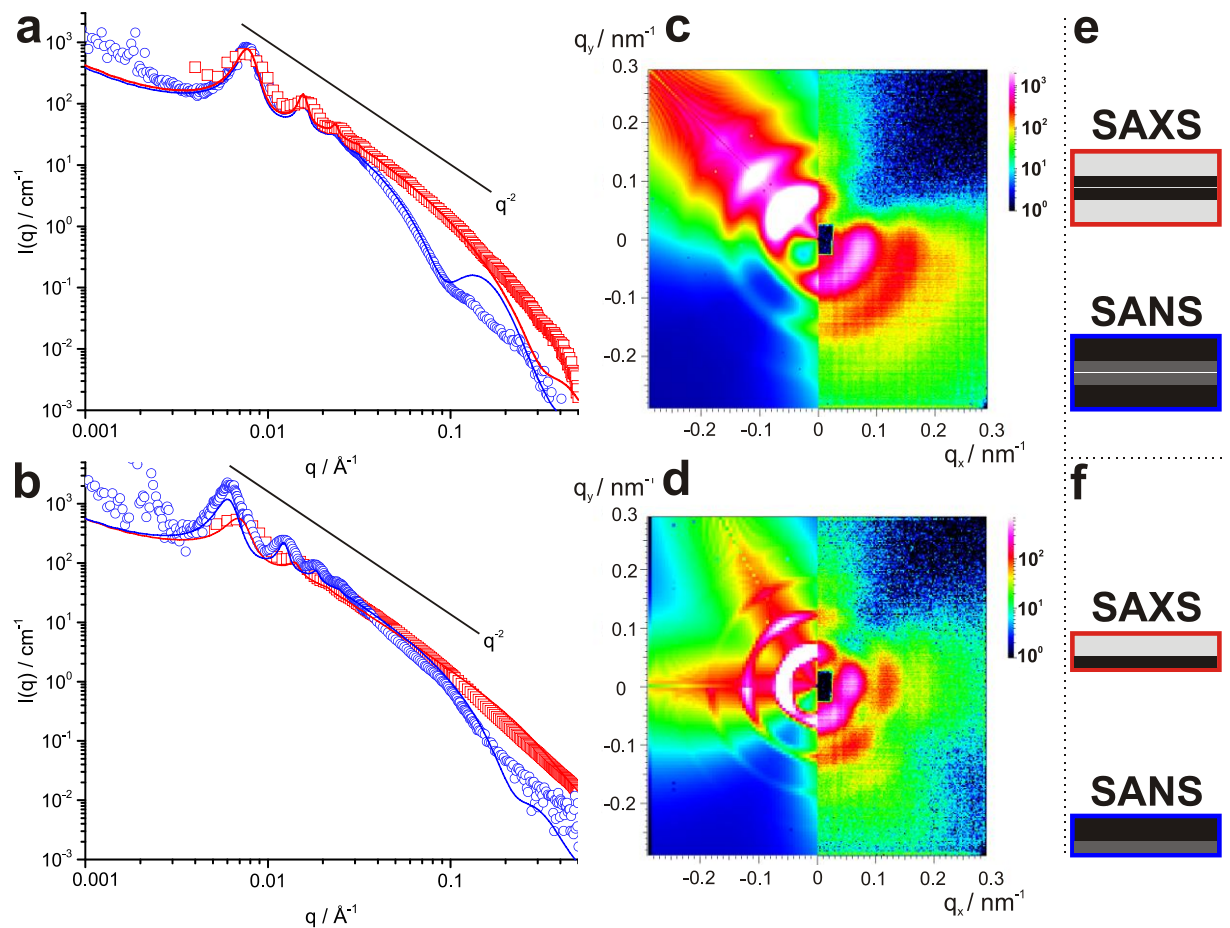


**Figure S8** SAXS- and SANS-pattern of PEI-EO modified bilayers in  $\text{D}_2\text{O}$  before (a, c) and after cleaving (b, d). To assist comparison, 1D SANS data are normalized to the SAXS data. On the left radial averaged data (a, b) of SAXS (red squares), SANS (blue circles) and theoretical intensities (bold lines) are shown. The thin lines indicate a  $q^{-2}$  scaling behavior. The schemes on the right (e, f) depict corresponding SAXS- (red border) and SANS (blue border) contrasts. In the middle 2D SANS raw data (c right side, d right side) are shown, taken at a sample to detector distance of 8 m. Modeling for PEI-EO modified bilayers (c, left side) (3.3 wt%; description by hamburger model:  $D = 2000 \text{ nm}$ ,  $h = 2.1 \text{ nm}$ ,  $h + 2l = 5.8 \text{ nm}$ ,  $d = 80 \text{ nm}$ ; contrast ratio of  $1/h$  was set to 0.064 for SAXS and 2.88 for SANS). Modeling for cleaved Janus platelets (d, left side) (description by disc model with  $D = 2000 \text{ nm}$ ; SANS 2.9 wt%, thickness  $h = 3.0 \text{ nm}$ ,  $d = 102 \text{ nm}$ ; SAXS: 3 wt%,  $h = 1.05 \text{ nm}$ ,  $d = 88 \text{ nm}$ ).

**SANS and SAXS measurement of the PEI-EO modified platelets**

Cleaving of PEI-EO modified bilayers was followed by SAXS and SANS in D<sub>2</sub>O (Figure S8). Even though both methods are sensitive to the scattering of the PEI-EO modification, the SAXS intensity is more dominated by the strong electron contrast of the layered silicate (Figure S8, red line and Table S1). Due to the better scattering contrast of the PEI-EO modification and the solvent (D<sub>2</sub>O) SANS is more sensitive to the modification (Table S1).

Clear differences between SAXS and SANS become evident in the high q-range.

A sharp first form factor minimum as observed for unmodified bilayers (Figure 2) is not detected in SAXS. This effect is most probably due to variations in the density or thickness of the PEI-EO coating. The complete individualization of platelets by osmotic swelling is proven by the large separation distances *d* observed. The PEI-EO modified bilayers and the cleaved Janus platelet both exhibit a preferred orientation in the 1 mm pathway cuvette as indicated by the anisotropic 2D SANS scattering patterns (Figure S8, c and d). The scattering intensities of the PEI-EO modified bilayers (Figure S8, a and c) can be described using the simple model of separated hamburgers. The averaged overall thickness of the modified bilayer was found to be 5.8 nm from the fit of the SANS data.

As expected, cleaving bilayers into Janus-platelets results in a significant change of the form factor and the minimum in the SANS pattern shifts to higher q-values (Figure S8, b and d), indicating a reduced platelet thickness. The modeling of a Janus particle is, however, very challenging. We used a very simplified approach based on the different SAXS and SANS contrasts and the description of the particles as homogeneous discs. The SAXS patterns can be approximated by a disc with a thickness *h* = 1.05 nm and the SANS intensity with *h* = 3.0 nm.

**Table S1:** SAXS and SANS bulk contrasts in D<sub>2</sub>O. In suspension, the contrast will be further lowered by incorporation of D<sub>2</sub>O into the PEI-EO layer.

sample	composition	density [g/cm <sup>3</sup> ]	SAXS contrast [10 <sup>-6</sup> Å <sup>-2</sup> ]	SANS contrast [10 <sup>-6</sup> Å <sup>-2</sup> ]
Na-hectorite	Na <sub>0.5</sub> [Mg <sub>2.5</sub> Li <sub>0.5</sub> ]Si <sub>4</sub> O <sub>10</sub> F <sub>2</sub>	2.8	23.781	4.379
EO	C <sub>2</sub> H <sub>4</sub> O	1.13	10.487	0.639
PEI	C <sub>2</sub> H <sub>5</sub> N	1.03	9.769	0.569
H <sub>2</sub> O	H <sub>2</sub> O	0.997	9.441	-0.559
D <sub>2</sub> O	D <sub>2</sub> O	1.107	9.429	6.375

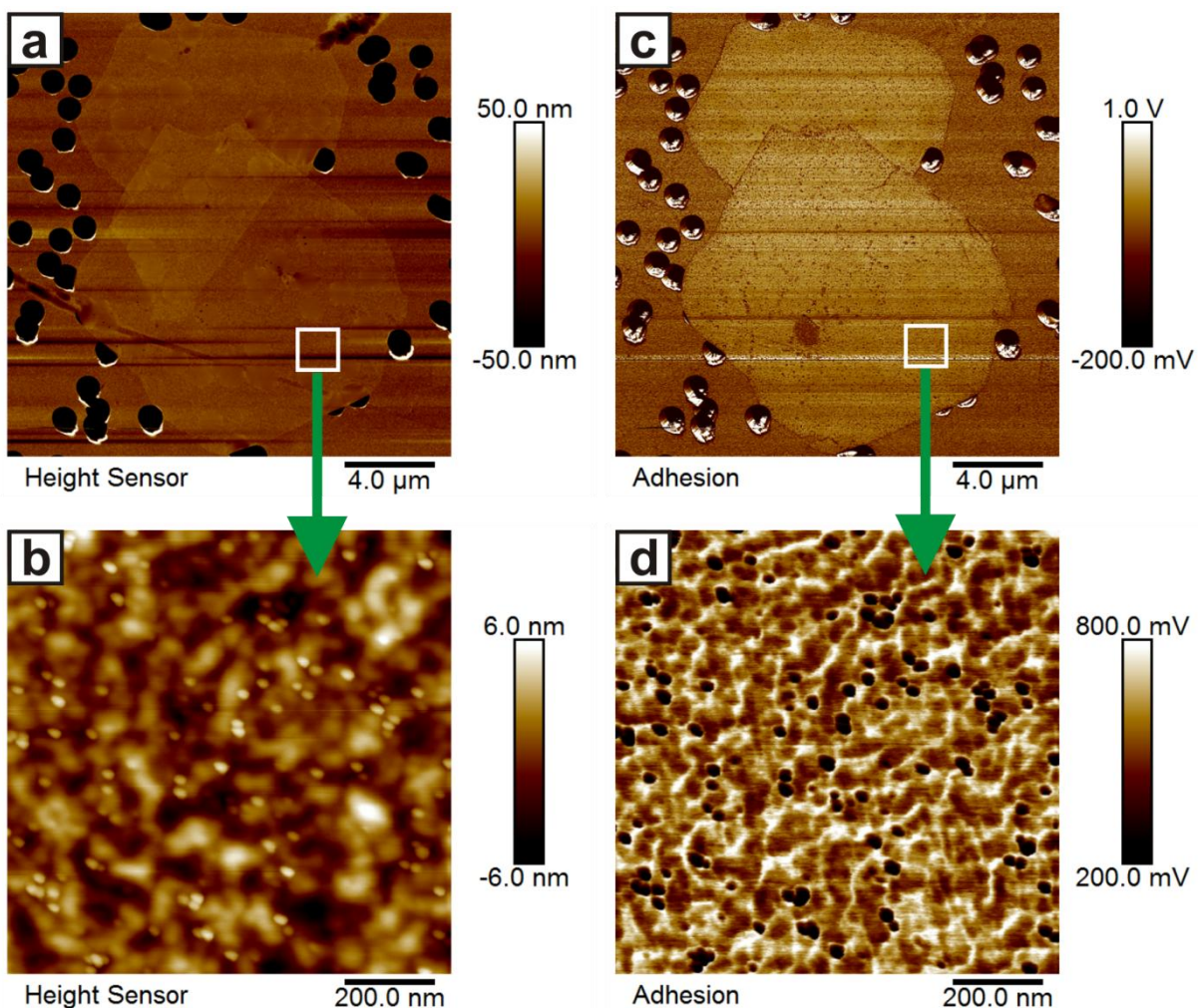


**Figure S9.** Bilayer sample with both external surfaces modified with polyamido amine dendrimers (PAMAM G10): In the AFM images a, b (height sensor) and c, d (adhesion channel) different platelets with a surface homogeneously patterned with dendrimer are visible. Corresponding topographical- as well as adhesion-data zoom-ins illustrate a homogeneous dendrimer-coverage on all platelets (dots) (b, d). The fractional surface coverage results from the RSA-like adsorption.

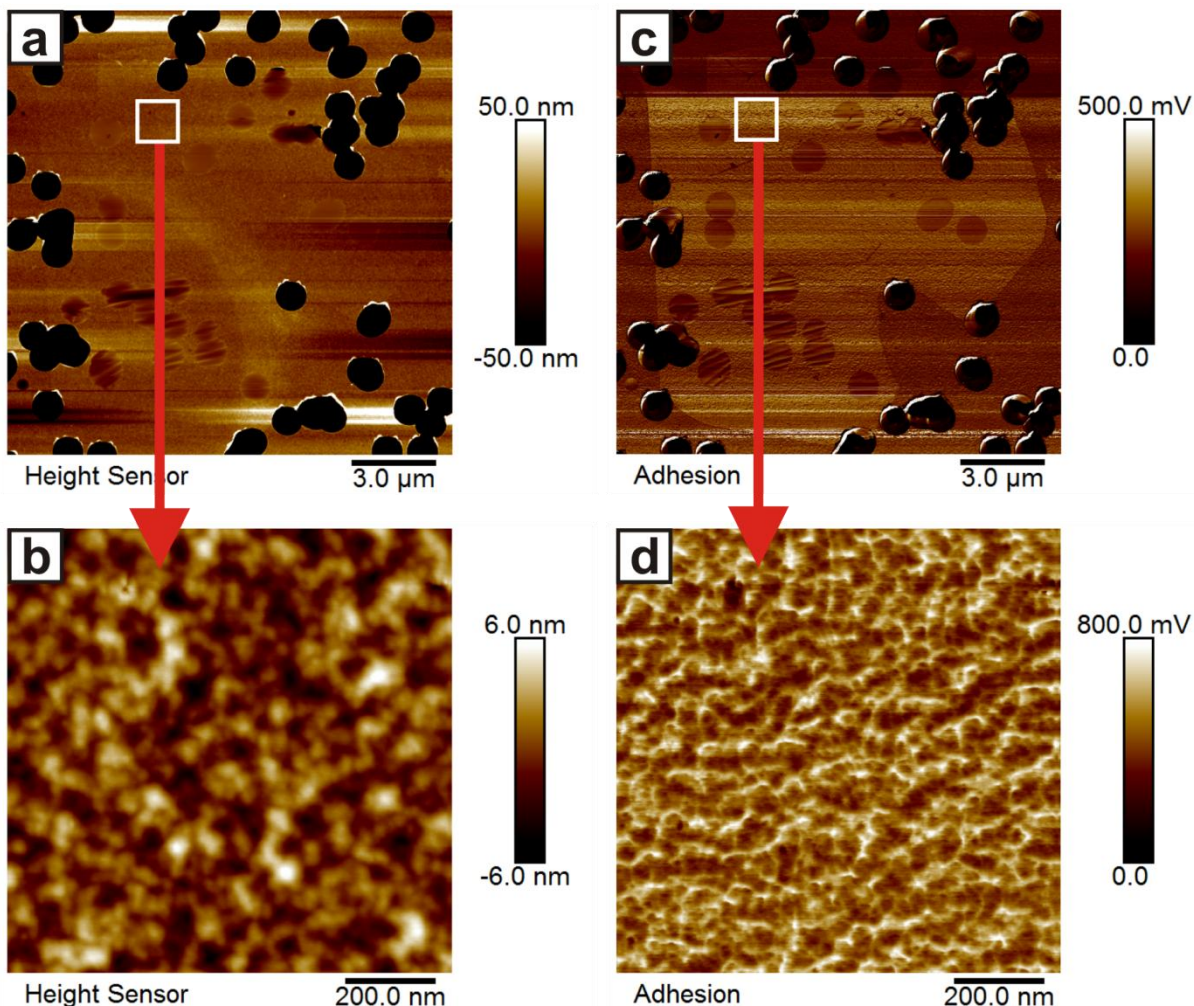


**Figure S10.** Pristine bilayer sample on a micropore-filter. In the AFM image a, b (height sensor) and c, d (adhesion channel) a smooth surface without any dendrimer traces is shown. Corresponding topographical as well as adhesion-data zoom-ins illustrate the dendrimer-free surface (b, d).

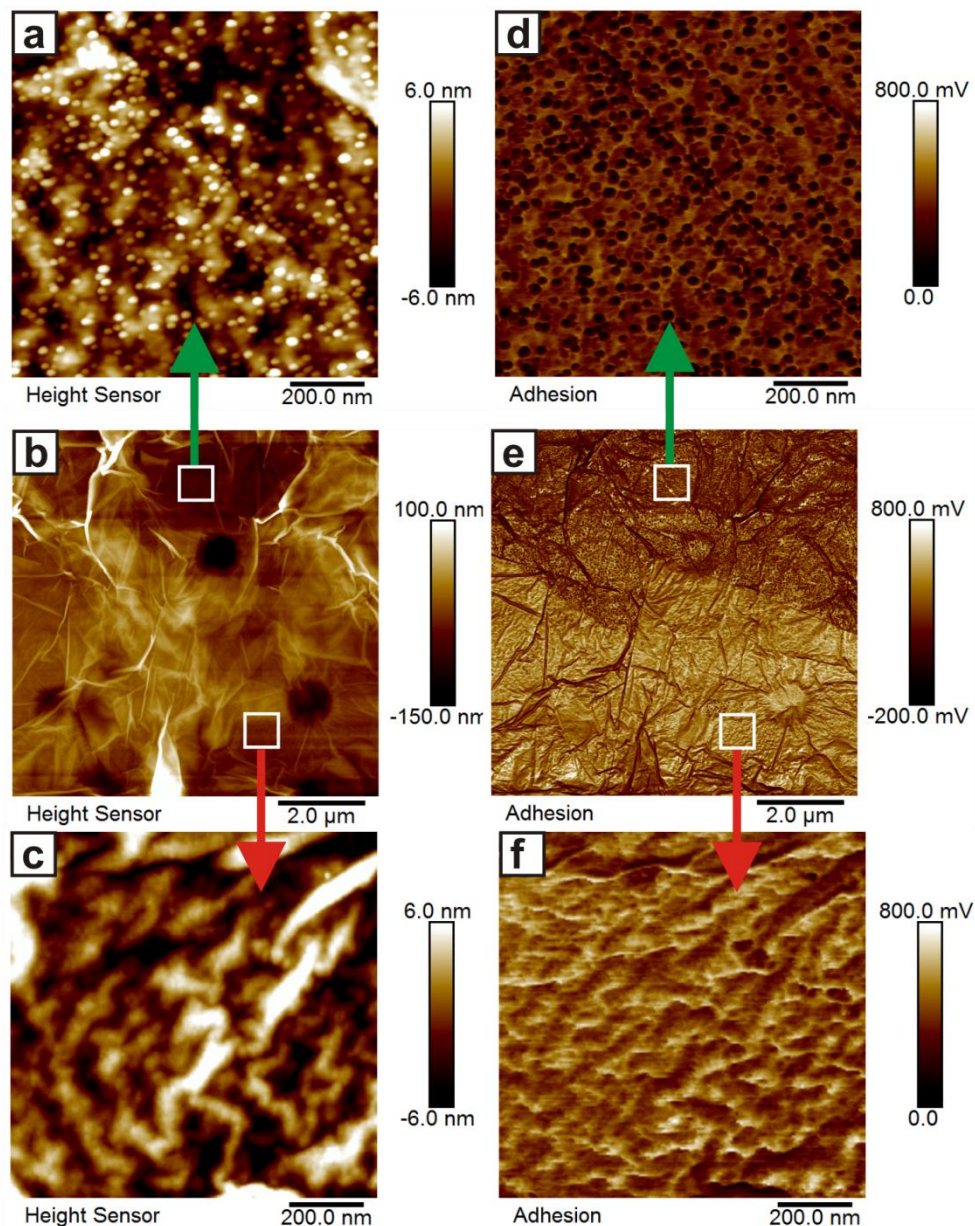


**Figure S11.** Janus-modification: In the AFM images a, b, c (height sensor) and d, e, f (adhesion channel) two different platelet surfaces can be clearly distinguished. The adhesion-data of the overview image e clearly show a contrast variation between a dendrimer covered platelet (top) and a PEI-EO covered platelet (bottom). Corresponding topographical- as well as adhesion-data zoom-ins visualize the dendrimer-free (c, f) and dendrimer-covered (a, d) platelet surface.

### Supporting references

- [1] J. Breu, W. Seidl, A. J. Stoll, K. G. Lange, T. U. Probst, *Chem. Mater.* **2001**, *13*, 4213-4220.
- [2] M. Stöter, D. A. Kunz, M. Schmidt, D. Hirsemann, H. Kalo, B. Putz, J. Senker, J. Breu, *Langmuir* **2013**, *29*, 1280-1285.
- [3] S. Förster, S. Fischer, K. Zielske, C. Schellbach, M. Sztucki, P. Lindner, J. Perlich, *Adv. Colloid Interface Sci.* **2011**, *163*, 53-83.
- [4] D. A. Kunz, J. Erath, D. Kluge, H. Thurn, B. Putz, A. Fery, J. Breu, *ACS Appl. Mater. Interfaces* **2013**, *5*, 5851-5855.
- [5] D. A. Kunz, P. Feicht, S. Gödrich, H. Thurn, G. Papastavrou, A. Fery, J. Breu, *Adv. Mater.* **2013**, *25*, 1337-1341.
- [6] D. M. Moore, R. C. Reynolds, M. Duane, *X-ray diffraction and the identification and analysis of clay minerals*, Oxford University Press, Oxford, U.K. **1997**.
- [7] M. W. Möller, D. Hirsemann, F. Haarmann, J. Senker, J. Breu, *Chem. Mater.* **2010**, *22*, 186-196.
- [8] H. Kalo, W. Milius, J. Breu, *RSC Adv.* **2012**, *2*, 8452-8459.
- [9] J. W. Gruner, *Amer. Mineral.* **1939**, *24*, 428-433.
- [10] M. Stöter, B. Biersack, S. Rosenfeldt, M. J. Leitl, H. Kalo, R. Schobert, H. Yersin, G. A. Ozin, S. Förster, J. Breu, *Angew. Chem. Int. Ed.* **2015**, *54*, 4963-4967.
- [11] E. Paineau, I. Bihannic, C. Baravian, A. M. Philippe, P. Davidson, P. Levitz, S. S. Funari, C. Rochas, L. J. Michot, *Langmuir* **2011**, *27*, 5562-5573.
- [12] J. Breu, W. Seidl, A. Stoll, Z. Anorg. Allg. Chem. **2003**, *629*, 503-515.

## 5.5 Kontrollierte Exfolierung von Schichtsilikaten

Matthias Stöter,<sup>[a]</sup> Dr. Sabine Rosenfeldt,<sup>[b]</sup> Prof. Dr. Josef Breu<sup>[a]</sup>

### Tunable exfoliation of synthetic clays

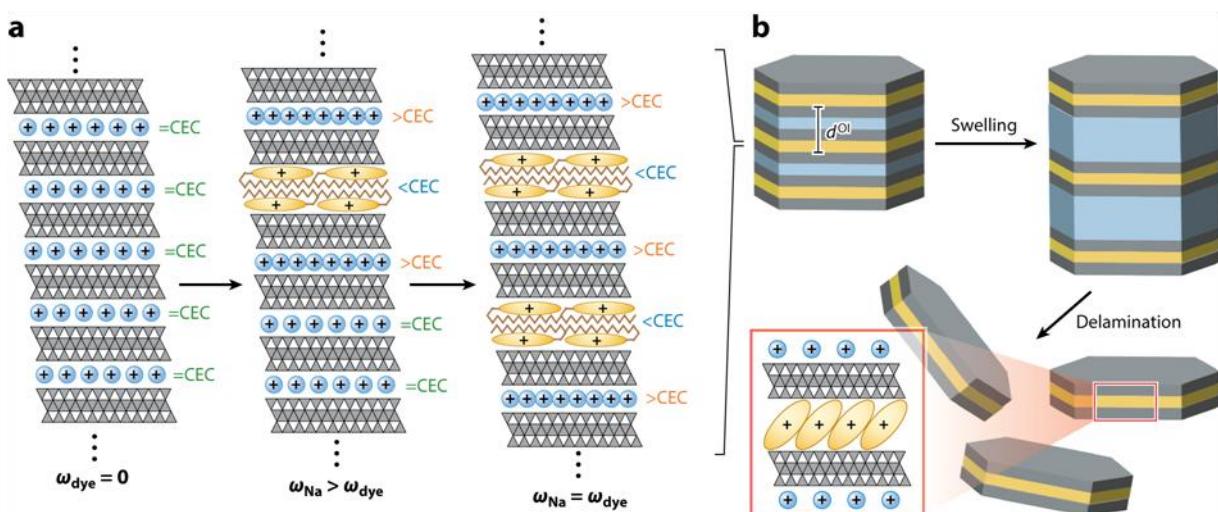
Erschienen in: Annual Review of Materials Research, 2015, 45, 129–51.

Reprinted with permission. Copyright 2015, Annual Reviews.

Impact Factor (2014) Annual Review of Materials Research: 11.854

<sup>[a]</sup> Lehrstuhl für Anorganische Chemie I, Universität Bayreuth, D-95440 Bayreuth, Germany

<sup>[b]</sup> Physikalische Chemie I, Universität Bayreuth, 95440 Bayreuth, Germany



Stöter M, et al. 2015.  
Annu. Rev. Mater. Res. 45:129–51

### Darstellung des Eigenanteils:

Das Konzept dieses Übersichtartikels stammt von Prof. Dr. Josef Breu. Die bisher unveröffentlichten SAXS Messung wurde von Dr. Sabine Rosenfeldt durchgeführt. Die Literaturrecherche, Auswahl und Überarbeitung der Graphiken führte ich durch. Verfasst wurde diese Publikation von Prof. Dr. Josef Breu und mir. Mein Eigenanteil beträgt ca. 80 %

## 5.5.1 Tunable exfoliation of synthetic clays



ANNUAL REVIEWS **Further**  
Click here for quick links to Annual Reviews content online, including:  
• Other articles in this volume  
• Top cited articles  
• Top downloaded articles  
• Our comprehensive search

**Keynote Topic**  
This article is part of the **2D Materials Beyond Graphene** keynote topic compilation.

# Tunable Exfoliation of Synthetic Clays

Matthias Stöter,<sup>1</sup> Sabine Rosenfeldt,<sup>2</sup> and Josef Breu<sup>1,\*</sup>

<sup>1</sup>Lehrstuhl für Anorganische Chemie I and <sup>2</sup>Physikalische Chemie, Universität Bayreuth, D-95440 Bayreuth, Germany; email: sabine.rosenfeldt@uni-bayreuth.de, Josef.Breu@uni-bayreuth.de

Annu. Rev. Mater. Res. 2015. 45:129–51

First published online as a Review in Advance on March 30, 2015

The *Annual Review of Materials Research* is online at [matsci.annualreviews.org](http://matsci.annualreviews.org)

This article's doi:  
[10.1146/annurev-matsci-070214-020830](https://doi.org/10.1146/annurev-matsci-070214-020830)

Copyright © 2015 by Annual Reviews.  
All rights reserved

\*Corresponding author

## Keywords

exfoliation, delamination, ordered interstratification, gas barrier, mechanical reinforcement, flame retardancy

## Abstract

The large hydration enthalpy of inorganic interlayer cations sandwiched between moderately negatively charged silicate layers endows to smectites (e.g., hectorite) remarkably rich intracrystalline reactivity compared with most other layered materials. Moreover, they are transparent and inert in most potential suspension media. Upon suspension in water, smectites readily swell. For homogeneous, melt-synthesized smectites, the degree of swelling can be tuned by choice of interlayer cation and charge density of the layer. Because swelling renders the clay stacks more shear labile, the efficiency of exfoliation by applying shearing forces can in turn be adjusted. Certain smectites even spontaneously delaminate into clay platelets of uniform thickness of 1 nm by progressive osmotic swelling. Osmotic swelling can also be applied to produce well-defined double stacks when one starts with ordered, interstratified heterostructures. Nanocomposites made with high-aspect-ratio fillers obtained this way show superior mechanical, flame retardancy, and permeability properties.

129

## 1. INTRODUCTION

**Exfoliation:** slicing of tactoids into thinner stacks

**Delamination:**

exfoliation of a layered material to the level of individual layers, a state in which translational symmetry along the stacking direction is destroyed

**Mica:** a general term for platy phyllosilicates of 2:1 layers and a layer charge of approximately  $-1.0$  per formula unit

**Tactoid:** a stack of layers; because individual layers are stacked with frequent faults or even in a completely random way, stacks of layers lack strict crystallographic coherence and consequently should not be referred to as crystals

Cooperativity ties the physical properties of solid materials strongly to (translational) symmetry. In layered materials, bonding is by definition profoundly anisotropic. As a consequence, the translational symmetry is prone to be disturbed by planar defects, interstratification, and exfoliation (1–3). Delaminating the material into single or ultrathin layers destroys translational symmetry along the stacking direction (4). As the translational symmetry is modulated, for instance, the phononic (5), electronic (6), ferroic (7), electrochemical, and mechanical (8, 9) properties change dramatically. For example, a dense but random (turbostratic) stacking of two-dimensionally crystalline WS<sub>2</sub> sheets shows unprecedentedly ultralow thermal conductivity (5). Graphene is a two-dimensional topological insulator in which a weak spin-orbital coupling produces a small band gap at the Dirac points (10). In contrast to the bulk material, single-atomic layer MoS<sub>2</sub> is piezoelectric (7). Subnanometer-thick layers of delaminated graphene oxide or 2:1-layered silicates show high tensile strength while being extremely flexible with regard to wrinkling (9, 11–14).

Besides these physical effects, exfoliation increases the total surface and the aspect ratio of a layered material. In this line, multilayer stacks of titanium carbide (a member of the MXene family of materials) were recently shown to have excellent volumetric capacity at extremely high charging rates (15). When micaceous fillers are incorporated into polymer matrices, the specific surface area is converted into a specific interface area. The improvement of properties like bulk modulus (16) and permeability (17, 18) crucially depend, in a highly nonlinear manner, on the aspect ratio. The aspect ratio may be increased either by synthesizing tactoids with larger lateral extension or by making them thinner (exfoliation). At a given lateral dimension for increasing the aspect ratio, an economical, anisotropic, top-down process is needed that imparts high shearing forces preferentially along the plane of the tactoid, allowing for selective exfoliation while minimizing platelet breakage (**Figure 1**).

Aspect ratio, platelet stiffness, the specific interface area, the absolute number of platelets per weight, and the distance between platelets at a given filler content are, however, highly correlated. In some cases, a complete delamination to individual layers may even be disadvantageous. For instance, for nanocomposites a higher interface area may be favorable, whereas the decreased

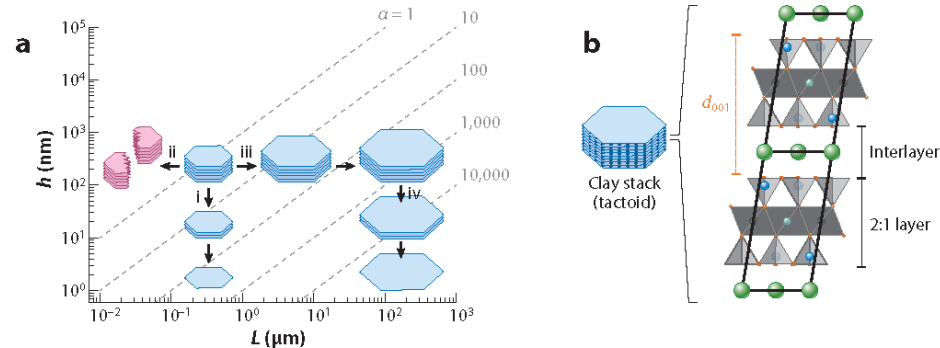


**Figure 1**

(a) The reduction of the tactoid height ( $h$ ) by exfoliation/delamination (*i*) increases the aspect ratio ( $\alpha$ ), whereas fracture (*ii*) decreases  $\alpha$ . Enlargement of the tactoid diameter  $L$  achieved by advancing synthesis conditions (*iii*) followed by complete delamination (*iv*) gives access to ultrahigh aspect ratios. The dashed lines mark decadal isopleths of  $\alpha$ . (b) The structure of a 2:1-layered silicate. The basal spacing ( $d_{001}$ ) is the sum of interlayer height and silicate layer thickness and represents the periodicity along the stacking direction. Adapted with permission from Reference 19.

**Table 1** Selection of layered materials mentioned in the text

	Conductive	Insulating	
		Cationic	Anionic
Charged	$\text{Li}_x\text{C}_6$	Layered double hydroxides	Smectites (e.g., hectorite and montmorillonite)
	$\text{C}_m^{+*}\text{X}^- \cdot n\text{HX}$ ( $\text{HX} = \text{H}_2\text{SO}_4$ , $\text{HNO}_3$ )		Graphite oxide
	$\text{Li}_x\text{MoS}_2$ , $\text{Li}_x\text{TiS}_2$		Vermiculite
	$\text{K}_4\text{Nb}_6\text{O}_{17}$		Mica
Neutral	Graphite	Kaolinite	
	$\text{MoS}_2$ , $\text{TiS}_2$	Talc	
	MXenes		

stiffness of the tactoids may be detrimental for mechanical reinforcement. Consequently, the optimum may be achieved for a multistack of a certain tactoid thickness. Controlling the degree of exfoliation is therefore highly desirable and requires fine-tuning the subtle balance of shearing forces provided by the different processes and the shearing lability of the material. We review potential solutions to this challenge, with a special focus on synthetic clay minerals as well-defined and well-characterized model compounds.

## 2. TUNING THE STACKING INTERACTION

The likelihood of tactoid breakage is related to the tensile strength and is determined by (partially) covalent, in-plane bonding. Adjacent layers in the tactoid are held together by comparatively weak forces like van der Waals, hydrogen bonding, and Coulomb attraction. As a consequence of this anisotropic bonding, many layered compounds can accommodate various ions or molecules into the interlayer space between adjacent layers. This intracrystalline reactivity is a unique characteristic of layered compounds. Guest species are, however, intercalated only if the intracrystalline reaction is thermodynamically favored. For neutral layers (Table 1), the strongest possible driving force for intercalation is thus hydrogen bonding to functional groups at the basal surfaces of the layers. For instance, for kaolinite, many intercalation compounds of strongly hydrogen-bonding neutral molecules are known (20–26). In rare cases, intercalation may not be strictly topotactic, as the guest may eventually replace the pristine functional group at the basal surface (a hydroxyl group in the case of kaolinite) and may become grafted to the basal plane, changing the composition of the layer (27). For talc, which lacks functional groups at the basal surface and offers only van der Waals interactions for potential guest molecules, no intercalation compounds are known due to lack of a strong driving force.

For conducting layered hosts (Table 1), intercalation can be forced upon by (electro)chemistry. By removing  $\text{C}_m^{2+}\text{SO}_4^{2-} \cdot n\text{H}_2\text{SO}_4$  or adding  $\text{Li}_x\text{C}_6$  electrons (28–31), the layers in graphite become at least formally charged, and concomitantly counterions must be introduced between the layers to assure charge neutrality. Similarly, dichalcogenides can easily be lithiated (e.g.,  $\text{Li}_x\text{TiS}_2$ ) (32). If harsh conditions must be applied to drive the redox reactions, the intercalation compounds produced, however, inherit the redox potentials/electromotive forces needed in the reaction and may, in turn, be strong reducing or oxidizing agents. Consequently, some of the compounds readily deintercalate when suspended in noninert solvents like water (33).  $\text{Li}_x\text{MoS}_2$ , for instance, has a strongly negative redox potential and deintercalates almost completely when immersed in water (34, 35).

---

**Talc:** group name for platy phyllosilicates of 2:1 layers and a layer charge of ~0 per formula unit

---

**Table 2 Comparison of charge densities and hydration enthalpies of smectites and layered double hydroxides**

	Smectites	Layered double hydroxides
Equivalent areas ( $\text{\AA}^2 \text{ charge}^{-1}$ )	119–40 for $0.2 < x < 0.6$	40–24 for $0.3 < x < 0.33$
Hydration enthalpy ( $\text{kJ mol}^{-1}$ ) <sup>a</sup>	$\text{H}^+$ : 1,090	$\text{Br}^-$ : 347
	$\text{Li}^+$ : 519	$\text{Cl}^-$ : 381
	$\text{Na}^+$ : 409	$\text{NO}_3^-$ : 314
	$\text{K}^+$ : 322	$\text{SO}_4^{2-}$ : 1,059
	$\text{Mg}^{2+}$ : 1,921	$\text{CO}_3^{2-}$ : 1,314

<sup>a</sup>Data from Smith (53).

If such charged intercalation compounds (Table 1) are, however, stable in the suspension medium, the solvation enthalpy of the interlayer ions represents a strong driving force for further intercalation. This additional incorporation of neutral solvent molecules is referred to as swelling. The expansion of the interlayer space must again be thermodynamically feasible, meaning that the solvation enthalpy must be high enough to overcome the electrostatic attraction between the interlayer space and the charged layers. Highly charged layers like  $\text{K}_4\text{Nb}_6\text{O}_{17}$  do not swell unless most of the  $\text{K}^+$  is exchanged for protons ( $\text{H}_x\text{K}_{4-x}\text{Nb}_6\text{O}_{17}$ ) with a very large hydration enthalpy (Table 2) (36). Similarly, mica (e.g., biotite  $[\text{K}]_{\text{inter}}^{[\text{Mg},\text{Fe}]};\text{oct}^{[\text{Si}_3\text{Al}]^{[\text{tet}]}}\text{O}_{10}(\text{OH},\text{F})_2$ ) is unable to swell due to the combination of high charge density and comparatively low hydration enthalpy of  $\text{K}^+$ , whereas a brittle mica with  $\text{Na}^+$  in the interlayer ( $[\text{Na}_2]_{\text{inter}}^{[\text{Mg}_3]^{[\text{oct}^{[\text{Si}_2\text{Al}_2]^{[\text{tet}]}(\text{OH},\text{F})_2]}}$ ) readily swells with water (37).

In any case, increasing interlayer space weakens attractive forces between individual layers and renders the tactoids more shear labile and thus more prone to exfoliation when shear forces are applied, e.g., by ball milling. Moreover, the neutral solvent molecules may be instantly deintercalated by thermal shock. The concomitant rapid volume expansion pops the tactoids (38, 39). Expanded vermiculite and expanded graphite are made this way from hydrated vermiculite and  $\text{C}_m^{2+}\text{SO}_4^{2-} \cdot n\text{H}_2\text{SO}_4$ , respectively. The rapid expansion, however, triggers not only exfoliation but also a good deal of platelet breakage, and thermal shock is thus not the best approach to maximize aspect ratio.

An important, but frequently overlooked, aspect of charged layered systems is that Coulomb attraction strongly favors segregation of counterions: If counterions of different sizes are offered to neutralize the charged layers, they tend to segregate into different interlayer spaces because this behavior minimizes the average basal spacing and thus maximizes the Coulomb interaction for the mixed system. Similarly, in equilibrium at intermediate charge densities, staging is thermodynamically favored for graphite intercalation (31). In staged intercalation compounds, the overall stoichiometry is assured by the ratio of ion-containing interlayers and pristine graphene-like interlayers. The two types of interlayers are furthermore stacked in an ordered fashion, leading to a superstructure along the stacking direction that can easily be detected by X-ray diffraction. Alternating structures with two, three, or even four graphene layers followed by one lithium layer are known (40).

Staging is frequently encountered with conducting layers, probably because the charge densities of individual layers can easily be adjusted by simply reshuffling electrons. In contrast, examples of ordered interstratifications are very rare with insulating layered materials because charge densities in this class cannot be adjusted easily as intercalation proceeds. Only a limited number

#### Vermiculite:

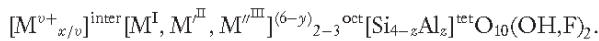
group name for platy swelling phyllosilicates of 2:1 layers and a layer charge of approximately  $-0.9$  to  $-0.6$  per formula unit

of rectorite-type clay materials with *Reichweite I*<sup>1</sup> have been described (41, 42) and are discussed in detail below. These staged or ordered interstratified structures have the potential to allow for delamination of the material into multistacks with a well-defined number of layers (43, 44).

Not only are insulating layered materials, like swelling clay minerals (smectites), stable over a wide range of electrochemical potentials and thus in most suspension media, but they also tend to be more transparent than low-band-gap materials, which is advantageous, for instance, in optical applications.

The intracrystalline reactivity of insulating charged layered materials is closely related to the charge density and the solvation enthalpy of the interlayer ions. The swelling of smectites with water, for instance, can easily be adjusted by cation exchange (hydration enthalpy) and by controlling the composition (layer charge).

The negative layer charge of smectites, vermiculites, and micas is, however, generated by an isomorphous substitution of structural ions in the octahedral sheet (e.g.,  $Mg^{2+}$  with  $Li^{+}$ ) and/or the tetrahedral sheet (e.g.,  $Si^{4+}$  with  $Al^{3+}$ ). The general formula is



To produce a homogeneous intracrystalline reactivity, a homogeneous charge density is necessary, and thus isomorphous substitution must be strictly statistical. The materials must represent true solid solutions. Monte Carlo simulations of the order-disorder behavior of cations in the octahedral sheets of various such 2:1 silicate layers have, however, suggested that, for most compositions, the octahedral cations segregate into domains within a layer. The layers then inevitably exhibit charge heterogeneities when made at low temperatures (45). Moreover, within a tactoid, charge density also varies between adjacent layers (46). Although the degree of segregation is highly dependent on the nature of the cation, temperatures exceeding 1,000 K are often necessary to achieve a statistical solid solution with a homogeneous charge density. At lower genesis temperatures, the different cations begin to cluster, resulting in domains of higher and lower charge density. Genesis of natural clay minerals like montmorillonite typically takes place at low to moderate temperatures (<400 K), and thus the charge density of these abundant natural materials varies spatially between different layers as well as within domains in a single layer.

Swelling is, in turn, a good indicator of charge heterogeneities. The degree of swelling in water in a first approximation reflects the balance of the solvation enthalpy of interlayer cations or anions and attractive forces between the hydrated ions and the charged surface (van der Waals, hydrogen, and Coulomb interactions). Increasing layer charge increases attractive forces between the layers and tends to retard swelling in, e.g., water and organic solvents like ethylene glycol (46–48). For charge-homogeneous samples, the hydration enthalpy obtained at a certain relative humidity (RH) is high enough to swell the layer by incorporating one, two, or three water layers. Because the charge density is homogeneous, the number of cations in the interlayer space is uniform, and hence the reactivity towards hydration of all interlayers in the tactoid is the same. With increasing RH, all interlayer space then transforms at the same time into the next hydration state, and sharp, steplike transitions between hydration states should be observed. In natural clays with charge heterogeneity, however, rather randomly interstratified domains are formed in which different hydration states of one, two, or three water layers are concurrently present for any given RH (48). Because the basal spacing varies randomly within the coherence length of the X-ray beam, a weighted average of the  $d$  spacings is observed, which is of limited analytical value (49).

<sup>1</sup>This notation for superstructures is preferred in the clay community.

**Rectorite:** a regular interstratification of mica and smectite in a 1:1 ratio

**Smectite:** a group name for platy swelling phyllosilicates of 2:1 layers and a layer charge of approximately –0.6 to –0.2 per formula unit

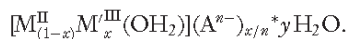
**Montmorillonite:** dioctahedral clay mineral of the smectite group with mainly isomorphous octahedral substitution of  $Mg^{2+}$  with trivalent cations such as  $Al^{3+}$  or  $Fe^{3+}$

**Hectorite:**

trioctahedral clay mineral of the smectite group with mainly octahedral substitution of  $Mg^{2+}$  with  $Li^+$

Clays made from the melt at synthesis temperatures exceeding 1,000 K show homogeneous charge density. Consequently, as expected, swelling in water produces sharp transitions between the different hydration steps (50). Moreover, partial ion exchange with cations of different sizes (42) or different hydration enthalpies (41) forms ordered interstratifications of *Reichweite I* similar to staging in graphite.

The intracrystalline reactivity of smectites is, for two reasons, much higher than the reactivity of so-called cationic clays like layered double hydroxides (LDHs). For LDHs, positively charged layers are generated by the isomorphous substitution of octahedral cations (e.g.,  $Mg^{2+}$ ) with cations of higher ionic charge (e.g.,  $Al^{3+}$ ). The general formula is



LDHs typically show values for  $x$  of  $0.2 < x < 0.33$ , giving a charge density of one positive charge per  $24\text{--}40 \text{ \AA}^2$  (equivalent area). This value is significantly higher than typical charge densities of smectites with equivalent areas of  $119\text{--}40 \text{ \AA}^2$ . Moreover, in LDHs the positive charge is compensated for by anions, which tend to have significantly lower hydration enthalpies than do the isovalent cationic counterparts (Table 2). As for smectites, the degree of swelling of LDHs in water depends on (a) the type of anion that determines both hydrogen bonding to the hydroxyl groups residing at the basal plane and the hydration enthalpy and (b) the composition of the hydroxyl layers defining the charge density (51). The interactions between adjacent layers in the tactoids may be further modulated by hydrogen bonding between intercalated water molecules (52).

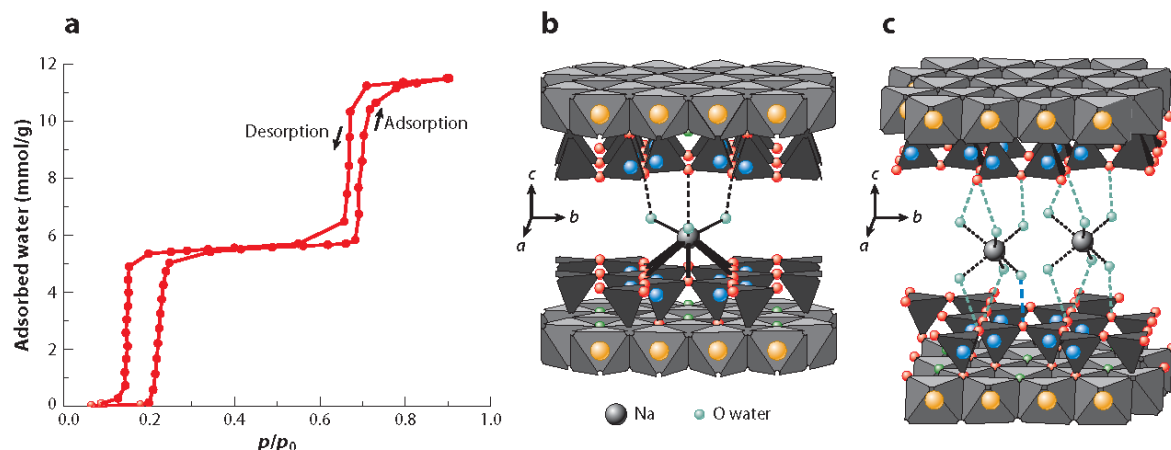
The higher charge density of LDHs, possibly supported by hydrogen bonding of interlayer species to hydroxyl groups at the basal surfaces, in combination with lower hydration enthalpies of interlayer anions renders LDHs less shear labile compared with smectites. Delamination of LDHs was nevertheless reported to be possible in formamide, probably because hydrogen bonds are weakened in this suspension medium (54).

In contrast to LDHs, 2:1-layered silicates with charge densities in the regime of smectites can easily be exfoliated in water by applying shear forces (55). Different methods for shearing may be used and are discussed below in detail. Furthermore, spontaneous delamination of tactoids in water into single, 1-nm-thick 2:1 layers is reported for combinations of low to moderate charge densities ( $120\text{--}50 \text{ \AA}^2 \text{ charge}^{-1}$ ) and monovalent cations of high hydration enthalpy like  $Li^+$  and  $Na^+$  (4, 19, 56). The swelling of smectites in water is therefore discussed next in more detail.

### 3. SWELLING OF SMECTITES IN WATER AND ITS IMPLICATIONS FOR EXFOLIATION

As discussed above, the tendencies of interlayer cations to solvate cause clay minerals to expand the interlayer space and to accommodate water molecules. Two swelling regimes can be identified. At low water concentration, a series of discrete hydration steps is realized. This swelling regime is referred to as crystalline swelling. Under certain circumstances, crystalline swelling may be followed by osmotic swelling, in which continuum electrostatic forces govern the interactions between adjacent layers. Osmotic swelling was first observed for graphite oxide as early as 1932 (57) and was shortly thereafter confirmed for montmorillonite (58).

The swelling phenomenon of natural clay minerals is always masked by charge density heterogeneities inherent in the material. Thus, henceforth we focus on synthetic hectorites synthesized from the melt at temperatures well above 1,000 K.

**Figure 2**

(a) Water vapor sorption isotherm of a melt-synthesized  $\text{Na}_{0.5}$ -hectorite ( $x = 0.5$ ) as a function of the relative humidity ( $p/p_0$ ). Modified from Reference 42. Copyright 2014, American Chemical Society. (b,c) The corresponding hydrated structures of (b) one-layer and (c) two-layer hydrate. Only the upper and lower tetrahedral sheets are shown. Adapted with permission from Reference 64.

### 3.1. Crystalline Swelling

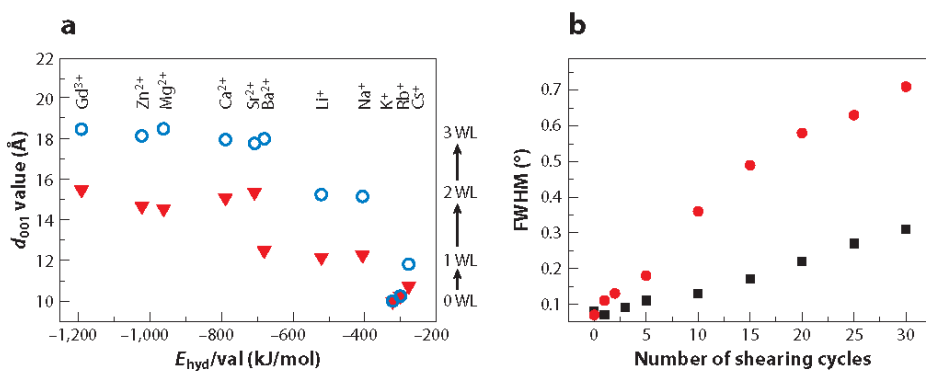
2:1-layered silicates form hydrated crystalline structures in humid air, in water of higher ionic strength, and in water/organic solvent mixtures. If synthetic hectorites are exposed to humid air, one, two or three water layers are incorporated into the interlayer space, depending on the RH and on the type of interlayer cation (59, 60). In contrast to the case for natural clays—in which, due to charge heterogeneity, interstratified domains of different hydration states are concomitantly present and hydration curves are more sluggish (48)—for synthetic hectorite, there are sharp transitions between the crystalline hydration states (Figure 2a), indicating a uniform intracrystalline reactivity.

On the basis of various simulation studies, the hysteresis observed between different hydration states suggests that the transition between hydration steps must be regarded to be phase changes that are controlled by thermodynamics (61, 62). The molecular origin of the observed energy barrier between different hydration states is the breaking and formation of hydrogen bonds with the clay surface (63).

With slightly higher layer charge, these hydrogen bonds become strong enough to ensure a well-defined phase relationship of adjacent silicate layers. For the one- and two-layer hydrate of  $[\text{Na}_{0.7}]_{\text{inter}}^{\text{ter}} [\text{Mg}_{2.3}\text{Li}_{0.7}]^{\text{oct}} [\text{Si}_4]^{\text{tet}} \text{O}_{10}\text{F}_2$ , the hydrated interlayer cations bridge the interlayer space by hydrogen bonding, thus reinforcing an ordered stacking of the layers, and crystals instead of tactoids are obtained (Figure 2b,c). The crystals not only are three-dimensionally ordered but are large enough to allow for a reliable single-crystal structure refinement for hydrated smectite phases (64).

### 3.2. Tuning Shear Lability by Ion Exchange

At a given charge density (here  $[\text{Na}_{0.5}]_{\text{inter}}^{\text{ter}} [\text{Mg}_{2.5}\text{Li}_{0.5}]^{\text{oct}} [\text{Si}_4]^{\text{tet}} \text{O}_{10}\text{F}_2$  is defined as  $\text{Na}_{0.5}$ -hec, where hec means hectorite), which implies a certain strength of the Coulomb interactions along the

**Figure 3**

(a) Hydration states of hectorites as obtained from X-ray diffraction measurements as a function of selected interlayer cations. The  $d_{001}$  values for moist samples (blue circles) and samples air dried at 40% relative humidity (red triangles) are plotted versus the enthalpy of hydration per valence of the interlayer cations. Observed  $d_{001}$  values correspond to various states of hydration, with 0, 1, 2, or 3 intercalated water layers (WL). (b) Evolution of full width at half-maximum (FWHM) values of the  $d_{001}$  reflections for two-layer hydrate of  $\text{Na}_{0.5}\text{-hec}$  (black squares) and three-layer hydrate of  $\text{Mg}_{0.5}\text{-hec}$  (red dots) with the number of applied shearing cycles. Hec denotes hectorite. Reproduced with permission from Reference 65. Copyright 2010, American Chemical Society.

stacking direction, the shear lability of tactoids can be tuned by simple ion exchange (65). Because the hydration enthalpy per charge can be varied over a wide range with the choice of interlayer cation (Table 2 and Figure 3a), it is possible to switch between the different phases in the crystalline swelling regime at a given RH by the proper choice of interlayer cation. At 40% RH (Figure 3a),  $\text{K}_{0.5}\text{-hec}$  does not intercalate any water,  $\text{Na}_{0.5}\text{-hec}$  adopts the one-layer hydrate state, and  $\text{Mg}_{0.5}\text{-hec}$  hydrates to the level of the two-layer hydrate. Increasing the water activity by immersing the compounds into water increases the degree of hydration:  $\text{K}_{0.5}\text{-hec}$  still does not intercalate any water,  $\text{Na}_{0.5}\text{-hec}$  adopts the two-layer hydrate, and  $\text{Mg}_{0.5}\text{-hec}$  adopts the three-layer hydrate.

The structure of the three-layer hydrate is unknown. Simulations of this hydration state propose three types of water molecules (66). Similar to the known one- and two-layer hydrates, the first type of interlayer water is part of the first hydration shell of the cation and is located in the middle of the interlayer plane. The second type forms two water planes with hydrogen bonds to the two basal surfaces of the 2:1 silicate layers enclosing the interlayer space. The third water type fills interstitials. The additional layer of water in the interlayer space represents an efficient lubricant and renders the three-layer hydrate most shear labile. Increasing basal spacing reduces the attractive Coulomb and van der Waals interactions between the positively charged interlayer space and the negatively charged silicate layer significantly by a factor of  $1/d$  and  $1/d^6$  for Coulomb and van der Waals interactions, respectively (65). Consequently, the  $\text{Mg}_{0.5}\text{-hec}$  should be exfoliated more efficiently by mechanical agitation than is, for instance,  $\text{Na}_{0.5}\text{-hec}$ .

### 3.3. Mechanical Exfoliation

The main goal of the physical treatment is the mechanical shearing of tactoids into thinner stacks (exfoliation) while avoiding breakage of the tactoids; such breakage would inevitably reduce the aspect ratio of the clay (Figure 1). Consequently, milling systems that operate with unidirectional

shearing forces are preferred. Microfluidizer and stirred media mills are therefore the preferred instruments because these techniques provide the highest shearing forces. In the literature, ultrasound is most frequently used to disperse and/or exfoliate materials. In our experience, however, ultrasonic treatment preferentially breaks the clay platelets. This breakage may be related to recent work on so-called graphene drums. Graphene can be used as a mechanical resonator in the same way that a musician uses a drumhead. Microwave-frequency light “plays” these graphene drums (67). Similarly, ultrasound may excite undulations perpendicular to platelets acting as nanomembranes that eventually lead to breakage.

When one applies the same shearing load, as expressed by the number of shearing cycles, for the three-layer hydrate of  $Mg_{0.5}$ -hec ( $d_{001} = 18.7 \text{ \AA}$ ) the full width at half-maximum (FWHM) of the  $d_{001}$  reflections increases significantly faster than in the case of the less-hydrated two-layer hydrate of  $Na_{0.5}$ -hec ( $d_{001} = 15.1 \text{ \AA}$ ) (Figure 3b) (65). The FWHM values can be related to the tactoid height, and thinner stacks have higher corresponding FWHM values, suggesting that exfoliation is more efficient for the more shear-labile  $Mg_{0.5}$ -hec (68). For the sake of completeness, we mention that the FWHM is not defined solely by the size of the coherently scattering domains but is also influenced by other factors like strain or random interstratifications. Consequently, reliable absolute stack heights cannot be derived from FWHM, but samples within a series can safely be compared. More reliable tactoid heights of clay tactoids can be obtained, for instance, by atomic force microscopy (AFM) (69).

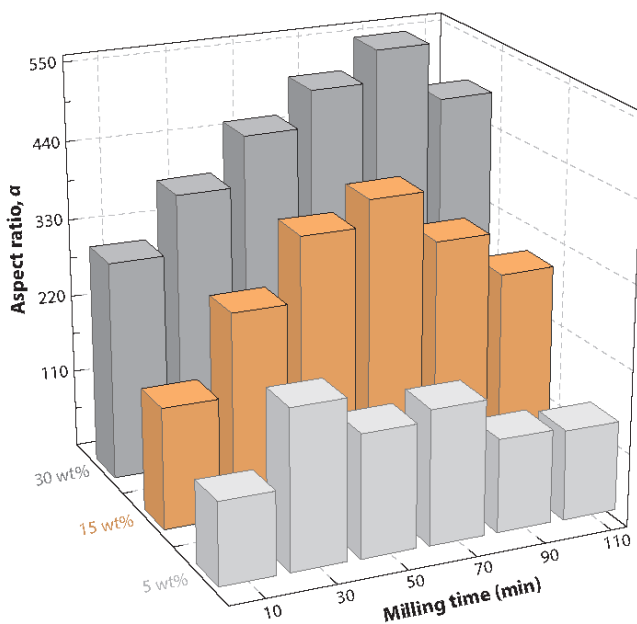
The microfluidizer injects the layered silicate suspension with high pressure into a reaction chamber equipped with a micrometer-diameter channel that is split into a V-shaped shearing geometry. The channel diameter, unfortunately, limits the maximum lateral diameter of tactoids that can be processed. As expected, the more highly swollen  $Mg_{0.5}$ -hec is more shear labile than the less-expanded  $Na_{0.5}$ -hec. The results, moreover, suggest that, by the choice of interlayer cation and the number of shearing cycles, exfoliation can be tuned to a certain degree to deliver tactoids of a certain preferred thickness.

Ball milling, also known as stirred media milling, is an alternative method for the generation of high unidirectional shear stresses (70–72). This method allows the processing of unlimited lateral particle sizes and allows for high solid contents. A broad range of process parameters that influence shearing performance can be varied (55). For instance, according to the stress model, which describes the physical process in stirred media mills, the solid content ( $m_p$ ) of a dispersion is inversely proportional to the specific energy ( $E_s$ ) applied (Equation 1) (70, 71):

$$E_s = \frac{\Delta E}{m_p}. \quad 1.$$

Because the energy input  $\Delta E$  during the milling process is kept constant, the specific energy ( $E_s$ ) decreases with increasing solid content ( $m_p$ ).

Figure 4 shows the influence of the milling time and solid content on aspect ratios of  $Mg_{0.5}$ -hec. The obtained aspect ratio is smaller for low solid contents and decreases for longer milling times due to platelet breakage. Static light-scattering (SLS) measurements of the ball-milled samples showed that a reduction of  $E_s$  reduces platelet breaking (55). Consequently, the maximum aspect ratio was achieved using the highest processable clay content of 30 wt% with a milling time of 90 min. This aspect ratio was ten times higher than the aspect ratio of the pristine hectorite. As with microfluidizing, ball milling proves to be an efficient method to control the exfoliation rate and to gain certain control over the platelet thickness of a shear-labile layered compound. A variation in platelet thicknesses and layer sizes due to platelet breaking is, however, expected whenever mechanical forces are used (69).

**Figure 4**

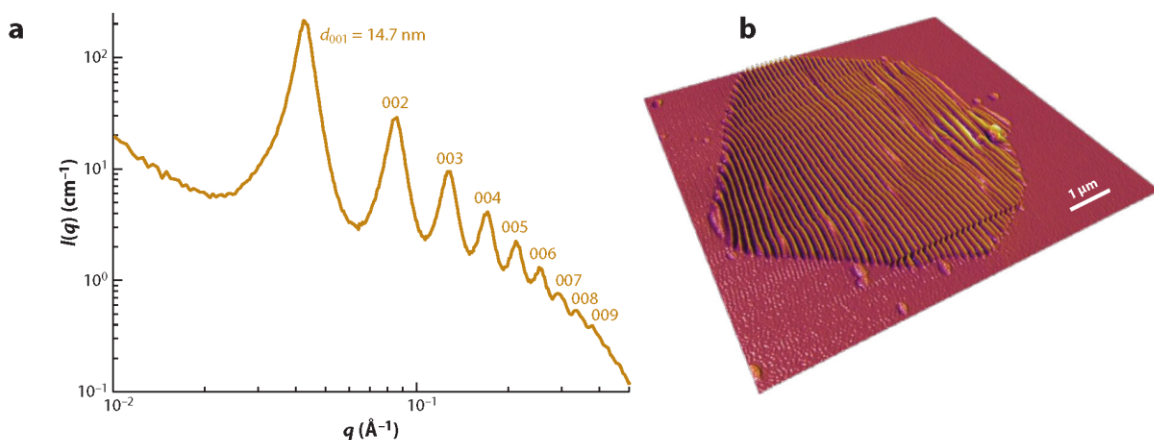
Evolution of estimated aspect ratios ( $\alpha$ ) with milling time for dispersions of different  $Mg_{0.5}$ -hectorite contents. The pristine hectorite showed an average  $\alpha$  of  $\sim 50$ . Reproduced with permission from Reference 55.

### 3.4. Osmotic Swelling

Even when one combines the most versatile shearing techniques with the most shear-labile hydrate phase, the brutal mechanical impact on the platelets leads to some degree of breakage. The aspect ratio of the materials can still be improved but never achieves the maximum value that is encoded in the lateral extension of the pristine material. The preferred method of choice in delamination therefore builds on unsolicited disintegration of the stacks. Certain smectites are a rare example of such spontaneous delamination through progressive osmotic swelling. Osmotic swelling represents the most gentle, cheap, and scalable route to obtain perfectly delaminated clay platelets of uniform thickness of 1 nm.

Diverse studies with different methods such as AFM, transmission electron microscopy (TEM), small-angle X-ray scattering (SAXS), and light scattering provided proof of complete delamination into individual layers for various low-charge layered silicates with  $Li^+$  and  $Na^+$  as interlayer cations (4, 19, 56, 73, 74). Whereas both of these two smallest alkali cations and all divalent cations readily solvate to form outer-sphere complexes in the interlayer space, divalent cations with progressive swelling at any time stay in contact with both adjacent silicate layers and pin them together, hampering osmotic swelling (73, 75–77).  $Li^+$  and  $Na^+$ , however, predominantly stay in close contact with only one of the two silicate layers surrounding the particular interlayer space. The interlayer cations side with one silicate layer, whereby a diffuse double-layer setup evolves and the silicate layers formerly encompassing an interlayer space start to repel each other electrostatically (58).

The repulsion continues all the way to a separation correlating with the Debye length ( $\approx 20$  nm at the charge density of  $Na_{0.5}$ -hec), whereby the interaction between the individual

**Figure 5**

(a) Measured one-dimensional SAXS pattern of a gel sample of long-term annealed Na<sub>0.5</sub>-hectorite (17-wt% Na<sub>0.5</sub>-hectorite). The rational 00l series illustrates a homogeneous swelling of the sample (S. Rosenfeldt, M. Stöter, T. Weiß, S. Förster & J. Breu, unpublished results). (b) AFM topographical image of a typical wrinkled delaminated nanoplatelet of Na<sub>0.5</sub>-hectorite on a stress-released polydimethylsiloxane substrate. Panel b reproduced from Reference 9 with permission. Copyright 2013, American Chemical Society.

silicate layers becomes nil and the material may therefore be regarded to be completely delaminated. Reductions of the negative surface potentials and compression of the diffuse double layer have been observed in organic solvents and in electrolytes like sodium chloride, and ultimately such conditions hamper osmotic swelling (3).

Melt-synthesized [Na<sub>0.5</sub>]<sup>inter</sup>[Mg<sub>2.5</sub>Li<sub>0.5</sub>]<sup>oct</sup>[Si<sub>4</sub>]<sup>tet</sup>O<sub>10</sub>F<sub>2</sub> does not spontaneously delaminate in water (50, 78). Surprisingly, and for reasons not yet fully understood, it may, however, be activated by long-term (6-week) annealing at 1,040°C. When various amounts of water are added to this annealed Na<sub>0.5</sub>-hec, it swells osmotically, and gel formation is observed (74). Below the Debye length, the separation driven by the electrostatic repulsion is adjusted to meet the given water/clay ratio. For 17-wt% hectorite, the homogeneous intracrystalline reactivity assures a perfectly rational 00l series with a  $d$  spacing of 147 Å, as indicated by SAXS (**Figure 5a**).

AFM images of samples of higher dilutions illustrate that the Na<sub>0.5</sub>-hec tactoids completely delaminated into 1-nm-thick nanoplatelets. Consequently, when the platelet diameter as obtained by SLS was considered, median aspect ratios of more than 18,000 were obtained for this material.

Furthermore, these platelets are highly flexible, as shown by a novel wrinkling technique. A polydimethylsiloxane (PDMS) substrate was uniaxially stretched, and a suspension of hectorite was placed onto the PDMS surface. After gentle drying and stress release, wrinkled nanoplatelets were obtained (**Figure 5b**).

Two-dimensional Fourier transformation of the wrinkled surface gives a sharp peak, indicating a uniform in-plane modulus within the whole platelet area. Obviously, no structural defects like holes are generated during osmotic delamination due to its gentle nature. This case is in contrast to that of delaminated graphite oxide, for which, due to harsh oxidation during synthesis, holes are generated, which may be detrimental to mechanical reinforcement in nanocomposites or for gas barrier applications (79). For Na<sub>0.5</sub>-hec, the wrinkling experiment, however, corroborates that hectorite nanoplatelets are defect free, have uniform stiffness, and have structural homogeneity. From the Fourier transformation, a mean in-plane modulus of 142 ± 17 GPa was calculated. This value is 20% lower than the in-plane modulus of mica. Connecting more silicate layers to a mica

sandwich via interlayer cations protruding into surface corrugations of the silicate layers makes the stack more stiff than a singular layer. The high optical transparency and the high aspect ratio, as well as the absence of impurities, render this delaminated clay the perfect filler for high-gas-barrier applications.

#### 4. HOW TO IMPROVE LATERAL EXTENSION

After complete delamination has been accomplished, the aspect ratio can be further improved only if one succeeds in increasing the lateral diameters of the pristine tactoids. Although the platy habitus of layered compounds reflects the anisotropic bonding situation, the absolute extension along the two principal directions is determined by nucleation and growth rates and hence by the factors controlling relative supersaturation. If the layer structure is composed of different subunits, as are 2:1-layered silicates, in which two tetrahedral sheets are condensed to a central octahedral sheet (**Figure 1b**), strain buildup due to subunit misfit also comes into play. In this case, the particular composition and local variations thereof may be crucial factors limiting the maximum tactoid size.

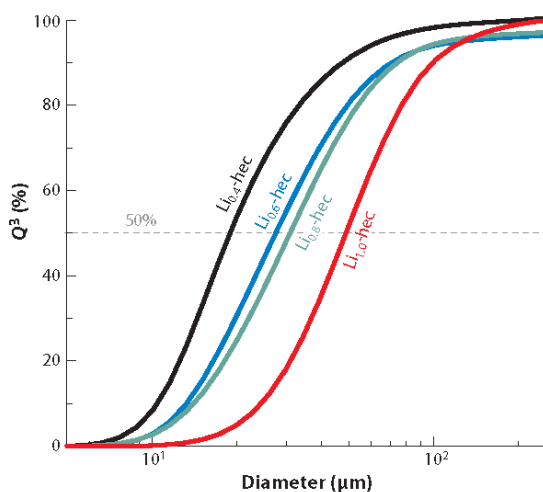
The solubility of silicates in hydrous fluids is generally low. Synthesis in water starting with precursors like tetraethoxysilane therefore tends to produce high supersaturations and consequently high nucleation rates, and the clay tactoids obtained generally have diameters in the nano range. Nonuniform distribution of isomorphous substitution may additionally contribute to local strain and in this way further limit tactoid growth. Rising temperature improves the situation, but even hydrothermal synthesis still yields nanosized (<100-nm) materials (80). Commercially available synthetic hectorites (e.g., Laponite from BYK), for instance, come in typical diameters of <30 nm (81). These materials are excellent rheological additives because of the high ratio of edge area to basal plane area and are used in cosmetics and paint colors. For applications as filler or barrier materials, however, Laponite has an insufficient aspect ratio.

In contrast to hydrothermal synthesis, careful optimization of melt synthesis yields much larger tactoid sizes in the range of several micrometers (50, 82, 83). Furthermore, by varying the composition, the misfit between the subunits may be minimized to further increase the lateral diameter. The composition can, of course, be varied only within the particular charge density limits that still allow for osmotic swelling. These limits are particularly high for  $\text{Li}^+$  as the interlayer cation because of its high hydration enthalpy.

A systematic variation in the composition of Li-hec ( $[\text{Li}_x]^{\text{inter}}[\text{Mg}_{3-x}\text{Li}_x]^{\text{oct}}[\text{Si}_4]^{\text{tet}}\text{O}_{10}\text{F}_2$ ) made by melt synthesis shows that platelet sizes increase with increasing Li content, and median values of up to 50  $\mu\text{m}$  can be obtained (**Figure 6**) (19). The composition cannot be varied independently of layer charge, and the improved cohesion along the stacking direction may also assist in minimizing strain and may push the limits of lateral tactoid growth. With  $\text{Li}^+$ , even the highest charged compound still delaminates spontaneously, and 1-nm-thick platelets with diameters of more than 10  $\mu\text{m}$  could be observed in AFM (19).

#### 5. ORDERED INTERSTRATIFICATIONS AND THEIR DELAMINATION INTO DEFINED MULTISTACKS

As mentioned above, the Coulomb attraction in charged layered compounds strongly favors the segregation of counterions. To the best of our knowledge, layered silicates are the only member in the group of insulating charged layered compounds for which rectorite-type, ordered (*Reichweite I*), interstratified superstructures have been found. Ordered interstratifications of different inorganic cations were observed for synthetic hectorites and natural vermiculites, both of which are characterized by a homogeneous intracrystalline reactivity based on charge

**Figure 6**

Particle size distributions, as analyzed by SLS, of Li-hec synthesized with different compositions and layer charges ( $x$ ) (colored lines). Hec denotes hectorite. Reproduced with permission from Reference 19.

homogeneity. Regularly ordered inorganic-organic intercalation compounds were synthesized with different cationic amphiphiles, and numerous potential applications of these materials were explored (42, 84–89).

If counterions of different solvation enthalpy are offered to neutralize the charged layers, interstratifications can be made of interlayers that osmotically swell and that therefore are shear-labile and nonswelling shear-stiff interlayers. If these two types of interlayers are stacked in an ordered superstructure fashion, these tailored ordered interstratifications have the potential to allow for delamination of the material into multistacks with a well-defined number of layers (44). Any kind of mechanical exfoliation will fail to produce defined platelet thicknesses; instead, a distribution of multistacks is obtained. The only defined thickness that can be obtained is the single layer, which nevertheless requires complete delamination that can be achieved only by spontaneous osmotic swelling. Because multistacks have their own set of defined chemical and physical properties, controlled synthesis of multistacks is, however, highly desirable. Moreover, when one is attempting to restack a delaminated material into a one-dimensionally ordered array, all platelets must have the same thickness to obtain a perfectly textured self-supporting film. Ordered mixed-layer materials of two different strictly alternating interlayers (*Reichweite I*) closely resemble the natural mineral rectorite, which also shows a regularly interstratified sequence of nonhydrated  $K^+$  and hydrated  $Na^+$  interlayers. In the older literature, it was generally accepted that the regular alteration of hydrated and nonhydrated interlayers in rectorite coincided with alternating, pronouncedly different densities of interlayer cations (90). These regular charge density variations of smectite-type and mica-type interlayer cation densities are, in turn, thought to be the consequence of an ordered stacking of polar 2:1 silicate layers. Each layer in the stack is identical and contains an aluminum-rich and an aluminum-poor tetrahedral sheet. The up-down alternation of these polar layers results in two distinct interlayer spaces. The smectite-like interlayer space is adjacent to low-charge tetrahedral sheets, and the mica-like one is adjacent to high-charge tetrahedral sheets (91).

To cross-check this hypothesis, we reinvestigated the mechanism of formation of ordered interstratifications by using well-characterized and strictly charge-homogeneous  $Na_{0.5}$ -hec. This particular layered silicate clearly has symmetric, nonpolar layers because the origin of the charge

is in the octahedral sheet and no substitution is possible in tetrahedral sheets. The periodicity along the stacking direction is one silicate layer, and no trace of a superstructure exists in the starting material. Nevertheless, with the synthetic  $\text{Na}_{0.5}$ -hec, perfect superstructures that cannot be explained with existing ideas can be obtained. A rational 00/ series with low coefficient of variation and narrow FWHM of the reflections is observed (42). Consequently, another simpler and more rapid mechanism has to be established that breaks symmetry along the stacking direction and that differentiates between two distinct interlayer spaces in an ordered fashion. This deeper understanding of the mechanism paves the way to a generally applicable and scalable route to such ordered interstratified materials.

When  $\text{Na}_{0.5}$ -hec is partially ion exchanged with organic cations that expand the interlayer space, the Coulomb attraction forces the organic cations, e.g., a stilbazolium dye [N-hexadecyl-4-(3,4,5-trimethoxystyryl)-pyridinium], to segregate into densely packed organic interlayers. If the packing density of the organic interlayer is optimal at a loading that mismatches the charge density of the silicate layer, this first exchanged organic interlayer acts as a nucleus for an ordered interstratified domain. The two silicate layers encompassing this first organic interlayer still require local charge balance. Consequently, inorganic cations have to be reshuffled into the interlayers below and above the organic nucleus to accomplish the local charge balance. Consequently, the symmetry is broken, and the charge densities in the interlayers start to become strictly alternating (**Figure 7a**, middle). Aside from strict alternation, to achieve perfectly ordered stacking, the probability ( $\omega$ ) of the two types of interlayers has to be equal (**Figure 7a**, right). In the example here, the charge density of the organic interlayers and the charge density of the inorganic interlayers are below and above the charge density of the host lattice, respectively. Consequently, 40% of the total cation exchange capacity is satisfied by the organic cation and 60% by hydrated  $\text{Na}^+$ . With other combinations, however, these percentages are reversed, underscoring the general nature of the mechanism (42). Through application, during exchange, of a solvent that assures

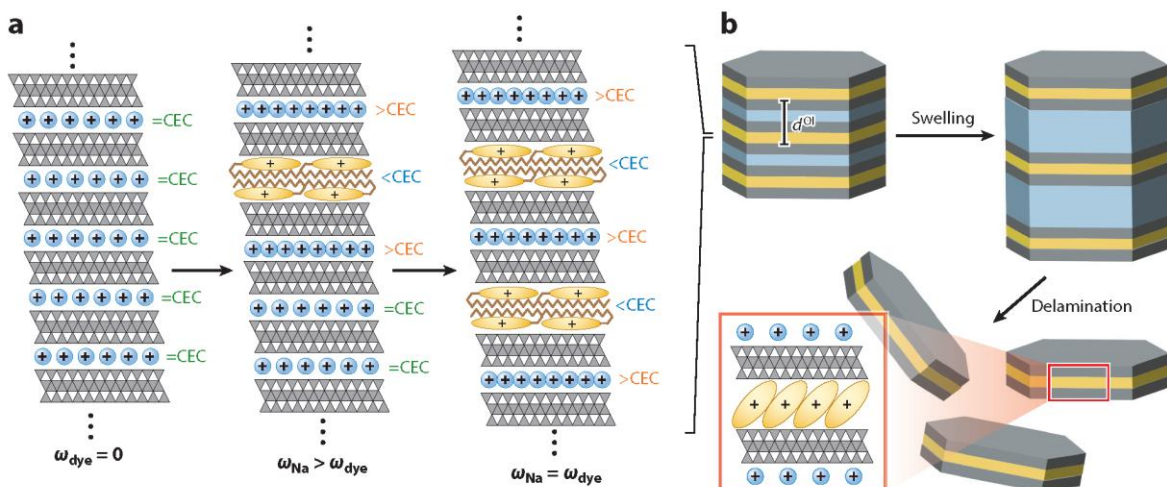


**Figure 7**

(a) Scheme explaining the nucleation of an ordered interstratified (OI) domain by intercalation of a single, densely packed interlayer with lower interlayer cation densities [ $<\text{CEC}$  (cation exchange capacity)] into initially homogeneously distributed ( $=\text{CEC}$ ), hydrated  $\text{Na}^+$  interlayers. Modified from Reference 42. Copyright 2014, American Chemical Society. (b) Delamination of the OI heterostructured powder along swollen  $\text{Na}^+$  interlayers (blue), producing water-dispersible double stacks with an oriented layer of encapsulated hydrophobic functional organic (yellow). Modified from Reference 44. Copyright 2015, Wiley.

sufficient solubility of both the organic and inorganic cations, equilibration can be achieved, and antiphase domain boundaries can be remedied. Equilibration experiments proved the ordered interstratification to be the thermodynamically stable phase.

Of course, the alternating variation of interlayer charge density can be forced upon the system only if the charge density of the host lattice is perfectly homogeneous. For this reason, to the best of our knowledge, ordered interstratifications have never been reported for natural montmorillonites.

The symmetry along the stacking direction can be broken not only by the packing restrictions on the organic interlayer cations imposed by the interlayer space, but also by interlayer cations of profoundly different selectivities for the interlayer space. When partially exchanging  $\text{Na}_{0.5}\text{-hec}$  with  $\text{K}^+$ , the two types of interlayer cations segregate because of their largely different hydration enthalpies (41). Moreover, the higher selectivity of the  $\text{K}^+$  for the interlayer space induces fluctuations of the interlayer cation densities to the limit, at which interlayers that carry an excess of charge density compared with the host lattice and that are predominantly  $\text{K}^+$  occupied start to collapse. The collapsed high-charge interlayers again act as a nucleus for an ordered interstratified material (41).

These interstratified structures still contain an osmotically swelling  $\text{Na}^+$  interlayer. Thus, they can spontaneously be delaminated into double stacks of two highly transparent, flexible silicate layers that encapsulate a central organic layer of oriented functional molecules (**Figure 7b**).

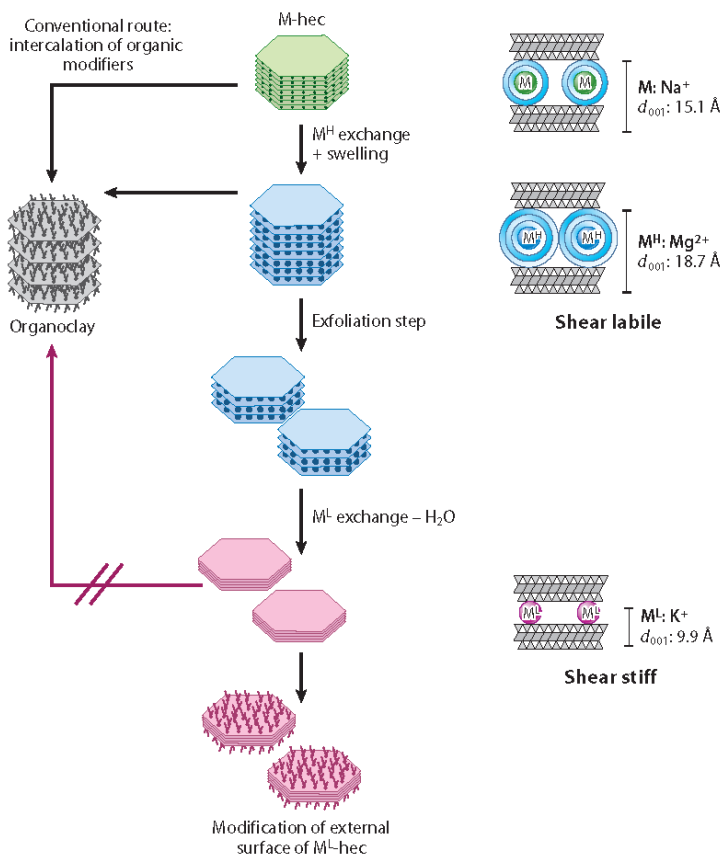
For many industrial applications, functional organic molecules have to be protected against thermal, biological, and/or oxidative degradation processes (92, 93). The encapsulation into an inorganic host achieved in such double stacks protects the sandwiched functional molecule from coming into direct contact with the outer gaseous or liquid phase. Furthermore, encapsulation improves the processability of the organic functional species due to increased water solubility (susceptibility) and/or the opportunity for masking and targeting biologically active pharmaceutical compounds (94–96). The structural anisotropy of the layered host additionally assures a well-defined orientation of the intercalated, functional molecule in the confined interlayer space (97–99), which is of key importance for the efficiency of light absorption in organic solar cells, for spintronics, and for polarized emission of light (100–102). Self-supporting films or composite films casted from suspensions of double stacks encapsulating the fluorescent stilbazolium dye proved that the high aspect ratio promotes the formation of perfectly textured films that show polarized adsorption due to the quasi-epitaxial orientation of the encapsulated functional molecule (44).

## 6. APPLICATION OF HIGH-ASPECT-RATIO SYNTHETIC HECTORITES IN NANOCOMPOSITES

### 6.1. Mechanical Reinforcement

The specific interface area and the aspect ratio are crucial parameters for the reinforcement of commodity polymers by compounding them with micaceous nanofillers like clays. Therefore, processing parameters that maximize exfoliation are usually chosen, thereby increasing both aspect ratio and specific interface area (103). However, it is usually overlooked that exfoliation concomitantly also diminishes the stiffness of multistacks and that the number of independent particles per weight increases dramatically, whereas the average interparticle distance consequently decreases. In this context, fine-tuning the intracrystalline reactivity opens new pathways to improve not only the bulk modulus of the nanocomposites but also, most importantly for technical use, the fracture toughness.

As discussed above in the context of  $\text{Na}_{0.5}\text{-hec}$ , the subtle balance between layer charge and hydration enthalpy of different interlayer cations allows for controlled transformation between

**Figure 8**

Production of shear-stiff, mica-like nanoplatelets and the selective modification of their external basal planes.  $M$ ,  $M^H$ , and  $M^L$  indicate interlayer cations with different hydration states:  $M^L = 0$  water layers (WL),  $M = 2$  WL, and  $M^H = 3$  WL. Modified from Reference 65. Copyright 2010, American Chemical Society.

a highly hydrated state and a nonhydrated state by simple cation exchange (65). This transition between hydration states cannot be observed for natural montmorillonite due to both the heterogeneity of charge density and the lower average layer charge. The highly hydrated and therefore shear-labile state, in which  $Mg^{2+}$  cations occupy the interlayer space ( $d_{001} = 18.6 \text{ \AA}$ ), allows for efficient mechanical exfoliation, increasing the aspect ratio. Subsequent cation exchange with  $K^+$  yields a collapsed, nonswollen, shear-stiff (104, 105), mica-like nanofiller ( $d_{001} = 9.9 \text{ \AA}$ ) (Figure 8). This nanofiller combines the best of two worlds: the stiffness of a mica sandwich and an aspect ratio significantly higher than what can be obtained with natural montmorillonite. The pristine  $K^+$  nanomica obtained at this stage still carries hydrated inorganic  $K^+$  on the outer basal surface. To transfer the filler into a hydrophobic polymer matrix, its surface tension has to be lowered. A polycationic macroinitiator is employed for modification of the nanomica (106). This polymeric modifier cannot intercalate between the silicate layers, and cation exchange is restricted to the outer basal surfaces. This type of organophilization to O-hec minimizes the amount of modifier needed while preserving the stiffness of the mica-like nanofiller (107).

O-hec-filled nanocomposites offer significantly improved elastic modulus (+30%) without reducing strength (108). Most notably, fracture toughness may be increased by 63% at a filler content as low as 0.80 vol% for solution-blended O-hec nanocomposites. In contrast to the case of O-hec for a well-dispersed montmorillonite nanocomposite, the tensile strength is significantly reduced. Due to insufficient interfacial strength, the stress concentration promotes partial debonding at a certain stress level, eventually leading to void formation. Premature failure is then induced by the growth of these voids and by the eventual coalescence of adjacent micro voids into macro voids, an event that strongly depends on the interparticle distance. Increasing the number of particles by disaggregation or exfoliation thus fosters void growth at relatively low applied stress and is therefore responsible for premature failure. In this context, the interparticle distance at any given filler content also depends on the platelet diameter. As the lateral extension of montmorillonite nanoplatelets is one order of magnitude smaller than that of O-hec, the number of platelets per volume is at least two orders of magnitude higher. Consequently, no premature failure was observed for the comparatively few huge O-hec platelets, and the strength was not reduced for this nanocomposite at any filler content (108).

## 6.2. Gas Barrier

There is a huge industrial demand for flexible, transparent barrier packaging for a myriad of applications ranging from food packaging to encapsulation of optoelectronic devices like flexible organic solar cells and flexible organic light-emitting diodes (OLEDs) (109). Amorphous polymer matrices are flexible and transparent but are far too permeable. For most applications, the permeability for both water vapor and oxygen must be reduced, and by several orders of magnitude. For instance, for OLED packaging, the permeability must be reduced by at least six orders of magnitude (110). Because a barrier needs to be assured for both a hydrophilic permeant and a hydrophobic permeant, the permeability cannot be reduced by adjusting the solubility of the unlike permeants in the polymer matrix. Rather, permeability must be reduced by a nonselective reduction of the diffusion. In this regard, the incorporation of platy-impermeable fillers into the nanocomposite forces the permeant to go around the impermeable platelet, generating a tortuous path for diffusion, and as such efficiently reduces permeability. The relative reductions achievable in theory depend nonlinearly on aspect ratio and filler content (17, 18). Thus, tortuous path theory therefore clearly suggests that for this particular application, the aspect ratio must be maximized.

Consequently, spontaneous and complete delamination by osmotic swelling of tactoids with lateral diameters as obtained by optimizing melt synthesis and composition delivers the platelets of choice for this nanocomposite application. Comparing the permeability of self-supporting films of various commercially available synthetic and natural layered silicates with the permeability of melt-synthesized Li-hec proved the superiority of the latter (111). Filling the gaps between clay platelets with a polymer matrix further reduced the permeability (112). The best barrier properties were observed for osmotically delaminated, melt-synthesized Na<sub>0.5</sub>-hec ( $\alpha = 25,000$ ) incorporated into a commercial two-component polyurethane film. For this film, oxygen transmission rates as low as  $3.7 \times 10^{-3} \text{ cm}^3 \text{ m}^{-2} \text{ day}^{-1} \text{ bar}^{-1}$  were found for 1.5- $\mu\text{m}$ -thick films. The absolute values correspond to a reduction of the permeability by  $\approx 6$  orders of magnitude compared with the permeability of the neat matrix (113).

## 6.3. Flame Retardancy Applications

With the promotion of polymer materials, solid-fuel capacity in our daily environment has steadily increased over the last few decades. Consequently, flame retardancy requirements have been

tightened. At the same time, due to environmental and health reasons, various very efficient halogenated molecular flame retardants, like polybrominated diphenyl ether, need to be replaced by more environmentally friendly and nontoxic compounds (114). Possible alternatives are inorganic materials like aluminum trihydroxide (ATH) and magnesium dihydroxide (MDH). However, very high loadings of ATH and MDH (40–70 wt%) are required to obtain the same flame retardant activity and, of course, are detrimental to the mechanical properties of these polymers (115, 116). Layered compounds have shown great potential as alternative synergistic flame retardants. Significant reductions of the peak of heat release rate (PHRR), which is one of the most meaningful indicators of flame retardancy performance, were obtained at relatively low filler loadings of less than 5 wt% (117, 118). A study using a surface-modified LDH in polystyrene (PS) illustrated that, for the reduction of the PHRR, the aspect ratio of the layered structure is more important than the total specific surface area of the filler (115). Similar results were obtained in a study that compared the flame retardancy of two layered silicates of different aspect ratios, a natural montmorillonite ( $\alpha \leq 50$ ) and melt-synthesized Li-hec ( $\alpha > 1,000$ ), dispersed in PS. The PS sample combined with as little as 3-wt% Li-hec showed intumescence-like behavior and a reduction of PHRR of 57%, which is much higher than the reduction of PHRR of 38% obtained with the same amount of a natural montmorillonite (119). To what extent different parameters such as specific interface area and aspect ratio have a role in reducing the permeability of gaseous pyrolysis products and in potentially improving the fracture toughness of the char produced during burning is not clear. Dispersion quality, however, is an important factor in the flame retardancy performance of clay-based nanocomposites. A solution-blended PS sample with 3-wt% shear-stiff nanomica ( $\alpha = 350$ ) showed a much higher reduction of PHRR (47%) than did the corresponding melt-blended nanocomposite (which had a reduction of PHRR of 28%) (120). TEM images indicated (120) that this higher reduction can be attributed to the better dispersion achieved by solution blending.

### DISCLOSURE STATEMENT

The authors are not aware of any affiliations, memberships, funding, or financial holdings that might be perceived as affecting the objectivity of this review.

### LITERATURE CITED

1. Lagaly G. 1979. Layer charge of regular interstratified 2:1 clay-minerals. *Clays Clay Miner.* 27:1–10
2. Jasmund K, Lagaly G. 1993. *Tonminerale und Tone: Struktur, Eigenschaften, Anwendungen und Einsatz in Industrie und Umwelt*. Darmstadt, Ger.: Steinkopff
3. Lagaly G, Ziesmer S. 2003. Colloid chemistry of clay minerals: the coagulation of montmorillonite dispersions. *Adv. Colloid Interface Sci.* 100:105–28
4. Norrish K. 1954. The swelling of montmorillonite. *Discuss. Faraday Soc.* 18:120–34
5. Chiritescu C, Cahill DG, Nguyen N, Johnson D, Bodapati A, et al. 2007. Ultralow thermal conductivity in disordered, layered WSe<sub>2</sub> crystals. *Science* 315:351–53
6. Rao C, Matte H, Maitra U. 2013. Graphene analogues of inorganic layered materials. *Angew. Chem. Int. Ed.* 52:13162–85
7. Wu W, Wang L, Li Y, Zhang F, Lin L, et al. 2014. Piezoelectricity of single-atomic-layer MoS<sub>2</sub> for energy conversion and piezotronics. *Nature* 514:470–74
8. Kunz D, Max E, Weinkamer R, Lunkenbein T, Fery A, Breu J. 2009. Deformation measurements on thin clay tactoids. *Small* 5:1816–20
9. Kunz DA, Erath J, Kluge D, Thurn H, Putz B, et al. 2013. In-plane modulus of singular 2:1 clay lamellae applying a simple wrinkling technique. *ACS Appl. Mater. Interfaces* 5:5851–55
10. Kane CL, Mele EJ. 2005. Z<sub>2</sub> topological order and the quantum spin Hall effect. *Phys. Rev. Lett.* 95:146802

11. Kunz DA, Feicht P, Goedrich S, Thurn H, Papastavrou G, et al. 2013. Space-resolved in-plane moduli of graphene oxide and chemically derived graphene applying a simple wrinkling procedure. *Adv. Mater.* 25:1337–41
12. Stankovich S, Dikin DA, Piner RD, Kohlhaas KA, Kleinhammes A, et al. 2007. Synthesis of graphene-based nanosheets via chemical reduction of exfoliated graphite oxide. *Carbon* 45:1558–65
13. Stankovich S, Dikin DA, Dommett GH, Kohlhaas KM, Zimney EJ, et al. 2006. Graphene-based composite materials. *Nature* 442:282–86
14. Dikin DA, Stankovich S, Zimney EJ, Piner RD, Dommett GH, et al. 2007. Preparation and characterization of graphene oxide paper. *Nature* 448:457–60
15. Mashtalir O, Naguib M, Mochalin VN, Dall'Agnese Y, Heon M, et al. 2013. Intercalation and delamination of layered carbides and carbonitrides. *Nat. Commun.* 4:1716
16. Halpin JC, Kardos JL. 1976. Halpin-Tsai equations—review. *Polym. Eng. Sci.* 16:344–52
17. Cussler EL, Hughes SE, Ward WJ, Aris R. 1988. Barrier membranes. *J. Membr. Sci.* 38:161–74
18. Nielsen LE. 1967. Models for the permeability of filled polymer systems. *J. Macromol. Sci. A* 1:929–42
19. Kalo H, Möller MW, Kunz DA, Breu J. 2012. How to maximize the aspect ratio of clay nanoplatelets. *Nanoscale* 4:5633–39
20. Duer MJ, Rocha J, Klinowski J. 1992. Solid-state NMR studies of the molecular motion in the kaolinite:DMSO intercalate. *J. Am. Chem. Soc.* 114:6867–74
21. Li Y, Sun D, Pan X, Zhang B. 2009. Kaolinite intercalation precursors. *Clays Clay Miner.* 57:779–86
22. Komori Y, Sugahara Y, Kuroda K. 1998. A kaolinite-NMF-methanol intercalation compound as a versatile intermediate for further intercalation reaction of kaolinite. *J. Mater. Res.* 13:930–34
23. Komori Y, Enoto H, Takenawa R, Hayashi S, Sugahara Y, Kuroda K. 2000. Modification of the interlayer surface of kaolinite with methoxy groups. *Langmuir* 16:5506–8
24. Franco F, Cruz MDR. 2004. Factors influencing the intercalation degree ('reactivity') of kaolin minerals with potassium acetate, formamide, dimethylsulphoxide and hydrazine. *Clay Miner.* 39:193–205
25. Tonle IK, Letaief S, Ngameni E, Detellier C. 2009. Nano-hybrid materials from the grafting of imidazolium cations on the interlayer surfaces of kaolinite. Application as electrode modifier. *J. Mater. Chem.* 19:5996–6003
26. Letaief S, Detellier C. 2007. Functionalized nano-hybrid materials obtained from the interlayer grafting of aminoalcohols on kaolinite. *Chem. Commun.* 2007:2613–15
27. Hirsemann D, Koester TKJ, Wack J, van Wullen L, Breu J, Senker J. 2011. Covalent Grafting to  $\mu$ -hydroxy-capped surfaces? A kaolinite case study. *Chem. Mater.* 23:3152–58
28. Schafhäul C. 1840. Über die Verbindungen des Kohlenstoffes mit Silicium, Eisen und andern Metallen, welche die verschiedenen Gattungen von Gusseisen, Stahl und Schmiedeeisen bilden. *J. Prakt. Chem.* 21:129–57
29. Hofmann U, Frenzel A. 1930. Quellung von Graphit und die Bildung von Graphitsäure. *Ber. Dtsch. Chem. Ges. A/B* 63:1248–62
30. Hofmann U, Frenzel A, Csalán E. 1934. Die Konstitution der Graphitsäure und ihre Reaktionen. *Justus Liebigs Ann. Chem.* 510:1–41
31. Winter M, Besenhard JO, Spahr ME, Novak P. 1998. Insertion electrode materials for rechargeable lithium batteries. *Adv. Mater.* 10:725–63
32. Schöllhorn R, Weiss A. 1973. Hydration, layer solvate formation and cation exchange of nonstoichiometric ternary sulfides of titanium. *Z. Naturforsch. B* 28:711–15
33. Butz T, Leif A, Besenhard JO. 1984. Metastable configurations during lithium intercalation into 2H-TaS<sub>2</sub>. *Rev. Chim. Miner.* 21:556–87
34. Benavente E, Santa Ana MA, Mendizabal F, Gonzalez G. 2002. Intercalation chemistry of molybdenum disulfide. *Coord. Chem. Rev.* 224:87–109
35. Schöllhorn R, Weiss A. 1974. Cation exchange reactions and layer solvate complexes of ternary phases M<sub>x</sub>MoS<sub>2</sub>. *J. Less Common Met.* 36:229–36
36. Adireddy S, Carbo CE, Rostamzadeh T, Vargas JM, Spinu L, Wiley JB. 2014. Peapod-type nanocomposites through the in situ growth of gold nanoparticles within preformed hexaniobate nanoscrolls. *Angew. Chem. Int. Ed.* 53:4614–17

37. Kalo H, Milius W, Bräu M, Breu J. 2013. Synthesis and single crystal structure refinement of the one-layer hydrate of sodium brittle mica. *J. Solid State Chem.* 198:57–64
38. Weiss Z, Valaskova M, Seidlerova J, Supkova-Kristkova M, Sustai O, et al. 2006. Preparation of vermiculite nanoparticles using thermal hydrogen peroxide treatment. *J. Nanosci. Nanotechnol.* 6:726–30
39. Obut A, Girgin I. 2002. Hydrogen peroxide exfoliation of vermiculite and phlogopite. *Miner. Eng.* 15:683–87
40. Besenhard JO, Fritz HP. 1983. The electrochemistry of black carbons. *Angew. Chem. Int. Ed.* 22:950–75
41. Möller MW, Hirsemann D, Haarmann F, Senker J, Breu J. 2010. Facile scalable synthesis of rectorites. *Chem. Mater.* 22:186–96
42. Stöter M, Biersack B, Reimer N, Herling M, Stock N, et al. 2014. Ordered heterostructures of two strictly alternating types of nanoreactors. *Chem. Mater.* 26:5412–19
43. Shih CJ, Vijayaraghavan A, Krishnan R, Sharma R, Han JH, et al. 2011. Bi- and trilayer graphene solutions. *Nat. Nanotechnol.* 6:439–45
44. Stöter M, Biersack B, Rosenfeldt S, Leid MJ, Kalo H, et al. 2015. Encapsulation of functional organic compounds in nanoglass for optically anisotropic coatings. *Angew. Chem. Int. Ed.* In press; doi: 10.1002/anie.201411137
45. Palin EJ, Dove MT, Hernandez-Laguna A, Sainz-Diaz CL. 2004. A computational investigation of the Al/Fe/Mg order-disorder behavior in the dioctahedral sheet of phyllosilicates. *Am. Mineral.* 89:164–75
46. Lagaly G. 1981. Characterization of clays by organic compounds. *Clay Miner.* 16:1–21
47. Brindley GW. 1966. Ethylene glycol and glycerol complexes of smectites and vermiculites. *Clay Miner.* 6:237–59
48. Ferrage E, Lanson B, Sakharov BA, Geoffroy N, Jacquot E, Drits VA. 2007. Investigation of dioctahedral smectite hydration properties by modeling of X-ray diffraction profiles: influence of layer charge and charge location. *Am. Mineral.* 92:1731–43
49. Hofmann U. 1942. Neues aus der Chemie des Tons. *Chemie* 55:283–89
50. Breu J, Seidl W, Stoll AJ, Lange KG, Probst TU. 2001. Charge homogeneity in synthetic fluorohectorite. *Chem. Mater.* 13:4213–20
51. Hou XQ, Bish DL, Wang SL, Johnston CT, Kirkpatrick RJ. 2003. Hydration, expansion, structure, and dynamics of layered double hydroxides. *Am. Mineral.* 88:167–79
52. Radha S, Jayanthi K, Breu J, Kamath PV. 2014. Relative humidity-induced reversible hydration of sulfate-intercalated layered double hydroxides. *Clays Clay Miner.* 62:53–61
53. Smith DW. 1977. Ionic hydration enthalpies. *J. Chem. Educ.* 54:540–42
54. Liu ZP, Ma RZ, Osada M, Iyi N, Ebina Y, et al. 2006. Synthesis, anion exchange, and delamination of Co-Al layered double hydroxide: assembly of the exfoliated nanosheet/polyanion composite films and magneto-optical studies. *J. Am. Chem. Soc.* 128:4872–80
55. Ziadeh M, Chwalka B, Kalo H, Schütz MR, Breu J. 2012. A simple approach for producing high aspect ratio fluorohectorite nanoplatelets utilizing a stirred media mill (ball mill). *Clay Miner.* 47:341–53
56. Segad M, Hanski S, Olsson U, Ruokolainen J, Akesson T, Jonsson B. 2012. Microstructural and swelling properties of Ca and Na montmorillonite: (in situ) observations with cryo-TEM and SAXS. *J. Phys. Chem. C* 116:7596–601
57. Hofmann U. 1932. Eindimensionale Quellung von Graphitsäure und Graphit. (Die Reaktionsweisen des Graphits.) *Kolloid Z.* 61:297–304
58. Hofmann U, Kurd E, Diederich W. 1933. Kristallstruktur und Quellung von Montmorillonit. (Das Tonmineral der Bentonitton.) *Z. Kristallogr.* 86:340–48
59. Berghout A, Tunega D, Zaoui A. 2010. Density functional theory (DFT) study of the hydration steps of  $\text{Na}^+/\text{Mg}^{2+}/\text{Ca}^{2+}/\text{Sr}^{2+}/\text{Ba}^{2+}$ -exchanged montmorillonites. *Clays Clay Miner.* 58:174–87
60. Bérend I, Cases J-M, François M, Uriot J-P, Michot L, et al. 1995. Mechanism of adsorption and desorption of water vapor by homoionic montmorillonites. 2. The  $\text{Li}^+$ ,  $\text{Na}^+$ ,  $\text{K}^+$ ,  $\text{Rb}^+$  and  $\text{Cs}^+$ -exchanged forms. *Clays Clay Miner.* 43:324–36
61. Tambach TJ, Bolhuis PG, Smit B. 2004. A molecular mechanism of hysteresis in clay swelling. *Angew. Chem. Int. Ed.* 43:2650–52
62. Laird DA, Shang C, Thompson ML. 1995. Hysteresis in crystalline swelling of smectites. *J. Colloid Interface Sci.* 171:240–45

63. Tambach TJ, Bolhuis PG, Hensen EJM, Smit B. 2006. Hysteresis in clay swelling induced by hydrogen bonding: accurate prediction of swelling states. *Langmuir* 22:1223–34
64. Kalo H, Milius W, Breu J. 2012. Single crystal structure refinement of one- and two-layer hydrate of sodium fluorohectorite. *RSC Adv.* 2:8452–59
65. Möller MW, Handge UA, Kunz DA, Lunkenbein T, Altstadt V, Breu J. 2010. Tailoring shear-stiff, mica-like nanoplatelets. *ACS Nano* 4:717–24
66. Dazas B, Ferrage E, Delville A, Lanson B. 2014. Interlayer structure model of tri-hydrated low-charge smectite by X-ray diffraction and Monte Carlo modeling in the Grand Canonical ensemble. *Am. Mineral.* 99:1724–35
67. Singh V, Bosman S, Schneider B, Blanter Y, Castellanos-Gomez A, Steele G. 2014. Optomechanical coupling between a multilayer graphene mechanical resonator and a superconducting microwave cavity. *Nat. Nanotechnol.* 9:820–24
68. Scherrer P. 1918. Bestimmung der Größe und der inneren Struktur von Kolloidteilchen mittels Röntgenstrahlen. *Nachr. Ges. Wiss. Gött.* 2:96–100
69. Cao T, Fasulo PD, Rodgers WR. 2010. Investigation of the shear stress effect on montmorillonite platelet aspect ratio by atomic force microscopy. *Appl. Clay Sci.* 49:21–28
70. Kwade A. 2003. A stressing model for the description and optimization of grinding processes. *Chem. Eng. Technol.* 26:199–205
71. Kwade A, Schwedes J. 2007. Wet grinding in stirred media mills. In *Handbook of Powder Technology: Particle Breakage*, ed. AD Salman, M. Ghadiri, MJ Hounslow, pp. 251–382. Amsterdam: Elsevier Sci. B.V.
72. Vdovic N, Jurina I, Skapin SD, Sondi I. 2010. The surface properties of clay minerals modified by intensive dry milling—revisited. *Appl. Clay Sci.* 48:575–80
73. Schramm LL, Kwak JCT. 1982. Influence of exchangeable cation composition on the size and shape of montmorillonite particles in dilute suspension. *Clays Clay Miner.* 30:40–48
74. Störter M, Kunz DA, Schmidt M, Hirsemann D, Kalo H, et al. 2013. Nanoplatelets of sodium hectorite showing aspect ratios of ~20,000 and superior purity. *Langmuir* 29:1280–85
75. Segad M, Jonsson B, Cabane B. 2012. Tactoid formation in montmorillonite. *J. Phys. Chem. C* 116:25425–33
76. Shomer I, Mingelgrin U. 1978. Direct procedure for determining number of plates in tactoids of smectites—Na-Ca-montmorillonite case. *Clays Clay Miner.* 26:135–38
77. Skipper NT, Lock PA, Titiloye JO, Swenson J, Mirza ZA, et al. 2006. The structure and dynamics of 2-dimensional fluids in swelling clays. *Chem. Geol.* 230:182–96
78. Kalo H, Möller MW, Ziadeh M, Dolejs D, Breu J. 2010. Large scale melt synthesis in an open crucible of Na-fluorohectorite with superb charge homogeneity and particle size. *Appl. Clay Sci.* 48:39–45
79. Feicht P, Kunz DA, Lerf A, Breu J. 2014. Facile and scalable one-step production of organically modified graphene oxide by a two-phase extraction. *Carbon* 80:229–34
80. Kloprogge JT, Komarneni S, Amonette JE. 1999. Synthesis of smectite clay minerals: a critical review. *Clays Clay Miner.* 47:529–54
81. Li L, Harnau L, Rosenfeldt S, Ballauff M. 2005. Effective interaction of charged platelets in aqueous solution: investigations of colloid laponite suspensions by static light scattering and small-angle X-ray scattering. *Phys. Rev. E* 72:051504
82. Breu J, Seidl W, Senker J. 2004. Synthesis of three dimensionally ordered intercalation compounds of hectorite. *Z. Anorg. Allg. Chem.* 630:80–90
83. Breu J, Seidl W, Stoll A. 2003. Disorder in smectites in dependence of the interlayer cation. *Z. Anorg. Allg. Chem.* 629:503–15
84. Ijdo WL, Lee T, Pinnavaia TJ. 1996. Regularly interstratified layered silicate heterostructures: precursors to pillared rectorite-like intercalates. *Adv. Mater.* 8:79–83
85. Ijdo WL, Pinnavaia TJ. 1998. Staging of organic and inorganic gallery cations in layered silicate heterostructures. *J. Solid State Chem.* 139:281–89
86. Ijdo WL, Pinnavaia TJ. 2001. Amphiphilic layered silicate clay for the efficient removal of organic pollutants from water. *Green Chem.* 3:10–12

87. Ijdo WL, Pinnavaia TJ. 1999. Solid solution formation in amphiphilic organic-inorganic clay heterostructures. *Chem. Mater.* 11:3227–31
88. Ozsoz M, Erdem A, Ozkan D, Kerman K, Pinnavaia TJ. 2003. Clay/sol-gel-modified electrodes for the selective electrochemical monitoring of 2,4-dichlorophenol. *Langmuir* 19:4728–32
89. Ozkan D, Kerman K, Meric B, Kara P, Demirkhan H, et al. 2002. Heterostructured fluorohectorite clay as an electrochemical sensor for the detection of 2,4-dichlorophenol and the herbicide 2,4-D. *Chem. Mater.* 14:1755–61
90. Brown G. 1984. Crystal structures of clay minerals and related phyllosilicates. *Philos. Trans. R. Soc. A* 311:221–40
91. Stixrude L, Peacor DR. 2002. First-principles study of illite-smectite and implications for clay mineral systems. *Nature* 420:165–68
92. Sanchez C, Julian B, Belleville P, Popall M. 2005. Applications of hybrid organic-inorganic nanocomposites. *J. Mater. Chem.* 15:3559–92
93. Sanchez C, Belleville P, Popall M, Nicolle L. 2011. Applications of advanced hybrid organic-inorganic nanomaterials: from laboratory to market. *Chem. Soc. Rev.* 40:696–753
94. Chen Y, Chen HR, Shi JL. 2013. In vivo bio-safety evaluations and diagnostic/therapeutic applications of chemically designed mesoporous silica nanoparticles. *Adv. Mater.* 25:3144–76
95. Ruiz-Hitzky E. 2003. Functionalizing inorganic solids: towards organic-inorganic nanostructured materials for intelligent and bioinspired systems. *Chem. Rev.* 3:88–100
96. Ruiz-Hitzky E, Aranda P, Darder M, Rytwo G. 2010. Hybrid materials based on clays for environmental and biomedical applications. *J. Mater. Chem.* 20:9306–21
97. Zhou CH, Shen ZF, Liu LH, Liu SM. 2011. Preparation and functionality of clay-containing films. *J. Mater. Chem.* 21:15132–53
98. Takagi S, Shimada T, Ishida Y, Fujimura T, Masui D, et al. 2013. Size-matching effect on inorganic nanosheets: control of distance, alignment, and orientation of molecular adsorption as a bottom-up methodology for nanomaterials. *Langmuir* 29:2108–19
99. Fujimura T, Shimada T, Hamatani S, Onodera S, Sasai R, et al. 2013. High density intercalation of porphyrin into transparent clay membrane without aggregation. *Langmuir* 29:5060–65
100. Guskova O, Schünemann C, Eichhorn KJ, Walzer K, Levichkova M, et al. 2013. Light absorption in organic thin films: the importance of oriented molecules. *J. Phys. Chem. C* 117:17285–93
101. Kunz DA, Leitl MJ, Schade L, Schmid J, Bojer B, et al. 2015. Quasi-epitaxial growth of  $[\text{Ru}(\text{bpy})_3]^{2+}$  by confinement in clay nanoplatelets yields polarized emission. *Small* 11:792–96
102. Nino MA, Kowalik IA, Luque FJ, Arvanitis D, Miranda R, de Miguel JJ. 2014. Enantiospecific spin polarization of electrons photoemitted through layers of homochiral organic molecules. *Adv. Mater.* 26:7474–79
103. Paul DR, Robeson LM. 2008. Polymer nanotechnology: nanocomposites. *Polymer* 49:3187–204
104. Brune DA, Bicerano J. 2002. Micromechanics of nanocomposites: comparison of tensile and compressive elastic moduli, and prediction of effects of incomplete exfoliation and imperfect alignment on modulus. *Polymer* 43:369–87
105. Heinz H, Vaia RA, Farmer BL. 2006. Interaction energy and surface reconstruction between sheets of layered silicates. *J. Chem. Phys.* 124:224713
106. Ziadeh M, Weiss S, Fischer B, Förster S, Altstädt V, et al. 2014. Towards completely miscible PMMA nanocomposites reinforced by shear-stiff, nano-mica. *J. Colloid Interface Sci.* 425:143–51
107. Fischer B, Ziadeh M, Pfaff A, Breu J, Altstädt V. 2012. Impact of large aspect ratio, shear-stiff, mica-like clay on mechanical behaviour of PMMA/clay nanocomposites. *Polymer* 53:3230–37
108. Ziadeh M, Fischer B, Schmid J, Altstädt V, Breu J. 2014. On the importance of specific interface area in clay nanocomposites of PMMA filled with synthetic nano-mica. *Polymer* 55:3770–81
109. Burrows PE, Graff GL, Gross ME, Martin PM, Shi MK, et al. 2001. Ultra barrier flexible substrates for flat panel displays. *Displays* 22:65–69
110. Kumar RS, Auch M, Ou E, Ewald G, Jin CS. 2002. Low moisture permeation measurement through polymer substrates for organic light emitting devices. *Thin Solid Films* 417:120–26
111. Möller MW, Lunkenbein T, Kalo H, Schieder M, Kunz DA, Breu J. 2010. Barrier properties of synthetic clay with a kilo-aspect ratio. *Adv. Mater.* 22:5245–49

112. Möller MW, Kunz DA, Lunkenbein T, Sommer S, Nennemann A, Breu J. 2012. UV-cured, flexible, and transparent nanocomposite coating with remarkable oxygen barrier. *Adv. Mater.* 24:2142–47
113. Kunz DA, Schmid J, Feicht P, Erath J, Fery A, Breu J. 2013. Clay-based nanocomposite coating for flexible optoelectronics applying commercial polymers. *ACS Nano* 7:4275–80
114. Law RJ, Herzke D, Harrad S, Morris S, Bersuder P, Allchin CR. 2008. Levels and trends of HBCD and BDEs in the European and Asian environments, with some information for other BFRs. *Chemosphere* 73:223–41
115. Diar-Bakerly B, Beyer G, Schobert R, Breu J. 2012. Significance of aspect ratio on efficiency of layered double hydroxide flame retardants. In *Fire and Polymers VI: New Advances in Flame Retardant Chemistry and Science*, pp. 407–25. Washington, DC: Am. Chem. Soc.
116. Beyer G. 2001. Flame retardant properties of EVA-nanocomposites and improvements by combination of nanofillers with aluminium trihydrate. *Fire Mater.* 25:193–97
117. Morgan AB. 2006. Flame retarded polymer layered silicate nanocomposites: a review of commercial and open literature systems. *Polym. Adv. Technol.* 17:206–17
118. Zhu J, Morgan AB, Lamelas FJ, Wilkie CA. 2001. Fire properties of polystyrene-clay nanocomposites. *Chem. Mater.* 13:3774–80
119. Schütz MR, Kalo H, Lunkenbein T, Breu J, Wilkie CA. 2011. Intumescence-like behavior of polystyrene synthetic clay nanocomposites. *Polymer* 52:3288–94
120. Schütz MR, Kalo H, Lunkenbein T, Groschel AH, Muller AHE, et al. 2011. Shear stiff, surface modified, mica-like nanoplatelets: a novel filler for polymer nanocomposites. *J. Mater. Chem.* 21:12110–16

## 5.6 Neue Einblicke in die Delaminierung von Schichtverbindungen

Sabine Rosenfeldt,<sup>[a]</sup> Matthias Stöter,<sup>[b]</sup> Mathias Schlenk,<sup>[a]</sup> Thomas Martin,<sup>[b]</sup> Rodrigo Q. Albuquerque,<sup>[c]</sup> Stephan Förster,<sup>[a]</sup> and Josef Breu<sup>[b]\*</sup>

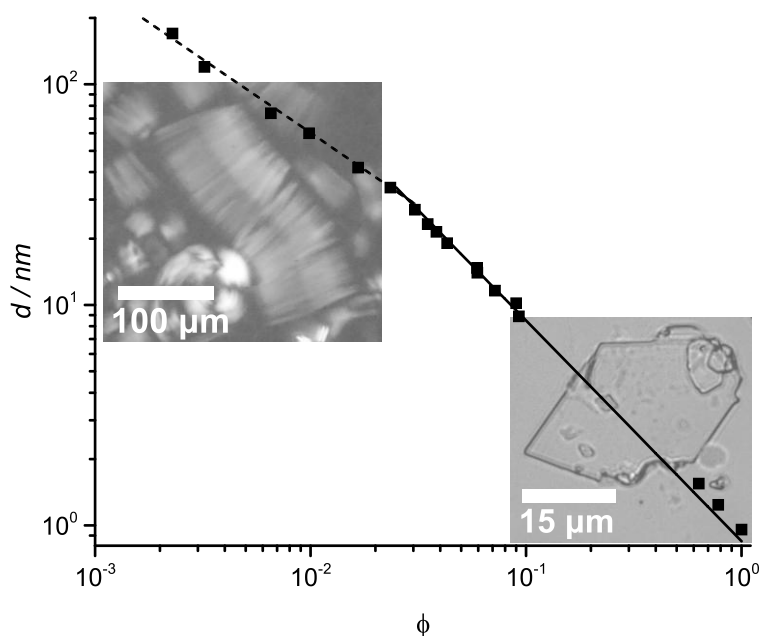
### In Depth Insights into the Key Steps of Delamination of Charged 2D Materials

Manuskript eingereicht 2016

<sup>[a]</sup> Physikalische Chemie I, Universität Bayreuth, 95440 Bayreuth

<sup>[b]</sup> Lehrstuhl für Anorganische Chemie I, Universität Bayreuth, D-95440 Bayreuth

<sup>[c]</sup> São Carlos Institute of Chemistry, University of São Paulo, Av. Trab. São-carlense 400, 13560-970 São Carlos, Brazil.



#### Darstellung des Eigenanteils:

Das Konzept dieses Artikels stammt von Dr. Sabine Rosenfeldt, Prof. Dr. Josef Breu und mir. Die Durchführung der SAXS Messungen, deren Auswertung und Interpretation wurden hauptsächlich von Dr. Sabine Rosenfeldt (Physikalische Chemie I) durchgeführt. Die Simulation des 3-Schichthydrats wurde von Dr. Rodrigo Q. Albuquerque (Universität São Paulo, Brasilien) erstellt. Die Herstellung der verdünnten Suspensionen und die Untersuchung der Doppelbrechung der verschiedenen Hectoritsuspensionen wurden von mir durchgeführt. Verfasst wurde diese Publikation von Prof. Dr. Josef Breu, Dr. Sabine Rosenfeldt und mir. Mein Eigenanteil beträgt ca. 40 %

## 5.6.1 In Depth Insights into the Key Steps of Delamination of Charged 2D Materials

### In Depth Insights into the Key Steps of Delamination of Charged 2D Materials

**Sabine Rosenfeldt,<sup>1</sup> Matthias Stöter<sup>2</sup>, Mathias Schlenk<sup>1</sup>, Thomas Martin<sup>2</sup>, Rodrigo Queiroz Albuquerque,<sup>3</sup> Stephan Förster,<sup>\*1</sup> and Josef Breu<sup>\*2</sup>**

<sup>1</sup> Physical Chemistry I, University of Bayreuth, Universitätsstrasse 30, 95440 Bayreuth, Germany

<sup>2</sup> Inorganic Chemistry I, University of Bayreuth, Universitätsstrasse 30, 95440 Bayreuth, Germany

<sup>3</sup> São Carlos Institute of Chemistry, University of São Paulo, Av. Trab. São-carlense 400, 13560-970 São Carlos, Brazil.

**KEYWORDS:** delamination, monolayer formation, nanosheet, small-angle X-ray scattering, hectorite

**ABSTRACT:** Delamination is a key step to obtain individual layers from inorganic layered materials needed for fundamental studies and applications. For layered van-der-Waals materials like graphene the adhesion forces are small allowing for mechanical exfoliation, whereas for ionic layered materials like layered silicates the energy to separate adjacent layers is considerably higher. Quite counter intuitively, we show for a synthetic layered silicate ( $\text{Na}_{0.5}$ -hectorite) that a scalable and quantitative delamination by simple hydration is possible for high and homogeneous charge density, even for aspect ratios as large as 20000. A general requirement is the separation of adjacent layers by solvation to a distance where layer interactions become repulsive (Gouy-Chapman length). Further hydration up to 34 nm leads to the formation of a highly ordered lamellar liquid crystalline phase (Wigner crystal). Up to 8 higher-order reflections indicate excellent positional order of individual layers. The Wigner crystal melts when the interlayer separation reaches the Debye length, where electrostatic interactions between adjacent layers are screened. The layers become weakly charge-correlated. This is indicated by fulfilling the classical Hansen-Verlet and Lindeman criteria for melting. We provide insight into the requirements for layer separation and controlling the layer distances for a broad range of materials and

outline an important pathway for the integration of layers into devices for advanced applications.

## Introduction

Two-dimensional (2D) materials have an atomic organization where the bond strengths along two dimensions are much stronger compared to the third dimension (1). The crystal structures typically consist of thin layers of atoms with strong directional bonding within the layers and much weaker interactions between the layers. If the layers are neutral, they form van-der-Waals solids with only weak layer interaction. Prominent examples for these materials are graphene and transition metal dichalcogenides such as MoS<sub>2</sub>, WS<sub>2</sub> or WSe<sub>2</sub>. For charged layers such as in layered silicates the layer interactions are much stronger. Exfoliated or delaminated nanosheets of 2D-materials have unusual phononic (2), electronic (3, 4), ferroic (5), electrochemical (6), and mechanical properties (7, 8) which are used in phononics, photovoltaics, semiconductors and electrodes. Those properties are strongly tied to the limitation or annihilation of translational symmetry along the stacking direction. When individual monolayers are homogeneously dispersed in a matrix, the related composite materials have a maximized, huge surface-to-volume ratio, and for large aspect ratios (ratio of diameter to layer thickness) these materials process a very small percolation threshold to provide electrical and thermal conductivity, mechanical strength, and large tortuous paths for diffusion barriers. Therefore, control over the layer thickness and interlayer distance is essential. For van-der-Waals solids the weak interlayer interaction energies (4 – 7 kJ/mol) may be overcome by mechanical forces (mechanical exfoliation). A simple and prominent case being the exfoliation of graphene layers using “Scotch tape” (9). The “Scotch tape” method is, however, limited to fundamental research in small scale. Various other techniques ranging from epitaxial growth to mechanical exfoliation, potentially assisted by surface active compounds or by rendering the starting material more shear labile by intercalation reactions, have been shown to yield 2D materials. Established techniques, however, tend to produce broad distributions of layers (5, 10-12) because separation by mechanical exfoliation is incomplete and, moreover, usually comes along with some breakage of the layers.

The same conclusions are valid for the exfoliation of ionic layers, where the exfoliation process is even more difficult due to the stronger attractive interactions between the layers, which are of the order of 100 kJ/mol and larger. Separation procedures almost exclusively rely on mechanical exfoliation with the aid of intercalation of large ions, molecules or surface active compounds, albeit with generally poor and incomplete exfoliation. Even in case of high shear rates, the aspect ratio is not pushed to its intrinsic maximum defined by the pristine lateral extension of the inorganic stacks. Contrary,

infinite osmotic swelling represents a gentler, cheap and scalable route to utterly slicing down layered material into singular layers.

The principle of osmotic swelling goes back to the swelling of graphite oxide (1932) (13) and montmorillonite (14). Here we report a systematic study of the exfoliation of a synthetic 2D layered silicate via osmotic swelling. The study provides direct insight into the conditions for ionic layer separation and outlines the lyotropic phase behavior at extreme aspect ratios of layered material of over more than 4 orders of magnitude in concentration from the dry powder to highly dilute solutions.

## Results and Discussions

Osmotic delamination is known to require a well-defined homoionic layered material with high and very homogeneous charge density. Natural layered silicates suffer from pronounced charge density modulations at all length scales (15). Even synthetic layered silicates when synthesized at temperatures below 1000 K will show a non-uniform intracrystalline reactivity. As a consequence, part of the stacks do not show osmotic swelling at all, or the separation between adjacent layers varies randomly and a weighted average of the *d*-spacings is observed which is of limited analytical value (16). Moreover, all the above mentioned materials need to be ion-exchanged and/or purified in some way prior to swelling experiments. For instance, for montmorillonite a selective dissolution of amorphous auxiliary minerals like iron oxihydroxids is applied, where concomitantly ion exchange occurs and homoionic Na-montmorillonite is obtained (17). Following purification, the ionic strength needs to be reduced and finally the suspensions need to be re-concentrated physically, e.g. by sedimentation or centrifugation, to solid contents where liquid crystalline phases (LC) phases are observed. There is of course a risk that for kinetic reasons during the concentration equilibrium structures might not be readily achieved (18). Here we use a synthetic hectorite with a composition in the unit cell of  $[\text{Na}_{0.96}]^{\text{inter}}[\text{Mg}_{5.14}\text{Li}_{0.94}]^{\text{oct}}[\text{Si}_8]\text{O}_{20}\text{F}_4$  (two formula units per unit cell and therefore abbreviated as Na<sub>0.5</sub>-hectorite) that has been synthesized from the melt at temperatures well above 1000 K (19). The material does not require any purification and shows a homogeneous intracrystalline reactivity. With this material at hand, swelling can be studied starting with a 1D crystalline dry powder all the way into the LC regime and beyond simply by adding increasing amounts of water.

### Regime I: Crystalline Swelling (attractive)

The first steps of layer separation occur via discrete hydration steps as indicated by the adsorption isotherm (Fig. 1a) of synthetic Na<sub>0.5</sub>-hectorite (19).

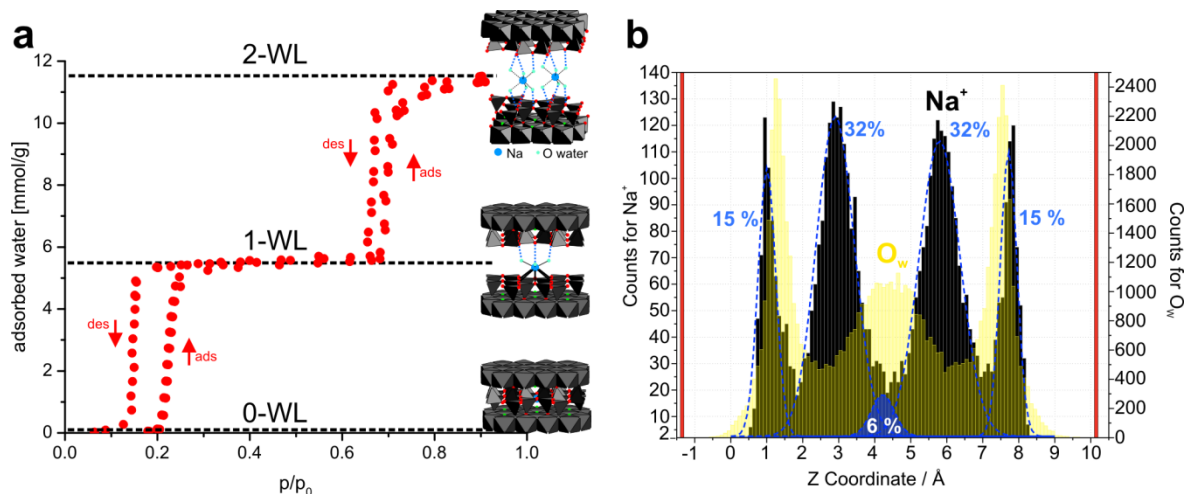


**Figure 1.** (a) Water vapor sorption isotherm of  $\text{Na}_{0.5}$ -hectorite and corresponding hydrated structures of 0-, 1-, 2-WL hydrates. (b) histogram of the Z-distribution of  $\text{Na}^+$  (black bars) and oxygens (" $\text{O}_w$ ", yellow bars) of water molecules in the interlayer space of the hectorite obtained during 1 ns of MD simulation (NVT, 300 K). Red bars represent the plane of basal oxygens of the tetrahedral layers. The five blue gaussians are the deconvoluted peaks of the black bars.

The transitions from non-hydrated (0-WL) to the first water layer (1-WL) and the second water layer (2-WL) occur at threshold partial pressures of  $p/p_0 = 0.22$  and  $p/p_0 = 0.64$ , respectively. The observed hysteresis indicates that the phase transitions are first-order, which is also suggested by MD-simulations (26-28). All structures consist of equidistant layers with long-range 1D ordering within a stack which is referred to as tactoid. Adjacent layers are stacked in an uncorrelated mode (turbostratic stacking). For more highly charged layered silicates in some rare cases three-dimensionally ordered phases can be obtained making crystal structure solutions of 1-WL and 2-WL hydrates available (20, 21).

In the 1-WL state an inner sphere Na-hydrate complex is observed where  $\text{Na}^+$  is in direct contact with basal oxygen atoms on one side and is coordinated by three water molecules on the other side. In the 2-WL state an outer sphere hexaaquo- $\text{Na}^+$ -complex occupies the middle of the interlayer space with symmetrical hydrogen bonding to both adjacent basal oxygen planes (20).

For the more highly charged synthetic hectorite, the 3-WL structure is not accessible within the studied humidity range. It has been observed for natural montmorillonites of lower charge density, where the hexaaquo- $\text{Na}^+$ -complexes were found to predominantly stay in close contact with only one of the silicate layer surfaces (22). To verify this configuration for the synthetic  $\text{Na}^+$ -hectorite, we performed MD-simulations of the 3-WL structure. Details of the calculations are given in the Supporting Information. We found

that 30% of the Na<sup>+</sup>-cations were coordinated to the basal oxygens and formed an inner-sphere complex, similar as in the 1-WL structure. 64% formed hexaaquo-Na<sup>+</sup>-cations located at distances of 0.24 Å away from the surface, similar as in the 2-WL structure. Additionally, 6% formed a hexaaquo-Na<sup>+</sup>-complex in the center of the interlayer space. Upon increasing hydration (0-WL → 1-WL → 2-WL → 3-WL) we observe a structural evolution from surface associated non-hydrated, partially and fully hydrated counterions to surface detached counterions. In the 3-WL phase the surface separated counterions start localizing in the midplane between the two surfaces. This resembles the build-up of the classical counterion double layer structure (Grahame model) with a sequence of three layers: (a) The first layer is the inner Helmholtz plane, where the counter ions are located at the charged surface, (b) followed by an outer Helmholtz plane with surface-separated, fully hydrated ions, and (c) a diffusive double layer with non-localized ions at the midplane (where the electric field vanishes). A full development of the diffuse double layer would eventually lead to electrostatic repulsion (22, 23) driving the separation of adjacent layers.

### **Transition I: Crystalline to Osmotic Swelling**

To obtain insight into the conditions for separation of charged layers as a first approximation the relevant interaction energies and length scales may be estimated applying simple physical models:

- a) For ion-ion interactions an important length scale is the Bjerrum length  $l_B = \frac{e^2}{4\pi\epsilon\epsilon_0 k_B T}$ , which is the distance at which Coulomb interactions between ions are equal to the thermal energy  $k_B T$ .  $e$  is the elementary charge,  $\epsilon_0$  the vacuum permittivity, and  $\epsilon$  the dielectric constant. Taking water ( $\epsilon = 78$ ) at  $T = 298.15$  K (25°C), the Bjerrum length is equal to  $l_B = 0.71$  nm.
- b) For ion-surface interactions the relevant length scale is the Gouy-Chapman length  $l_{GC} = \frac{1}{2\pi d_B \sigma_s}$ , the distance of an ion to a charged surface where electrostatic surface-ion interactions are equal to the thermal energy.  $\rho_s$  is the surface charge density (in units of 1/m<sup>2</sup>). For a charge density of 1 charge per nm<sup>2</sup> (0.96 charges per 2(a×b) = 0.95 nm), as in the present system, the Gouy-Chapman length is equal  $l_{GC} = 0.22$  nm.

c) As a measure of the degree of electrostatic coupling of the ions to the surface, one

defines a coupling parameter  $\Xi = \frac{l_B}{l_{GC}}$ , where in case of  $\Xi \gg 1$  the counterions are

strongly coupled to the surface. For the present case we have  $\Xi = 3.2$  such that the surface-coupling of counterions is significant.

d) The Debye length is given by  $l_D = \left( \frac{\varepsilon \varepsilon_0 k_B T}{2N_A e^2 c_I} \right)^{1/2}$  and is the length scale beyond

which electrostatic interactions are screened. If no specific measures are taken to remove impurities from aqueous solutions, one has a typical ion concentration of  $c_I = 10^{-4}$  mol/l which corresponds to a Debye length of  $l_D = 30$  nm.

These electrostatic length scales will be related to the layer surface separation  $h$  to distinguish different regimes with characteristic properties.

The onset of repulsion of adjacent silicate layers is related to the trade-off between short-range attractive electrostatic interactions, hydration forces, and counterion translational entropy. For small  $h$  in the order of the Gouy-Chapman length ( $h \approx l_{GC}$ , Regime I) we have a competition between attractive surface-counterion interactions with an energy  $F_{el} \approx -hk_B T / l_{GC}$  and a repulsive entropic contribution due to the translational entropy of the counterions, given by  $F_S \approx k_B T \ln h$ , which is increasing with increasing layer surface separation  $h$ . Both contributions result in an osmotic pressure between the surfaces given

by  $\Pi = \sigma_s \frac{\partial F}{\partial d} \approx l_{GC} \sigma_s k_B T \left( \frac{2l_{GC}}{h} - 1 \right)$ . For layer surface separation  $h > 2l_{GC} = 0.44$  nm

according to this simple model, repulsive interactions are expected.

For layered silicates, the initial separation during crystalline swelling is driven by the strong hydration forces, which for  $\text{Na}^+$  involve an energy of 406 kJ/mol.

With the layer thickness of 0.96 nm as determined by the interlayer distance of non-hydrated  $\text{Na}_{0.5}\text{-hectorite}$  (19), the 2-WL structure would already be expected to be in the repulsive regime ( $h \approx 1.55 - 0.96\text{nm} = 0.59\text{nm}$ ). Experimentally, 2-WL is, however, found to be still stabilized at a discrete hydration state by attractive interactions. Lateral ion correlations, van der Waals interactions and hydrogen bonding are, however, neglected. Within the given assumptions a value of 0.59 is therefore not yet significantly larger than the threshold of 0.44 calculated. For the 3-WL structure,  $h \approx 1.83 - 0.96\text{nm} = 0.87\text{nm}$ , the repulsive regime is finally entered. The interactions applied in the MD simulation are more realistic and correctly indicated the transition to the repulsive regime with the 3-WL

structure. While the absolute threshold values might not be correct, the calculation suggest that layer charge variations may easily lead to a situation where domains with repulsive and attractive interactions might coexist within a layer. Even when relatively small, the latter will prevent the separation of adjacent layers by osmotic swelling. This problem will become increasingly severe with increasing lateral diameter of the tactoids.

## Regime II: Osmotic Swelling in the Gouy-Chapman Regime

After the attractive short-range surface-ion interactions have been overcome by hydration such that  $h \gg 2l_{GC}$ , repulsive interactions between the layers dominate. Further addition of water will then lead to a continuous further separation of the layers. This regime is characterized by the length scales  $h \gg l_{GC}, h \ll l_D$ . This regime is referred to as **Gouy-Chapman regime**. Here the osmotic pressure between adjacent layers separated by a

distance  $h$  is given by  $\Pi \approx \frac{\pi k_B T}{2l_B} \frac{1}{h^2}$  and thus becomes independent of the surface charge density. The osmotic pressure is dominated by electrostatics and therefore quite long-ranged and inversely proportional to  $h^2$ .

As suggested by this model, with addition of water the layers separate to  $d > 1.83$  nm and the silicate/water mixture forms transparent gels. Gel formation has been noticed as early as in the 1930s and at that time was related to the “house-of-cards” model, a connected network of edge-basal plane interactions of layers (23). An alternative interpretation of the gel phase has been proposed by Langmuir in 1938 who described it as a lamellar lyotropic phase (24). This has been later confirmed by Michot and Miyamoto (2006) for a series of layered silicates including nontronite, montmorillointe (25-27), beidellite (28), laponite (18), fluorotetrasilicic mica (29) and fluorohectorite (29, 30). Lamellar lyotropic phases were also found by *Gabriel et al.* in 2001 for a solid acid,  $H_3Sb_3P_2O_{14}$  (31), and by *Geng et. al.* for  $H_{0.8}[Ti_{1.2}Fe_{0.8}]O_4 \bullet H_2O$  (32).

The pristine sample in the dried state represents a statistically isotropic microcrystalline sample with mean diameters of 18 µm and tactoids heights of typically 1.5 µm (Fig. S1). The uniquely homogeneous intracrystalline reactivity of the synthetic  $Na_{0.5}$ -hectorite, now allowed a systematic investigation of osmotic swelling by small-angle X-ray scattering (SAXS, Fig. 2 a,b and Figs. S3). Consistent with the observation of Langmuir, Michot and Miyamoto, 2D-scattering patterns of the bulk samples show a series of concentric, equidistant diffraction rings which are characteristic for lamellar lyotropic structures. The scattering patterns are highly anisotropic due to shear-alignment of the highly swollen tactoids during filling of the gels in the X-ray capillary. A high scattering intensity is found at the equator indicating that the layers align parallel to the surface of the vertically

mounted capillary. A quantitative analysis applying model calculations reveal orientational order parameters as high as  $S = 0.8$  (see table S1, Supporting Information).

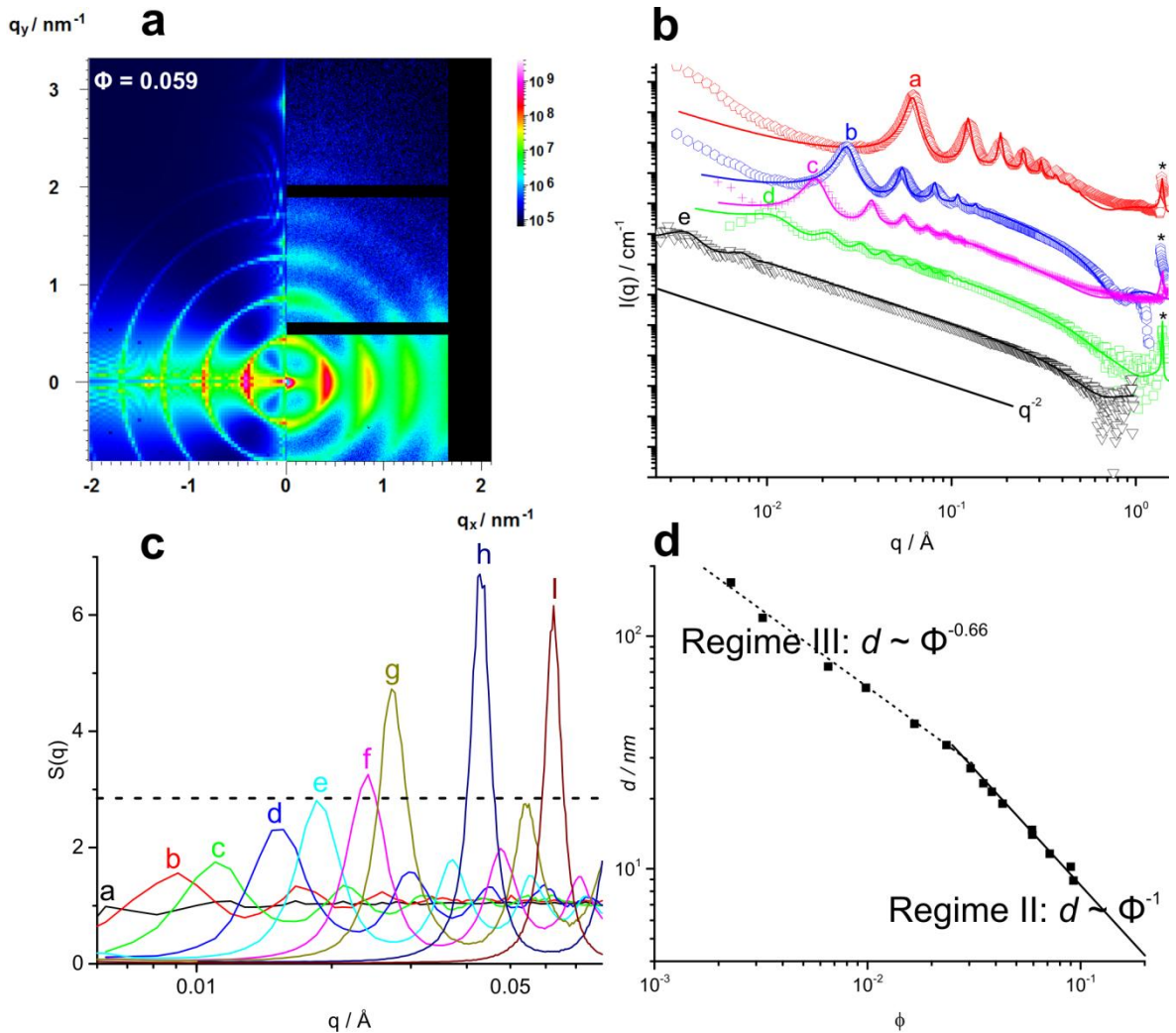


**Figure 2:** (a) 2D-SAXS pattern at volume fraction  $\phi = 0.059$ . On the right side, experimental data are plotted, on the left side modelled patterns are shown. (b) The one-dimensional (1D) SAXS intensity show a shift of the  $001$  reflection to higher  $d$ -spacings with decreasing concentration and the concentration independent position of the  $hk$ -band (asterisk) at high  $q$ . (a.  $\phi = 0.090$  (red pentagons); b:  $\phi = 0.035$  (blue hexagons); c:  $\phi = 0.024$  (magenta crosses), d:  $\phi = 0.010$  (green squares) and e:  $\phi = 0.0016$  (black triangles). Calculated scattering curves and the  $q^{-2}$ -scaling law of layers are given by solid lines. (c) Structure factor of swollen lyotropic phases at different volume fractions. a)  $\phi = 0.003$ ; b)  $\phi = 0.007$ ; c)  $\phi = 0.010$ , d)  $\phi = 0.017$ , e)  $\phi = 0.024$ , f)  $\phi = 0.030$ ; g)  $\phi = 0.035$ ; h)  $\phi = 0.059$ ; i)  $\phi = 0.090$ . The dashed line at  $S(q) = 2.85$  marks the Hansen-Verlet rule where melting is expected. (d) Scaling relation  $d$ -spacing as a function of volume fraction. The solid line corresponds to a 1D-swelling law following the equation  $d = D/\phi$ , which fits both crystalline swelling and Wigner crystal regime. The gradient in the nematic sol regime (dashed line) follows a distinct scaling ( $d \sim \phi^{-0.66}$ ).

In Fig. 2b the azimuthally averaged data are given. For higher concentrations we observe a rational series (1:2:3:...) of  $00l$ -reflections indicating the formation of a lyotropic lamellar phase. Up to 8 higher order reflections underline the excellent positional order of adjacent

individual layers. Upon dilution the peak positions shift to lower  $q$ -values, indicating increasing separation of the silicate layers due to progressing swelling. The interlayer distance reaches values up to 170 nm for  $\phi = 0.002$ . The observed  $q^{-2}$ -scaling of the scattering intensity over nearly the whole scattering curve confirms the presence of thin layers with very large lateral dimensions. For the higher concentrations, where the signal-to-noise ratio is higher, it is possible to determine the first minimum of the form factor oscillations at high  $q$  (Fig. 2b), which allows to derive the thickness of the layers to  $d_0 = 0.85$  nm. Please note, that the monolayer thickness derived from shallow minimum of SAXS form factor modeling is slightly smaller than the monolayer thickness of 0.96 nm obtained from the interlayer distance of non-hydrated  $\text{Na}_{0.5}$ -hectorite (19). The deviation can be explained by the assumption of homogeneous electron density over the platelet thickness in the SAXS modeling.

The solid lines are quantitative fits to the measured scattering intensities using a model of stacked layers where the scattered intensity is given by  $I(q) = b^2 \rho P(q, d_0, D_0) [1 + \beta(q)(Z(q, d, D) - 1)G(q, \delta)]$ , where  $b$  is the scattering contrast between the silicate layers and the solution,  $\rho$  the number density of the layers,  $P(q)$  the form factor, which depends on the scattering vector  $q$ , the layer thickness  $d_0$ , and the lateral layer dimension  $D_0$ .  $Z(q)$  is the lattice factor determining interlayer distance (or lamellar long period)  $d$  as well as the peak width, which is related to the lateral size  $D$  of the ordered domains.  $G(q)$  is the Debye-Waller factor, which depends on the mean deviation  $\delta$  of the layers from their ideal lattice point. The term  $S(q) = [1 + \beta(q)(Z(q, d, D) - 1)G(q, \delta)]$  is the structure factor, which will be discussed in a separate section. The measured scattering intensities could be well fitted to this expression, keeping the layer thickness  $d_0 = 0.85$  nm and the lateral layer dimension  $D_0 = 18$   $\mu\text{m}$  constant. The data are summarized in Table S1 in the Supporting Information.

The  $\lambda$ -shaped 11/02-band (asterisk in Fig. 2b) is observed for all dilutions at the same  $q$ -values ( $q \sim 1.4$   $\text{\AA}^{-1}$ ), indicating that the  $(hk)$ -plane structure of the silicate layers are not influenced by the swelling in the  $00l$  direction of the tactoids. The lamellar distance is plotted as a function of volume fraction in Fig. 2d. For high volume fractions  $\phi > 0.025$  we observe a linear dependence following  $d = d_0 / \phi$  typical for lamellar systems (25) corroborating monolayers uniformly separated by water. As a result of strong repulsive interactions the layers localize on a highly ordered lattice, thereby maximizing their

separation. This phase phenomenologically resembles a Wigner crystal, which is known to occur for electrons in plasmas, when their repulsive interactions become much larger than their kinetic energy such that they couple and are positionally strongly correlated.

The Wigner-like phase can be considered as a homogeneous single gel phase with no voids between the microcrystalline domains of highly swollen tactoids.

### **Transition II: Melting of Wigner Crystal (Delamination)**

The scaling relation given in Fig. 2d shows a kink at  $\phi = 0.025$ . Below this volume fraction a weaker concentration dependence of the layer distance,  $d \sim \phi^{-0.66}$ , is obtained indicating the transition to a more disordered regime. At the same concentration the shear orientation seen in 2D SAXS pattern relaxes (Fig. S3). Further the relative lattice derivations from the lattice points  $\delta$  reaches values over 10% (cf. table S1). According to the Lindeman-criterium (33) lattice melting is expected for relative displacements larger than 10%. In good agreement with all the other criteria the structure factor (Fig. 2c) confirms the melting transition, fulfilling the Hansen-Verlet criterion according to which the melting transition corresponds to a value of  $S(q) = 2.85$ . Larger values correspond to ordered solid, smaller values to a molten solid. This value is crossed at a volume fraction of  $\phi = 0.025$ . This shows that for  $d \sim l_D$ , the Wigner lattice melts due to the screening of the long-range electrostatic interaction.

### **Regime III: Osmotic Swelling in the Screened Regime**

When the interlayer distance becomes larger than the Debye-length  $l_D \approx 30$  nm, a new regime characterized by  $h \gg l_{GC}, h \gg l_D$  is reached. Here, electrostatic interactions are screened beyond length scales of  $l_D$  and the osmotic pressure is given by

$$\Pi \approx \frac{8k_B T}{\pi d_B l_D^2} e^{-d/l_D} \text{ with a strongly screened repulsive interaction. The weakening of}$$

electrostatic repulsion at transition II leads to reduced correlations of adjacent layers and melting of the Wigner crystal. As a consequence, in regime III a weaker concentration dependence of the interlayer distance, namely  $d \sim \phi^{-0.66}$  (Fig. 2d) is observed. For self-assembled systems of conventional molecular surfactant or block-copolymer micelles, a change in the exponential of the equation  $d \sim \phi^{-\beta}$  signals a transition between different topologies:  $\beta = 1$ ,  $\beta = 1/2$ , and  $\beta = 1/3$  for lamellar, cylindrical (rod like), and spherical topologies, respectively. An isotropic phase with freely rotating layers would be signalled by  $\beta = 1/3$ . A value of  $\beta = 2/3$  would be characteristic of a bicontinuous phase (34, 35).

As such topological changes cannot occur for insoluble silicate layers at this point the physical reason behind the  $\beta = 0.66$  dependency is unclear. *Michot et al.* observed for size classified nontronite also a discontinuity of the scaling from  $\phi^{-1}$  to a variety of different slopes, depending on the size fraction (26). The observed slopes were therefore described by a mixture of freely rotating small platelets scaling with  $\phi^{-1/3}$  and a lyotropic lamellar phase of larger platelets scaling with  $\phi^{-1}$ . Although  $\text{Na}_{0.5}\text{-hectorite}$  is also polydisperse, the smallest diameters seen in static laser scattering are still in the micron range (19). Hence the  $\phi^{-1/3}$  can only be observed for  $d >$  micron range and freely rotating layers therefore can be ruled out at  $d$ -spacings where the discontinuity ( $d^* \approx 34 \text{ nm}$ ) is observed.

Please note, that we do not observe a macroscopic phase separation in regime III at concentrations  $0.025 < \phi < 0.0015$ . Thus, the change in the exponent may be a result from entering a microphase segregation, where an ordered lamellar phase of silicate layers (phase A) is in equilibrium with a dilute microphase of higher water content (phase B). In phase B separated, but not freely rotating, layers may have a folded and undulated conformation reducing the effective lateral extension, thereby gaining conformational entropy. Similar behavior is reported for amphiphilic lamellar systems, where lamellae unbind and separate from a lamellar stack, yet then fold and close to form vesicles, such that there is a concentrated ordered lamellar phase in equilibrium with a dilute vesicular phase.

Alternatively, for entropic reasons the layers might use the degrees of freedom gained beyond 34 nm separation to translate laterally beyond the former crystal edges of the tactoid and by this increase the effective diameter. These changes will both reduce the packing efficiency of the microdomains which might result in formation of water filled voids in-between individual tactoids. Less obvious could be a potential contribution from a metamorphosis of the tactoid morphology accompanying swelling. While expanding the interlayer space the morphology of the tactoid is gradually converted from a platelet to a wormlike rod (morphology conversion is illustrated by a swelling movie provided as supporting information). The pristine tactoids typically have an aspect ratio of 12 (Fig. S4). The aspect ratio is actually inverted to 0.2 at a separation of the individual silicate layers of about 60 nm ( $\phi \approx 0.01$ ). At these late stages of osmotic swelling the electrostatic repulsion between basal planes is increasingly screened, and repulsion between the edges might then become the dominating interparticle force. Moreover, with the inversion of the aspect ratio, the relative contribution of basal surfaces and edge surfaces of the tactoids is changed drastically. Initially with platy morphology, edge-edge-contacts are statistically very unlikely. At later stages, edge-edge-contacts between the rods could be

dominating. The observed slope of  $\phi^{-0.66}$  might therefore be the result of mixing rod swelling and plate swelling.

Regime III is characterized by increasing widths and decreasing intensities of the Bragg peaks, indicating a reduction of the coherence length in the ordered domains, and loss of higher order reflections, corresponding to larger deviations from the lattice points. For very dilute solutions eventually the peaks would be at very low q-values, out of the range of our SAXS-setup, with a  $q_{\min}$  corresponding to  $d \sim 170$  nm and  $\phi > 0.0023$ .

At  $\phi = 0.0015$ , the suspension is still viscous with no macroscopic phase separation as indicated by optical inspection with polarized light. Experimentally, we observed no visible phase separation even over a period of several months. It may nevertheless be that at much longer periods ( $> 1$  year) and despite very slow kinetics segregation might occur (36). Below this volume fraction the two microphases start to macroscopically phase separate by gravitation as shown in Fig. 3 and Fig. S5. Interestingly, for suspensions with  $0.0008 < \phi < 0.0004$  (Fig. 3b-d) after two days phase separation results in a layered superstructure with periodicities of several millimeters. At some point, tactoids with smaller lateral diameters will start to rotate freely and it is most likely these volumes that segregate to the top. Of course, this supernatant volume increases with progressing dilution (Fig. 3b-f).

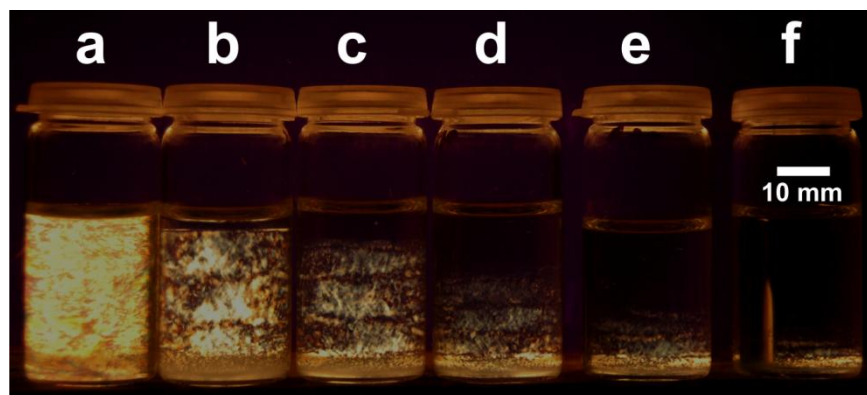


**Fig. 3:** Macroscopic phase separation of  $\text{Na}_{0.5}\text{-hectorite}$  suspensions observed between crossed polarizer and analyzer. (a)  $\phi = 0.0015$ ; (b)  $\phi = 0.0008$ ; (c)  $\phi = 0.0005$ ; (d)  $\phi = 0.0004$ ; (e)  $\phi = 0.0003$ ; (f)  $\phi = 0.0002$ .

Eventually, upon sufficient dilution a single dilute phase will be reached if the layer separation is of the order of the lateral dimension of the layers, e.g. if  $\phi \sim \frac{d_0}{D_0}$ . Due to the high median aspect ratio of 18000, this concentration is calculated to be  $\phi \sim 0.000056$ . Indeed, a suspension close to this concentration ( $\phi = 0.00009$ ) appears to be a single

phase. It is shear-birefringent because there is still shear-induced alignment of the layers (Fig. S6). The birefringence disappears after cessation of shear.

### Conclusions:

In conclusion we show that the delamination of charged layers requires that the layer separation exceeds the Gouy-Chapman length ( $h > 2l_{GC}$ ) such that interactions between adjacent layers become repulsive, leading to an osmotic swelling. In the electrostatically attractive regime ( $h \sim l_{GC}$ ) layer separation occurs by discrete hydration steps. During initial steps of osmotic swelling the classical double layer structure consisting of an inner and outer Helmholtz plane followed by a diffuse double layer is established. Upon further hydration there is a regime of strong osmotic-repulsion (Gouy-Chapman regime), where the layers form a highly ordered one-dimensional Wigner crystal. When the interlayer distances reaches the Debye-length, a new regime with screened osmotic repulsion is entered, accompanied by a melting of the Wigner crystal and formation of a first microscopically phase separated system. Macroscopic phase separation by gravitation does not set in until much lower concentrations ( $\phi < 0.0015$ ). At very low concentrations ( $\phi < \sim 0.0001$ ) finally a homogeneous dilute phase is reached. The aspect of high charge density, charge homogeneity and the structure and property of the lamellar phases are both relevant fundamentally, as well as for applications e.g. as fillers in nanocomposite films used as gas barrier.

### Acknowledgments

The financial support from the German Research Foundation, in the frame of the Collaborative Research Center (SFB 840): “From particulate nanosystems to mesotechnology” is highly acknowledged.

### References

1. Blackmore A V, Miller R (1961) Tactoid size and osmotic swelling in calcium montmorillonite. *Soil Sci Soc Amer Proc* 25, 169-173.
2. Chiritescu C, Cahill DG, Nguyen N, Johnson D, Bodapati A, Kebinski P, Zschack P (2007) Ultralow thermal conductivity in disordered, layered WSe<sub>2</sub> crystals. *Science* 315, 351-353.
3. Takada K, Sakurai H, Takayama-Muromachi E, Izumi F, Dilanian R A, Sasaki T (2003) Superconductivity in two-dimensional CoO<sub>2</sub> layers. *Nature* 422, 53-55.

4. Novoselov K S, Geim AK, Morozov S V, Jiang D, Zhang Y, Dubonos S V, Grigorieva I V, Firsov A A (2004) Electric field effect in atomically thin carbon films. *Science* 306, 666-669.
5. Wu W, Wang L, Li Y, Zhang F, Lin L, Niu S, Chenet D, Zhang X, Hao Y, Heinz T F, Hone J, Wang Z L (2014) Piezoelectricity of single-atomic-layer MoS<sub>2</sub> for energy conversion and piezotronics. *Nature* 514, 470-474.
6. Mashtalir O, Naguib M, Mochalin V N, Dall'Agnese Y, Heon M, Barsoum M W, Gogotsi Y (2013) Intercalation and delamination of layered carbides and carbonitrides. *Nat Commun* 4, 1716.
7. Suk J W, Piner R D, An J, Ruoff R S (2010) Mechanical Properties of Mono layer Graphene Oxide. *Acs Nano* 4, 6557-6564.
8. Kunz D A, Feicht P, Goedrich S, Thurn H, Papastavrou G, Fery A, Breu J (2013) Space-Resolved In-Plane Moduli of Graphene Oxide and Chemically Derived Graphene Applying a Simple Wrinkling Procedure. *Adv Mater* 25, 1337-1341.
9. Novoselov K S, Jiang D, Schedin F, Booth T J, Khotkevich V V, Morozov S V, Geim A K (2005) Two-dimensional atomic crystals. *Proc Natl Acad Sci USA* 102, 10451-10453.
10. Butz B, Dolle C, Niekiel F, Weber K, Waldmann D, Weber H B, Meyer B, Spiecker E (2014) Dislocations in bilayer graphene. *Nature* 505, 533-537.
11. Kim S S, Van Khai T, Kulish V, Kim Y H, Na H G, Katoch A, Osada M, Wu P, Kim H W (2015) Tunable Bandgap Narrowing Induced by Controlled Molecular Thickness in 2D Mica Nanosheets. *Chem Mater* 27, 4222-4228.
12. Lotya M, Hernandez Y, King P J, Smith R J, Nicolosi V, Karlsson L S, Blighe F M, De S, Wang Z M, McGovern I T, Duesberg G S, Coleman J N (2009) Liquid Phase Production of Graphene by Exfoliation of Graphite in Surfactant/Water Solutions. *J Am Chem Soc* 131, 3611-3620.
13. Hofmann U (1932) Eindimensionale Quellung von Graphitsäure und Graphit. Die Reaktionsweisen des Graphits. *Kolloid Z* 61, 297-304.
14. Hofmann U, Kurd E, Diederich W (1933) Kristallstruktur und Quellung von Montmorillonit (Das Tonmineral der Bentonittone). *Z Kristallogr* 86, 340-348.

15. Lagaly G (1981) Characterization of Clays by Organic-Compounds. *Clay Miner* 16, 1-21.
16. Ferrage E, Lanson B, Sakharov B A, Geoffroy N, Jacquot E, Drits V A (2007) Investigation of dioctahedral smectite hydration properties by modeling of X-ray diffraction profiles: Influence of layer charge and charge location. *Amer Mineral* 92, 1731-1743.
17. Mehra O P, Jackson M L (1958) Iron oxide removal from soils and clays by dithionite-citrate system buffered with sodium bicarbonate. *Clays Clay Miner* 7, 317-327.
18. Paineau E, Bihannic I, Baravian C, Philippe A M, Davidson P, Levitz P, Funari S S, Rochas C, Michot L J (2011) Aqueous Suspensions of Natural Swelling Clay Minerals. 1. Structure and Electrostatic Interactions. *Langmuir* 27, 5562-5573.
19. Stöter M, Kunz D A, Schmidt M, Hirsemann D, Kalo H, Putz B, Senker J, Breu J (2013) Nanoplatelets of Sodium Hectorite Showing Aspect Ratios of ~ 20000 and Superior Purity. *Langmuir* 29, 1280-1285.
20. Kalo H, Milius W, Breu J (2012) Single Crystal Structure Refinement of One- and Two-layer Hydrate of Sodium-Fluorohectorite. *RSC Adv* 2, 8452-8459.
21. Kalo H, Milius W, Bräu M, Breu J (2013) Synthesis and single crystal structure refinement of the one-layer hydrate of sodium brittle mica. *J. Solid State Chem.* 198, 57-64.
22. Skipper N T, Lock P A, Titiloye J O, Swenson J, Mirza Z A, Howells W S, Fernandez-Alonso F (2006) The structure and dynamics of 2-dimensional fluids in swelling clays. *Chem Geo.* 230, 182-196.
23. Hofmann U, Hausdorf A (1942) Kristallstruktur und innerkristalline Quellung des Montmorillonits. *Z Kristallogr* 104, 265-293.
24. Langmuir I (1938) The Role of Attractive and Repulsive Forces in the Formation of Tactoids, Thixotropic Gels, Protein Crystals and Coacervates. *J Chem Phys* 6, 873-896.
25. Michot L J, Bihannic I, Maddi S, Funari S S, Baravian C, Levitz P, Davidson P (2006) Liquid-crystalline aqueous clay suspensions. *Proc Natl Acad Sci USA* 103, 16101-16104.

26. Michot L J, Bihannic I, Maddi S, Baravian C, Levitz P, Davidson P (2008) Sol/gel and isotropic/nematic transitions in aqueous suspensions of natural nontronite clay. Influence of particle anisotropy. 1. Features of the I/N transition. *Langmuir* 24, 3127-3139.
27. Michot L J, Baravian C, Bihannic I, Maddi S, Moyne C, Duval J F L, Levitz P, Davidson P (2009) Sol-Gel and Isotropic/Nematic Transitions in Aqueous Suspensions of Natural Nontronite Clay. Influence of Particle Anisotropy. 2. Gel Structure and Mechanical Properties. *Langmuir* 25, 127-139.
28. Paineau E, Antonova K, Baravian C, Bihannic I, Davidson P, Dozov I, Imperor-Clerc M, Levitz P, Madsen A, Meneau F, Michot L J (2009) Liquid-Crystalline Nematic Phase in Aqueous Suspensions of a Disk-Shaped Natural Beidellite Clay. *J Phys Chem B* 113, 15858-15869.
29. Miyamoto N, Iijima H, Ohkubo H, Yamauchi Y (2010) Liquid crystal phases in the aqueous colloids of size-controlled fluorinated layered clay mineral nanosheets. *Chem Commun* 46, 4166-4168.
30. Hemmen H, Ringdal N I, De Azevedo E N, Engelsberg M, Hansen E L, Meheust Y, Fossum J O, Knudsen K D (2009) The Isotropic-Nematic Interface in Suspensions of Na-Fluorohectorite Synthetic Clay. *Langmuir* 25, 12507-12515.
31. Gabriel J C, Camerel F, Lemaire B J, Desvaux H, Davidson, P, Batail P (2001) Swollen liquid-crystalline lamellar phase based on extended solid-like sheets. *Nature* 413, 504-508.
32. Geng F, Ma R, Nakamura A, Akatsuka K, Ebina Y, Yamauchi Y, Miyamoto N, Tateyama Y, Sasaki T (2013) Unusually stable ~100-fold reversible and instantaneous swelling of inorganic layered materials. *Nat Commun* 4:1632.
33. Lindemann F A (1910) The calculation of molecular vibration frequencies. *Z Phys* 11, 609-615.
34. Hyde S T (2001) in *Handbook of Applied Surface and Colloid Chemistry*, ed. Holmberg, K. (John Wiley & Sons, Chichester), pp. 299-332.
35. Hyde S T (1997) Swelling and structure. Analysis of the topology and geometry of lamellar and sponge lyotropic mesophases. *Langmuir* 13, 842-851.

36. Ruzicka B, Zaccarelli E, Zulian L, Angelini R, Sztucki M, Moussaid A, Narayanan T, Sciortino F (2011) Observation of empty liquids and equilibrium gels in a colloidal clay. *Nat Mater* 10, 56-60.
37. Breu J, Seidl W, Stoll A J, Lange K G, Probst T U (2001) Charge homogeneity in synthetic fluorohectorite. *Chem Mater* 13, 4213-4220.
38. Foerster S, Fischer S, Zielske K, Schellbach C, Sztucki M, Lindner P, Perlich J (2011) Calculation of scattering-patterns of ordered nano- and mesoscale materials. *Adv Colloid Interface Sci* 163, 53-83.
39. Martinez L, Andrade R, Birgin E, Martinez J (2009) PACKMOL: A Package for Building Initial Configurations for Molecular Dynamics Simulations. *J Comput Chem* 30, 2157-2164.
40. Plimpton S (1995) Fast Parallel Algorithms for Short-Range Molecular-Dynamics. *J Comput Phys* 117, 1-19.
41. Cygan R T, Liang J J, Kalinichev A G (2004) Molecular models of hydroxide, oxyhydroxide, and clay phases and the development of a general force field. *J Phys Chem B* 108, 1255-1266.
42. Marry V, Dubois E, Malikova N, Durand-Vidal S, Longeville S, Breu J (2011) Water Dynamics in Hectorite Clays: Influence of Temperature Studied by Coupling Neutron Spin Echo and Molecular Dynamics. *Environ Sci Technol* 45, 2850-2855.
43. Berendsen H J C, Grigera J R, Straatsma T P (1987) The Missing Term in Effective Pair Potentials. *J Phys Chem* 91, 6269-6271.
44. Humphrey W, Dalke A, Schulter K (1996) VMD: Visual molecular dynamics. *J Mol Graph* 14, 33-38.

## 5.6.2 Supporting Information

### Supporting Information

In Depth Insights into the Key Steps of Delamination of Charged 2D Materials

**Sabine Rosenfeldt,<sup>1</sup> Matthias Stöter<sup>2</sup>, Mathias Schlenk<sup>1</sup>, Thomas Martin<sup>2</sup>, Rodrigo Queiroz Albuquerque,<sup>3</sup> Stephan Förster,<sup>\*1</sup> and Josef Breu<sup>\*2</sup>**

<sup>1</sup> Physical Chemistry I, University of Bayreuth, Universitätsstrasse 30, 95440 Bayreuth, Germany

<sup>2</sup> Inorganic Chemistry I, University of Bayreuth, Universitätsstrasse 30, 95440 Bayreuth, Germany

<sup>3</sup> São Carlos Institute of Chemistry, University of São Paulo, Av. Trab. Sao-carlense 400, 13560-970 São Carlos, Brazil.

### Materials and Methods

#### Supporting data

1. One water layer (1 WL) state of Na<sub>0.5</sub>-Hectorite
2. MD Simulations
3. Calculation of the volume fraction
4. 2D scattering patterns
5. Change of the tactoid morphology upon swelling
6. Illustration of an isotropic phase
7. Shear induced birefringence of an isotropic phase

## Materials and Methods

### Synthesis and sample preparation

$\text{Na}_{0.5}$ -hectorite with the composition  $[\text{Na}_{0.96}]^{\text{inter}}[\text{Mg}_{5.14}\text{Li}_{0.94}]^{\text{oct}}[\text{Si}_8]\text{O}_{20}\text{F}_4$  was synthesized by melt synthesis in a closed molybdenum crucible according to the published procedure (37). After synthesis the material was annealed for 6 weeks at 1045°C to improve intracrystalline reactivity, charge homogeneity and phase purity as recently described (19).  $\text{Na}_{0.5}$ -hectorite gels were prepared in closed glass vessels by addition of deionized water (Millipore) to  $\text{Na}_{0.5}$ -hectorite in its one water layer hydrated form (stored at 43% relative humidity adjusted using a saturated aqueous  $\text{K}_2\text{CO}_3$ -solution). The suspensions were equilibrated for 48 hours at ambient conditions.

### Small-Angle X-Ray Scattering (SAXS)

All small-angle X-ray scattering (SAXS) data reported here were measured using the small-angle X-ray system “Double Ganesha AIR” (SAXSLAB, Denmark). The X-ray source of this laboratory-based system is a rotating anode (copper, MicoMax 007HF, Rigaku Corporation, Japan) providing a micro-focused beam. The data are recorded by a position sensitive detector (PILATUS 300K, Dectris). To cover the range of scattering vectors between 0.004-2.0 Å<sup>-1</sup> different detector positions were used. The measurements were done in 1 mm glass capillaries (Hilgenberg, code 4007610, Germany) at room temperature. The circularly averaged data were normalized to incident beam, sample thickness and measurement time before subtraction of the solvent. The data analysis was performed with the software Scatter (version 2.5) (38).

### Wide angle powder x-ray diffraction (PXRD)

X-ray diffraction pattern of the  $\text{Na}_{0.5}$ -hectorite powder was obtained in transmission mode on a Stoe Stadi P power diffractometer ( $\text{Cu K}_\alpha$  radiation, Ge monochromator, linear positron sensitive detector). In order to fix the environmental conditions like relative humidity and texture effects, the measurements were performed in sealed Lindemann glass capillaries.

### Water Vapor Sorption Isotherm

The isotherm was measured with a Belsorp-max (BEL JAPAN INC.) at 25 °C.  $\text{Na}_{0.5}$ -hectorite powder was dried prior to measurement at 120 °C under vacuum (0.1 mbar) for 12 h.

### Computational Details

A supercell of fluorohectorite with  $a = 41.9456 \text{ \AA}$ ,  $b = 54.522 \text{ \AA}$ ,  $c = 18.4240 \text{ \AA}$ ,  $\alpha = \gamma = 90^\circ$ , and  $\beta = 96.42^\circ$  (1872 atoms) and stoichiometry  $\text{Na-Si}_8\text{-Mg}_6\text{-O}_{20}\text{-F}_4$  was first generated using the Accelrys program, the two  $\text{SiO}_2$  hexagonal cavities in direct contact with the interlamellar space being kept eclipsed. Water molecules were included using the

Packmol program (39). The number of water molecules ( $n$ ) was first optimized by doing several Molecular Dynamics (MD) simulations with the NPT ensemble at 300 K and 1 atm and varying  $n$ , from where  $n = 729$  was found, corresponding to a  $d_{\text{spacing}}$  of 18.29 Å. Then, simulations with the NVT canonical ensemble and Nosé–Hoover thermostat at 300 K were done using  $n = 729$  and that value of  $d_{\text{spacing}}$  fixed to investigate the distribution of Na ions and water molecules in the interlamellar space, as well as the Radial Distribution Function (RDF) involving the Na–Na and Na–OH<sub>2</sub> (Na–O<sub>w</sub>) pairs. For the NVT ensemble the lamellae were frozen. The simulations were done with the LAMMPS program (40) with the CLAYFF force field (41). The van der Waals parameters for Fluorine were taken from Ref (42). The SPC/E water model (43) was used in all simulations and the bond distances and bond angles of all water molecules were constrained to the original SPC/E values using the SHAKE algorithm. Periodic boundary conditions along X, Y and Z were used in all simulations. Inner and outer cutoffs of 9 and 11 Å, respectively, were adopted for the van der Waals interactions and 9 Å for the electrostatic ones. The latter were also computed using the Particle-Mesh-Ewald method. Equations of motion were integrated using the velocity-Verlet method and a timestep of 1 fs was used. After equilibrating the system, typically with 200 ps (= 2x10<sup>5</sup> MD steps), a production phase of 1 ns was used to calculate the Z-distribution of Na and O<sub>w</sub> atoms in the inter-lamellar space, and RDF functions. An isomorphous distribution of Mg<sup>2+</sup> and Li<sup>+</sup> cations was assumed in the octahedral layer and consequently, the Mg charge was set to meet the total layer charge. The following charges (in electron charge units) were then used for the clay atoms: +1.83 (Mg), +1 (Na), -1 (F), +2.09 (Si), -1.235 (O). The parametrization of CLAYFF, which has originally included Li<sup>+</sup> in the octahedral layer, has slightly different values: +1.35 (Mg), +1 (Na), -1 (F), +2.09 (Si), -1.06 (O). The charges were optimized to reduce the peak of the RDF calculated for the Na–Na pair at R < 4.0 Å, since previous experimental results (20) suggest that two Na<sup>+</sup> atoms coordinated to the same water molecule and therefore less than 4 Å apart from each other are not often observed. Trajectories were visualized with the VMD program (44).

## Supporting Data

### 1. One water layer (1 WL) state of $\text{Na}_{0.5}\text{-Hectorite}$

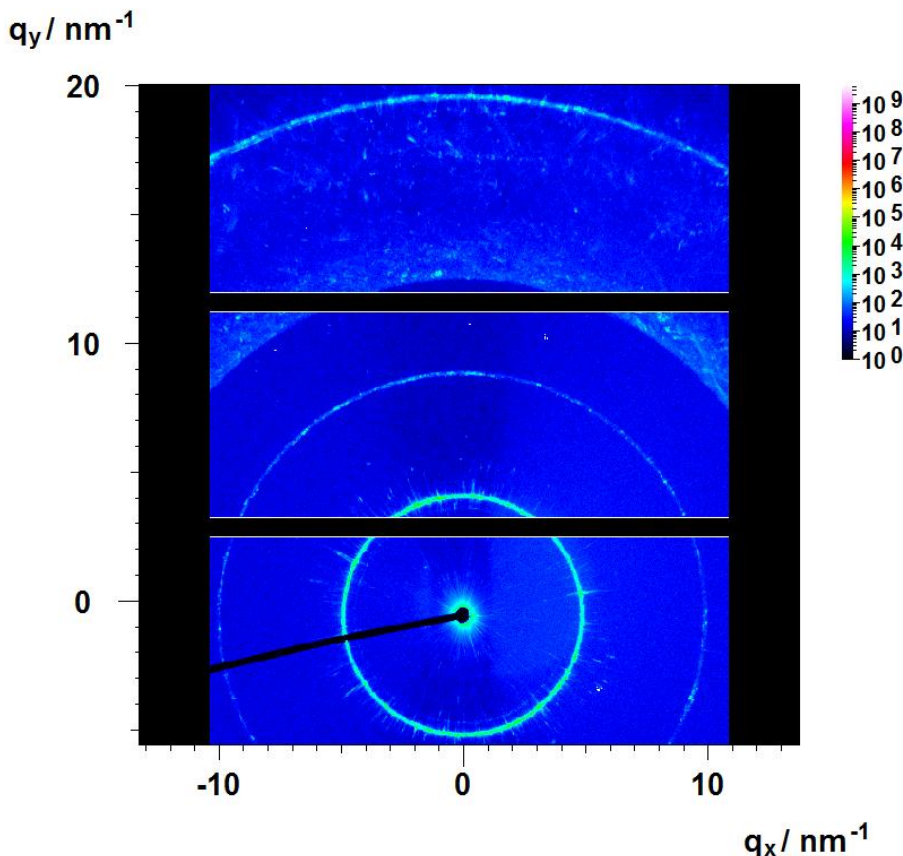


**Figure S1.** 2D SAXS pattern of the 1 WL-powder shows statistically oriented tactoids.

### 2. MD-simulations

Figure S2, left shows one snapshot of the hydrated hectorite obtained by MD simulation (NVT, 300K) that highlights the  $\text{Na}^+$  distribution (blue spheres) in the interlayer space. A more detailed distribution of  $\text{Na}^+$  and oxygen of water molecules ( $\text{O}_w$ ) in the interlayer space was obtained by averaging the positions of those atoms during 1 ns of MD simulation, as shown in the histogram (Figure 1b in the manuscript). The  $\text{H}_2\text{O}/\text{Na}^+$  ratio of 15.2 used in the simulations corresponded to a *d*-spacing of 18.29 Å. Most interlayer cations are octahedrally coordinated by water molecules at distances of 2.4 Å (Figure S2, right). More than half of the water molecules are non-coordinated, since each  $\text{Na}^+$  can be complexed by a maximum of 6 water molecules.

The formation of three layers of  $\text{H}_2\text{O}$  is readily identified from the histogram (Figure 1b, yellow bars) and  $\text{Na}^+$  cations (Figure 1b, black bars) are positioned between those layers. The two main populations calculated for  $\text{Na}^+$  are  $\approx 1.45$  Å apart from the central water layer and  $\approx 1.6$  Å apart from the two outer water layers. These values are in fair

agreement with the experimental value of 1.32-1.37 Å obtained for a higher charged hectorite with 2 water layers (2-WL) reported in the literature (20).

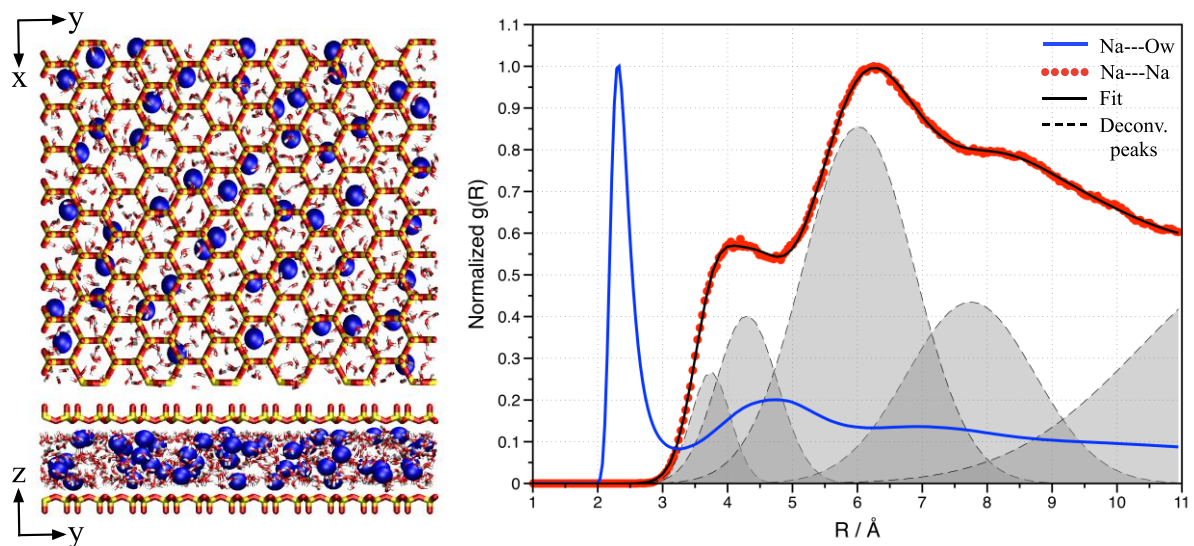


**Figure S2.** Left: MD Snapshot (NVT, 300 K) of the hydrated hectorite highlighting the  $\text{Na}^+$  distribution (blue spheres). Si, O and H atoms are yellow, red and white, respectively. Right: Radial Distribution Functions (RDF) for the  $\text{Na--Na}$  (red dots) and  $\text{Na--Ow}$  (blue line) pairs calculated by averaging the atomic positions during 1 ns of MD simulation. The  $\text{Na--Na}$  signal was deconvoluted into the gray gaussians, which add up to give the black line. The  $\text{Na--Ow}$  average distance (blue line) has a maximum at 2.4 Å which is expected for octahedrally coordinated  $\text{Na}^+$ . The maximum probability of finding the  $\text{Na--Na}$  pair lies at 6.25 Å (red dots). 3.5 % of the  $\text{Na--Na}$  pairs are on average 3.75 Å apart, which indicates they would be complexed to one or two oxygens from shared water molecules. However, the deconvoluted peaks reveal that most  $\text{Na--Na}$  pairs are separated by 6.0 Å, which nicely agrees with experimental results (20).

The  $\text{Na}^+$  distribution (Figure 1b, black bars) was deconvoluted into five gaussians (blue dashed lines) in order to quantify the amount of  $\text{Na}^+$  in closer contact with the basal planes. The majority ( $\approx 64\%$ ) of the  $\text{Na}^+$  form outer sphere hexaquocomplexes which are found in direct contact to the basal oxygens of the tetrahedral layers encompassing the interlayer space with a projected  $\text{O}_\text{b}-\text{Na}$ -distance of  $\approx 4$  Å. This type of interlayer cations reassembles what has been found in the single crystal refinement of the 2-WL structure (20). A considerably smaller number of  $\text{Na}^+$  ( $\approx 30\%$ ) form an inner-sphere complex with a projected  $\text{O}_\text{b}-\text{Na}$ -distance of  $\approx 2$  Å where the cation is coordinated by basal oxygens and interlayer water molecules resembling the situation in 1-WL (20). We attribute the occurrence of these inner-sphere complexes to the higher charge density of the synthetic hectorite as compared to montmorillonite. The increased charge density will shift the

subtle balance between hydration enthalpy of interlayer cations and Coulomb attraction to the silicate layers.

In total four maxima are of course observed for the two types of Na-complexes in contact with either the top or the bottom basal plane. A smaller fraction of  $\text{Na}^+$ -hexaquocomplexes ( $\approx 6\%$ ), however, resides at the center of the interlayer space at the same Z-coordinate as the central water layer giving rise to a diffuse double layer situation (Figure 1b).

### 3. Calculation of the volume fraction

The volume fraction  $\phi$  was obtained via  $\phi = \frac{(m_{\text{hec}} - m_{\text{interlayer water}})/\rho_{\text{hec}}}{\frac{(m_{\text{hec}} - m_{\text{interlayer water}})}{\rho_{\text{hec}}} + \frac{(m_{\text{water}} + m_{\text{interlayer water}})}{\rho_{\text{water}}}}$ ,

where  $\rho_{\text{hec}} = 2.8 \text{ g/cm}^3$  is the bulk density,  $m_{\text{hec}}$  the mass of the 1 WL  $\text{Na}_{0.5}$ -hectorite, respectively. The mass of interlayer water ( $m_{\text{interlayer water}}$ ) corresponds to the water content of the 1 WL  $\text{Na}_{0.5}$ -hectorite

#### 4. 2D-scattering patterns

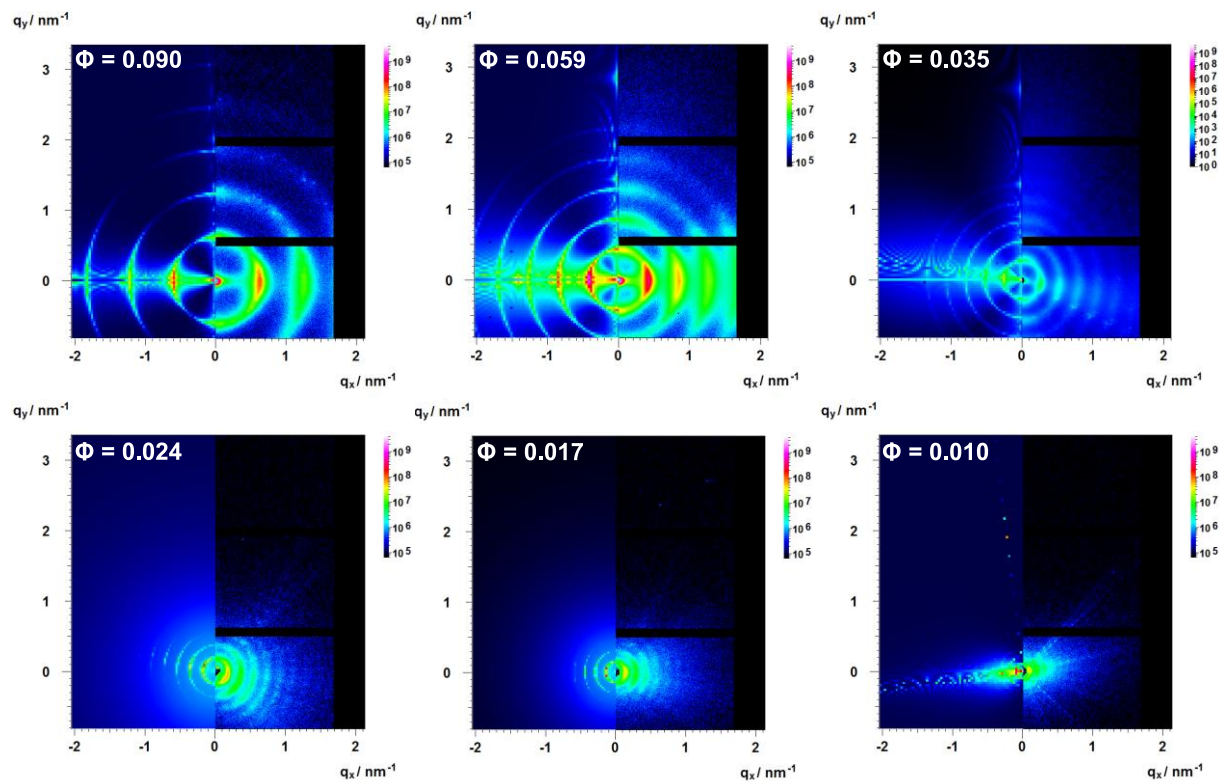


**Figure S3.** 2D-SAXS-patterns of  $\text{Na}_{0.5}$ -hectorite suspensions at different concentrations.

On the right side of the patterns, experimental data are plotted, on the left side modeled patterns are shown that were obtained applying the parameters of the tactoid lattice parameters given in Table 1

The insets in the left halves of the scattering patterns in Figure S2 show the calculated scattering patterns, which are in very good agreement with the measured scattering patterns (right halves). The narrow orientational distribution of individual layers in the tactoids give rise to arc-shaped Bragg-reflections that can be described by a model orientational distribution functions (Maier-Saupe or Gaussian) that allows one to compute the orientational order parameter  $S$  which is defined by  $s = \langle \frac{3\cos^2\alpha - 1}{2} \rangle$ , where  $\alpha$  is the angle between the local director and the disc axis. A value of  $S = 0$  is expected for randomly orientated phases and  $S = 1$  for perfect aligned layers. We observed values between  $S = 0.8$  for a concentrated sample ( $\phi = 0.090$ ) and  $S = 0.3$  for a highly diluted sample ( $\phi = 0.003$ ) (Table S1). Even the latter is still in the range typically observed for LC phases.

**Table S1.** Parameters of the tactoid lattice of 1D-SAXS data of  $\text{Na}_{0.5}$ -hectorite-gels.

	Regime II - Wigner Crystal				Regime III				
	0.090	0.059	0.035	0.024	0.017	0.010	0.007	0.003	0.002
volume fraction $\phi$	0.090	0.059	0.035	0.024	0.017	0.010	0.007	0.003	0.002
Unit cell $d$ [nm]	10.2	14.7	23.3	34.0	42.0	58.0	74.0	120.0	170.0
displacement $\delta$ [nm]	0.6	1.1	2.0	2.8	5.0	7.0	10.0	16.0	28
relative displacement	6%	8%	9%	9%	15%	12%	14%	22%	17%
structure factor $S(q)$	6.2	6.7	4.7	2.8	2.3	1.8	1.6	1.1	-
order parameter $S$	0.8	0.7	0.6	-	0.4	0.3	-	0.3	-

### 5. Change of the tactoid morphology upon swelling

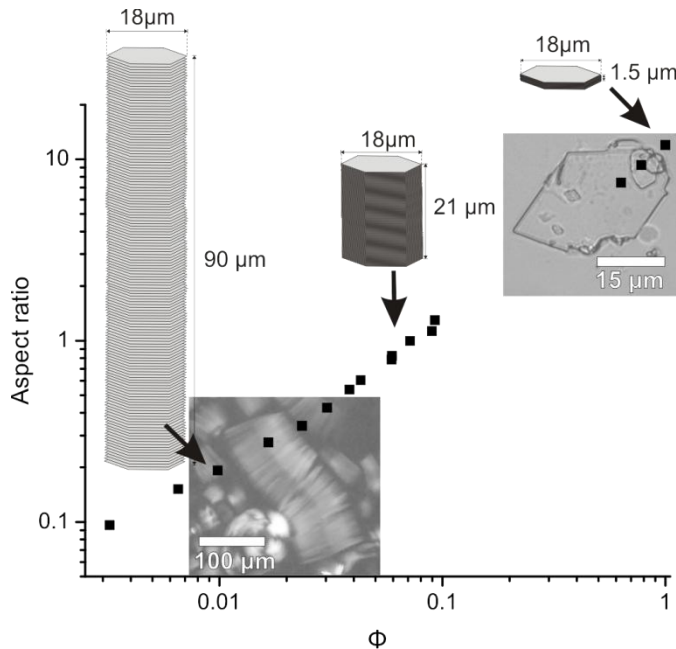


**Figure S4.** Evaluation of the aspect ratio (tactoid diameter divided by tactoid height). The insets show microscope images of swollen tactoids which are observed between crossed polarizers.

### 6. Illustration of an isotropic phase

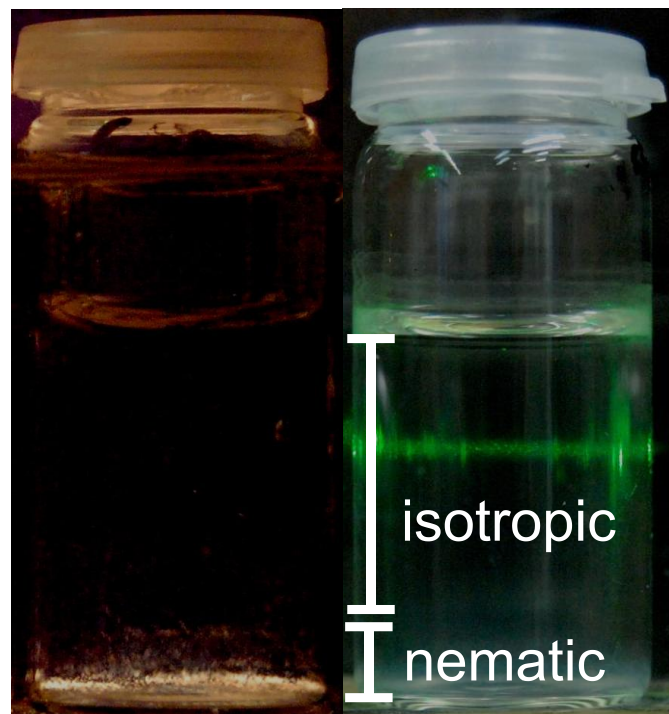


**Figure S5.**  $\text{Na}_{0.5}$ -hectorit dispersion ( $\phi = 0.0002$ ) between crossed polarizer (left) and under daylight (right). The scattering of the green laser pointer (right) illustrates the presence of an isotropic phase.

### 7. Shear induced birefringence of an isotropic phase

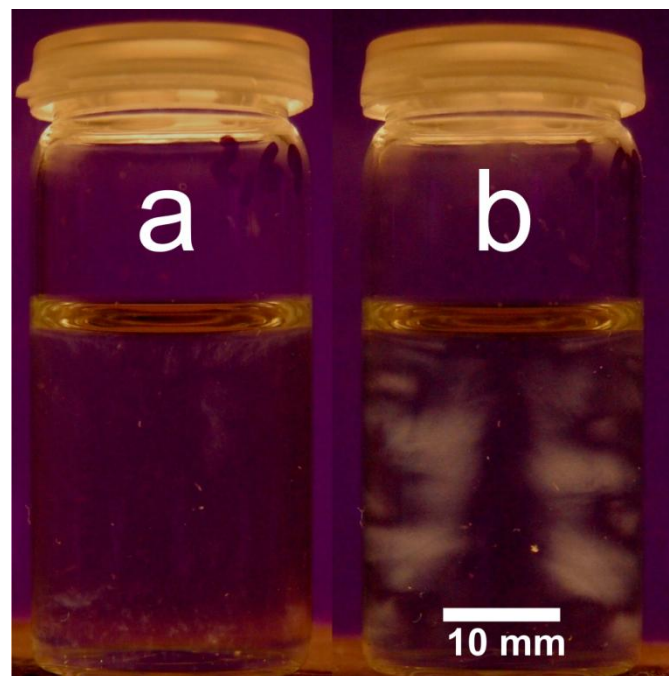


**Figure S6:**  $\text{Na}_{0.5}$ -hectorite suspension ( $\phi = 0.00009$ ) observed between crossed polarizer and analyzer (a) at rest (b) stirred.

## References

1. Blackmore, A., V & Miller, R. (1961) Tactoid size and osmotic swelling in calcium montmorillonite *Soil Sci Soc Amer Proc* **25**, 169-173.
2. Chiritescu, C., Cahill, D. G., Nguyen, N., Johnson, D., Bodapati, A., Kebelinski, P. & Zschack, P. (2007) Ultralow thermal conductivity in disordered, layered WSe<sub>2</sub> crystals *Science* **315**, 351-353.
3. Takada, K., Sakurai, H., Takayama-Muromachi, E., Izumi, F., Dilanian, R. A. & Sasaki, T. (2003) Superconductivity in two-dimensional CoO<sub>2</sub> layers *Nature* **422**, 53-55.
4. Novoselov, K. S., Geim, A. K., Morozov, S. V., Jiang, D., Zhang, Y., Dubonos, S. V., Grigorieva, I. V. & Firsov, A. A. (2004) Electric field effect in atomically thin carbon films *Science* **306**, 666-669.
5. Wu, W., Wang, L., Li, Y., Zhang, F., Lin, L., Niu, S., Chenet, D., Zhang, X., Hao, Y., Heinz, T. F. et al. (2014) Piezoelectricity of single-atomic-layer MoS<sub>2</sub> for energy conversion and piezotronics *Nature* **514**, 470-474.
6. Mashtalir, O., Naguib, M., Mochalin, V. N., Dall'Agnese, Y., Heon, M., Barsoum, M. W. & Gogotsi, Y. (2013) Intercalation and delamination of layered carbides and carbonitrides *Nat. Commun.* **4**, 1716.
7. Suk, J. W., Piner, R. D., An, J. & Ruoff, R. S. (2010) Mechanical Properties of Mono layer Graphene Oxide *Acs Nano* **4**, 6557-6564.
8. Kunz, D. A., Feicht, P., Goedrich, S., Thurn, H., Papastavrou, G., Fery, A. & Breu, J. (2013) Space-Resolved In-Plane Moduli of Graphene Oxide and Chemically Derived Graphene Applying a Simple Wrinkling Procedure *Adv. Mater.* **25**, 1337-1341.
9. Novoselov, K. S., Jiang, D., Schedin, F., Booth, T. J., Khotkevich, V. V., Morozov, S. V. & Geim, A. K. (2005) Two-dimensional atomic crystals *Proc. Natl. Acad. Sci. USA* **102**, 10451-10453.
10. Butz, B., Dolle, C., Niekiel, F., Weber, K., Waldmann, D., Weber, H. B., Meyer, B. & Specker, E. (2014) Dislocations in bilayer graphene *Nature* **505**, 533-537.
11. Kim, S. S., Van Khai, T., Kulish, V., Kim, Y. H., Na, H. G., Katoch, A., Osada, M., Wu, P. & Kim, H. W. (2015) Tunable Bandgap Narrowing Induced by Controlled Molecular Thickness in 2D Mica Nanosheets *Chem. Mater.* **27**, 4222-4228.
12. Lotya, M., Hernandez, Y., King, P. J., Smith, R. J., Nicolosi, V., Karlsson, L. S., Blighe, F. M., De, S., Wang, Z. M., McGovern, I. T. et al. (2009) Liquid Phase

- Production of Graphene by Exfoliation of Graphite in Surfactant/Water Solutions *J. Am. Chem. Soc.* **131**, 3611-3620.
13. Hofmann, U. (1932) Eindimensionale Quellung von Graphitsäure und Graphit. Die Reaktionsweisen des Graphits *Kolloid Z.* **61**, 297-304.
  14. Hofmann, U., Kurd, E. & Diederich, W. (1933) Kristallstruktur und Quellung von Montmorillonit (Das Tonmineral der Bentonittone) *Z. Kristallogr.* **86**, 340-348.
  15. Lagaly, G. (1981) Characterization of Clays by Organic-Compounds *Clay Miner.* **16**, 1-21.
  16. Ferrage, E., Lanson, B., Sakharov, B. A., Geoffroy, N., Jacquot, E. & Drits, V. A. (2007) Investigation of dioctahedral smectite hydration properties by modeling of X-ray diffraction profiles: Influence of layer charge and charge location *Amer. Mineral.* **92**, 1731-1743.
  17. Mehra, O. P. & Jackson, M. L. (1958) Iron oxide removal from soils and clays by dithionite-citrate system buffered with sodium bicarbonate *Clays Clay Miner.* **7**, 317-327.
  18. Paineau, E., Bihannic, I., Baravian, C., Philippe, A. M., Davidson, P., Levitz, P., Funari, S. S., Rochas, C. & Michot, L. J. (2011) Aqueous Suspensions of Natural Swelling Clay Minerals. 1. Structure and Electrostatic Interactions *Langmuir* **27**, 5562-5573.
  19. Stöter, M., Kunz, D. A., Schmidt, M., Hirsemann, D., Kalo, H., Putz, B., Senker, J. & Breu, J. (2013) Nanoplatelets of Sodium Hectorite Showing Aspect Ratios of ~□□□□□ and Superior Purity *Langmuir* **29**, 1280-1285.
  20. Kalo, H., Milius, W. & Breu, J. (2012) Single Crystal Structure Refinement of One- and Two-layer Hydrate of Sodium-Fluorohectorite *RSC Adv.* **2**, 8452-8459.
  21. Kalo, H., Milius, W., Bräu, M. & Breu, J. (2013) Synthesis and single crystal structure refinement of the one-layer hydrate of sodium brittle mica *J. Solid State Chem.* **198**, 57-64.
  22. Skipper, N. T., Lock, P. A., Titiloye, J. O., Swenson, J., Mirza, Z. A., Howells, W. S. & Fernandez-Alonso, F. (2006) The structure and dynamics of 2-dimensional fluids in swelling clays *Chem. Geol.* **230**, 182-196.
  23. Hofmann, U. & Hausdorf, A. (1942) Kristallstruktur und innerkristalline Quellung des Montmorillonits *Z. Kristallogr.* **104**, 265-293.

24. Langmuir, I. (1938) The Role of Attractive and Repulsive Forces in the Formation of Tactoids, Thixotropic Gels, Protein Crystals and Coacervates *J. Chem. Phys.* **6**, 873-896.
25. Michot, L. J., Bihannic, I., Maddi, S., Funari, S. S., Baravian, C., Levitz, P. & Davidson, P. (2006) Liquid-crystalline aqueous clay suspensions *Proc. Natl. Acad. Sci. USA* **103**, 16101-16104.
26. Michot, L. J., Bihannic, I., Maddi, S., Baravian, C., Levitz, P. & Davidson, P. (2008) Sol/gel and isotropic/nematic transitions in aqueous suspensions of natural nontronite clay. Influence of particle anisotropy. 1. Features of the I/N transition *Langmuir* **24**, 3127-3139.
27. Michot, L. J., Baravian, C., Bihannic, I., Maddi, S., Moyne, C., Duval, J. F. L., Levitz, P. & Davidson, P. (2009) Sol-Gel and Isotropic/Nematic Transitions in Aqueous Suspensions of Natural Nontronite Clay. Influence of Particle Anisotropy. 2. Gel Structure and Mechanical Properties *Langmuir* **25**, 127-139.
28. Paineau, E., Antonova, K., Baravian, C., Bihannic, I., Davidson, P., Dozov, I., Imperor-Clerc, M., Levitz, P., Madsen, A., Meneau, F. et al. (2009) Liquid-Crystalline Nematic Phase in Aqueous Suspensions of a Disk-Shaped Natural Beidellite Clay *J. Phys. Chem. B* **113**, 15858-15869.
29. Miyamoto, N., Iijima, H., Ohkubo, H. & Yamauchi, Y. (2010) Liquid crystal phases in the aqueous colloids of size-controlled fluorinated layered clay mineral nanosheets *Chem. Commun.* **46**, 4166-4168.
30. Hemmen, H., Ringdal, N. I., De Azevedo, E. N., Engelsberg, M., Hansen, E. L., Meheust, Y., Fossum, J. O. & Knudsen, K. D. (2009) The Isotropic-Nematic Interface in Suspensions of Na-Fluorohectorite Synthetic Clay *Langmuir* **25**, 12507-12515.
31. Gabriel, J. C., Camerel, F., Lemaire, B. J., Desvaux, H., Davidson, P. & Batail, P. (2001) Swollen liquid-crystalline lamellar phase based on extended solid-like sheets *Nature* **413**, 504-508.
32. Geng, F., Ma, R., Nakamura, A., Akatsuka, K., Ebina, Y., Yamauchi, Y., Miyamoto, N., Tateyama, Y. & Sasaki, T. (2013) Unusually stable ~100-fold reversible and instantaneous swelling of inorganic layered materials *Nat Commun* **4**, 1632.
33. Lindemann, F. A. (1910) The calculation of molecular vibration frequencies *Z. Phys* **11**, 609-615.
34. Hyde, S. T. (2001) in *Handbook of Applied Surface and Colloid Chemistry*, ed. Holmberg, K. (John Wiley & Sons, Chichester), pp. 299-332.

35. Hyde, S. T. (1997) Swelling and structure. Analysis of the topology and geometry of lamellar and sponge lyotropic mesophases *Langmuir* **13**, 842-851.
36. Ruzicka, B., Zaccarelli, E., Zulian, L., Angelini, R., Sztucki, M., Moussaid, A., Narayanan, T. & Sciortino, F. (2011) Observation of empty liquids and equilibrium gels in a colloidal clay *Nat. Mater.* **10**, 56-60.
37. Breu, J., Seidl, W., Stoll, A. J., Lange, K. G. & Probst, T. U. (2001) Charge homogeneity in synthetic fluorohectorite *Chem. Mater.* **13**, 4213-4220.
38. Foerster, S., Fischer, S., Zielske, K., Schellbach, C., Sztucki, M., Lindner, P. & Perlich, J. (2011) Calculation of scattering-patterns of ordered nano- and mesoscale materials *Adv. Colloid Interface Sci.* **163**, 53-83.
39. Martinez, L., Andrade, R., Birgin, E. & Martinez, J. (2009) PACKMOL: A Package for Building Initial Configurations for Molecular Dynamics Simulations *J. Comput. Chem.* **30**, 2157-2164.
40. Plimpton, S. (1995) Fast Parallel Algorithms for Short-Range Molecular-Dynamics *J. Comput. Phys.* **117**, 1-19.
41. Cygan, R. T., Liang, J. J. & Kalinichev, A. G. (2004) Molecular models of hydroxide, oxyhydroxide, and clay phases and the development of a general force field *J. Phys. Chem. B* **108**, 1255-1266.
42. Marry, V., Dubois, E., Malikova, N., Durand-Vidal, S., Longeville, S. & Breu, J. (2011) Water Dynamics in Hectorite Clays: Influence of Temperature Studied by Coupling Neutron Spin Echo and Molecular Dynamics *Environ. Sci. Technol.* **45**, 2850-2855.
43. Berendsen, H. J. C., Grigera, J. R. & Straatsma, T. P. (1987) The Missing Term in Effective Pair Potentials *J. Phys. Chem.* **91**, 6269-6271.
44. Humphrey, W., Dalke, A. & Schulten, K. (1996) VMD: Visual molecular dynamics *J. Mol. Graph* **14**, 33-38.

## 6. Publikationsliste

### 6.1 Publikationen

Rosenfeldt, S.; **Stöter, M.**; Schlenk, M.; Martin, T.; Albuquerque, R. Q.; Förster, S.; Breu, J. In depth insights into the key steps of delamination of charged 2D materials. *submitted 2016.*

**Stöter, M.**; Gödrich, S.; Feicht, P.; Rosenfeldt, S.; Thurn, H.; Neubauer, J. W.; Seuss, M.; Lindner, P.; Kalo, H.; Möller, M.; Fery, A.; Förster, S.; Papastavrou, G.; Breu<sup>i</sup> Controlled exfoliation of layered silicate heterostructures into bilayers and their conversion into giant Janus-platelets. *Angew. Chem. Int. Ed.* **2016**, DOI: 10.1002/anie.201601611

Hausner, J.; Fischer, B.; **Stöter, M.**; Edenharter, A.; Schmid, J.; Kunz, R.; Rosenfeldt, S.; Altstädt, V.; Breu, J. Increasing time of ignition for PS-clay nanocomposites filled with  $[Fe(bpy)_3]^{2+}$ -modified hectorite. *Polym. Degrad. Stabil.* **2016**, 128, 141–148.

**Stöter, M.**; Biersack, B.; Rosenfeldt, S.; Leitl, M. J.; Kalo, H.; Schobert, R.; Yersin, H.; Ozin, G. A.; Förster, S.; Breu, J. Encapsulation of Functional Organic Compounds in Nanoglass for Optically Anisotropic Coatings. *Angew. Chem. Int. Ed.* **2015**, 54, 4963-4967.

**Stöter, M.**; Biersack, B.; Rosenfeldt, S.; Leitl, M. J.; Kalo, H.; Schobert, R.; Yersin, H.; Ozin, G. A.; Förster, S.; Breu, J. Nanoglas-Verkapselung funktionaler organischer Verbindungen für optisch anisotrope Beschichtungen. *Angew. Chem.* **2015**, 127, 5047-5051.

**Stöter, M.**; Rosenfeldt, S.; Breu, J. Tunable Exfoliation of Synthetic Clays. *Annu. Rev. Mater. Res.* **2015**, 45, 129-151.

**Stöter, M.**; Biersack, B.; Reimer, N.; Herling, M.; Stock, N.; Schobert, R.; Breu, J. Ordered Heterostructures of Two Strictly Alternating Types of Nanoreactors. *Chem. Mater.* **2014**, 26, 5412-5419.

**Stöter, M.**; Kunz, D. A.; Schmidt, M.; Hirsemann, D.; Kalo, H.; Putz, B.; Senker, J.; Breu, J. Nanoplatelets of Sodium Hectorite Showing Aspect Ratios of ~20000 and Superior Purity. *Langmuir*. **2013**, 29, 1280-1285.

You, S. J.; Kunz, D.; **Stöter, M.**; Kalo, H.; Putz, B.; Breu, J.; Talyzin, A. V. Pressure-Induced Water Insertion in Synthetic Clays. *Angew. Chem. Int. Ed.* **2013**, 52, 3891-3895.

## 6.2 Konferenzbeiträge

- 2014 GDCh-Vortragstagung FG Festkörperchemie und Materialforschung - Dresden  
*Ordered functional heterostructures via simple intercalation reactions* (Poster)
- 2015 Bayreuther Polymer Symposium - Bayreuth  
*Tailor-made fillers for functional coatings* (Poster)
- 2015 Covestro-Doktorandenworkshop - Bayreuth  
*Maßgeschneiderte Füllstoffe für funktionale Coatings* (Vortrag)
- 2015 SFB 840 Doktorandenworkshop - University of Massachusetts, Amherst (USA)  
*Controlled exfoliation of synthetic clays* (Vortrag)

## 6.3 Presseveröffentlichungen

- 2015 Chemie.de  
innovations-report.de  
Informationsdienst Wissenschaft (idw)  
*Farbstoff im Glas-Sandwich - Durch Quellung von Tonmaterialien hydrophobe funktionale Moleküle verkapseln*  
<http://www.chemie.de/news/151988/farbstoff-im-glas-sandwich.html>  
<http://www.innovations-report.de/html/berichte/biowissenschaften-chemie/farbstoff-im-glas-sandwich.html>  
<https://idw-online.de/en/news626876>
- 2015 Chemistryviews.org  
TG Techno - Nanotechnology Zone  
nanowerk.com  
*A Dye in a Glassy Sandwich: Swelling of a layered clay mineral leads to encapsulation of functional hydrophobic organic molecules*  
[http://www.chemistryviews.org/details/ezine/7553021/A\\_Dye\\_in\\_a\\_Glassy\\_Sandwich.html](http://www.chemistryviews.org/details/ezine/7553021/A_Dye_in_a_Glassy_Sandwich.html)  
<http://www.nanowerk.com/nanotechnology-news/newsid=39294.php>  
<http://tgtechno.com/nanotechnologyzone/index.php/news/research-news/4703-a-dye-in-a-glassy-sandwich-swelling-of-a-layered-clay-mineral-leads-to-encapsulation-of-functional-hydrophobic-organic-molecules>
- 2015 Phys.org  
*Technique encapsulates functional hydrophobic organic molecules*  
<http://phys.org/news/2015-03-technique-encapsulates-functional-hydrophobic-molecules.html>

## 7. Danksagung

Ich möchte mich bei allen Menschen bedanken, die mich im Laufe der Promotion und während des Masterstudiums an der Universität Bayreuth unterstützt haben. Es war durch Euch eine sehr schöne Zeit.

Mein ganz besonderer Dank gilt meinem Betreuer Herrn Prof. Dr. Josef Breu, der mir dieses interessante und spannende Promotionsthema ermöglichte, der mich während der gesamten Promotion immer unterstützt hat, sich bei meinen Fragen stets Zeit nahm, der mir die benötigten Freiheiten bei der Forschung lies, mich aber, wenn nötig, wieder auf den richtigen Weg zurückführte.

An dieser Stelle möchte ich mich auch für die tolle, weil fruchtbare, fachlich interessante und sehr unterhaltsame Zusammenarbeit mit den zahlreichen Mitarbeitern der anderen Chemielehrstühle an der Universität Bayreuth bedanken. Besonders zu erwähnen sind hier Dr. Sabine Rosenfeldt und Prof. Dr. Stephan Förster aus der Physikalischen Chemie I; Dr. Bernhard Biersack und Prof. Dr. Schobert aus der Organischen Chemie I und Sebastian Gödrich und Prof. Dr. Georg Papastavrou aus der Physikalischen Chemie II, sowie Herrn Prof. Dr. Jürgen Senker aus der Anorganischen Chemie III. Es ist großartig, dass so eine enge und gute Zusammenarbeit der verschiedenen Lehrstühle an der Universität Bayreuth möglich ist.

Mein Dank gilt ferner der sehr guten Unterstützung aus meinen Kooperationen außerhalb der Universität Bayreuth. Für die gute Zusammenarbeit bei der Probencharakterisierung und die fruchtbaren Diskussionen möchte ich mich bei Dr. Markus Leitl und Herrn Prof. Dr. Hartmut Yersin von der Universität Regensburg sowie Neele Reimer und Herr Prof. Dr. Norbert Stock von der Universität Kiel bedanken.

Außerdem möchte ich mich für die sehr schöne Zeit, die Unterstützung, die netten Unterhaltungen bei allen Freunden und Mitarbeitern der beiden Lehrstühle Anorganische Chemie I und Anorganische Chemie III bedanken.

In diesem Zusammenhang sind natürlich meine langjährigen Laborkollegen Dr. Hussein Kalo und Josef Hausner zu erwähnen, durch welche meine Arbeit in unserem kleinen Labor immer besonders abwechslungsreich und unterhaltsam war. Bei Paul Niemietz, Dominik Greim und Marco Schmidt möchte ich mich für das unermüdliche ehrenamtliche Engagement der Betreuung des Kaffeezimmers bedanken.

Zum Schluss danke ich den drei großartigen Familien aus dem Herzen Ostfrieslands: Meinen Eltern, Geschwistern und Großeltern, sowie der Familie Hardt aus Horsten und der

## 7. Danksagung

Familie Thedinga aus Esens danke ich für die unablässige Unterstützung und den Rückhalt während meines langjährigen „Auslandsaufenthaltes“.

Ich möchte schließen mit dem herzlichen Dank an meine einzigartige, geliebte Frau Ann-Kathrin und an meine beiden geliebten Kinder Eike Dirk und Antja Lina ohne die diese Arbeit nicht möglich gewesen wäre. Danke Euch für die Liebe, das Vertrauen, den Zuspruch und den Rückhalt, die mir in allen Phasen dieser Arbeit immer sicher waren.

## 8. Erklärung des Verfassers

### (Eidesstattliche) Versicherungen und Erklärungen

(§ 5 Nr. 4 PromO)

*Hiermit erkläre ich, dass keine Tatsachen vorliegen, die mich nach den gesetzlichen Bestimmungen über die Führung akademischer Grade zur Führung eines Doktorgrades unwürdig erscheinen lassen.*

(§ 8 S. 2 Nr. 5 PromO)

*Hiermit erkläre ich mich damit einverstanden, dass die elektronische Fassung meiner Dissertation unter Wahrung meiner Urheberrechte und des Datenschutzes einer gesonderten Überprüfung hinsichtlich der eigenständigen Anfertigung der Dissertation unterzogen werden kann.*

(§ 8 S. 2 Nr. 7 PromO)

*Hiermit erkläre ich eidesstattlich, dass ich die Dissertation selbständig verfasst und keine anderen als die von mir angegebenen Quellen und Hilfsmittel benutzt habe.*

(§ 8 S. 2 Nr. 8 PromO)

*Ich habe die Dissertation nicht bereits zur Erlangung eines akademischen Grades anderweitig eingereicht und habe auch nicht bereits diese oder eine gleichartige Doktorprüfung endgültig nicht bestanden.*

(§ 8 S. 2 Nr. 9 PromO)

*Hiermit erkläre ich, dass ich keine Hilfe von gewerblichen Promotionsberatern bzw. -vermittlern in Anspruch genommen habe und auch künftig nicht nehmen werde.*

.....  
Ort, Datum, Unterschrift